

ADVANCED CONTROL APPROACHES FOR RENEWABLE ENERGY
INTEGRATION TO IMPROVE OVERALL STABILITY AND RELIABILITY OF
POWER GRID

by

Anuprabha Ravindran Nair

A dissertation submitted to the faculty of
The University of North Carolina at Charlotte
in partial fulfillment of the requirements
for the degree of Doctor of Philosophy in
Electrical Engineering

Charlotte

2021

Approved by:

Dr. Sukumar Kamalasan

Dr. Yogendra Kakad

Dr. Abasifreke Ebong

Dr. Michael Smith

Dr. Joanna K. Krueger

©2021
Anuprabha Ravindran Nair
ALL RIGHTS RESERVED

ABSTRACT

ANUPRABHA RAVINDRAN NAIR. Advanced Control Approaches For Renewable Energy Integration To Improve Overall Stability And Reliability Of Power Grid.

(Under the direction of DR. SUKUMAR KAMALASADAN)

Renewable energy-based electric power generation is receiving more attention due to the increasing power demand and environmental concerns. The interconnection of these distributed resources to the grid is based on the grid code standards to ensure power quality, reliability, and security. The intermittent nature of the renewable penetrated grid, along with phasing out of conventional generation units, new HVDC lines, and long-distance transmissions from remote areas, impose several challenges to grid stability. Hence it is crucial to explore control approaches that can efficiently control these Distributed Energy Resources (DERs) to improve the overall power quality and reliability. This dissertation presents modeling, stability studies, and advanced control architectures that can support and coordinate the Wind Energy Conversion Systems (WECS) and other inverter-based Distributed Energy Resources (DERs) to improve the quality of the generation, transmission, and distribution systems. The first part of the work proposes advanced adaptive-based robust sensorless control approaches for rotor side and grid side control of DFIG based WECS. Further, the dissertation discusses the challenges of transferring high power of renewable penetrated grid and some possible solutions and control approaches. Finally, the work efficiently coordinates the available resources to ensure power quality in a distribution network. All the proposed designs are validated using simulation results developed by dynamic models or through real-time simulators, which proves the ability of the advanced controllers to improve grid reliability. The quantification based on standard metrics used for performance improvements discussed in each design shows that the designs have exceptional advantages compared with conventional controllers.

DEDICATION

This dissertation is dedicated to my beloved parents Ravindran and Ambika, my sister Vidhyapriya, brother in law Vivek, my nephew Vaishnav and my husband Sreekumar and son Srihari whose prayers and support has paved the way for this study.

ACKNOWLEDGEMENTS

I would like to express my sincere gratitude to Dr. Sukumar Kamalasan for giving me this opportunity and for all his guidance that helped me shape my skills as a researcher. I would also like to thank Dr. Michael Smith for his time and guidance during this journey.

I would also like to express my sincere thanks to the advisory committee of Dr. Yogendra Kakad, Dr. Abasifreke Ebong, and Dr. Joanna. K.Krueger for their time and support.

I would like to thank UNC Charlotte Graduate School, the ECE department, and PEISL Lab for providing suitable facilities and GASP to perform research.

I would also like to express my sincere gratitude for the graduate assistantships offered by the department and funded by NSF and Siemens.

I am also grateful to my team members and friends who have been motivating me throughout this study.

Last but not least, I would like to express my sincere thanks to my family, my husband Sreekumar, and my son Srihari for their support and inspiration throughout this journey.

TABLE OF CONTENTS

LIST OF TABLES	xii
LIST OF FIGURES	xiv
CHAPTER 1: INTRODUCTION	1
1.1. Requirements for Grid Integration of DFIG Based WECS	2
1.2. Technical Challenges	4
1.2.1. Intermittent and uncontrollable nature of wind speed	4
1.2.2. Challenges in managing grid stability, reliability and power quality	4
1.2.3. Wind power transmission over long distance networks	5
1.3. State-of-the-art of DFIG Control Techniques to Meet Grid Code	6
1.3.1. WECS Classification	7
1.3.2. DFIG Configuration and Converter Control	8
1.3.3. Solutions to Meet Grid Code Requirements	12
1.4. Dissertation: Objectives and Contributions	18
CHAPTER 2: PARAMETRICALLY ROBUST MUTUAL INDUCTANCE ESTIMATION BASED ADAPTIVE CONTROL ARCHITECTURE FOR DFIG	21
2.1. Introduction	21
2.1.1. State-of-the-Art	22
2.1.2. Main Contributions	23
2.2. Adaptive Control Framework	24
2.2.1. Proposed Speed Observer	24
2.2.2. Modification to RSC Controller	26

2.2.3.	Identification Methodology	27
2.2.4.	EMVC Framework	28
2.2.5.	Improved Dynamic Reactive Power Support Capability	31
2.3.	Simulation and Experimental Results	32
2.3.1.	Simulation Results	32
2.3.2.	Experimental Validation	38
2.3.3.	Scalability Test Results	41
2.4.	Chapter Summary	44
CHAPTER 3: A SENSORLESS ADAPTIVE GRID SIDE CONTROL APPROACH FOR DFIG		46
3.1.	Introduction	46
3.1.1.	State-of-the-Art	47
3.1.2.	Main Contributions	48
3.2.	Speed Observer for DFIG	49
3.3.	Recursive Least Squares System Identification	50
3.4.	Minimum Variance Control	52
3.5.	Simulation and Experimental Results	55
3.5.1.	Simulation Results	55
3.5.2.	Experimental Validation	59
3.6.	Chapter Summary	63

CHAPTER 4: PROPOSAL FOR MULTIPLE INPUT MULTIPLE OUTPUT (MIMO) IDENTIFICATION BASED COORDINATED FREQUENCY CONTROL ARCHITECTURE FOR DFIG	65
4.1. Introduction	65
4.1.1. State-of-the-Art	66
4.1.2. Main Contributions	68
4.2. Frequency Control Architecture	68
4.2.1. Inertial Control	70
4.2.2. Droop Control	71
4.2.3. Pitch Angle Control	72
4.3. Simulation Results	74
4.3.1. Test1: Analysis of Kinetic Energy Control	75
4.3.2. Test2: Analysis of Droop Control	79
4.3.3. Test3: Analysis of Pitch Control Loop	79
4.4. MIMO Coordination Frequency Control Approach for Grid Connected DFIG	82
4.4.1. Development of Mathematical Model for the Coordinated Approach	83
4.4.2. Coordinated Control Approach	88
4.5. Preliminary Results	89
4.5.1. Case A : Analysis for a Sub Synchronous Constant Wind Speed	89
4.5.2. Case B : Analysis for a Super Synchronous Constant Wind Speed	91
4.5.3. Case C : Analysis for a Varying Wind Speed	92

4.6. Future Works	93
4.7. Chapter Summary	95
CHAPTER 5: MODELING OF DFIG INTEGRATED WEAK GRID AND DYNAMIC PERFORMANCE ANALYSIS WITH SYN- CHRONOUS CONDENSER	97
5.1. Introduction	97
5.1.1. State-of-the-Art	98
5.1.2. Major Contributions	100
5.2. Mathematical Model of Weak Power Grid Model	100
5.2.1. Modeling of the Grid	101
5.2.2. Mathematical Modeling of Type4 Wind Farm	102
5.3. An Investigation of Grid Stability Based on Small Signal Anal- ysis and Proposal of Adaptive PLL Control	104
5.3.1. Development of Small Signal Representation of the Power Grid Model with PLL	104
5.3.2. Stability Analysis Based on the Small Signal Model and the Impact of PLL	111
5.3.3. Proposed Control Architecture With Adaptive Grid Model	120
5.3.4. Simulation Results	125
5.4. Possible Solutions to Improve Stability of Wind on Weak Grid	137
5.5. Impact of Synchronous Condenser on Wind Integrated Weak Grid Systems	138
5.5.1. Mathematical Modeling of SC	138
5.5.2. Steady State Analysis	139
5.5.3. Transient Analysis	140

5.5.4.	Effect of Synchronous Condenser at PCC	140
5.5.5.	Effect of Synchronous Condenser Parameters on Stability and Oscillation	141
5.5.6.	Performance Comparison of Different Compensation Techniques	147
5.6.	Future Works	153
5.7.	Chapter Summary	155
CHAPTER 6: A COORDINATED OPTIMAL FEEDBACK CONTROL FOR MITIGATION OF MOTOR STARTING VOLTAGE SAGS IN DER INTEGRATED DISTRIBUTION NETWORKS		156
6.1.	Introduction	156
6.1.1.	State-of-the-Art	157
6.1.2.	Major Contributions	158
6.2.	Proposed Control Architecture	159
6.2.1.	MIMO Identification for Coordinated control	160
6.2.2.	Linear Quadratic Regulator	163
6.3.	Proposed Coordinated Control Approach	166
6.3.1.	Design of DG Local Controller (LC)	167
6.3.2.	Design of Coordinated Controller (CC)	167
6.4.	Implementation of Proposed Coordinated Controller	169
6.5.	Simulation Results	171
6.5.1.	Test 1: Performance Analysis with One Motor Two DG	171
6.5.2.	Test 2: Performance Analysis with Two Motor Two DG with Motor Close to DG at Bus 79	174

6.5.3.	Test 3: Performance Analysis with Two Motor Two DG with Motor Close to DG at Bus 5	176
6.5.4.	Test 4: Scalability Test on 123 Bus Distribution System with Single and Multiple VSDG	179
6.5.5.	Test 5: Scalability Test on 123 Bus Distribution System with Multiple VSDG and Motor	182
6.6.	Chapter Summary	186
CHAPTER 7: AN OPTIMAL POLICY-DRIVEN INTEGRATED CONTROL FRAMEWORK FOR GRID-TIED INVERTERS BASED ON FREQUENCY DECOMPOSITION METHODOLOGY		187
7.1.	Introduction	187
7.1.1.	State-of-the-Art	188
7.1.2.	Major Contributions	189
7.2.	Three Phase Inverter Model in $d - q$ Reference Frame	190
7.3.	Overview of Proposed Methodology	192
7.3.1.	Policy Generation	193
7.3.2.	Proposed Integrated Control Architecture	200
7.4.	Simulation Results	203
7.4.1.	Analysis on IEEE 13 bus system	203
7.4.2.	Scalability Test	213
7.5.	Chapter Summary	217
CHAPTER 8: CONCLUSIONS AND FUTURE WORK		219
REFERENCES		223
APPENDIX A: Machine Parameters		234
APPENDIX B: IEEE Test System		238

LIST OF TABLES

TABLE 1.1: Performance Comparison of Different WECS configurations	7
TABLE 1.2: Performance Comparison of Different MPPT Methods	14
TABLE 2.1: Relative Error Comparison	34
TABLE 2.2: Scalability Test Results	44
TABLE 3.1: Comparison of Different Test Results	59
TABLE 3.2: Comparison of RT-LAB Test Results	63
TABLE 4.1: Eigen Value Analysis and Participation of States for Case A	90
TABLE 4.2: Eigen Value Analysis and Participation of States for Case B	92
TABLE 4.3: Eigen Value Analysis and Participation of States for Case C	94
TABLE 5.1: Network Impedance for Different Test Cases	101
TABLE 5.2: Comparison of Simulation Results	134
TABLE 5.3: Summary of the Steady State (S.S) Analysis	139
TABLE 5.4: Analysis of Different SC Parameters on Stability	142
TABLE 5.5: Analysis of Different SC Parameters on Oscillations Frequencies	142
TABLE 5.6: Analysis of Exciter Gain Effect on Low Frequency Oscillation for a 50MVA SC	142
TABLE 5.7: Analysis of Transient Reactance Effect on Low Frequency Oscillation for a 50MVA SC	147
TABLE 6.1: Performance Analysis of Test1 Result with Proposed VSDG	174
TABLE 6.2: Performance Analysis of of Test 2 Result using the Proposed Control	175

TABLE 6.3: Performance Analysis of Test 3 Result with the Proposed VSDG	180
TABLE 6.4: Results of Scalability Test 4 and Test 5 with the Proposed VSDG	184
TABLE 6.5: Relation of Percentage Steady State Error to Number of DGs	185
TABLE 7.1: Comparison of Test Results VC: Vector Control, PC: Proposed Control	207
TABLE 7.2: Comparison of Scalability Test Results VC: Vector Control, PC: Proposed Control	217
TABLE A.1: DFIG Parameters	234
TABLE A.2: Synchronous Generator Parameters	235
TABLE A.3: Parameters of WRIM used in HIL	236
TABLE A.4: Parameters of Synchronous Condenser	237

LIST OF FIGURES

FIGURE 1.1: General Schematic of DFIG.	8
FIGURE 1.2: Reactive Power Control	12
FIGURE 1.3: Voltage Control Loop	12
FIGURE 1.4: MPPT Control	13
FIGURE 1.5: Convention Pitch Control Loop	15
FIGURE 1.6: LVRT Standard Set by FERC	17
FIGURE 2.1: DFIG based Wind Energy Conversion Systems (WECS).	25
FIGURE 2.2: Schematic Diagram of the Proposed Adaptive Controller.	26
FIGURE 2.3: Proposed EMVC based Control Architecture.	28
FIGURE 2.4: Test1: Rotor Angle in Radians for 50% L_m Increase.	33
FIGURE 2.5: Test1: Angle Offset Error(deg) for L_m Variation.	33
FIGURE 2.6: Test1: Rotor Speed Estimation Error for L_m Variation.	34
FIGURE 2.7: Test2: Stator Terminal Voltage.	35
FIGURE 2.8: Test2: Frequency Support during Terminal Voltage Variation.	35
FIGURE 2.9: Test2: Reactive Power Support during Terminal Voltage Variation.	36
FIGURE 2.10: Test3: Terminal Voltage during Fault.	36
FIGURE 2.11: Test3: Frequency Support during Fault.	37
FIGURE 2.12: Test4: Terminal Voltage during LVRT.	37
FIGURE 2.13: Test4: Comparison of Reactive Power Support during LVRT.	38

FIGURE 2.14: Test4: Speed Estimation Error during LVRT with a L_m change.	38
FIGURE 2.15: Schematic of Proposed Control Model for RT-LAB.	39
FIGURE 2.16: Percentage Speed Estimation Error for L_m variation.	40
FIGURE 2.17: Angle Offset Error(deg) for L_m Variation.	40
FIGURE 2.18: Terminal Voltage and Reactive Power Support during Grid Voltage Sag.	41
FIGURE 2.19: Comparison of Actual Speed and Estimated Speed during L_m Variation.	41
FIGURE 2.20: One Line Diagram of the Test System used to Perform Scalability Test.	42
FIGURE 2.21: Case A: Speed Estimation Error during an L_m Change.	43
FIGURE 2.22: Case A: Angle Offset Error during an L_m Change.	43
FIGURE 2.23: Case A: Estimated Rotor Speed during an L_m Change.	44
FIGURE 2.24: Case B: PCC voltage during Sudden Load Change.	44
FIGURE 2.25: Case B: Reactive Power during Sudden Load Change.	45
FIGURE 3.1: Schematic Diagram of the Proposed Adaptive Controller.	52
FIGURE 3.2: Proposed System Identification based Control Structure Augmented to Conventional Vector Control for DFIG.	53
FIGURE 3.3: One Line Diagram of the Test System used to Analyze the Performance of the Proposed Controller	56
FIGURE 3.4: Test 1: Wind Speed used to Test the Performance of Proposed Controller.	56
FIGURE 3.5: Test 1: DFIG Rotor Speed Estimation with Proposed Control.	57
FIGURE 3.6: Test 1: Speed Estimation Error for Proposed Identification based Control for Wind Speed shown in Figure.3.4.	57

FIGURE 3.7: Test 2: Comparison between PCC Voltage Regulation from DFIG when using Vector Control and Proposed Identification based Control during Voltage Sag due to Grid Fault.	58
FIGURE 3.8: Test 2: Comparison between DC Link Voltage Variation from DFIG when using Vector Control and Proposed Identification based Control during Voltage Sag due to Grid Fault.	58
FIGURE 3.9: Test 3: Comparison of PCC Voltage during Speed Sensor Failure for Vector Control and Proposed Identification based Control.	59
FIGURE 3.10: Schematic of Proposed Control Model for RT-LAB.	60
FIGURE 3.11: Wind Speed used for Real Time Simulation of Proposed Controller.	61
FIGURE 3.12: DFIG Rotor Speed Estimation with Proposed Control.	61
FIGURE 3.13: Speed Estimation Error for Proposed Identification based Control for Wind Speed shown in Figure.3.11.	61
FIGURE 3.14: Comparison of PCC Voltage during Three Phase Fault for Vector Control and Proposed Identification based Control.	62
FIGURE 3.15: Comparison of DC Link Voltage during Three Phase Fault for Vector Control and Proposed Identification based Control.	62
FIGURE 3.16: Comparison of PCC Voltage during Dynamic Load Changes for Vector Control and Proposed Identification based Control.	63
FIGURE 3.17: Comparison of DC Link Voltage during Dynamic Load Changes for Vector Control and Proposed Identification based Control.	64
FIGURE 3.18: Comparison of PCC Voltage during Speed Sensor Failure for Vector Control and Proposed Identification based Control.	64
FIGURE 4.1: Typical Frequency Response Characteristics[88].	69
FIGURE 4.2: Power Versus Turbine Speed Curve for Different Wind Velocities	72

FIGURE 4.3: Performance Coefficient Versus Tip Speed ratio Curve for Different Wind Velocities	72
FIGURE 4.4: Deloaded Power Curves for Wind Turbines[40]	73
FIGURE 4.5: One Line Diagram of Reduced Two Area Test System	74
FIGURE 4.6: Rotor Speed for Different Wind Velocities with Kinetic Energy Control	75
FIGURE 4.7: Active Power Output with Kinetic Energy Control	76
FIGURE 4.8: Frequency Improvement with Kinetic Energy Control with Different Inertial Constants at 10m/s	77
FIGURE 4.9: Active Power Output with Kinetic Energy Control with Different Inertial Constants at 10m/s	77
FIGURE 4.10: Rotor Speed with Kinetic Energy Control with Different Inertial Constants at 10m/s	78
FIGURE 4.11: Active Power Output with Kinetic Energy Control with Different Inertial Constants at 7m/s	78
FIGURE 4.12: Rotor Speed with Kinetic Energy Control with Different Inertial Constants at 7m/s	79
FIGURE 4.13: Frequency with Droop Control at 10m/s	80
FIGURE 4.14: Active power with Droop Control at 10m/s	80
FIGURE 4.15: Frequency Improvement with Pitch Control at 13m/s	81
FIGURE 4.16: Pitch Angle Defined by the Loop at 13m/s	81
FIGURE 4.17: Schematic of Proposed Coordinated Control Architecture	82
FIGURE 4.18: Detailed Overview of Proposed Coordinated Frequency Control Architecture	89
FIGURE 4.19: Grid Frequency Deviation with Proposed Coordinated Control Architecture for Case A	90

FIGURE 4.20: Output Power with Proposed Coordinated Control Architecture for Case A	91
FIGURE 4.21: Grid Frequency Deviation with Proposed Coordinated Control Architecture for Case B	91
FIGURE 4.22: Output Power with Proposed Coordinated Control Architecture for Case B	92
FIGURE 4.23: Grid Frequency Deviation with Proposed Coordinated Control Architecture for Case C	93
FIGURE 4.24: Wind Speed used for Analysis of Case C	93
FIGURE 4.25: Stator Power with Proposed Coordinated Control Architecture for Case A	94
FIGURE 4.26: Pitch Angle Reference with Proposed Coordinated Control Architecture for Case C	94
FIGURE 4.27: Delta P Calculated with Proposed Coordinated control Architecture for Case C	95
FIGURE 5.1: WTG Integrated Weak Grid Model.	100
FIGURE 5.2: Structure of Synchronous Generator Model.	102
FIGURE 5.3: General Structure of Type 4 Wind Turbine Generator.	102
FIGURE 5.4: Grid-Side Converter Control System.	103
FIGURE 5.5: Small Signal Model of a Synchronous Reference Frame PLL.	109
FIGURE 5.6: a) PCC Voltage Variations with Grid Strength. b) PCC Reactive Power Variations with Grid Strength.	111
FIGURE 5.7: Impact of PLL Bandwidth on Transient Stability	112
FIGURE 5.8: Bode Diagram of Closed Loop PLL Model.	114
FIGURE 5.9: Bode Diagram to Explain the Influence of Proportional Gain K_p on Stability, Bandwidth and Oscillation Frequency with K_i as 65.	115

FIGURE 5.10: Bode Diagram to Explain the Influence of Integral Gain K_i on Stability, Bandwidth and Oscillation Frequency.	116
FIGURE 5.11: Impact of PLL Gain on Steady-State Stability.	117
FIGURE 5.12: Variation in Oscillation Frequency with Proportional Gain Constant based on Simulation.	117
FIGURE 5.13: Variation in Oscillation Frequency with Integral Gain Constant.	118
FIGURE 5.14: Bode diagram to Explain the Influence of Integral Gain K_i on Stability, Bandwidth and Oscillation Frequency with K_p as 60.	119
FIGURE 5.15: Block Diagram of the WTG Grid Side Converter with the PLL.	120
FIGURE 5.16: Proposed PLL Auto-Tune Control Architecture with a Type-4 WTG Integrated Weak Grid Model.	122
FIGURE 5.17: Proposed Adaptive PLL Control Flow Architecture.	125
FIGURE 5.18: Schematic of HIL Real-Time Simulations Performed with OPAL-RT.	126
FIGURE 5.19: Test A: PCC Voltage.	127
FIGURE 5.20: Test A: Reactive Power Flow between PCC and Load Point in Fig. 5.16.	127
FIGURE 5.21: Test A: Calculated Line Impedance between PCC and Load Point in Fig. 5.16.	128
FIGURE 5.22: Test A: PLL Gain Values Calculated by the Algorithm.	129
FIGURE 5.23: Test A: Identified System Frequency with the Proposed PLL.	129
FIGURE 5.24: a) Test A: Comparison of the Inner d -Loop Behavior between the Proposed Control and Conventional Control with a Specific PLL Gain. b) Test A: Comparison of the Inner q -Loop Behavior between the Proposed Control and Conventional Control with a Specific PLL Gain.	130

FIGURE 5.25: Test B: Identified Grid Frequency during Random Grid Impedance.	131
FIGURE 5.26: Test B: PCC Voltage during Random Change in Grid Impedance.	131
FIGURE 5.27: Test B: Power Flow at PCC during Random Grid Impedance Variations.	132
FIGURE 5.28: Test B: Identified Grid Impedance.	132
FIGURE 5.29: Test B: PLL Gains Derived by the Proposed PLL for the Given Impedance Variation.	133
FIGURE 5.30: a) Test B: Behavior of Inner d -Loop for Test 2. b) Test B: Behavior of Inner q -Loop for Test 2.	133
FIGURE 5.31: Test C: Variable Wind Profile used for Analysis.	134
FIGURE 5.32: Test C: Identified Grid Impedance.	135
FIGURE 5.33: Test C: PCC Voltage during Ramp Change in Grid Impedance with Variable Wind Profile.	135
FIGURE 5.34: Test C: Identified Grid Frequency with and without Proposed PLL.	136
FIGURE 5.35: Test C: Power Flow at PCC during Ramp Change in Grid Impedance Variations with Variable Wind Profile.	136
FIGURE 5.36: Test C: PLL Gains Derived by the Proposed PLL for the Given Impedance Variation.	137
FIGURE 5.37: Fault Ride through Behavior for Three Phase to Ground Fault for Cases 5-12 of Table 5.1. PCC Voltage(left), PCC Power(right)	140
FIGURE 5.38: Fault Ride through Behavior for Three Phase to Ground Fault with SC at PCC for Cases 5-11 of Table 5.1. PCC Voltage(left), PCC Power(right)	141
FIGURE 5.39: PCC Voltage for Case8 with Different Excitation Limit.	143
FIGURE 5.40: Reactive Power for Case8 with Different Excitation Limit.	143

FIGURE 5.41: Effect of Lower Excitation Limit on PCC Voltage for Case5.	144
FIGURE 5.42: Reactive Power for Case5 with Different Excitation Limit.	144
FIGURE 5.43: Effect of Lower Excitation Limit and Condenser Rating on PCC Voltage for Case5.	145
FIGURE 5.44: Effect of Transient Reactance on Stability for Marginal Grid Strength Scenario	146
FIGURE 5.45: Reactive Power Support from SC during Different Transient Reactance for Marginal Grid Strength Scenario	146
FIGURE 5.46: Effect of Transient Reactance on PCC Voltage for a Weak Grid Scenario	146
FIGURE 5.47: PCC Voltage Variations with Different Inertial Constant for Case10.	147
FIGURE 5.48: PCC Voltage during Fault in a Weak Grid Scenario	148
FIGURE 5.49: Reactive Power Support during Fault in a Weak Grid Scenario	149
FIGURE 5.50: Comparison of PCC Voltage with SVC for Different Fault Types in a Weak Grid Scenario	149
FIGURE 5.51: Comparison of PCC Voltage with SC for Different Fault Types in a Weak Grid Scenario	150
FIGURE 5.52: Comparison of Minimum PCC Voltage and Fault Current for SVC with SC.	150
FIGURE 5.53: Comparison of PCC Voltage during Single Phase to Ground Fault.	151
FIGURE 5.54: Comparison of Reactive Power Offered during Single Phase to Ground Fault.	151
FIGURE 5.55: Comparison of PCC Voltage during Single Phase to Ground Fault.	152

FIGURE 5.56: Comparison of Reactive Power Offered during Single Phase to Ground Fault.	153
FIGURE 5.57: Proposed Control Architecture for Improving Stability as Grid Strength Reduces.	154
FIGURE 6.1: Proposed Overall Coordinated Control Architecture	159
FIGURE 6.2: Proposed Control Architecture	161
FIGURE 6.3: Structure of Linear Quadratic Regulator	164
FIGURE 6.4: Local Controller of DG	167
FIGURE 6.5: Proposed Coordinated Control Approach for VSDG	168
FIGURE 6.6: One Line Diagram of Test System with Proposed Architecture	169
FIGURE 6.7: Test 1-Test 3: One Line Diagram of System used for Performance Test	171
FIGURE 6.8: Test 1: VPCC for One motor Two VSDG with Local controller(LC)	172
FIGURE 6.9: Test.1.a: Reactive Power Support for Motor at Bus 78	173
FIGURE 6.10: Test.1.b: Reactive Power Support for Motor at Bus 7	173
FIGURE 6.11: Test 1: Optimal Gain for DGs as the Cost Function is Minimised	174
FIGURE 6.12: Test 2: PCC Voltage for Motor at Bus 76 for Local Control and Coordinated Control	175
FIGURE 6.13: Test 2: PCC Voltage for Motor at Bus 782 with Local Control and Coordinated Control	176
FIGURE 6.14: Test 2: Coordinated Reactive Power Support with DG at Bus 5 and Bus 79	177
FIGURE 6.15: Test 2: Cost Function for Different Control Inputs	177

FIGURE 6.16: Test2: Interface between Local Controller and Coordinated Controller	178
FIGURE 6.17: Test 3: VPCC for Motor at Bus 6 for Local Control and Coordinated Control	178
FIGURE 6.18: Test 3: VPCC for Motor at Bus 7 with Local Control and Coordinated Control	179
FIGURE 6.19: Test 3: Coordinated Reactive Power Support with DG at Bus 5 and Bus 79	179
FIGURE 6.20: Test 4 and Test 5: One Line Diagram of 123 Bus System used for Scalability Test.	180
FIGURE 6.21: Test4: Comparison of VPCC for Motor at Node 451 with Single and Multiple VSDG	181
FIGURE 6.22: Test 4: Coordinated Reactive Power Support for DG at Node 48	181
FIGURE 6.23: Test 4: Coordinated Reactive Power Support for DG at Node 350	182
FIGURE 6.24: Test 5: VPCC for Motor at Node 451	182
FIGURE 6.25: Test 5: VPCC for Motor at Node 251	183
FIGURE 6.26: Test 5: VPCC for Motor at Node 195	183
FIGURE 6.27: Test 5: Coordination of Reactive Power Support Offered by DGs	184
FIGURE 6.28: Percentage Voltage Error with Delayed Input	185
FIGURE 7.1: Typical Configuration of Three Phase Inverters with RES [1].	191
FIGURE 7.2: Schematic of the Proposed Hybrid Control Architecture	193
FIGURE 7.3: Frequency Decomposition and Signal Reconstruction.	195
FIGURE 7.4: Frequency Decomposition and Signal Reconstruction Flow Chart.	196

FIGURE 7.5: Schematic of the Test System (IEEE 13 bus) used to Analyze the Performance of the Proposed Controller.	204
FIGURE 7.6: Case A: PCC Voltage at Inverter Terminals during Fault.	205
FIGURE 7.7: Case A: Power Output of Inverter.	205
FIGURE 7.8: Case A: Control Policy Generated for Test Case A.	206
FIGURE 7.9: Case A: Frequency Spectrum of Inverter Output Current.	206
FIGURE 7.10: Case A: Dynamic System Matrix Derived using Nonlinear Optimization.	207
FIGURE 7.11: Case A: Dynamic Input Matrix Derived using Nonlinear Optimization.	207
FIGURE 7.12: Case B: PCC Voltage at Inverter Terminals during Load Change.	208
FIGURE 7.13: Case B: Power Output of Inverter during Load Change.	208
FIGURE 7.14: Case B: Control Policy Derived by Optimization Function during Load Change.	209
FIGURE 7.15: Case B: Frequency Spectrum of PCC Voltage during Load Change.	209
FIGURE 7.16: Case C: PCC Voltage at Inverter Terminals during Parameter Variations.	210
FIGURE 7.17: Case C: Power Output of Inverter during Parameter Variations.	210
FIGURE 7.18: Case D: Inverter Output during Case D.	211
FIGURE 7.19: Case D: Frequency Deviation from Nominal during Highly Varying Power Demand.	211
FIGURE 7.20: Case D: Frequency Spectrum of Inverter Output Current.	212
FIGURE 7.21: Case D: Control Policy Derived for Case D.	212
FIGURE 7.22: Case E: Inverter Output Corresponding to Case E.	213

FIGURE 7.23: Case E: Frequency Spectrum of Inverter Output Corresponding to Case E.	214
FIGURE 7.24: One Line Diagram of IEEE 123 Bus System used for Scalability Test.	215
FIGURE 7.25: Case 1: PCC Voltage of Inverter Corresponding to Grid Fault.	215
FIGURE 7.26: Case 1: Inverter Output Power during Grid Fault.	216
FIGURE 7.27: Case 1: Control Sequence Developed by the Proposed Control for Grid Fault.	216
FIGURE 7.28: Case 2: Inverter Output Power during Grid Fault.	217
FIGURE 7.29: Case 2: Control Input Sequence Developed by Proposed Control during Case 2.	218

CHAPTER 1: INTRODUCTION

Power grid complexity has increased now a days due to the increased dependency on renewable energy. According to the international renewable energy agency, increasing renewable energy usage will rapidly reduce pollution and climate impact and save upto 4.5 million USD per year worldwide by 2030. Power electronics technology has gained a critical role in integrating renewable energy sources to power grid. The increased integration and penetration has increased the challenges for solving grid problems like frequency regulation, voltage variation, low voltage ride through, and power quality management. Various trends in WECS and the various wind turbine generator system available in energy market has been discussed in [2].

This work first analyses the various WECS configuration and mainly focuses on most popular Type3 DFIG based WECS. DFIG based wind energy conversion system (WECS) occupies around 50% of the wind energy market [3]. The variable speed operations facilitates the control of grid voltage by controlling reactive power generation. But variable speed turbine demands the need for a power electronics converter which can cost upto 7% of cost of WECS. DFIGs have become popular in WECS mostly due to the requirement of smaller size power converters compared to the machine rating. Ability to maximize the power extracted from wind through variable speed operation is one another reason for its increased penetration in existing power network. The increased penetration has resulted in increased challenges to maintain the power quality after every system events [4].

Various control topologies has been proposed for DFIG based WECS. The most widely reported control topology for DFIG is vector control (VC) which allows independent control of machine torque and reactive power output. In this control

technique the d -axis of synchronously rotating reference frame is aligned with either stator flux [5] or the stator voltage [6] of the DFIG.

Although a good performance is achieved by the reference frame orientation based VC, it needs appropriate decoupling, introduces rotary transformation, and requires much tuning work assuming knowledge of system parameters to ensure machine's operational stability over the whole operating range due to the multiple loops in the controller [7, 8]. Also, the whole feedback loop is dependent on correct measurements of active power/rotor speed and reactive power (for outer loop) and rotor currents for inner loop which makes the controller heavily dependent on the sensors.

The major focus of this work can be summarized as:

- Grid code requirements for the integration of WECS.
- Technical challenges to meet the grid code.
- Various control framework to meet grid code requirements.
- Grid ancillary services provided by DFIG including frequency regulation capability, low voltage ride through capability.
- Identify the latest research direction in this area, it's need and future recommendations.
- Propose some advance control approaches that ensures superior performance over varying operating conditions compared to conventional static controller.

1.1 Requirements for Grid Integration of DFIG Based WECS

Grid integration of DER is based on specific grid codes imposed by each country. These grid codes may vary, mainly in Fault Ride through, Active power and frequency control, reactive power, and voltage control aspects. In the US, FERC has issued certain interconnection standards for wind energy connected to the transmission system

in 2005. Standard grid code IEEE 15.47 shows an evolution of grid support functions during the interconnection of Distributed Energy Resources with electric power systems. IEEE 15.47 issued in 2003 expects DFIG shall trip during abnormal voltage and frequency and shall not actively regulate voltage. However, as per the 2014 code, DFIG may actively regulate voltage, ride through abnormal voltage and frequency and provide frequency response. In the 2018 code, DFIG may provide an inertial response, actively regulate voltage, and provide a frequency response. As wind generation increases, the grid code will force WECS to provide more ancillary services which are not currently obligatory such as power oscillation damping. Then utilizing DFIG based WECS to provide ancillary services will not be a feature; it will be a must feature. [9]. Grid code requirements for WECS integration can be summarised as follows,

- Operating range of voltage : 0.95 to 1.05pu at PCC
- Power factor range : 0.95lag / lead
- Operating range of frequency should be within typical grid frequency variations of $\pm 0.05\text{Hz}$.
- Active power control for frequency stability and to prevent overhead on lines.
- Voltage Control: Grid code demands individual turbines to maintain their own terminal voltage to a constant value.
- Frequency Regulation capability is expected from wind farms
- Low voltage ride through capability : In case of voltage sag WT is required to remain connected to grid for a certain time before being allowed to disconnect. Some utilities also demand the WT to provide support during grid fault.

- Power quality: Wind farms are required to deliver power to grid with desired quality which includes constant voltage, voltage fluctuations and flicker only within a limit, harmonic current and frequency deviations within desirable range etc.

1.2 Technical Challenges

Integration of DFIG based WECS to existing grid imposes several technical challenges resulting in various power quality issues. These include,

1.2.1 Intermittent and uncontrollable nature of wind speed

The input to WECS is highly stochastic. This uncontrollable and unpredictable input can create several power quality issues while in grid-connected mode. Hence wind energy predictions methods need to be more efficient. Wind energy transmission in long-distance transmission lines is more challenging due to this intermittent nature. As the distance increases, wind farms try to push more reactive power to manage system stability. If the grid is weak, then long-distance transmission leads to instability. A study done by ERCOT work groups shows instability in the power grid with distance. This demands the use of additional VAR compensators to ensure better stability and reliability.

1.2.2 Challenges in managing grid stability, reliability and power quality

Integration of WECS to the existing grid should ensure voltage and frequency stability. Voltage stability can be ensured by providing reactive power to the grid, taking into account the operating states and limits. The frequency stability of the grid can be enhanced by short term active power control strategy. Research shows studies using virtual inertial control to utilize a portion of the kinetic energy from the rotor to support frequency.

Ensuring the reliable operation of the grid is another code requirement. Reliability is dependent on many factors like wind regime in the location, wind penetration level,

the correlation between multiple wind farms, etc. Reliability analysis of bulk electric transmission system related to WECS is discussed in [10]. [11, 12] shows some studies related to reliability management during the integration of WECS. In [10] Monte Carlo simulation is used for bulk transmission reliability assessment as it provides the framework to incorporate chronological characteristics of wind, load profiles, etc.

As the penetration of WECS in the power grid increases, several power quality issues like voltage flicker, frequency deviations, harmonic distortions will come into the picture. Switching operation of wind farms as well as the intermittent nature of wind results in voltage flicker. Several researchers show the voltage flicker caused by wind farms. [13] shows a study on maximum flicker on residential and commercial distribution feeders with remotely connected wind farms. In [14, 15] a comparison of flicker caused by fixed speed wind turbine and variable speed wind turbine has been studied. A simplified second-order model is used to predict and measure the flicker emission. Long-term frequency deviations due to power fluctuations are another power quality concern. Several researchers show control of output power variations from wind farms to improve the frequency deviations. The use of PWM-based inverters in DFIG based wind farms can result in the generation of harmonic currents. Several studies [16, 17] consider the shape and frequency of harmonics with changes in operating points of wind turbines, how the harmonics are penetrated through the network, and compensation techniques for harmonic reduction.

1.2.3 Wind power transmission over long distance networks

The dynamic nature of wind power needs to be analyzed for grid connections such that the power from inverters meets the grid code requirements. WECS should be able to supply maximum available power to the grid while at the same time it should absorb or deliver reactive power to maintain the voltage at the interconnection. Interconnection of large-scale offshore wind farms requires more flexible power transmission networks. Interconnecting large scale DFIG wind farms using a common

collector bus is discussed in [18, 19, 20]. These studies also emphasize the need for static synchronous compensators to facilitate connections to a weak grid. A study given in the CIGRE report demonstrates the integration issues like the distance of transmission increases. The weaker the grid, the more is the reactive power demand at PCC to maintain grid stability. The study clearly shows the need for VAR compensators to provide additional reactive power as the short circuit ratio of the grid decreases.

Other technical issues faced during WECS integration includes

- Grid Congestion and interconnection to weak grids
- Bidirectional power flow in distribution networks
- Optimized design and control of turbine power electronics
- Starting and synchronizing of wind farms to grid
- Sub synchronous resonance issues due to interaction of electric network and complex shaft gear system of wind turbine.

1.3 State-of-the-art of DFIG Control Techniques to Meet Grid Code

This section mainly focuses on current state-of-art in WECS integration and it's emerging technologies. Initial researches were done to analyse the advantages of different turbine system configuration. Maximum power point tracking control to extract maximum available power is supported by Type3 and Type4 variable speed WECS. Other major research areas include the ancillary services provided by WECS like reactive power control, low voltage ride through capability, frequency regulation capability etc. Each of these features along with the control topologies widely used to achieve these services are detailed below.

Table 1.1: Performance Comparison of Different WECS configurations

Type	Advantage	Disadvantage
Type1	Least expensive Rugged,Reliable	No reactive power support High Rotor Loss
Type2	Low Cost Constant power output	No reactive power support No MPPT
Type3	Reduced converter rating Support MPPT	Complex control Frequent maintenance
Type4	Full speed regulation Support MPPT	Costly Full speed converter

1.3.1 WECS Classification

Wind turbines can be classified to Horizontal Axis Wind Turbine (HAWT) and Vertical Axis Wind Turbine (VAWT) based on the rotating axis. Another classification is based on fixed speed and variable speed WECS. Using different combinations of generator, power electronics converter and turbine system different configurations of WECS can be obtained[21, 3]. For fixed speed fixed frequency system synchronous generator is preferred while for variable speed variable frequency is with DFIG based slip ring induction machine. Various WECS configurations include,

- Type1: Fixed Speed($\pm 1\%$) WECS with SCIG
- Type2: Semi Variable Speed ($\pm 10\%$) WECS with WRIG.
- Type3: Semi Variable Speed ($\pm 30\%$)WECS with DFIG.
- Type4: Semi Variable Speed ($\pm 100\%$)WECS with SCIG,PMSG,WRSR.

Table 1.1 shows the advantages and disadvantages of different WECS configurations. Both Type3 and 4 support MPPT while Type 3 is cost efficient as it demands only reduced power converters. This explains the reason for wide popularity of DFIG.

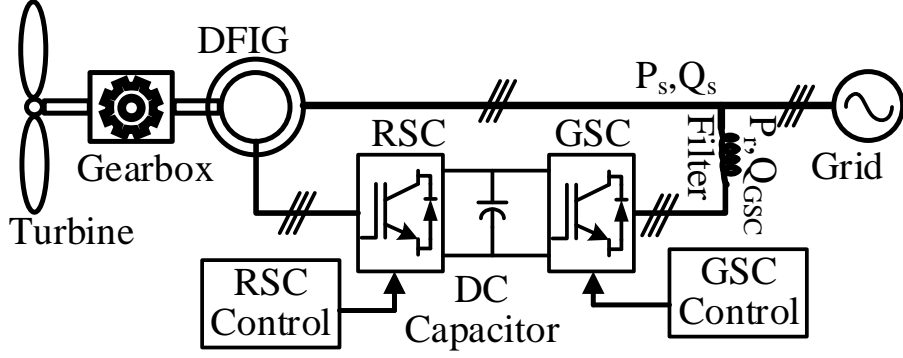


Figure 1.1: General Schematic of DFIG.

1.3.2 DFIG Configuration and Converter Control

General schematic of DFIG based wind farm is shown in Figure 1.1. The mechanical shaft of DFIG is connected to low speed turbine shaft and high speed generator shaft through gearbox setup. Stator of the DFIG is connected to grid directly while the rotor is also connected to grid via a back to back converter by a dc link capacitor. The converter needs to handle only the rotor power is an advantage of Type3 discussed in the above section. The mathematical model of an induction machine has been derived earlier in [22] using an arbitrarily rotating reference frame. In this paper, the equations modeling the DFIG in synchronously rotating reference frame using a generator convention is presented for comprehensibility[23, 24, 25]. In the convention used in this work, the current coming out of the stator and the current entering the rotor side is considered positive. The voltage and flux linkage equation representing DFIG in synchronously rotating $d - q$ reference frame is given by,

$$\begin{aligned} v_{dqs} &= -r_s i_{dqs} + j \frac{\omega_e}{\omega_b} \Psi_{dqs} + p \frac{\Psi_{dqs}}{\omega_b} \\ v'_{dqr} &= -r'_r i'_{dqr} + j \frac{\omega_e - \omega_r}{\omega_b} \Psi'_{dqr} + p \frac{\Psi'_{dqr}}{\omega_b} \end{aligned} \quad (1.1)$$

$$\begin{aligned}\Psi_{dq_s} &= -L_{ls}i_{dq_s} + L_m(i_{dq_s} + i'_{dqr}) \\ \Psi'_{dqr} &= -L'_{lr}i'_{dqr} + L_m(i_{dq_s} + i'_{dqr})\end{aligned}\quad (1.2)$$

Likewise, the instantaneous active (P_s) and reactive power (Q_s) from the stator in synchronously rotating d – q reference frame is given by,

$$\begin{aligned}P_s &= v_{qs}i_{qs} + v_{ds}i_{ds} \\ Q_s &= v_{qs}i_{ds} + v_{ds}i_{qs}\end{aligned}\quad (1.3)$$

Following assumptions are made for the design of the proposed adaptive controller for DFIG:

- The synchronously rotating reference frame is aligned with the stator flux. i.e $\Psi_{ds} = \Psi_s$, $\Psi_{qs} = 0$ and $v_{qs} = V_s$, $v_{ds} = 0$.
- The stator flux dynamics can be neglected when connected to a strong grid. i.e $p\Psi_{qs} = p\Psi_{ds} \approx 0$.

1.3.2.1 Control of Rotor Side Converter

The objective of the rotor-side converter (RSC) in the topology depicted in Figure 1.1 is to facilitate the delivery of active power extracted from wind and reactive power generated/consumed by DFIG stator to the grid by regulating the voltages applied on the rotor windings.

The rotor voltage equations can be written as,

$$\begin{aligned}v'_{dr} &= r'_r i'_{dr} + p \frac{\sigma L'_r i'_{dr}}{\omega_b} - \omega_{slip} \left(\frac{\sigma L_s L'_r}{L_m} i_{qs} - \frac{r_s L'_r}{L_m} i_{ds} \right) \\ v'_{qr} &= r'_r i'_{qr} + p \frac{\sigma L'_r i'_{qr}}{\omega_b} - \omega_{slip} \left(\frac{\sigma L_s L'_r}{L_m} i_{ds} - \frac{L'_r}{L_m} (v_{qs} + r_s i_{qs}) \right)\end{aligned}\quad (1.4)$$

where $\sigma = \frac{L'_r L_s - L_m^2}{L_s L'_r}$. From (1.4), it can be observed that the rotor d – q axis voltage referred to stator side can be divided into two components. i.e.

- component depending on dynamics of i'_{dr} and i'_{qr} respectively.
- compensation terms that couple the d – q axis component with one another.

Thus,

$$v'_{dr} = v''_{dr} + v'''_{dr} \quad (1.5)$$

$$v'_{qr} = v''_{qr} + v'''_{qr} \quad (1.6)$$

where

$$\begin{aligned} v''_{dr} &= \left(r'_r + p \frac{\sigma L'_r}{\omega_b} \right) i'_{dr} \\ v'''_{dr} &= -\omega_{slip} \left(\frac{\sigma L_s L'_r}{L_m} i_{qs} - \frac{r_s L'_r}{L_m} i_{ds} \right) \\ v''_{qr} &= \left(r'_r + p \frac{\sigma L'_r}{\omega_b} \right) i'_{qr} \\ v'''_{qr} &= -\omega_{slip} \left(\frac{\sigma L_s L'_r}{L_m} i_{ds} + \frac{L'_r}{L_m} (v_{qs} + r_s i_{qs}) \right) \end{aligned} \quad (1.7)$$

Using the assumption made (1.3) can be written as

$$\begin{aligned} P_s &= \frac{L_m v_{qs}}{L_s} \left(\frac{v''_{qr}}{r_r + p \frac{\sigma L_r}{\omega_b}} \right) \\ Q_s &= -\frac{v_{qs} \Psi_{ds}}{L_s} + \frac{L_m v_{qs}}{L_s} \left(\frac{v''_{dr}}{r_r + p \frac{\sigma L_r}{\omega_b}} \right) \end{aligned} \quad (1.8)$$

It can now be observed that the stator active and reactive power output of DFIG can be controlled by controlling the v''_{qr} and v''_{dr} component of rotor voltage respectively. Thus the goal of the RSC control of DFIG is to generate the proper sequence of v''_{qr} and v''_{dr} to regulate the stator active and reactive power.

1.3.2.2 Control of Grid Side Converter

The objective of the grid-side converter (GSC) in the topology depicted in Figure 1.1 is to permit the active power flow from rotor to the grid by regulating the dc-link voltage to a constant level. GSC is usually operated at unity power factor, but it is also possible to control the reactive power flow between the converter and the stator/grid. A VC approach is normally used with a reference frame oriented along the grid-voltage vector, enabling independent control of the active and reactive power flowing between the grid and the GSC. GSC is current regulated, with the d-axis current regulating the dc-link voltage and the q-axis current regulating the reactive power. the voltage balance across the inductor and resistor can be written as

$$\begin{bmatrix} V_{ai} \\ V_{bi} \\ V_{ci} \end{bmatrix} = R \begin{bmatrix} I_a \\ I_b \\ I_c \end{bmatrix} + pL \begin{bmatrix} I_a \\ I_b \\ I_c \end{bmatrix} + \begin{bmatrix} V_a \\ V_b \\ V_c \end{bmatrix} \quad (1.9)$$

where R and L are the line inductance and resistance, respectively Using the abc to d – q transformation, (4.21) is transformed into a synchronously rotating dq reference frame rotating at ω_e rad/s:

$$\begin{aligned} v_{di} &= Ri_d + pLi_d - \omega_e Li_q + v_d \\ v_{qi} &= Ri_q + pLi_q - \omega_e Li_d + v_q \end{aligned} \quad (1.10)$$

where ω_e is the angular frequency of the supply voltage, i_d and i_q is the d-axis and q-axis current from inverter. respectively, v_d and v_q is the d-axis and q-axis grid voltage respectively and v_{di} and v_{qi} is the d-axis and q-axis output voltage of the inverter. Thus the controller objective is to generate proper sequence of control voltages which controls i_d and i_q which then eventually controls DC link voltage and reactive power output (Q_{GSC}) respectively.

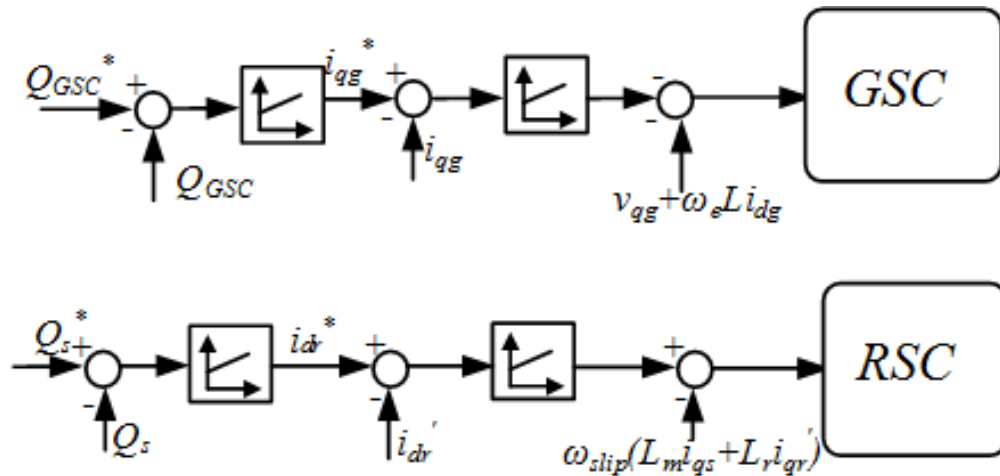


Figure 1.2: Reactive Power Control

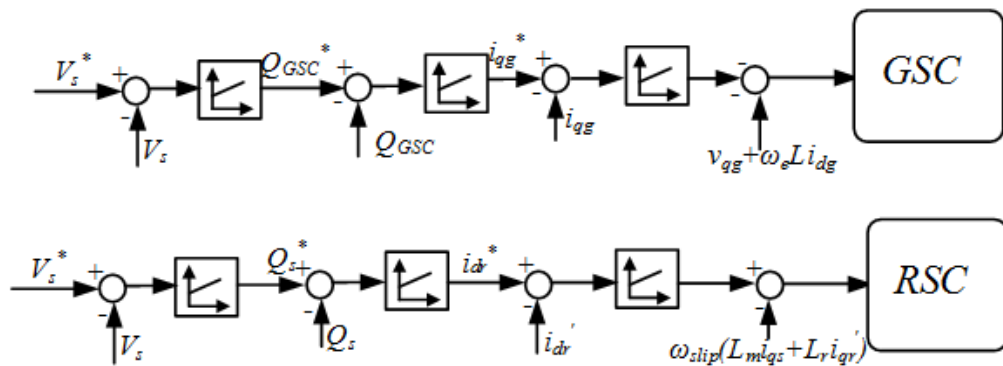


Figure 1.3: Voltage Control Loop

1.3.3 Solutions to Meet Grid Code Requirements

Current state of art for solutions to meet grid code requirement are reviewed in detail in the following section. Basic control framework used for meeting the code along with providing ancillary services are discussed in this section. The grid code requirements can be classified based on its impact on normal and abnormal operating conditions.

1.3.3.1 Maintaining Operating Range of Voltage

Both RSC and GSC together or either one of them can be used to maintain the voltage at grid connection point. Usually RSC will control the voltage at interconnec-

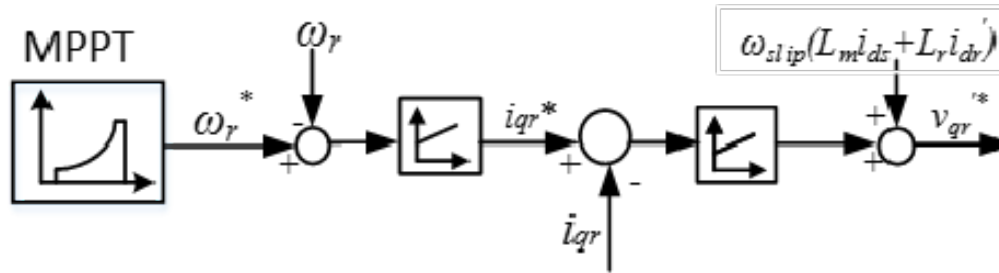


Figure 1.4: MPPT Control

tion point and GSC will perform reactive power control as shown in Figure 1.2 . For weak grids both the RSC and GSC can be made to control the voltage. Figure 1.3 shows the voltage control loop used to maintain the PCC voltage to reference. GSC voltage control loop can help to restore the grid voltage during fault. Voltage control loop in effect reduces the terminal voltage variations due to intermittent wind power and helps to improve the power quality when connected to weak grid.

1.3.3.2 Active Power Control or Speed Control of DFIG based WECS

RSC controls the active power output from DFIG. At wind speeds below the rated wind velocity, DFIG will be made to extract maximum power from available wind. The optimal shaft speed determined based on wind power characteristics drives the DFIG output to its maximum. RSC control then regulates the stator active power or shaft speed at an optimal value.

Maximum Power Point Tracking (MPPT) Control of DFIG Power speed characteristics of wind turbine defines the maximum energy that is captured from wind as shown in Figure.1.4. Mechanical power extracted from wind is a function of wind speed, blade pitch angle and shaft speed. This is expressed as,

$$P_m = \frac{1}{2} \rho V_w^3 \Pi r^2 C_p(\lambda) \quad (1.11)$$

where P_m is the power extracted from wind, ρ is the air density(kg/m^3), r is the radius swept by the wind blades, V_w is the wind velocity, C_p is the performance

Table 1.2: Performance Comparison of Different MPPT Methods

Type	Advantage	Disadvantage
Tip Speed Ratio Control	Efficient Faster	Need speed sensor Filter to minimize error
Optimal Torque Control	Simple Fast	No reactive power support Efficiency lower than TSR
Hill Climb Search Method	No sensors, efficient Low cost	MPP is slightly oscillating

coefficient and λ is the tip speed ratio.

$$\lambda = \frac{\omega_t r}{V_w} \quad (1.12)$$

where w_t is the mechanical rotor speed in rad/sec. Performance coefficient C_p can be controlled to maximize the energy extracted from wind. C_p has a peak value for a specific λ and then it drops off as tip speed ratio increases. Theoretical maximum value of C_p is 0.593. In typical turbine speed power curve for different wind velocities, power output has a peak value for certain rotor speed for each wind velocity. MPPT tracking aims at calculating this optimal rotor speed at which the peak power is extracted during varying wind speed conditions [26, 27]. Literature shows that different methods are studied for efficient tracking of MPPT [28, 29]. Table 1.2 shows the comparison of different control methods.

Several other studies on sensor less maximum power extraction, sliding mode control for energy optimization and some direct power control techniques are analysed in [30, 31].

1.3.3.3 Pitch Control of DFIG based WECS

Pitch controller is another active power control strategy which is enabled whenever wind speed exceeds the rated value. Pitch controller limits the mechanical output

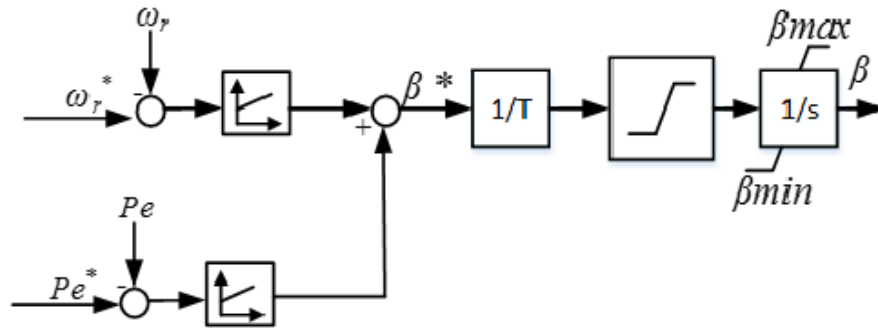


Figure 1.5: Conventional Pitch Control Loop

from wind turbine to the equipment rating [32, 33]. For below rated wind speed the pitch is set to minimum to maximize the mechanical power. The deviation of rotor speed from the optimal speed reference as well as deviation of mechanical power from rated value can simulate the pitch angle controller [34, 35, 36]. Conventional pitch control loop is shown in Figure 1.5. It clearly shows the relation of mechanical power output with pitch angle. Several studies have conducted making use of pitch controller to deload the wind turbine to create sufficient active power reserves for frequency regulation during grid-connected operations [37, 38, 32, 33].

1.3.3.4 Maintaining Operating Range of Frequency (Frequency Control)

WECS penetration into current grid is increasing day by day and so is the need to meet the grid code requirements. The concept of primary frequency regulation of grid-connected DFIG has been an important research topic. The concept of frequency regulation is by modulating the active power output from the DFIG. The modulating power ΔP is derived from droop control loop based on frequency deviation from nominal while the inertial loop derives modulating value proportional to rate of change of power. Since the rate of change of frequency is maximum during the initial period before nadir, the inertial loop is supposed to provide additional power support during the first few seconds after the frequency event.

Inertial loop converts the kinetic energy of the rotor to support this additional sup-

port during the inertial response time. Since the rotor speed range is between 0.8pu and 1.2pu, a greater amount of kinetic energy can be released to provide a additional power during frequency variations. The power reference to the RSC is updated by both the droop and inertial control loop considering the change of frequency and RO-COF. Several other research works has been done in this area with modified inertial loop based on variable gains instead of fixed gain to perform better during variable wind speed operations.

1.3.3.5 Reactive Power Control

Modern goal of grid integrated wind power plant is to make them behave like synchronous generation power plant. This is achieved by proper reactive power support during contingencies. One of the main reason for wide use of DFIG based wind farm is the decoupled control of active and reactive power due to vector control approach. Moreover both the RSC and GSC of a DFIG can be controlled to provide more reactive power to grid during voltage fluctuations [39, 40]. From equation 1.3 and 1.8, it is clear that reactive power is directly related to d-axis component of current. GSC uses voltage oriented reference frame where q axis current can regulate the reactive power output from GSC [41]. At UPF, RSC supports the entire reactive power needed. This reactive power has basically two components, one transferred through rotor and a portion of reactive power based on slip ratio that is transferred trough stator. For low wind speed the entire capability of GSC is not utilized. During voltage sags the GSC can be made to operate in non UPF mode to support more reactive power. Reactive power is controlled using two modes, power factor control mode and voltage control mode. The reactive power reference for both the control loops is derived from PCC voltage deviation from it's reference.

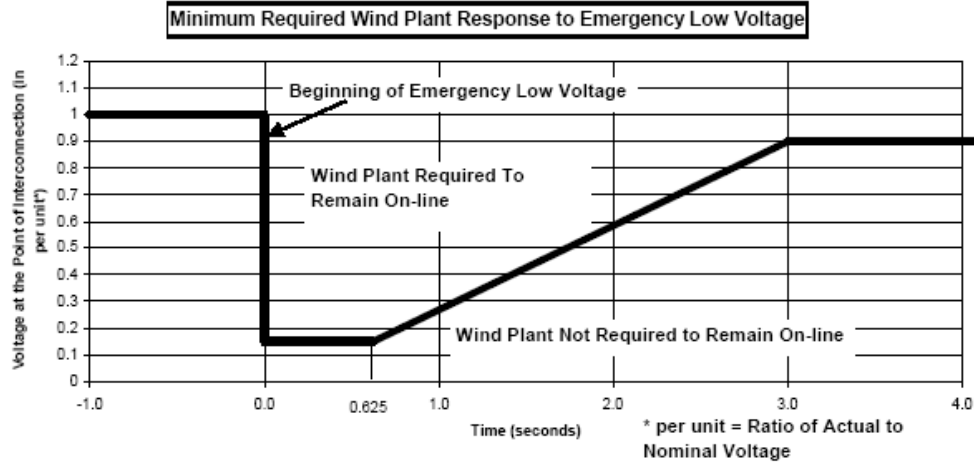


Figure 1.6: LVRT Standard Set by FERC

1.3.3.6 Low Voltage Ride Through Capability

Now a days many network operators demand WTs to stay connected to grid even during network faults ensuring LVRT capability [42]. Figure 1.6 shows the standard set by FERC in US. According to FERC for a fault duration of 625ms, the wind farm should stay connected to grid for at least 3seconds before getting disconnected. During this time wind farms are expected to supply maximum reactive current to grid to prevent any blackout. Soon after restoring the voltage, wind farms are expected to support maximum active power. During faults PCC voltage suddenly drops down to a very low value leading to a higher stator current transients. This results in higher voltage induced to rotor due to magnetic coupling which can lead to higher rotor currents. If the currents are limited within the converter limits DFIG can be better controlled during faults else it leads to instability [43, 44]. Increased reactive power supply especially during voltage sag can improve the AC voltage thereby enhancing the Low Voltage Ride Through(LVRT) capability of wind turbines [45].Major technologies and solutions to achieve LVRT feature includes use of active crow bar circuit, use of energy storage, use of improved rotor current control for stator flux regulation, external reactive power compensators and additional series grid side converters.

Active crow bar circuit Grid faults leads to voltage dip , over current transients and dc link fluctuations. these over voltage in dc link and over current in rotor can affect the RSC badly. Crow bar circuit short circuits the rotor winding during these dynamic conditions thereby protecting the RSC. Then GSC can be made to control the stator voltage by regulating the reactive power exchanged with the grid. Once the fault is removed the RSC connects back and controls the active and reactive power output. The voltage control from GSC is shifted back to RSC and operating mode is set back to UPF.

1.4 Dissertation: Objectives and Contributions

The detailed review performed in this chapter has given a clear idea of how different existing control topologies try to enhance the performance of DFIG based WECS during grid integration process. While the conventional vector control strategy enables the decoupled control of real and reactive power, any malfunction of the current or speed sensor can adversely impact it's performance leading to instability. This dissertation focus on the limitations and challenges faced by these conventional control strategies. Hence the motivation behind this dissertation is to provide advanced control strategies for the RES based DFIG wind farms that enhance the power quality and reliability at interconnection as well as their ability to provide other ancillary grid services like frequency regulation and low voltage ride through capability, power smoothing etc. Based on the above discussions, this dissertation aims to answer the following research questions:

- Is it possible to modify the conventional control strategy of DFIG to reduce its dependency on sensors.
- How to make the DFIG control robust to physical parameter variations that occur in real world scenario?
- How to ensure that these RES shows better performance maintaining the power

quality following a disturbance?

- Most of the control framework uses PI based static controllers which were not robust and the operating performance can get affected during dynamic operating conditions in the grid. What techniques can help DFIG to overcome the issues due to limited operating range of static conventional controllers?
- How to enhance the ancillary service capability include frequency regulation and voltage support in dynamic environment ensuring maximum efficiency?
- How to modify the control architecture to utilize the existing RES capability to enhance the operational reliability, power quality and stability in transmission and distribution systems?
- Is it possible to include the modified control architecture without demanding much of the structural changes in the existing power grid network? If so how to prioritize between the existing control architecture and modified control logic in an efficient manner?

The major contributions from this dissertation can be summarized as follows:

- The dissertation proposes a speed sensorless control strategy of DFIG based on extended error based minimum variance adaptive control framework.
- The dissertation also proposed a device level adaptive control framework based modification of Grid side converter control that ensures enhanced dynamic performance and grid voltage support feature. The proposed technique provide faster voltage recovery after a grid event.
- The dissertation proposes a coordinated control approach among different frequency control logic considering the mechanical and electrical dynamics occurring at different time frames using a RLS based MIMO identification approach.

- Enhancing the stability of wind on weak grid by modifying the grid side PLL and modified synchronous condenser based control strategy to enhance the stability of wind integrated to weak grids during high power transfer.
- The dissertation proposes an optimal state feedback control strategy for distributed generators to mitigate the starting voltage dip due to induction motors and other loads at distribution networks.
- The dissertation also discusses a modified control approach for RES at distribution networks to enhance the transient stability and reliability. Energy function based analysis considering the state energy and controller effect is used to prioritize among the conventional controllers and the proposed new adaptive control strategy.

CHAPTER 2: PARAMETRICALLY ROBUST MUTUAL INDUCTANCE ESTIMATION BASED ADAPTIVE CONTROL ARCHITECTURE FOR DFIG

This chapter demonstrates a novel robust adaptive speed control architecture that allows DFIG to operate independently of any speed sensors or position encoders. The proposed speed sensorless control based on extended minimum variance adaptive control takes care of issues due to machine parameter variations and sensor malfunctioning. The proposed speed observer is formulated using a rotor current-based reference adaptive system. A modified adaptive Rotor Side Converter (RSC) control loop is also proposed to ensure robustness to current sensor failure. The online identification for the adaptive control logic is based on the recursive least square estimation technique (RLS), while the adaptive control law is based on an extended version of the minimum variance control algorithm (EMVC). A modification for the terminal voltage control loop is proposed to ensure excellent dynamic performance for the proposed control. The reactive power reference for the vector control loop is calculated considering the rotor current component responsible for reactive power generation.

2.1 Introduction

Doubly fed induction generator-based wind energy conversions systems are most prominent due to their ability to work with a low-rated converter. The traditional reference frame-based vector control approach is widely used for decoupled control of real power (P) and reactive power (Q) output of DFIG. The vector control approach relies on measurement data such as rotor and stator currents and speed. This highlights the dependency of the conventional approach to devices like sensors that are prone to malfunction. This can lead to unexpected downtimes leading to large

economic losses. Hence sensorless control of DFIG has gained importance. Moreover, static controllers in conventional control limit the system's operating range during dynamic grid events. This highlights the need for an adaptive identification-based DFIG control approach. The effects of variations in physical parameters like stator winding resistance, mutual inductance, etc., and their effect on controller performances are yet another issue discussed, that affects the robustness of the DFIG based WECS system. The following section discusses state of the art in this area for a detailed analysis of the challenges faced by DFIG to ensure robust, reliable operation.

2.1.1 State-of-the-Art

Several different methods of MRAS based observer addressed in [46] focuses on Stator Flux Based MRAS Observer (SFMO) where stator flux and its estimates are calculated. An error function derived based on the cross-product of actual and estimated flux is used to derive the controller's gain. The same approach using rotor flux and its estimate are used in Rotor flux Based Observer (RFMO). In [47], the self-tuning PID controllers are replaced by Minimum variance controller (MVC), and in [48] sensorless speed estimation based on cross and dot product approach coupled with the MVC controller is presented. The paper compares the existing MRAS based speed estimation technique using static controllers with the MVC technique. The lack of an integrator in the MVC-based controller makes it fast-acting, and the identified system parameters using the least square technique make the error value zero within a few sampling times.

In [49], the speed estimation technique is incorporated with MVC based controller along with parameter estimation. The works show that the variation in machine mutual inductance can affect the performance of speed estimation badly. So online estimation of L_m at every instant is derived to improve the system performance by making the technique robust to parameter variations. Recently, several other approaches like recomputation of stator flux magnetizing current and estimation of

σ value at every instant have been proposed to improve the robustness of sensorless control systems. Various other sensorless control of DFIG has been discussed in [50, 51, 52, 53]. Several variations of parameter estimation like L_m estimation, sigma estimation, imrs recomputation techniques have been proposed in the literature to make the system parametrically robust. Sensorless estimation of rotor speed and position and the estimation of parameters for a robust control has also been addressed in [54, 55, 56, 57, 58, 59]. In [54], an MRAS based technique using electromagnetic torque as working error is proposed on a robust sensorless approach. In [55], an extended Kalman filter-based parameter estimation method has been proposed, while [56] uses the RLS algorithm to estimate the stator and rotor parameters. A neural network-based estimation method is proposed in [59].

2.1.2 Main Contributions

In this chapter, an extended RSC adaptive control logic based speed sensorless control of DFIG has been discussed. Compared to the conventional control approach, the architecture proposed here is independent of any speed sensors and the effect of machine parameter variations. The most prevalent features of the proposed technique include;

- The ability of the architecture to perform independently in the advent of speed and current sensor malfunctions.
- Controller's ability to auto-tune based on dynamic operating conditions.
- Enhanced stability and reliability over a wider operating range.
- Robustness to the variations in physical parameters due to temperature or other physical conditions.

The major contributions of the proposed work includes;

- Modified adaptive RSC control loop that ensures reliable operation of proposed sensorless control during rotor current sensor failures.
- Accurate estimation of the dynamic transfer function by the use of the recursive least square technique.
- Extended minimum variance control algorithm that makes the adaptive speed controller robust to the variations in electrical quantities due to parameter variations.
- Improved dynamic performance capability during parameter variations by the modified terminal voltage loop.
- Scalability studies with the real-time model of the practical power grid and DFIG.

The proposed framework is validated both in MATLAB Simulink and Opal RT's Real Time simulation platform for a 1.5MW Doubly Fed Induction Machine setup. Parameters are mentioned in Table A.1. An overview of grid connected proposed DFIG based WECS is shown in Figure 2.1

2.2 Adaptive Control Framework

The adaptive controller is an extended version of MVC, viz., EMVC. The architecture is illustrated in Figure 2.3. It consists of a speed observer, RSC controller and integrated EMVC.

2.2.1 Proposed Speed Observer

The speed observer is based on an MRAS technique which estimates the rotor current. The estimated value of the rotor current is then compared to the actual current that is measured and the error is reduced based on an online algorithm if the rotor angle error is equal to a minimum threshold value.

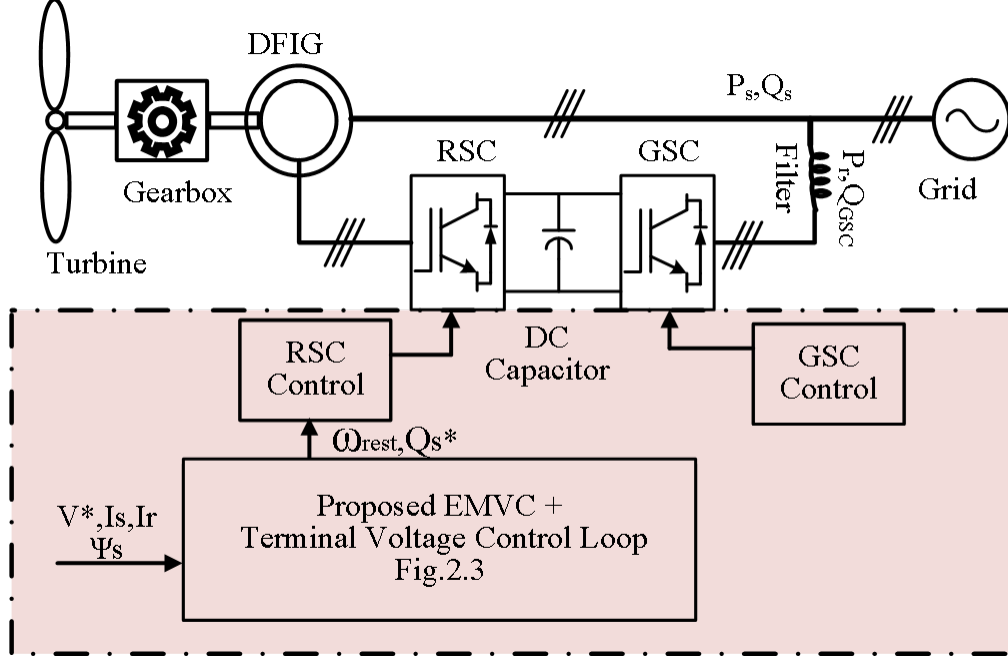


Figure 2.1: DFIG based Wind Energy Conversion Systems (WECS).

The measured rotor current I_r can be derived as,

$$I_r = \frac{\varphi_s + L_s I_s}{L_m} \exp^{-j\theta_r} \quad (2.1)$$

where θ_r is the rotor position measured with respect to stationary reference frame.

Correspondingly the estimated rotor current based on the estimated angle θ_{rest} can be represented as

$$I_{rest} = \frac{\varphi_s + L_s I_s}{L_m} \exp^{-j\theta_{rest}} \quad (2.2)$$

The currents (estimated and actual) match when the angular positions are within the threshold represented by an error function ϵ . This can be expressed as the angle

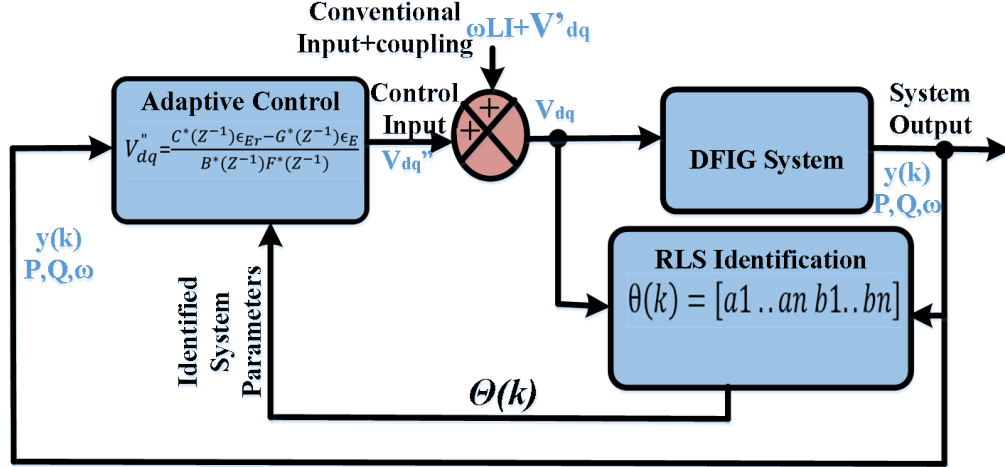


Figure 2.2: Schematic Diagram of the Proposed Adaptive Controller.

between dot and cross products of the estimated and actual rotor angles.

$$\epsilon = \frac{I_r \times I_{rest} \sin \theta_{err}}{I_r \bullet I_{rest} \cos \theta_{err}} \quad (2.3)$$

where θ_{err} is the angle difference between actual and estimated rotor current.

2.2.2 Modification to RSC Controller

As the above mentioned sensorless approach is dependent on current sensor measurements, the RSC is modified with an adaptive control framework to improve the robustness of the controller. Figure 2.2 illustrates the adaptive control modification for the RSC controller including the speed observer. For this design, the RSC control loop is integrated with an identifier having $V''_{dq}(k)$ as the input, and $\epsilon_E(k)$ as the output error. The output error can be the rotor speed error in active power control and reactive power error in the reactive power control loop. This can be represented as

$$\epsilon_E(k) = \frac{B(z^{-1})}{A(z^{-1})} \times V''_{dq}(k) \quad (2.4)$$

where

$$A(z^{-1})\epsilon_E(k) = B(z^{-1})V''_{dq}(k) \quad (2.5)$$

with

$$A(z^{-1}) = 1 + a_1z^{-1} + a_2z^{-2} + \dots + a_nz^{-n} \quad (2.6)$$

$$B(z^{-1}) = b_1z^{-1} + b_2z^{-2} + \dots + b_nz^{-n} \quad (2.7)$$

and $k = n + 1, n + 2, \dots, t$, t being the time index.

The main advantage of the proposed architecture is that it provides wider operating range and improves the overall stability margin. Also, the approach provides convergence properties in the wake of sensor malfunction or dynamic grid events due to the better estimation of $V''_{dq}(k)$.

2.2.3 Identification Methodology

The proposed adaptive control approach utilizes an online Recursive Least Squares (RLS) technique for identification. The details are discussed in [60]. The discrete Z domain representation of the identifier can be defined as

$$\frac{\epsilon_m(k)}{\omega_{rest}(k)} = \frac{b_1z^{-1} + b_2z^{-2}}{1 + a_1z^{-1} + a_2z^{-2}} \quad (2.8)$$

With the help of RLS, we can develop a mathematical model that which finds the coefficients a_1, a_2, b_1, b_2 online, that defines the dynamic representation of the system transfer function at every instant which converges when the error becomes less than the threshold. for every k

error can be represented as

$$\epsilon(k) = \frac{B(q^{-1})}{A(q^{-1})} \times \omega_{rest}(k) + \frac{C(q^{-1})}{A(q^{-1})} \times E(k) \quad (2.11)$$

where $\epsilon(k)$ represents the model output which is the error in rotor angle, $\omega_{rest}(k)$ represents the estimated speed which is the input to the model and model error or noise is represented in the form of $E(k)$.

From (2.11) the model error $E(k)$ with d as the time delay of the process can be represented as:

$$E(k) = \frac{A(q^{-1})\epsilon(k) - B(q^{-1})(q^{-d})\omega_{rest}(k)}{C(q^{-1})} \quad (2.12)$$

If,

$$\frac{C(q^{-1})}{A(q^{-1})} = F(q^{-1}) + \frac{G(q^{-1})}{A(q^{-1})} \quad (2.13)$$

Then,

$$\epsilon(k) = \frac{B(q^{-1})}{A(q^{-1})}\omega_{rest}(k) + F(q^{-1})E(k) + \frac{G(q^{-1})}{A(q^{-1})}E(k) \quad (2.14)$$

From (23) to (25) using algebraic identities get, Substituting for $E(k)$ in the above equation,

$$\epsilon(k) = \frac{B(q^{-1})}{A(q^{-1})}\omega_{rest}(k) + F(q^{-1})E(k) + \frac{G(q^{-1})}{C(q^{-1})}\epsilon(k) - \frac{G(q^{-1})B(q^{-1})}{A(q^{-1})C(q^{-1})}\omega_{rest}(k) \quad (2.15)$$

$$\epsilon(k) = F(q^{-1})E(k) + \frac{G(q^{-1})}{C(q^{-1})}\epsilon(k) - \frac{B(q^{-1})}{C(q^{-1})} \frac{C(q^{-1}) - G(q^{-1})}{A(q^{-1})}\omega_{rest}(k) \quad (2.16)$$

From (2.13)

$$\epsilon(k) = F(q^{-1})E(k) + \frac{G(q^{-1})}{C(q^{-1})}\epsilon(k) + \frac{B(q^{-1})}{C(q^{-1})}F(q^{-1})\omega_{rest}(k) \quad (2.17)$$

The variance of the output function is given by,

$$\begin{aligned} & \text{Min}\{E(Y(k+1))^2\} = \text{Min}E\{[(F(q^{-1})E(k+1))]^2\} + \\ & \text{Min}E\left\{\frac{G(q^{-1})}{C(q^{-1})}Y(k) + \frac{B(q^{-1})}{C(q^{-1})}F(q^{-1})u(k)\right\}^2 \end{aligned} \quad (2.18)$$

The proposed control algorithm defines the controlled output ω_{rest} . The variance of the above equation is minimum when

$$\frac{G(q^{-1})}{C(q^{-1})}\epsilon(k) + \frac{B(q^{-1})}{C(q^{-1})}F(q^{-1})\omega_{rest}(k) = 0 \quad (2.19)$$

where

$$\omega_{rest}(k) = -\frac{G(q^{-1})}{B(q^{-1})F(q^{-1})}\epsilon(k) \quad (2.20)$$

With this the controller output becomes

$$\epsilon(k) = F(q^{-1})E(k) \quad (2.21)$$

With the polynomials defined as

$$F(q^{-1}) = 1 \quad (2.22)$$

$$G(q^{-1}) = (c1 - a1)(q^{-1}) + (c2 - a2)(q^{-2}) \quad (2.23)$$

The controlled input to the plant, ω_{rest} is estimated based on the current value and past values of the output and error values as given by

$$\omega_{rest}(k) = -\frac{(c1 - a1)(q^{-1}) + (c2 - a2)(q^{-2})}{b1(q^{-1}) + b2(q^{-2})}\epsilon(k) \quad (2.24)$$

$$b1\omega_{rest}(k) + b2\omega_{rest}(k - 1) = a1\epsilon(k) + a2\epsilon(k - 1) - c1\epsilon(k) - c2\epsilon(k - 1) \quad (2.25)$$

From (2.21), $\epsilon(k) = E(k)$, model error can be equivalent to angle error and is treated with C coefficient. Therefore overall EMVC attains the following form

$$\omega_{rest}(k) = \frac{a1\epsilon(k) + a2\epsilon(k - 1) - c1E(k) - c2E(k - 1) - b2\omega_{rest}(k - 1)}{b1} \quad (2.26)$$

where $\epsilon(k)$ is the error in the rotor angle estimation. According to the proof $E(k)$ is also defined as the angle estimation error that occur in the system due to parameter variation. The sensitiveness of estimated rotor current to the variation in machines physical parameters can be explained by the following relation,

$$i_{rest} = \frac{\psi_s}{L_m} + \left(1 + \frac{L_{ls}}{L_m}\right) i_s \quad (2.27)$$

2.2.5 Improved Dynamic Reactive Power Support Capability

The $d - q$ axis based control architecture of RSC control loops allows the independent control of real and reactive power. For reactive power control, the outer stator terminal voltage control loop derives the reactive power. As the machine parameter varies, the estimated rotor speed differs from actual. Since the vector control approach relies on measured values of rotor current and speed, any form of parameter variation can be said to affect the performance capability of conventional vector

control approach. Reactive power on stator side is given by

$$Q_s = V_{qs}i_{ds} - V_{ds}i_{qs} \quad (2.28)$$

According to the convention, $d - q$ reference frame is assumed to be oriented along stator flux. Thus the above reactive power equation can be modified as,

$$Q_s = -\frac{V_{qs}\psi_{ds}}{L_s} + \frac{V_{qs}L_m}{L_s}i_{dr} \quad (2.29)$$

As it can be seen from (35), the variations in machines physical parameter affects the rotor current. The ability of the proposed architecture is that the modified terminal voltage due to controller adaptation identifies the exact rotor current requirements and ensures superior dynamic reactive power support capability of the sensor less system even during parameter variations.

2.3 Simulation and Experimental Results

2.3.1 Simulation Results

The proposed sensor less vector control scheme is tested on GE 1.5 MW wind turbine model based DFIG model on MATLAB Simulink. The performance of proposed architecture is validated based on following test cases.

2.3.1.1 Test1: Performance Validation with Change in Mutual Inductance

Performance of EMVC is tested for parameter variation and validated. The results are then compared with conventional MVC architecture to showcase the performance improvement. Figure 2.4 shows that the estimated rotor angle closely follows the actual rotor angle for a 50% increase in mutual inductance. Phase error due to parameter variation is corrected by MVC controller. However an offset of +6 degree change is observed on the rotor position with 50% increase in L_m and -6 degree for 30% decrease while using MVC based architecture. With proposed EMVC this

angle offset error is reduced to less than $1e-3$ as it can be observed from Figure 2.5. Figure 2.6 shows corresponding rotor speed estimation error. Table 2.1 shows a comparison of relative error in speed estimation as well as angle offset for both cases. The performance and accuracy of EMVC based control architecture can be validated from the results.

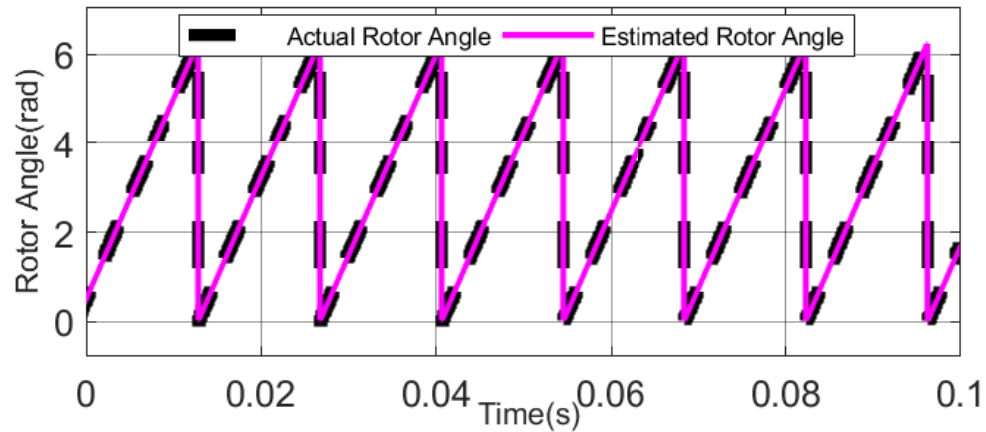


Figure 2.4: Test1: Rotor Angle in Radians for 50% L_m Increase.

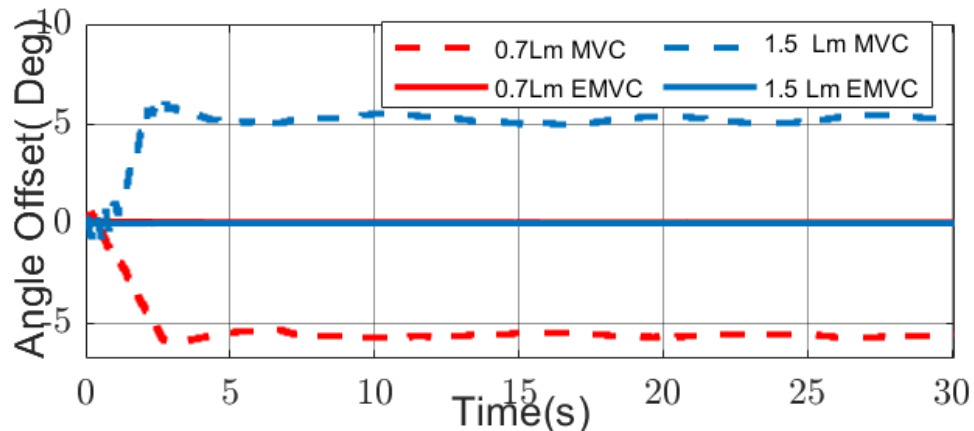


Figure 2.5: Test1: Angle Offset Error(deg) for L_m Variation.

2.3.1.2 Test2: Performance Validation with Change in Terminal Voltage

Performance of proposed architecture for a given terminal voltage variation is tested. Figure 2.7 shows the terminal voltage variation given as reference to the

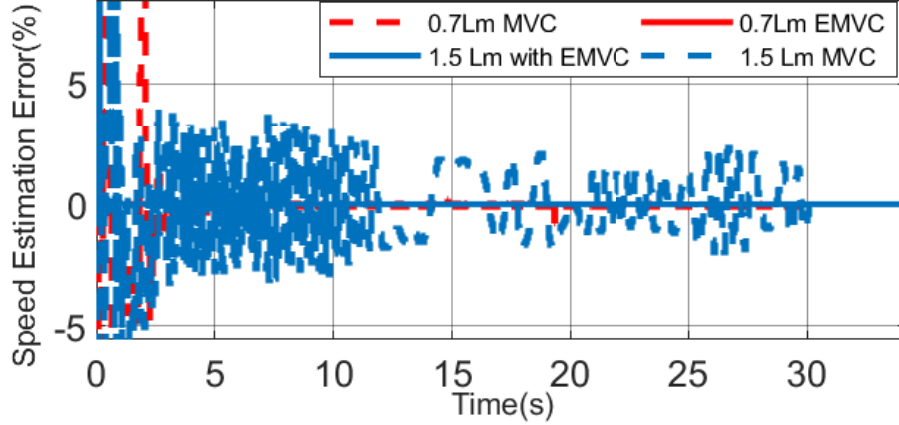


Figure 2.6: Test1: Rotor Speed Estimation Error for L_m Variation.

Table 2.1: Relative Error Comparison

	L_m Change	MVC	EMVC
Angle Offset Error(deg)	$0.7L_m$	-6	0.055
Angle Offset Error(deg)	$1.5L_m$	6	-0.0003
Speed Estimation Error(%)	$0.7L_m$	± 0.2	± 0.005
Speed Estimation Error(%)	$1.5L_m$	± 2.5	± 0.0022

outer voltage loop. Angle offset error using EMVC is unaffected by terminal voltage change even during L_m variation with frequency of the system maintained within $\pm 0.15\%$ as shown in Figure 2.8. Reactive power support during voltage variations is analyzed in Figure 2.9. As opposed to minimum variance architecture that doesn't consider the model estimation error, the proposed EMVC technique shows superior performance in case of voltage sags.

2.3.1.3 Test3: Reactive power Support during Faults

Reactive power support offered by the proposed control loop during faults is analyzed in this test case scenario. The test is performed with a three phase fault applied at 10s. Figure 2.10 shows the terminal voltage improvement and Figure 2.11 shows the reactive power support with EMVC during dynamic analysis. With the outer loop, terminal voltage settles down to 1 pu faster after the application of fault. As

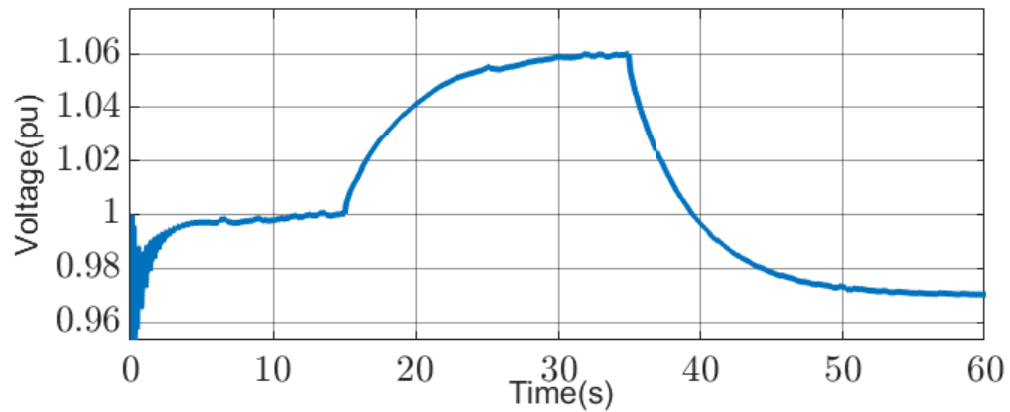


Figure 2.7: Test2: Stator Terminal Voltage.

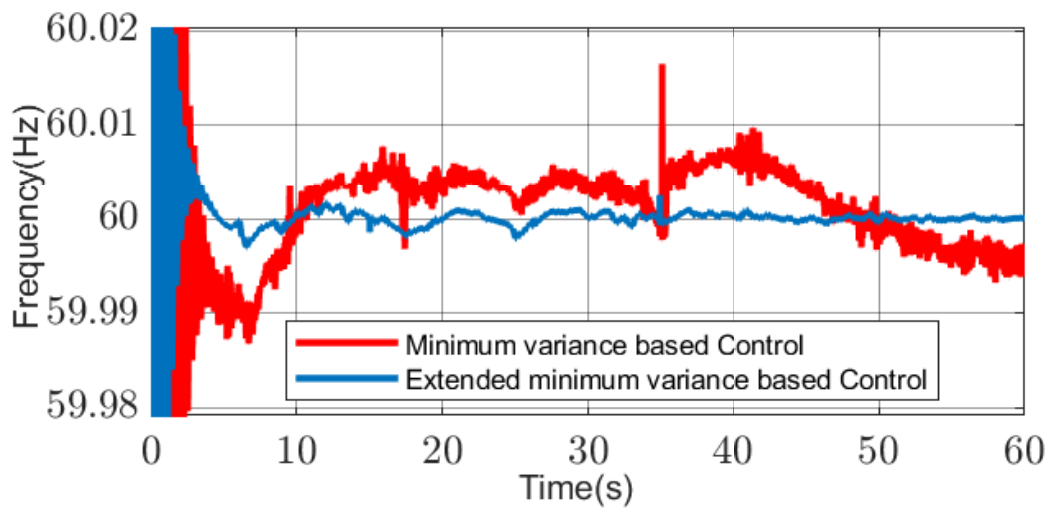


Figure 2.8: Test2: Frequency Support during Terminal Voltage Variation.

compared to conventional vector control loop that results in reactive power absorption affecting the terminal voltage, proposed control loop shows superior performance thereby ensuring greater dynamic stability.

2.3.1.4 Test4: Performance Validation with LVRT Capability

Performance improvement in LVRT capability with the modified terminal voltage control loop has been analysed in test4. Test4 is performed with a 50% increase in mutual inductance and the LVRT capability of DFIG with MVC controller along with usual terminal voltage loop is compared with the proposed EMVC controller with

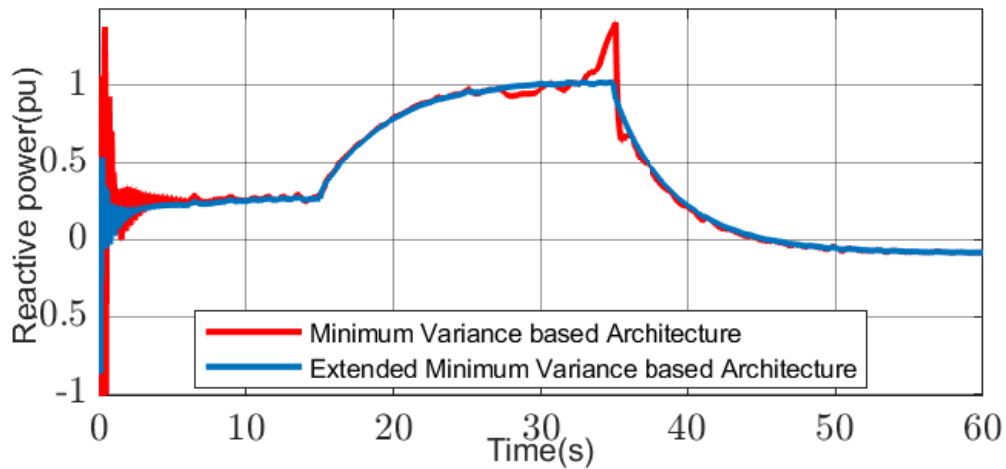


Figure 2.9: Test2: Reactive Power Support during Terminal Voltage Variation.

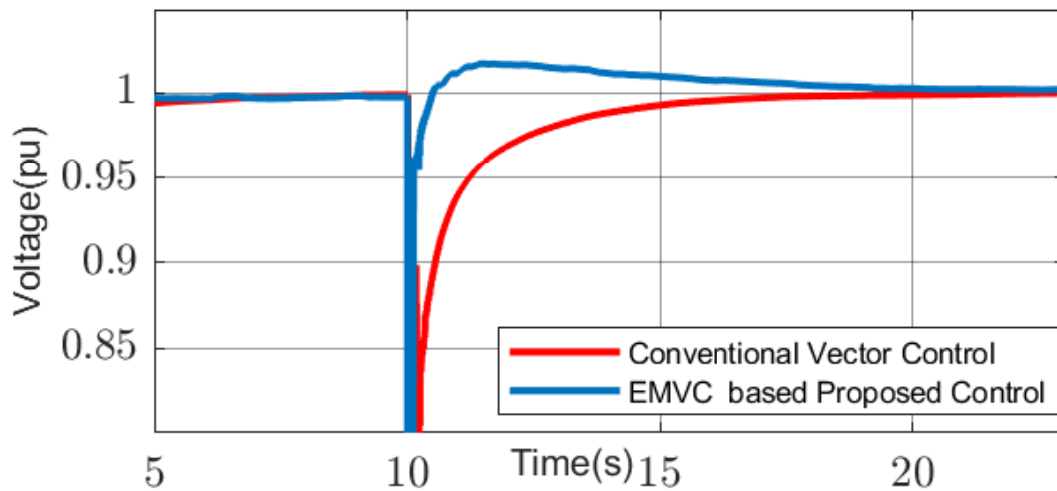


Figure 2.10: Test3: Terminal Voltage during Fault.

modified voltage loop. Figure 2.12 compares the stator terminal voltage of proposed architecture with that of MVC with normal terminal voltage loop. With modified loop, terminal voltage is back to 1pu faster with a slight 4% increase in terminal voltage with the modified loop due to the additional reactive power support offered by loop during the low voltage condition. This can be clearly seen in Figure 2.13. Additional reactive power support offered by the modified loop will help the DFIG for LVRT and rise back to nominal voltage faster. Figure 2.14 shows the percent-

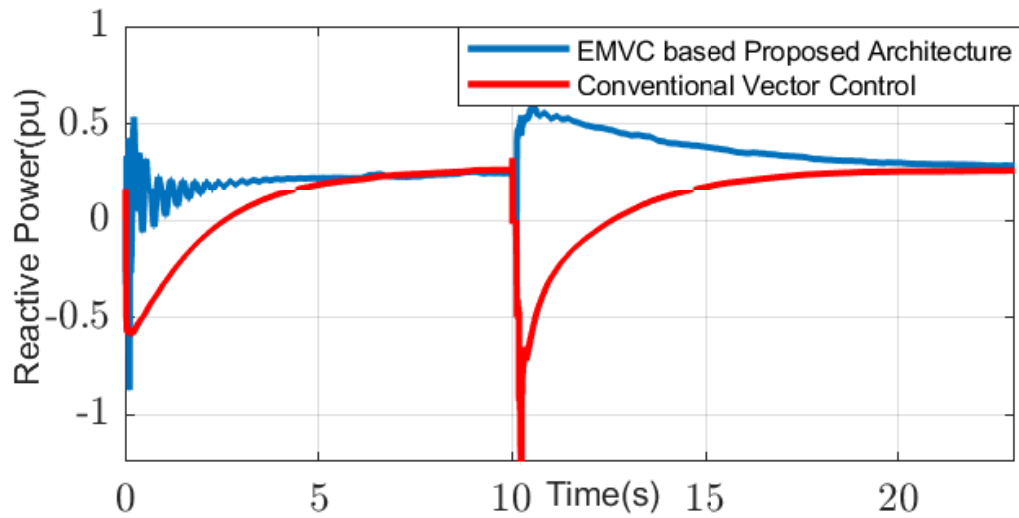


Figure 2.11: Test3: Frequency Support during Fault.

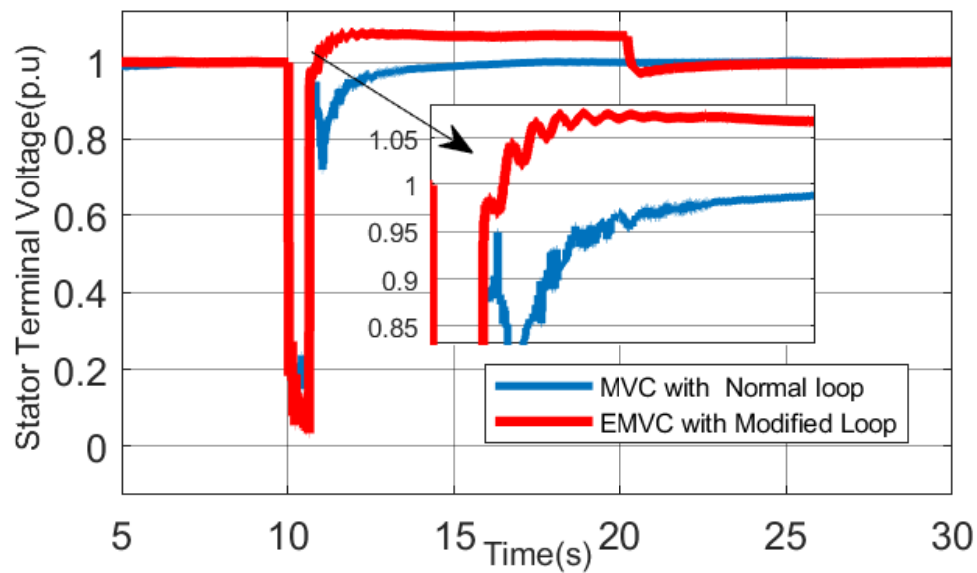


Figure 2.12: Test4: Terminal Voltage during LVRT.

age speed estimation error during LVRT. Figure 2.14 clearly shows that the speed estimation error is much reduced with EMVC as the effect of L_m change is nullified by EMVC. This shows the performance improvement with proposed architecture for LVRT capability of sensor less controlled DFIG.

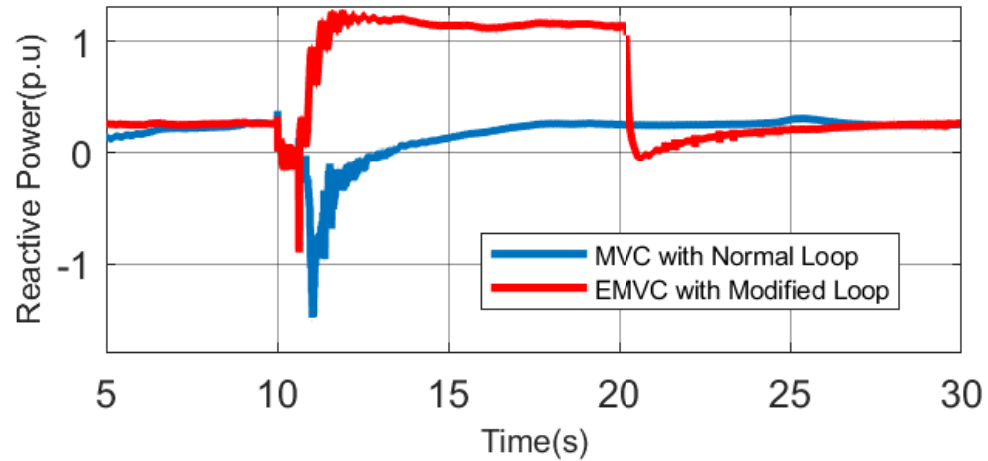


Figure 2.13: Test4: Comparison of Reactive Power Support during LVRT.

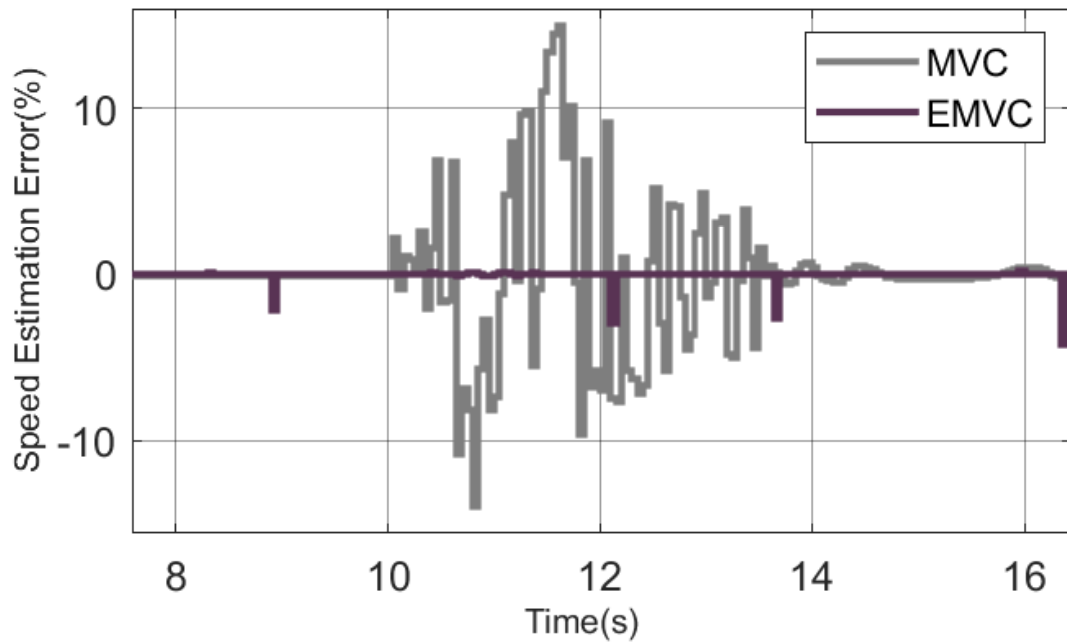


Figure 2.14: Test4: Speed Estimation Error during LVRT with a L_m change.

2.3.2 Experimental Validation

Real-time digital simulation are more close to the actual physical system due to the similar time step for execution. In order to achieve such precision the real time experimental validation of proposed algorithm is performed based on Hardware-in-the-Loop (HIL) simulator platform OPAL-RT. The simulation work for OPAL-RT

real time lab (RT-LAB) is first built in Simulink environment with SPS, RT-Events and Artemis block sets. A time step of $50\mu\text{s}$ is used in both Simulink and real time simulation. The Simulink model is then compiled to executable codes and executed in OPAL-RT platform over several parallel processors. The snapshot of the model for real time simulation is shown in Figure 2.15.

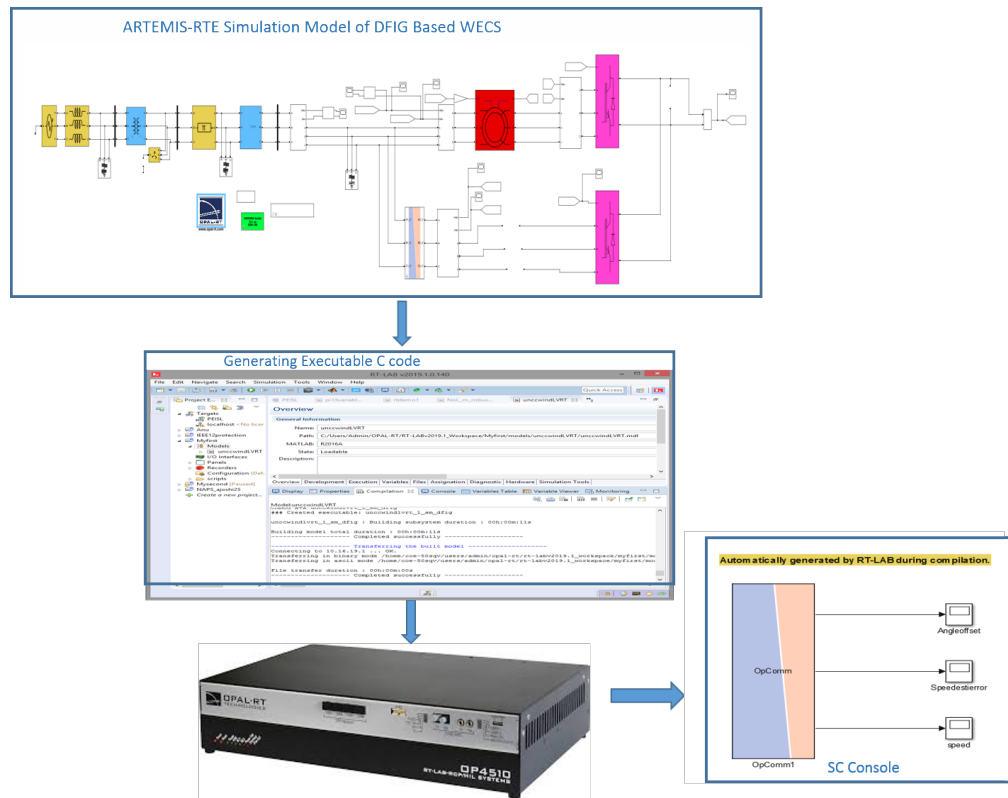


Figure 2.15: Schematic of Proposed Control Model for RT-LAB.

The real time performance of the proposed architecture is validated for machine parameter variations as well as for additional reactive power support during voltage sag to validate the proposed performance improvement. The test is performed with 50% increase as well as 30% decrease in machine mutual inductance. The proposed EMVC architecture has successfully reduced the angle offset error introduced into the system due to machine parameter variation. Figure 2.21 shows the percentage speed estimation error during L_m variation. For 50% increase in L_m the speed estimation percentage has a maximum value of 0.001% while for a 30% L_m decrease it is around

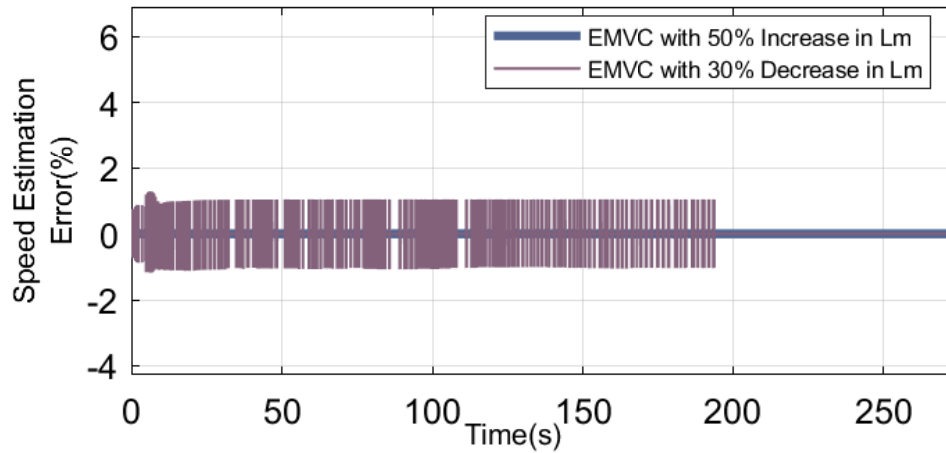


Figure 2.16: Percentage Speed Estimation Error for L_m variation.

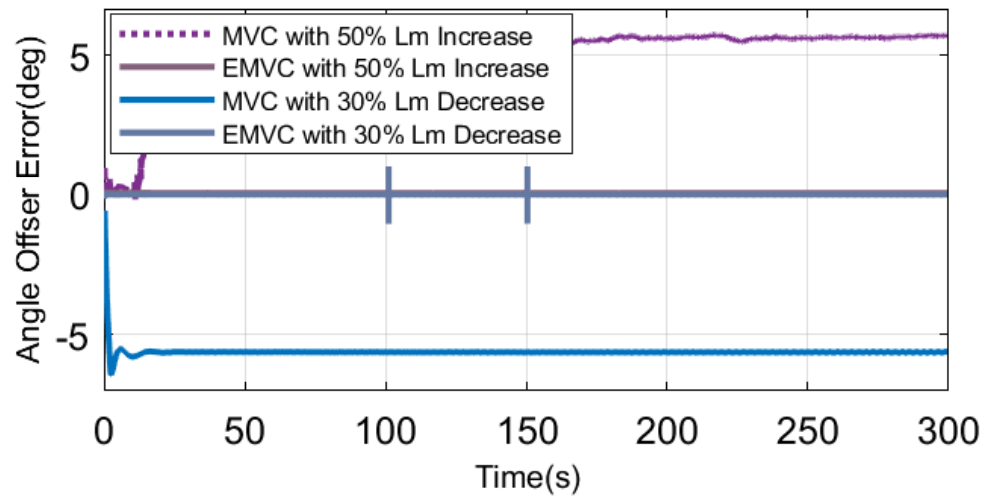


Figure 2.17: Angle Offset Error(deg) for L_m Variation.

1% for first few seconds and it then reduce to 0.001%. Figure 2.22 clearly shows the angle offset error of around 6deg and -6deg with MVC reduced to zero with proposed EMVC architecture. Figure 2.23 analyses the LVRT capability of DFIG with additional reactive power support offered by the modified terminal voltage control loop. Figure 2.19 compares the estimated rotor speed with actual rotor speed for $1.5L_m$ and $0.7L_m$ variations. There is a 1% error between estimated speed and actual speed during 30% reduction in L_m which then reduces to zero after few seconds while the error is close to zero for $1.5L_m$.

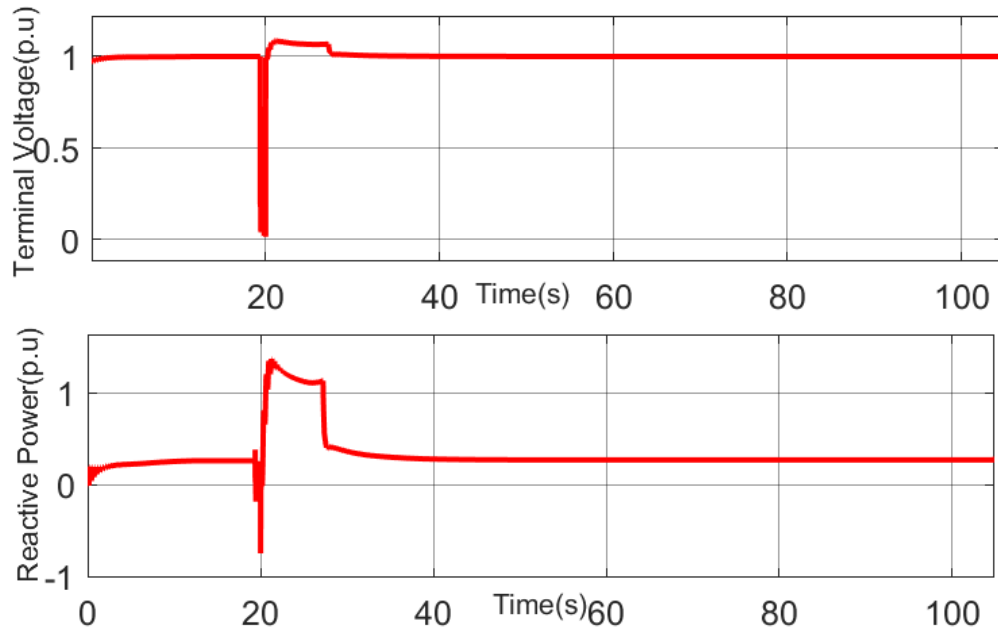


Figure 2.18: Terminal Voltage and Reactive Power Support during Grid Voltage Sag.

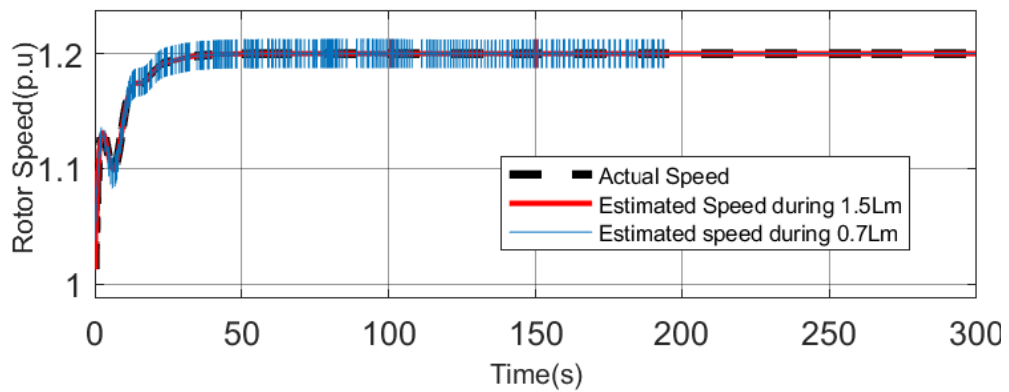


Figure 2.19: Comparison of Actual Speed and Estimated Speed during L_m Variation.

2.3.3 Scalability Test Results

The reliability of the proposed architecture in real grid is validated using a scalability test performed on 123bus system. Figure 2.20 shows the one line diagram of the test system used to perform the test cases. Case A analyses the scalability performance of the proposed system during parameter variation. Case B analyses the performance during a sudden load change. Table 2.2 summarizes the results of scalability test.

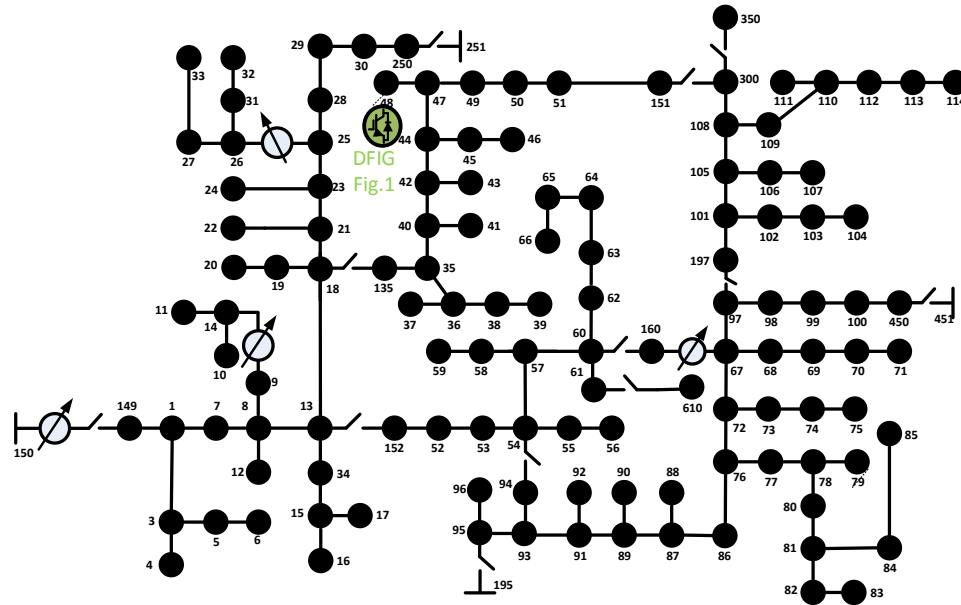


Figure 2.20: One Line Diagram of the Test System used to Perform Scalability Test.

2.3.3.1 Case A: Performance Validation with parameter variation

This test validates the ability of the system to nullify the effects of parameter variations in a real grid environment. All the test results are presented for the proposed system with a 50% increase and a 30% decrease in mutual inductance. Figure 2.21 shows the ability to efficiently estimate the speed with an error as low as $\pm 0.005\%$. Figure 2.22 shows the angle offset error during the variation. The results clearly depict the capability of the proposed system to effectively nullify the angle offset error by the modified MVC algorithm. Figure 2.23 shows that the proposed system can effectively estimate the rotor speed even in a scaled system without being impacted by side effects of parameter variations.

2.3.3.2 Case B: Performance Validation with sudden load change

Case B analyses the performance of the system during a sudden load change initiated at 5sec for a very short duration. Figure 2.24 and Figure 2.25 shows the PCC

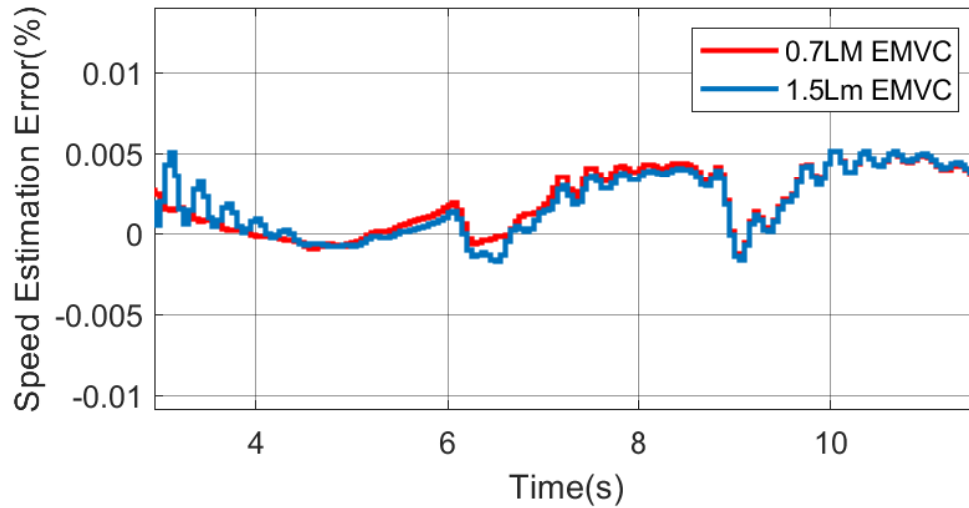


Figure 2.21: Case A: Speed Estimation Error during an L_m Change.

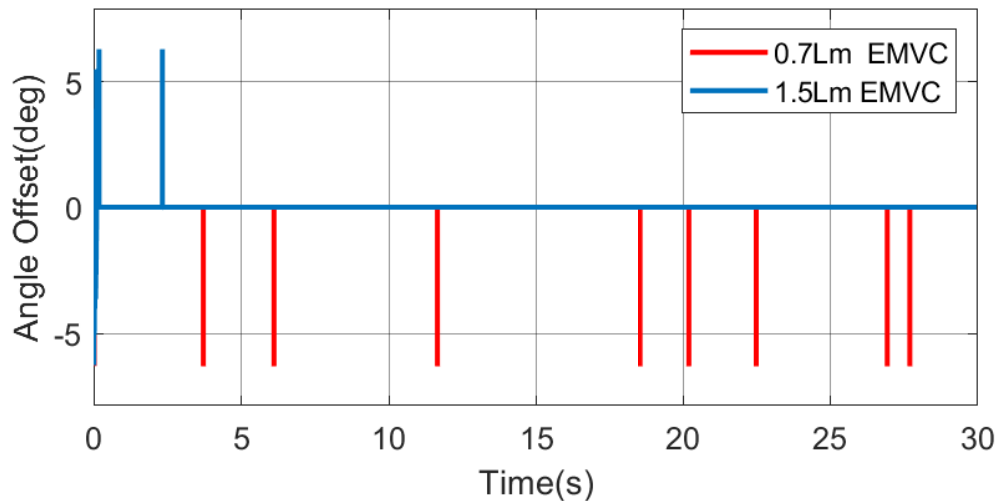


Figure 2.22: Case A: Angle Offset Error during an L_m Change.

voltage and reactive power support offered by the system during the event. The proposed system can very well maintain the terminal voltage faster to the desired nominal value with minimal reactive power support. 0.66% improvement in voltage profile is noticed with the proposed approach compared to the normal terminal voltage control loop approach.

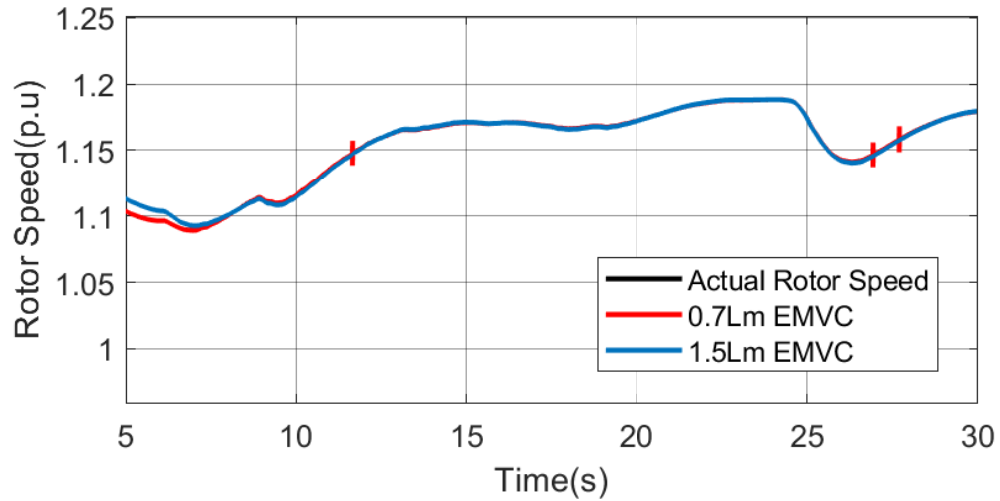


Figure 2.23: Case A: Estimated Rotor Speed during an L_m Change.

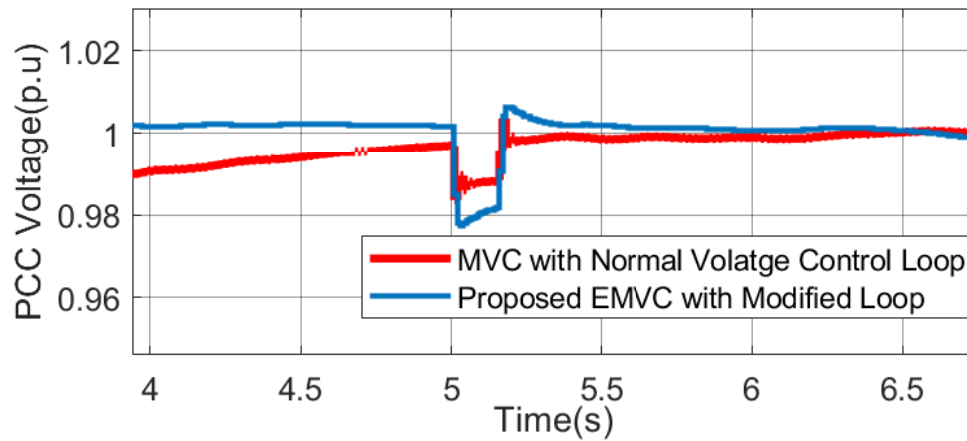


Figure 2.24: Case B: PCC voltage during Sudden Load Change.

Table 2.2: Scalability Test Results

		Value
Case A	Speed Estimation Error(%)	$\pm 0.005\%$
Case B	Voltage profile Improvement(%)	$\pm 0.66\%$

2.4 Chapter Summary

In this chapter, parametrically robust sensorless control of DFIG is presented. Sensorless control exempts the DFIG from all sorts of unwanted noise errors while using encoders. It can be observed that the proposed model is an effective alternative

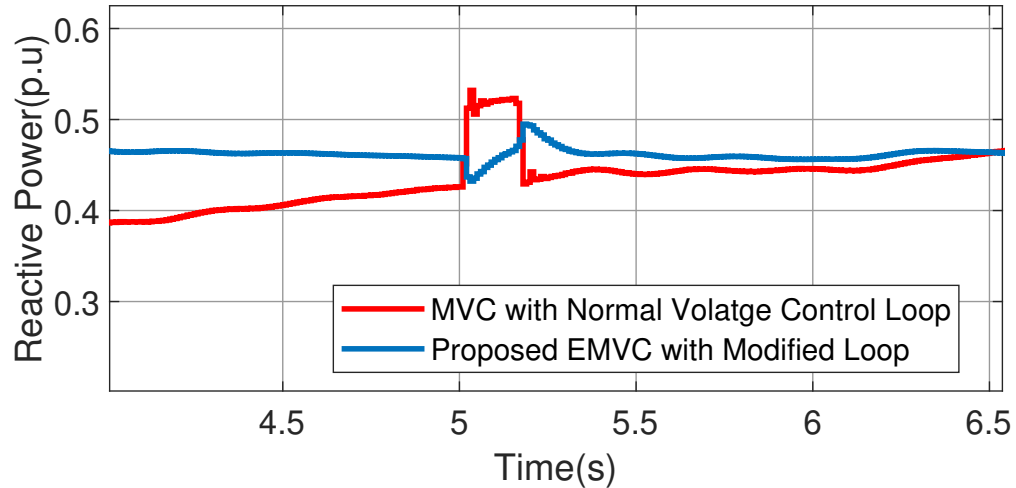


Figure 2.25: Case B: Reactive Power during Sudden Load Change.

to any parameter estimation methods, thereby reducing the computational burden and time needed for the estimation of the control loop. Moreover, the superiority of MVC controllers over other static integrator controllers makes this system robust and promises more reliable operation of DFIG based WECS. Error-based MVC can replace any L_m estimation technique without compromising its performance (i.e., better speed estimation and angle estimation) coupled with faster response. The terminal voltage control loop assures proper reactive power support in case of fault when operating in sensorless mode. The experimental validations based on real-time simulations show that the proposed architecture has improved the overall performance and robustness of the DFIG based sensorless control system.

CHAPTER 3: A SENSORLESS ADAPTIVE GRID SIDE CONTROL APPROACH FOR DFIG

In this chapter, a system identification based adaptive controller is proposed for a grid-connected doubly fed induction generator (DFIG). Recursive least squares (RLS) estimation based system identification provides the auto-regressive moving average exogenous (ARMAX) model of the system. A minimum variance control (MVC) architecture has been used that minimizes the variance of the system output from its reference set-point utilizing the identified model of the system. The proposed architecture simplifies the Grid Side Converter (GSC) control loop of DFIG and overrides the issues in conventional techniques due to bad sensors and effects due to parameters variations. The stability properties of the proposed controller are discussed. Theoretical results are validated using MATLAB-Simulink and real-time simulation platform for 1.5 MW wind turbine system. It is observed that the proposed architecture provides better performance.

3.1 Introduction

Wind Turbine Generators (WTG) has gained larger importance during last few decades. This is due to the advancement in technology in variable speed wind turbine generators. Among this, wind turbine generators (WTGs) based on DFIG and Permanent Magnet based Synchronous Generators (PMSG) are most prominent. DFIGs have become popular in Wind Energy Conversion System (WECS) mostly due to the fact that smaller size power converters (Rotor Side Converter (RSC) and Grid Side Converter (GSC)) can be used for control when compared to the machine rating. The other reasons for the wide usage is due to the fact that power extracted from wind can

be maximized through variable speed operation, and its ability to support grid voltage and frequency through use of supplementary control. The most widely reported control topology for DFIG is Vector Control (VC) which allows independent control of machine torque and reactive power output. In this control technique, the d -axis of synchronously rotating reference frame is aligned with either stator flux [5] or the stator voltage [6] of the DFIG. Detailed analysis of vector control approach for Pulse Width Modulation (PWM) based back-to-back converters of DFIG is explained and simulated in [5]. In [7], a direct power control approach of DFIG based on stator flux estimation is analyzed which demands the knowledge of only stator resistance. In [8], a predictive direct power control approach for DFIG is introduced. In both [7] and [8], control approach include multiple loops which demands appropriate decoupling, introduces rotary transformation, and requires much tuning work assuming knowledge of system parameters to ensure machine's operational stability over the whole operating range. VC is also highly dependent on correct measurements of active power/rotor speed and reactive power and rotor currents which makes the controller heavily dependent on the sensors. The other issue is malfunctions of position and speed sensor of the machine. The position encoders used in DFIG impose several challenges to robustness, reliability, and maintenance. In addition to excellent operation stability during dynamic events, the recent grid code demands WECS to perform ancillary services like voltage regulation, power smoothing, frequency regulation etc. Moreover, the use of static controllers demands re tuning during dynamically varying grid conditions as its operational reliability is limited within a specific range. Hence a detailed analysis of literature on performance challenges during dynamic events is analysed.

3.1.1 State-of-the-Art

Sensorless control of DFIG has gained importance because the use of speed and position sensors in DFIG can impact its robustness and error free operation. Relia-

bility of WTGs can directly impact the availability of wind power due to unexpected turbine downtime [61]. Earlier research work on sensorless control of DFIG shows that the rotor position is derived based on estimated and measured rotor current. Recently, state observers are used for rotor current estimation [62, 63] which are then used as feedback signals in VC so as to make WECS more reliable [64, 65, 66, 67, 68]. Based on the sensorless control, in [69], a modified GSC current controller has been proposed that overrides the issues due to conventional vector control. However, all these approaches still rely either on sensors which are prone to failures, or are not adaptive.

3.1.2 Main Contributions

To overcome large tuning work for non adaptive controllers, reduce the controller design complexity, dependency on sensors and knowledge of system parameters in VC, in this paper, an output feedback controller for the DFIG- GSC controller based on identified system model is proposed. The controller augments existing VC based RSC controller and provides a sensorless control architecture. The motivation behind the design of this controller is to increase the reliability of DFIG operation and simplify the controller design process. The major advantages of the proposed technique can be summarized as:

- The controller is tuned online and does not require proper knowledge about the DFIG system parameters.
- The design of proposed control technique is simple, robust, and feasible.
- The approach is scalable and can be implemented in real systems interconnected with larger power grid.
- The controller minimizes the use of speed sensor required for DFIG control.

3.2 Speed Observer for DFIG

The speed and position estimation of DFIG rotor is based on designing an adaptive model and a reference model inspired from [70, 71]. This technique reduces the error in the reference or measured and estimated current signal by dynamically adjusting the estimated rotor speed. An estimation of the rotor current, \hat{i}_r is computed based on measured stator voltage, v_s and stator current, i_s . In stationary reference frame, the p.u. stator flux can be computed as,

$$\Psi_s = -L_s i_s + L_m i_r e^{j\theta_r} \quad (3.1)$$

where i_r represents the measured rotor current (at slip frequency) and θ_r is the position of the rotor with respect to stationary reference frame. The estimated rotor current \hat{i}_r in stationary reference frame is obtained as,

$$\hat{i}_r = \frac{\psi_s + L_s i_s}{L_m} e^{-j\hat{\theta}_r} \quad (3.2)$$

where estimated rotor current is \hat{i}_r and estimation of the rotor angle is $\hat{\theta}_r$. Once an estimation of rotor current is obtained, an estimation of error between i_r and \hat{i}_r can be calculated by properly defining an error function. The error in $\alpha - \beta$ components between the measured rotor current i_r and estimated rotor current \hat{i}_r is defined as the angle between cross product and dot product between \hat{i}_r and i_r computed using atan2 function. Let 'c' represents the magnitude of the cross product between i_r and \hat{i}_r and 'd' represents the dot product between i_r and \hat{i}_r . The error function 'e' is defined using the 'arctangent' of the ratio of cross product and dot product as,

$$\epsilon = \text{atan2}\left(\frac{c}{d}\right) \quad (3.3)$$

It can be seen that the error is driven to zero when the cross product approaches zero and the dot product is some positive number. This happens when the measured current vector aligns with the estimated current vector. Small signal model of proposed estimator is defined in detail in [71]. Small signal model of the error function is then derived assuming that all the machine parameters are correctly known/estimated, and at the stable operating point can be obtained as,

$$\Delta\epsilon = \Delta\theta_{\text{err}} = \frac{\Delta\omega_r - \Delta\hat{\omega}_r}{s} \quad (3.4)$$

where $\Delta\epsilon$ is the error in alignment of \hat{i}_r with respect to i_r and $\Delta\omega_r$ and $\Delta\hat{\omega}_r$ are the deviations in the actual and estimated speed. The derived small signal model in (3.4) assumes ideal conditions ignoring the non-linear effects such as sampling delays, machine parameter variations and distortion in the DFIG voltages and currents. To deal with this non-linearities the relation between error ϵ and estimated rotor speed $\hat{\omega}_r$ is identified using the RLS based identification technique. This improves the controller robustness.

3.3 Recursive Least Squares System Identification

RLS technique is a computational algorithm that minimizes a weighted linear cost function which is a squared error between the measured output and the estimated output for a particular input signal. In this technique, a system model is first hypothesized and then updated online using the measurable system parameters so as to minimize the error between the estimated output and the actual output of the

system. Consider the following ARMAX model of the system [72, 73]:

$$y(k) = \frac{B(z^{-1})}{A(z^{-1})} \times u(k) + \frac{C(z^{-1})}{A(z^{-1})} \times \varrho(k) \quad (3.5)$$

where

$$A(z^{-1})y(k) = B(z^{-1})u(k) + C(z^{-1})\varrho(k) \quad (3.6)$$

$$A(z^{-1}) = 1 + a_1z^{-1} + a_2z^{-2} + \dots + a_{na}z^{-na} \quad (3.7)$$

$$B(z^{-1}) = b_1z^{-1} + b_2z^{-2} + \dots + b_{nb}z^{-nb} \quad (3.8)$$

$$C(z^{-1}) = 1 + c_1z^{-1} + c_2z^{-2} + \dots + c_{nc}z^{-nc} \quad (3.9)$$

and, $k = n + 1, n + 2, \dots, t$, where $n = \max\{na, nb, nc\}$, t is the time index, $u(k)$ is the control sequence applied to the system, $y(k)$ is the output sequence obtained from the system and $\varrho(k)$ represents the sequence of system disturbance and identification error combined. The prediction of the model parameters is calculated using (3.10) (3.7), which attempts to estimate the model using parameters that minimize the error variance, and is in the form of [72, 74]:

$$\hat{\theta}(k) = \hat{\theta}(k-1) + K(k)[y(k) - \hat{y}(k)] \quad (3.10)$$

where

$$K(k) = \frac{P(k-1)\phi(k+1)}{\lambda + \phi^T(k-1)P(k-1)\phi(k-1)} \quad (3.11)$$

$$P(k) = \frac{1}{\lambda} [I - K(k)\phi^T(k-1)]P(k-1) \quad (3.12)$$

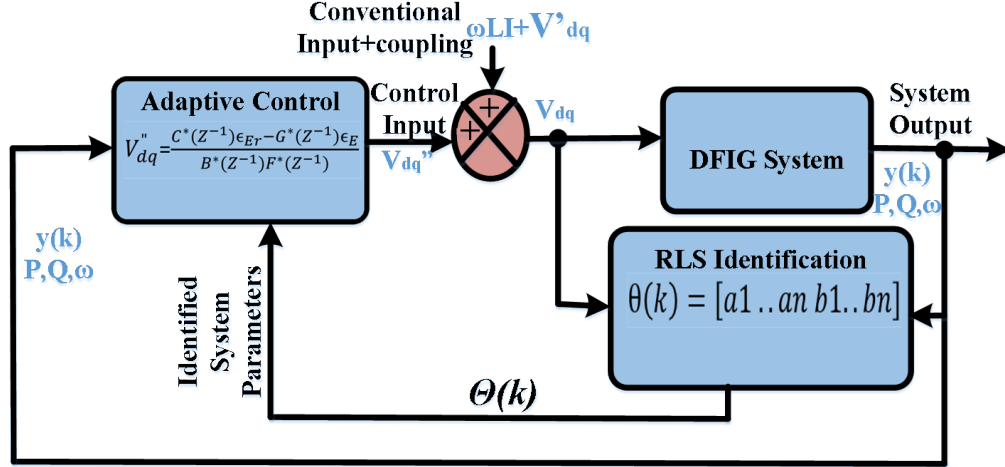


Figure 3.1: Schematic Diagram of the Proposed Adaptive Controller.

3.4 Minimum Variance Control

MVC has been in use in process control due to its properties like reducing deviation around the set-point, consideration of the disturbances that frequently occur in practical systems, simplicity of design and implementation [75, 74, 72]. The major advantage of MVC coupled with identified ARMAX model of the system is that the whole controller design process does not require any prior information about the process and disturbance dynamics. MVC design can be explained as follows. Consider the system model in (3.5), which can be written as,

$$y(k) = \frac{B^*(z^{-1})}{A^*(z^{-1})} z^{-d} u(k) + \frac{C^*(z^{-1})}{A^*(z^{-1})} \varrho(k) \quad (3.13)$$

where $d = n_a - n_b > 0$ is the pole excess of the system. Predicting the system output 'd' steps into the future, one gets,

$$\begin{aligned} y(k+d) &= \frac{C^*(z^{-1})}{A^*(z^{-1})} \varrho(k+d) + \frac{B^*(z^{-1})}{A^*(z^{-1})} u(k) \\ &= F^*(z^{-1}) \varrho(k+d) + \frac{G^*(z^{-1})}{A^*(z^{-1})} \varrho(k) + \frac{B^*(z^{-1})}{A^*(z^{-1})} u(k) \end{aligned} \quad (3.14)$$

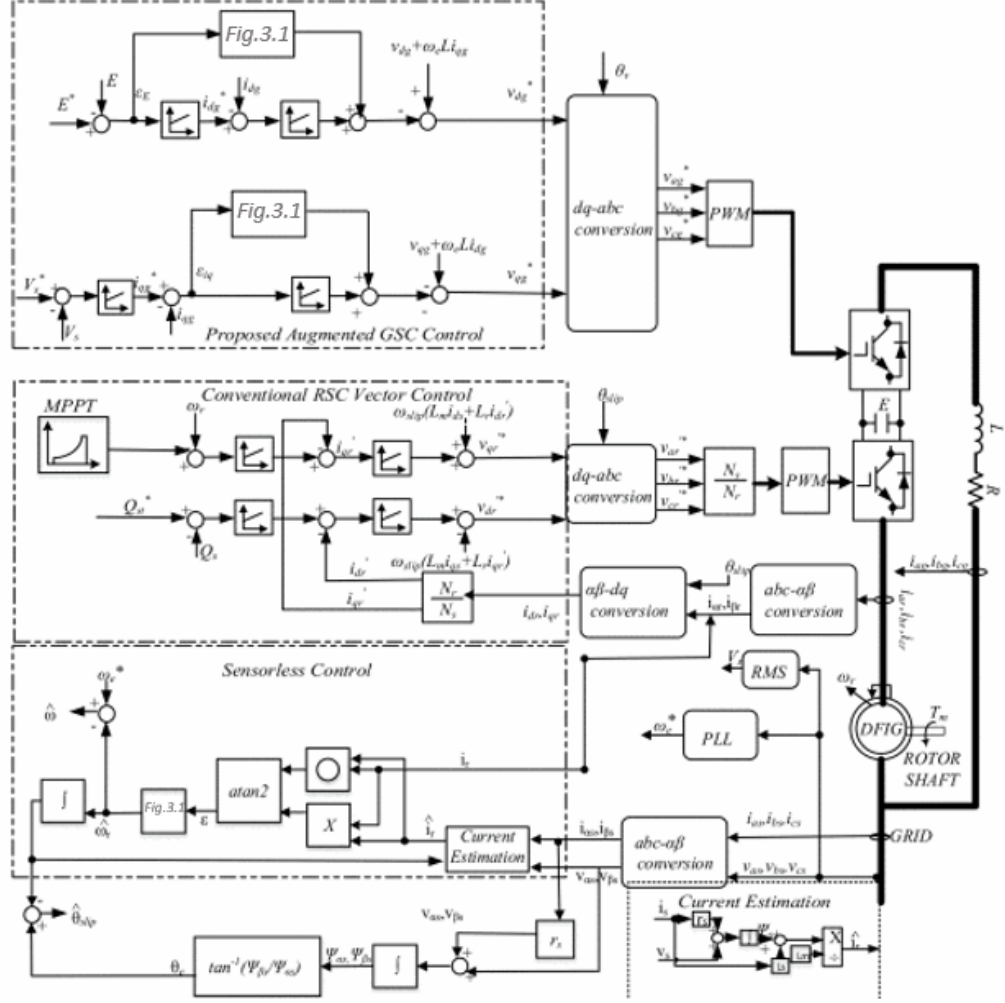


Figure 3.2: Proposed System Identification based Control Structure Augmented to Conventional Vector Control for DFIG.

where $F^*(z^{-1})$ and $G^*(z^{-1})$ are linked with $C^*(z^{-1})$ through the Diophantine equation:

$$C^*(z^{-1}) = A(z^{-1})F(z^{-1}) + z^{-d}G(z^{-1}) \quad (3.15)$$

Estimating $\varrho(k)$ from the original model, one gets,

$$\varrho(k) = \frac{A^*(z^{-1})y(k) - B^*(z^{-1})z^{-d}u(k)}{C^*(z^{-1})} \quad (3.16)$$

Substituting $\varrho(k)$ in $y(k+d)$,

$$y(k+d) = F^* \varrho(k+d) + \frac{G^*}{C^*} y(k) + \frac{B^* F^*}{C^*} u(k) \quad (3.17)$$

The purpose of MVC is to determine the control sequence $u(k)$ in such a way that the objective function

$$J = E\{[y(k+d) - y_r]^2\} \quad (3.18)$$

is minimized. In (7.35), E represents the expected value of deviation of estimated process output d steps ahead into the future and system reference input y_r . Using (3.17) and (7.35), the cost function is minimized when

$$E\left\{\left(\frac{G^*}{C^*} y(k) - y_r + \frac{B^* F^*}{C^*} u(k)\right)^2\right\}$$

is zero as $\varrho(k)$ being a white noise does not correlate with any other term in any time instant (except with itself when $\tau = 0$). The absolute time instant thus loses its importance. Thus, the optimal control sequence becomes as the one shown in (7.36).

$$u(k) = \frac{C^*(z^{-1})y_r - G^*(z^{-1})y(k)}{B^*(z^{-1})F^*(z^{-1})} \quad (3.19)$$

Applying the control sequence in (7.36) to system model in (3.5),

$$A^*(z^{-1})y(k) = -\frac{G^*(z^{-1})}{F^*(z^{-1})} z^{-d} y(k) + \frac{C^*(z^{-1})}{F^*(z^{-1})} y_r + C^*(z^{-1}) \varrho(k) \quad (3.20)$$

With few algebraic compilations, with use of (7.34),

$$\frac{C^*(z^{-1})}{F^*(z^{-1})} y(k) = \frac{C^*(z^{-1})}{F^*(z^{-1})} y_r + C^*(z^{-1}) \varrho(k) \quad (3.21)$$

Thus,

$$y(k) = y_r + F^*(z^{-1})\varrho(k) \quad (3.22)$$

Equation (3.22) shows that with the application of MVC, the system converges towards the reference set-point as the error $\varrho(k)$ is a white-noise with mean of zero, also note that the variance of output is only dependent on the variance of the noise.

The schematic of proposed control augmented to the conventional vector control is shown in Figure 3.2. As it can be observed in (4.12) and in conventional vector control scheme, a third order identification of the system is used in this work corresponding to first order lag representation of system and two cascaded PI controllers can represent the model for the closed loop system.

3.5 Simulation and Experimental Results

3.5.1 Simulation Results

To analyze the performance of the proposed system identification based control approach and compare it with the existing control techniques for DFIG, a set of simulation based tests have been performed on MATLAB-Simulink. The test system used for analysis of the proposed controller is shown in Figure 3.3. Table A.1 shows DFIG parameters used for modeling. Three test cases were performed to show the advantages of the proposed control in DFIG applications. In Test 1, the performance of the proposed controller presented shows equivalent or better control for wide operating range of the DFIG in dynamic wind conditions. Test 2 analyzes reactive power support capability during voltage sags. Low voltage ride through capability of DFIG operated with proposed control demonstrate that the proposed control can maintain operational stability even during grid disturbances. Test 3 showcase the robustness of the proposed control during sensor failure. Table 3.1 quantitatively compares the performance of vector control with proposed control.

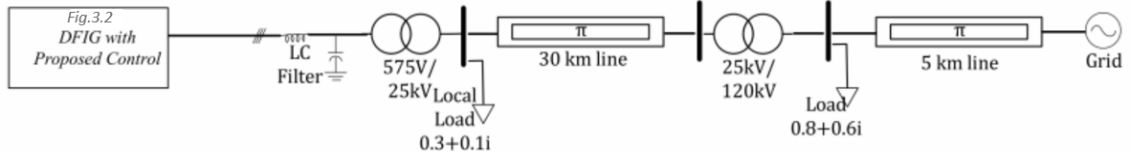


Figure 3.3: One Line Diagram of the Test System used to Analyze the Performance of the Proposed Controller

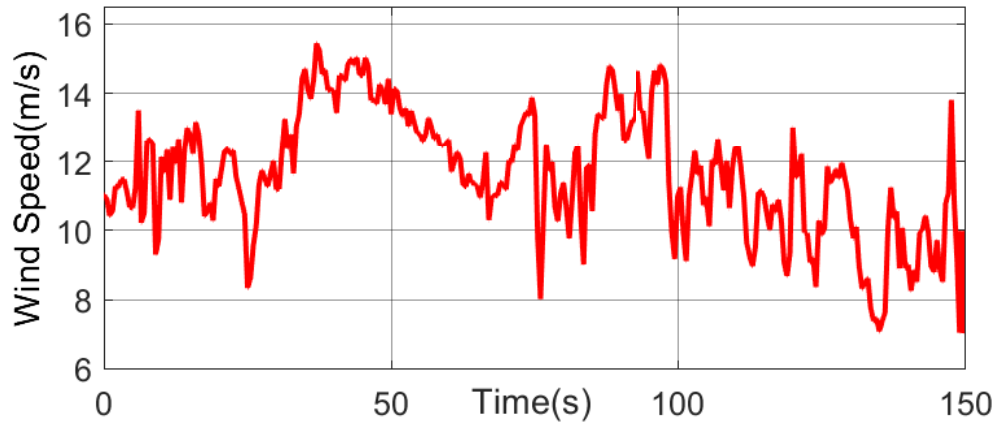


Figure 3.4: Test 1: Wind Speed used to Test the Performance of Proposed Controller.

3.5.1.1 Test 1: Validation of proposed controller

The proposed controller has been tested for wide range of operating regions using the actual wind power data obtained from [76] which is shown in Figure 3.4. This test is to analyze the applicability of the proposed controller in real-life operating scenarios. This set of test case uses the proposed GSC control along with the proposed speed estimation technique. Figure 3.5 shows the rotor speed estimation performance comparison with the proposed speed estimation technique. It can be seen that the proposed architecture accurately estimate the DFIG speed. Figure 3.6 shows the performance of proposed speed estimation technique with proposed identification based GSC control for wind speed shown in Figure 3.4. The estimation error within $\pm 0.5\%$ shows the reliability of proposed estimation technique.

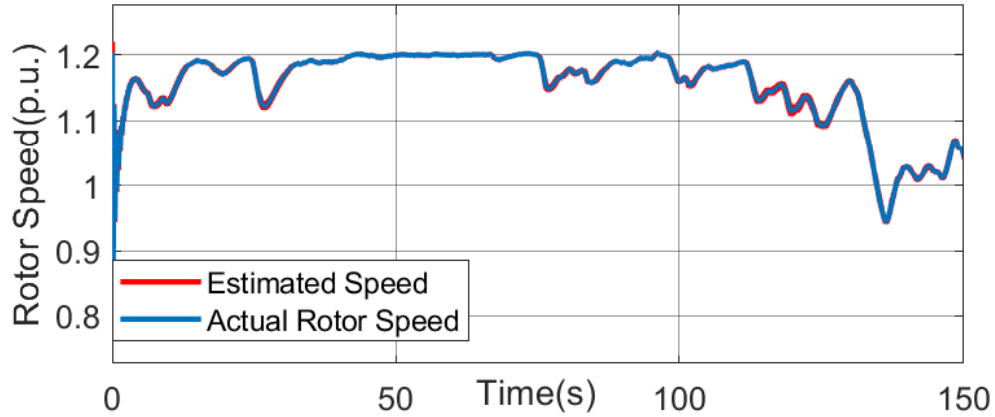


Figure 3.5: Test 1: DFIG Rotor Speed Estimation with Proposed Control.

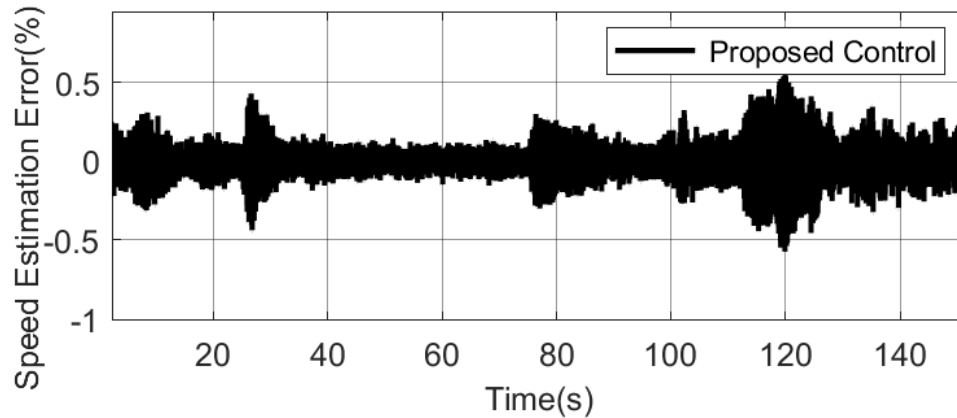


Figure 3.6: Test 1: Speed Estimation Error for Proposed Identification based Control for Wind Speed shown in Figure.3.4.

3.5.1.2 Test 2: Reactive Power Support Capability of Proposed Architecture

In this test, the performance of the proposed system identification based control technique has been evaluated for voltage sag. Figure 3.7 shows the performance comparison of the proposed controller and the conventional VC following a grid voltage sag at 10sec due to three phase to ground fault. It can be observed that with the proposed technique the voltage recovery is much faster as compared to the VC. Also, it is important to notice that the voltage rise phenomena does not occur with the proposed control due to the lack of error accumulation component in proposed control as opposed to VC. Peak overshoot of 1.5% has reduced down to 0.2% with

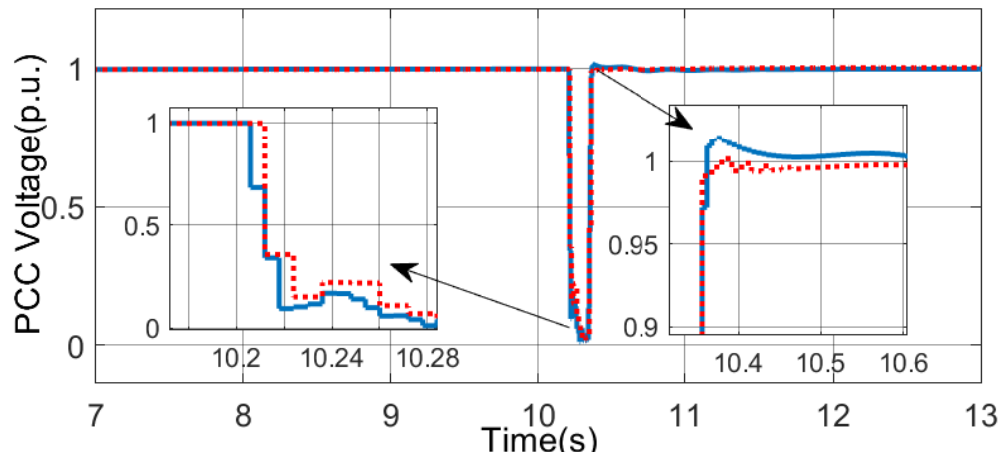


Figure 3.7: Test 2: Comparison between PCC Voltage Regulation from DFIG when using Vector Control and Proposed Identification based Control during Voltage Sag due to Grid Fault.

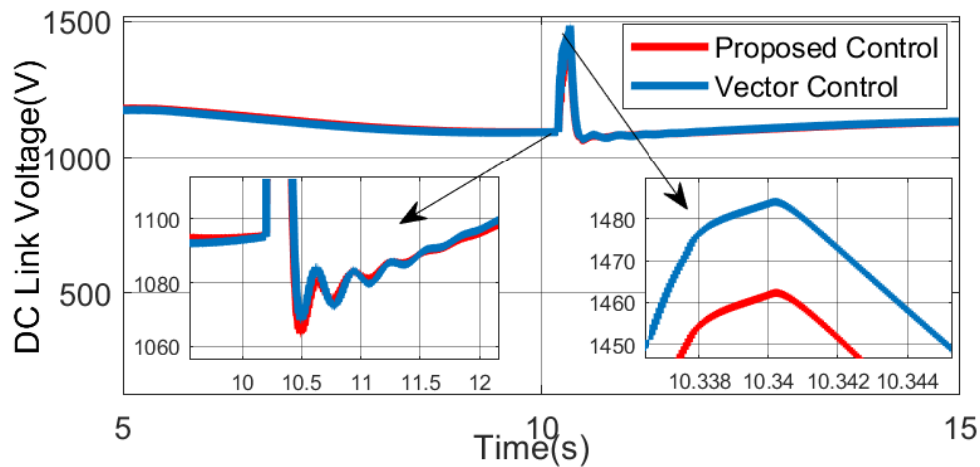


Figure 3.8: Test 2: Comparison between DC Link Voltage Variation from DFIG when using Vector Control and Proposed Identification based Control during Voltage Sag due to Grid Fault.

proposed control. Figure 3.8 shows that the peak deviation of DC link voltage has reduced by 1.48% with the proposed control. The test result showcases the improved low voltage ride through capability of proposed control during grid dynamics with its ability to settle down faster after the fault.

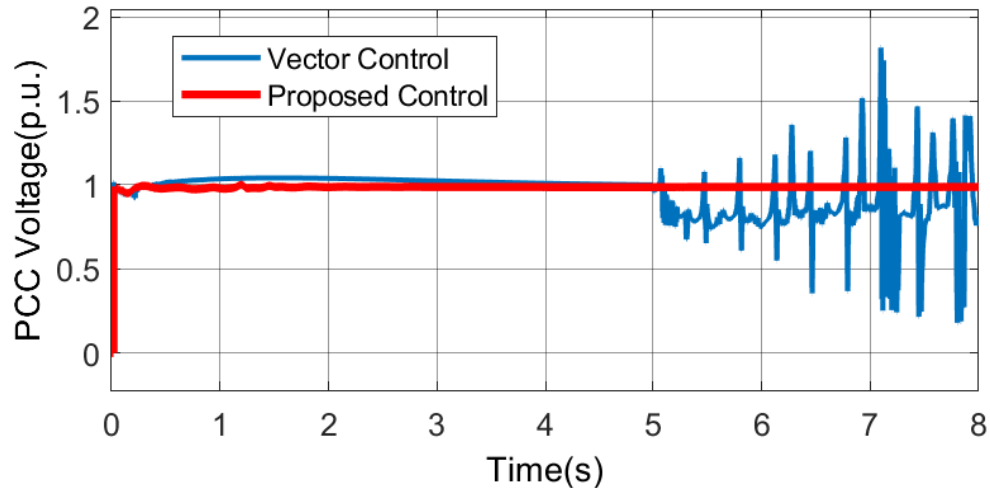


Figure 3.9: Test 3: Comparison of PCC Voltage during Speed Sensor Failure for Vector Control and Proposed Identification based Control.

Table 3.1: Comparison of Different Test Results

Control	Parameter Monitored	Vector Control	Proposed Control
Test1	<i>SpeedError</i>	NA	$\pm 0.5\%$
Test2	<i>VPCCPeakovershoot</i>	1.5%	0.2%
Test2	<i>DCLinkVoltageDeviation</i>	NA	1.48% less than VC
Test3	<i>SystemStability</i>	Unstable	Stable

3.5.1.3 Test 3: Performance Analysis during Rotor Speed Sensor Failure

To demonstrate the robustness of proposed control, rotor speed sensor failure is created for short duration of 0.2sec at 5sec of simulation. Figure 3.9 shows that the proposed control with the speed estimation is robust to sensor failure while with the vector control architecture stability of machine is lost.

3.5.2 Experimental Validation

Simulink results are validated using real-time digital simulation as they are more close to the actual physical system due to the similar time step for execution. In order to achieve such precision the real time experimental validation of proposed algorithm is performed based on Hardware-in-the-Loop (HIL) simulator platform OPAL-RT.

The simulation work for OPAL-RT real time lab (RT-LAB) is first built in Simulink environment with SPS, RT-Events and Artemis block sets. The Simulink model is then compiled to executable codes and executed in OPAL-RT platform over several parallel processors. The snapshot of the model for real time simulation is shown in Figure 5.18.

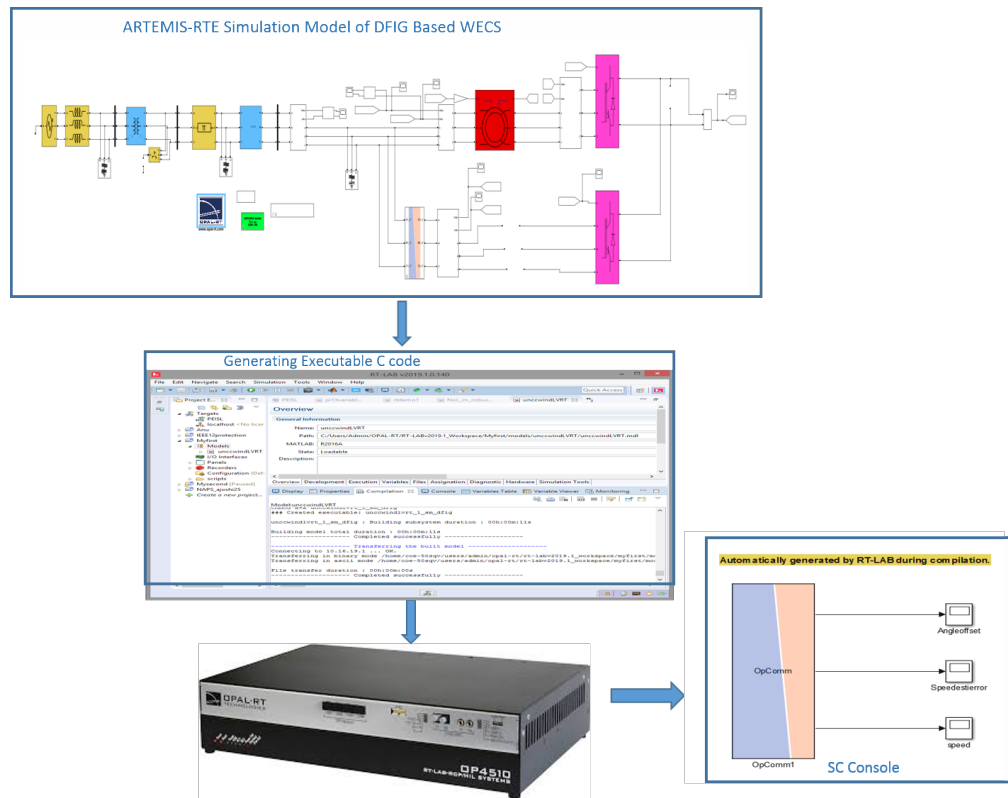


Figure 3.10: Schematic of Proposed Control Model for RT-LAB.

Real time simulations with real wind power data from [76] which is shown in Figure 3.11 is performed and the speed estimation and percentage error graphs are shown in Figure 3.12 and Figure 3.13. Results shows that the speed estimation error is within $\pm 0.42\%$ validating the reliability of proposed estimation technique. Figure 3.14 compares the PCC Voltage dip due to three phase to ground fault applied at 20sec for a duration of 0.13sec. With the proposed technique the voltage recovery is much faster as compared to the VC. It also overrides the voltage rise phenomena that occur with vector control. Figure 3.15 shows that the peak deviation of DC

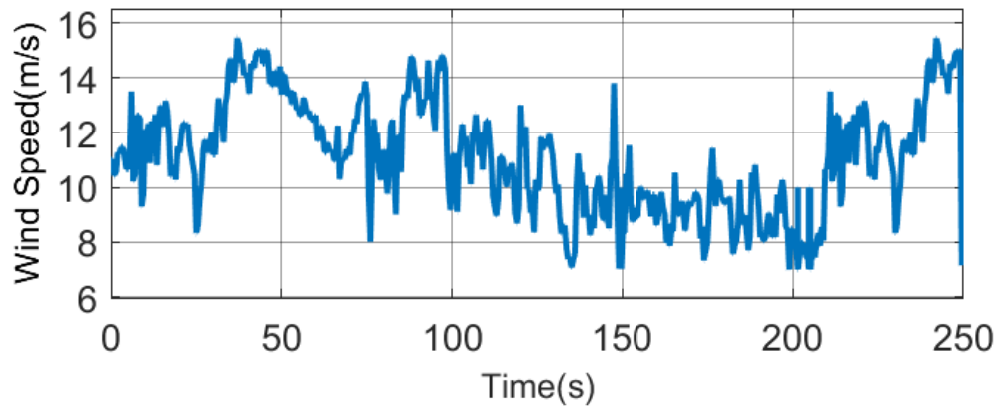


Figure 3.11: Wind Speed used for Real Time Simulation of Proposed Controller.

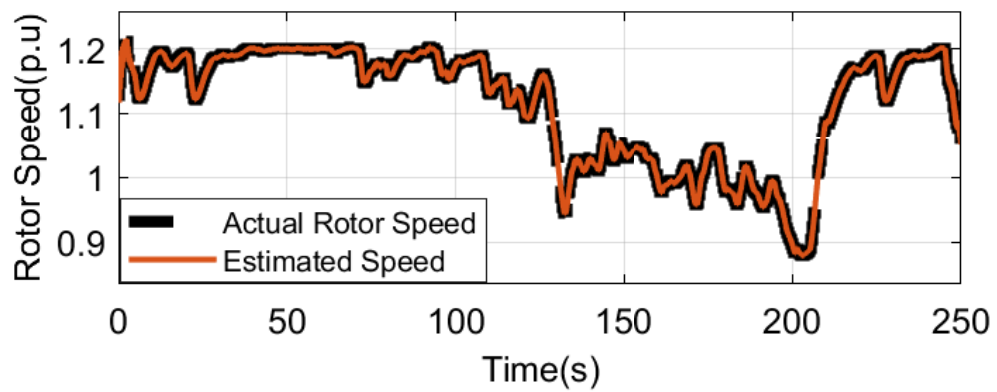


Figure 3.12: DFIG Rotor Speed Estimation with Proposed Control.

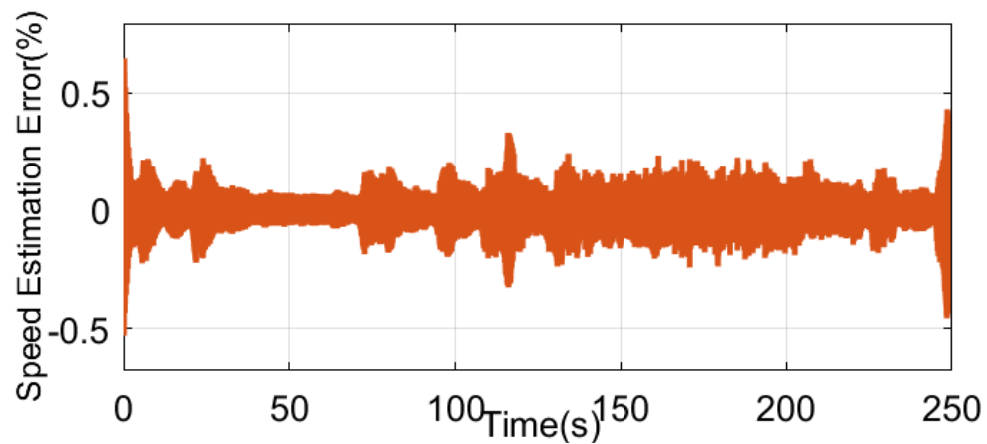


Figure 3.13: Speed Estimation Error for Proposed Identification based Control for Wind Speed shown in Figure.3.11.

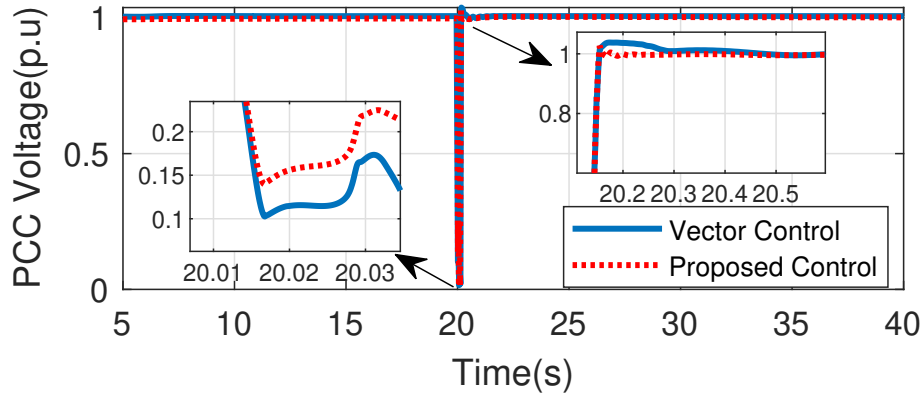


Figure 3.14: Comparison of PCC Voltage during Three Phase Fault for Vector Control and Proposed Identification based Control.

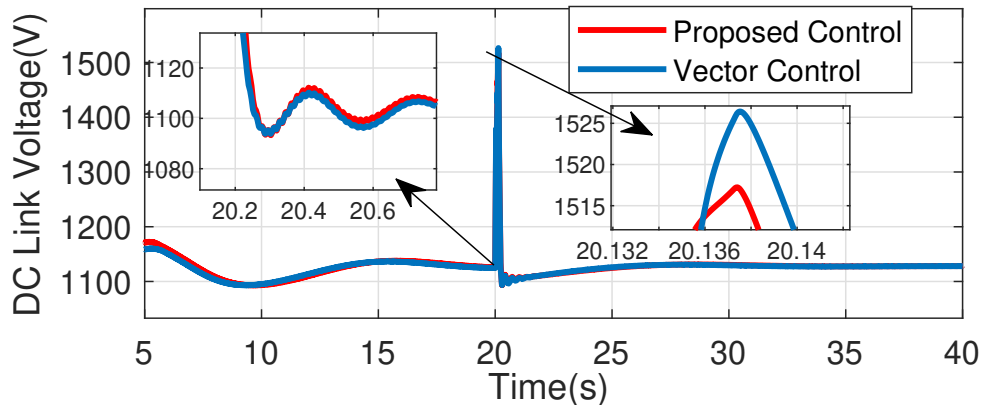


Figure 3.15: Comparison of DC Link Voltage during Three Phase Fault for Vector Control and Proposed Identification based Control.

link voltage has reduced by 0.58% with the proposed control. The test result showcase the improved low voltage ride through capability of proposed control during grid dynamics with its ability to settle down faster after the fault.

Figure 3.16 shows the variations in PCC voltage during dynamic load changes. PCC voltage dip as load increases is 1.84% lower with the proposed control compared to vector control approach. Figure 3.17 shows the deviation of DC link voltage from reference during dynamic load variations for proposed control in comparison to conventional vector control. The deviation of DC Link voltage shows the effect of GSC reactive power control action to bring back the PCC voltage to $1pu$. The large devia-

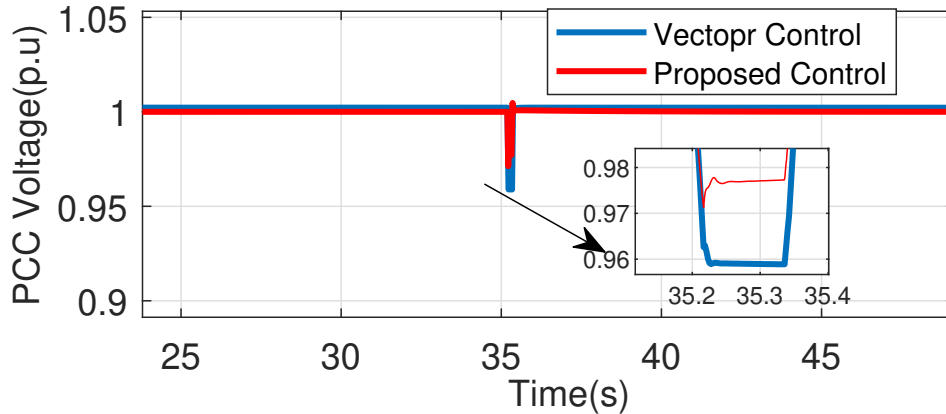


Figure 3.16: Comparison of PCC Voltage during Dynamic Load Changes for Vector Control and Proposed Identification based Control.

tions in DC link voltage occurs during the PCC voltage change at the instant of load change due to the faster control action of adaptive controllers compared to PI controllers. However, the deviations are less than $\pm 0.3\%$ of the steady state value, hence it will not impose any limitation to the practical implementation of the proposed architecture. The robustness of proposed control to speed sensor failure is real time validated in Figure 3.18. The real time validation with actual wind speed data assures that the practical implementation performs well with the proposed architecture. We do not anticipate any field or real-life implementation limitations for the proposed architecture. Table 3.2 shows the quantitative analysis of real time simulation results performed using OPAL-RT RT-LAB platform.

Table 3.2: Comparison of RT-LAB Test Results

Control	Parameter Monitored	Vector Control	Proposed Control
Sensorless	$SpeedError$	NA	$\pm 0.42\%$
Loadchange	$VPCCdip$	NA	1.82% less than VC

3.6 Chapter Summary

In this chapter, system identification-based decoupled control of grid side converter for a DFIG has been presented. The model of the DFIG based WT system is dis-

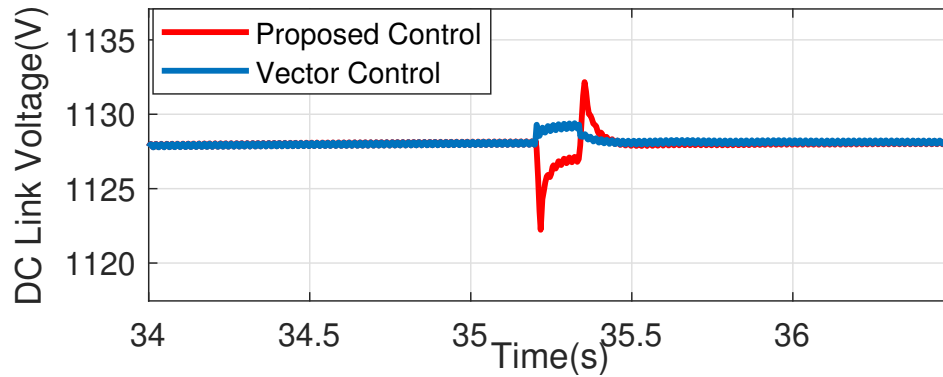


Figure 3.17: Comparison of DC Link Voltage during Dynamic Load Changes for Vector Control and Proposed Identification based Control.

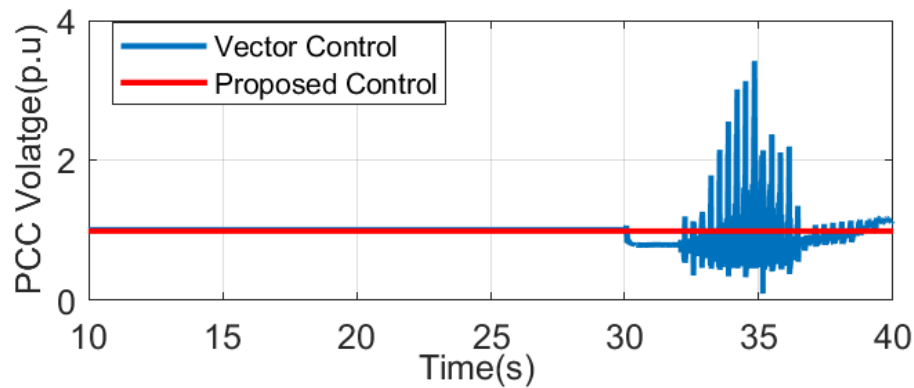


Figure 3.18: Comparison of PCC Voltage during Speed Sensor Failure for Vector Control and Proposed Identification based Control.

cussed, and the design approach of the proposed control is established. The results validated using simulations, and a real-time implementation platform shows that the proposed system identification-based approach results in better control of DC-link voltage fluctuations during dynamic operating conditions of DFIG. The sensorless control is so precise that the speed estimation error is limited to $\pm 0.42\%$, making the system robust to sensor failures. The peak overshoot in PCC voltage is reduced down to 0.2% with the proposed controller compared to vector control. The PCC voltage dip during dynamic load change also improved 1.82% with the proposed architecture. The real-time simulation results validate that the proposed architecture performs well during practical implementation.

CHAPTER 4: PROPOSAL FOR MULTIPLE INPUT MULTIPLE OUTPUT (MIMO) IDENTIFICATION BASED COORDINATED FREQUENCY CONTROL ARCHITECTURE FOR DFIG

This chapter discusses the issues and challenges faced by DFIG based WECS to maintain power system frequency stability. The recent grid interconnection standard expects WECS to provide ancillary services, including the frequency regulation capability. This chapter analyses the different state of the art in frequency control capabilities offered by DFIG based WECS. A detailed analysis of the performance of each of the control loops at different wind speeds is performed. The chapter discusses the need for a coordinated control approach, considering the operating points at different wind velocities. A detailed schematic of a MIMO-based coordinated frequency control has been proposed. The analysis done with a Type3 DFIG based GE 1.5MW wind turbine modeled in Matlab Simulink with a coordinated approach has been presented, and preliminary results are discussed.

4.1 Introduction

With the advent of the concept of sustainable energy, wind and solar-based renewable energy system has gained much importance. Along with the environmental and economic benefits, these increased renewable energy penetrations impose new challenges to power system stability and security. WECS penetration into the current grid is increasing day by day and hence the need to meet the grid code requirements. The concept of primary frequency regulation of grid-connected DFIG has been an important research topic. In US, FERC has issued certain interconnection standards for wind energy connected to the transmission system in 2005. Standard grid code

IEEE 15.47 shows an evolution of grid support functions during the interconnection of Distributed Energy Resources with electric power systems. IEEE 15.47 issued in 2003 expects DFIG shall trip during abnormal voltage and frequency and shall not actively regulate voltage. But as per the 2014 code, DFIG may actively regulate voltage and may ride through abnormal voltage and frequency and may provide frequency response. In the 2018 code, DFIG may provide an inertial response, shall be capable of actively regulating voltage, shall be capable of providing frequency response. As wind generation increases grid code will force WECS to provide more ancillary services that are not currently obligatory such as power oscillation damping. Then utilizing DFIG based WECS to provide ancillary services will not be a feature, it will be a must feature [9].

The intermittent and uncontrollable nature of wind speed imposes several technical challenges in managing grid stability, reliability, and power quality. The frequency stability of the grid can be enhanced by short term active power control strategy. Research shows studies using virtual inertial control to utilize a portion of the kinetic energy from the rotor to support frequency. Long term frequency deviations due to power fluctuations are another power quality concern. Several pieces of researches show control of output power variations from wind farms to improve the frequency deviations.

4.1.1 State-of-the-Art

Several frequency control techniques have been proposed in the literature to regulate the grid frequency within the desired range imposed by the grid code. In DFIG the rotor is connected to the grid via back to back converters thereby decoupling the rotor frequency from the grid frequency. This will reduce the overall inertia of the system compared to the synchronous machine-based generations. As a solution to these issues, the concept of virtual inertia has emerged. Inertial and droop control is one such approach which aims at adjusting the active power output of the signal

based on the frequency deviation. Frequency regulation based on inertial and droop control is a major focus in [77]. In this work, the phased control of DFIG is proposed where the power deviation signal is obtained using the droop coefficient. Different penetration levels are analyzed for the study. It is observed that as the penetration increases, the wind turbine responds quickly to frequency changes and it continues to fluctuate even after the primary frequency regulation.

A novel frequency control framework for primary frequency and inertial response for high wind penetration is discussed in [78]. This approach is based on reduced-order model design and is expected to operate under both subsynchronous and super synchronous wind speed. This work couples pitch control and power control to tackle the stability issues. Inertial and primary response feature is enabled by modifying the pitch angle of the system immediately following a frequency deviation. In both sub and super synchronous speed, WTG is temporarily deloaded to create a power reference to support the frequency deviation.

In [79] a novel integrated control strategy combining inertial control and pitch control has been proposed. Inertial control tries to support short term power using large kinetic energy stored in the rotating mass. In this integrated architecture long term support is provided by the pitch controller. The pitch controller acts on the reserved capacity of DFIG. The integrated control architecture is more efficient than the controllers acting alone. [80] presents another coordinated strategy that eliminates the secondary frequency drop. The strategy of over speed and torque reserve discussed is meant to support long term regulation. But the results validated in the work is considering one specific super synchronous wind speed. In [81] a primary frequency regulation framework involving imitated inertia and droop characteristics is discussed. This work also discusses a distributed coordination among WTs using a peer communication network. The work also uses an index of the state of energy to exploit the kinetic energy from all WTGS and at the same time distribute the

additional power demand among all turbines under coordination. A combined active and reactive power strategy to improve frequency stability is discussed in [82]. In active power-based strategy, droop loop and ROCOF loop ensures that active power output from wind is modulated to ensure frequency stability. Some other frequency regulation techniques have been discussed in [83, 84, 85].

4.1.2 Main Contributions

The major contributions of the work includes,

- Couples the frequency control loop in an efficient way to ensure that DFIG provides maximum power and efficiently regulate frequency stability considering the dynamic wind conditions.
- Efficient coordination of controllers considering the electrical and mechanical dynamics at the same time.
- Provides control of both subsynchronous and supersynchronous wind speed.
- MIMO identification to analyse the participation of each of the states on the grid frequency event.
- Integrating an online identification based adaptive framework in to the proposed system that will dynamically changes the controller gains accordingly is in the future scope of this work.

4.2 Frequency Control Architecture

Frequency deviations can occur in a power grid due to power imbalance happening in the system due to sudden load change, sudden loss of generation, etc. Frequency control relies on efficiently modulating the output power to meet the sudden deviations in frequency. Typical frequency response characteristics of a power system [86] are shown in Figure 4.1. The frequency response can be classified according to different

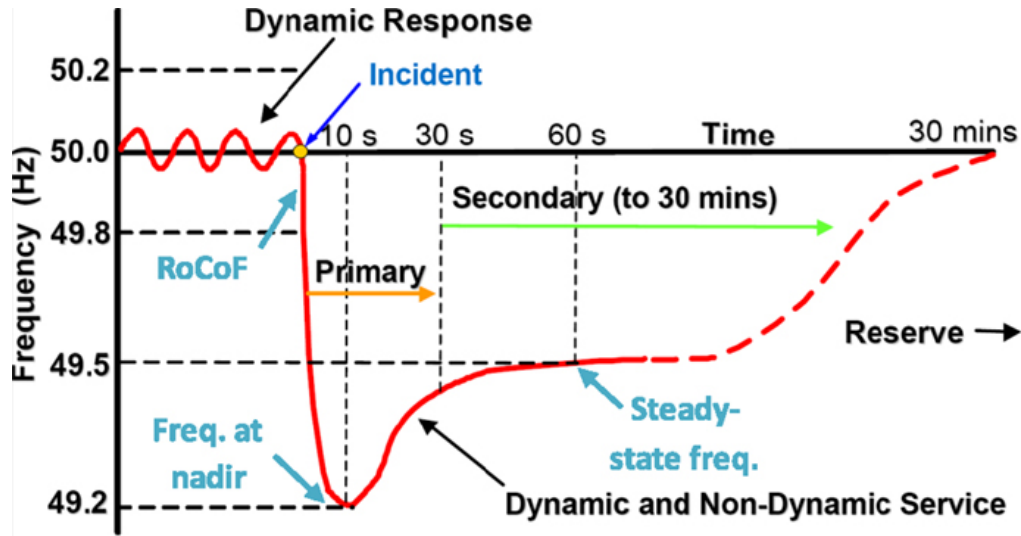


Figure 4.1: Typical Frequency Response Characteristics[88].

time scales. In response to an event like sudden load or generation change, the system frequency starts to fall. The rate of change of frequency at this initial few seconds at which the frequency drops from the nominal value is represented as RoCoF. This rate of change is related to the amount of kinetic energy stored in the rotating mass. But the synchronous machines in the system will provide additional power for a very short duration depending on the inertia of the system. This will last only for the first few seconds. If the system frequency declines beyond a certain range, the primary response also called as governor response starts modulating the power output to mitigate the deviation. This in practice will be by increasing the output from deloaded synchronous machines etc and can last up to 10s. After the primary response, the secondary and tertiary response acts to reduce the deviation and bring the frequency back to the nominal value. This involves automatic generation control, enabling additional power plants, load control, tie line power, etc.

According to recent grid code requirements, DERs should actively participate in these frequency response characteristics. But the intermittent nature of wind energy and the decoupling between rotor and the grid frequency in DFIG based WECS impose some challenges in offering these ancillary services. Several different frequency

control strategies which are most widely used in DFIG based WECS are discussed below. A detailed analysis of existing control topologies has been performed. Several test case scenarios are created with different operating conditions by varying wind speed conditions and frequency changes to identify the issues and challenges with the existing control techniques. The details are presented below.

4.2.1 Inertial Control

Inertial control provides additional power support during the first few seconds or inertial response time of the frequency response curve. This additional power is obtained from the kinetic energy of the rotating parts. Since DFIG cannot emulate this inertial power like as in a synchronous machine-based generator, kinetic energy here is emulated manually using control techniques known as synthetic or virtual inertia. The idea is to convert the kinetic energy of rotor to electrical energy. Thus as kinetic energy reduces the rotor speed declines. For the given torque, as the rotor speed declines the real power output increases.

The kinetic energy corresponding to the rotor of DFIG is expressed as,

$$E = \frac{1}{2}J\omega^2 \quad (4.1)$$

where J is the moment of inertia of the wind turbine [83]. When rotor speed changes from ω_1 to ω_2 there will be ΔE change in kinetic energy given by,

$$\Delta E = \frac{1}{2}J((\omega_1)^2 - (\omega_2)^2) \quad (4.2)$$

With a change in rotor speed, wind turbine can provide a short term power that can contribute towards frequency regulation. Since the rotor speed range is between 0.8pu and 1.2pu, a greater amount of kinetic energy can be released to provide additional power during frequency variations. The additional power that can be contributed by

inertial control is given by,

$$P = \frac{dE}{dt} = J\omega \frac{d\omega}{dt} \quad (4.3)$$

ΔP_2 is a function of the rate of change of frequency as follows,

$$\Delta P = -K_{inertial} \frac{df}{dt} \quad (4.4)$$

Thus the power reference to the RSC is updated by both the droop and inertial control loop considering the change of frequency and ROCOF. Several other research works has been done in this area with modified inertial loop based on variable gains instead of fixed gain to perform better during variable wind speed operations.

But there are some issues with this kinetic energy based control.

- Rotor Speed variations can cause oscillations.
- Rotor speed may exceed the operating range.
- Recovery period when rotor speed increases back to normal results in absorbing additional energy which can cause secondary drop.
- Chances of stall when employing KE control at low wind speed.

4.2.2 Droop Control

Droop control contributes towards the primary frequency response upto 10sec. It can emulate the governor response like in conventional synchronous based generation.

The deviation of frequency from nominal is proportional to power and is defined by the proportional constant of K_{droop} . If the frequency drops below the nominal value (due to increase in demand) Δf is positive and ΔP_1 is positive and adds to P_{MPPT} to increase the mechanical power output from turbine. If frequency increases above

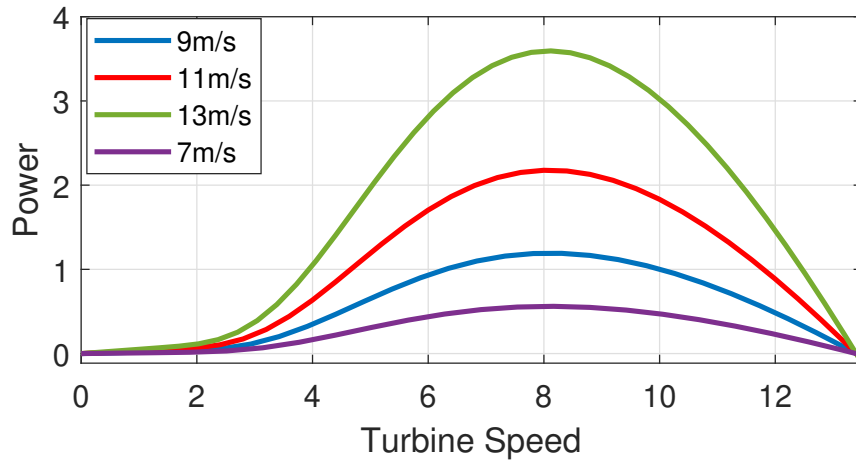


Figure 4.2: Power Versus Turbine Speed Curve for Different Wind Velocities

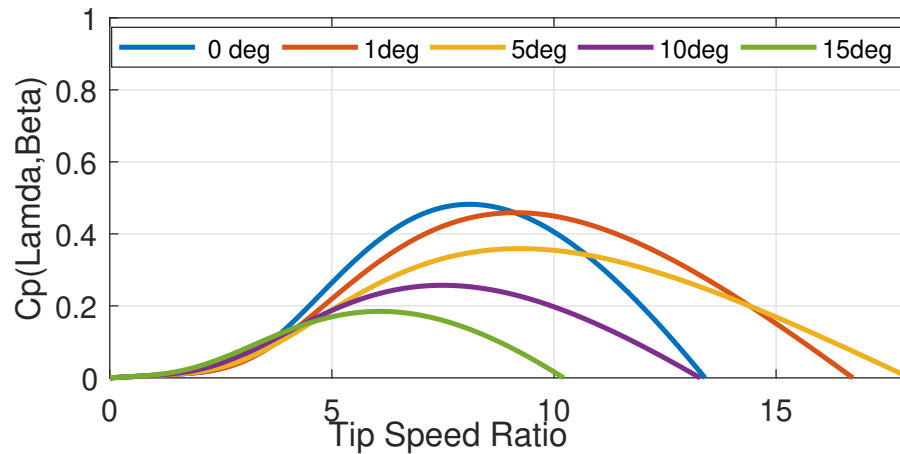


Figure 4.3: Performance Coefficient Versus Tip Speed ratio Curve for Different Wind Velocities

nominal value due to increased generation then Δf is positive and $\Delta P1$ goes negative reducing the overall power reference to RSC.

4.2.3 Pitch Angle Control

Pitch controller is another active power control strategy which is enabled whenever the wind speed exceeds the rated value. In any DFIG based WECS, the conventional pitch controller limits the mechanical output from wind turbine to the equipment rating. For wind speed below the rated value, the pitch is set to minimum so as to

maximize the mechanical power. Conventional pitch controller tracks the rotor speed and active power reference to ensure that it remains within the thermal mechanical or electrical limit of the machine. Figure 4.3 shows the simulation result of variation of performance coefficient for different pitch angles. It clearly show cases the relation of mechanical power output with pitch angle. Several studies has conducted making use of pitch controller to deload the wind turbine to create sufficient active power reserves for frequency regulation during grid connected operations[37, 38, 32, 33].

At super synchronous wind speed the conventional pitch control action sets a positive values of pitch, thereby limiting the output to the rated value. Conventional pitch controller sets the pitch angle to 0deg for sub synchronous operation. Hence at this sub synchronous speed the WTGs will be operating under maximum power extraction mode. But for the pitch controller based frequency regulation at sub synchronous speed, WTGS should be deloaded to a new operating point X or Z below the optimal point selected by MPPT algorithm denoted by Y in Figure 4.4.

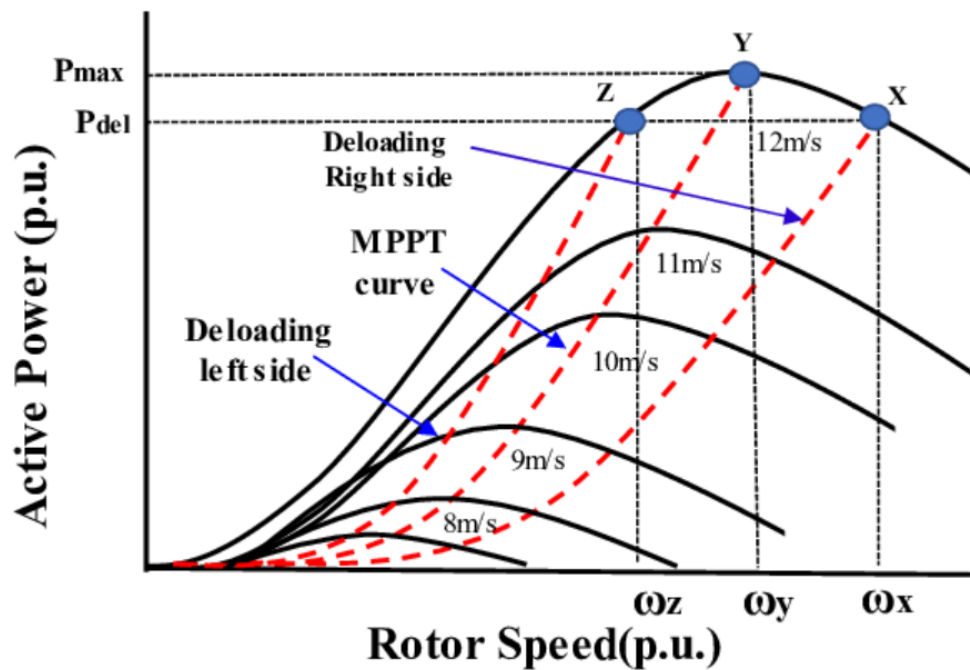


Figure 4.4: Deloaded Power Curves for Wind Turbines[40]

During any frequency event, pitch controller based frequency control sets the pitch angle from a positive value back to zero, which causes an increase in power. The operating point moves from X back to Y providing additional power to support frequency stability.

4.3 Simulation Results

The different control architectures discussed in Section 4.2 is tested on a GE 1.5MW wind turbine integrated on a reduced Kundur two area test system shown in Figure 4.5. Several different test cases are formulated to understand the effect of each of the control loops on frequency stability. The test cases are performed to analyse controller performance during variable wind speed operations and to showcase in detail the issues and challenges faced by the existing conventional frequency control techniques. The final objective is to formulate a coordinated control architecture based on wind speed that extract the maximum power out and at the same time provide excellent frequency regulation capability by dynamically adaptive control logic.

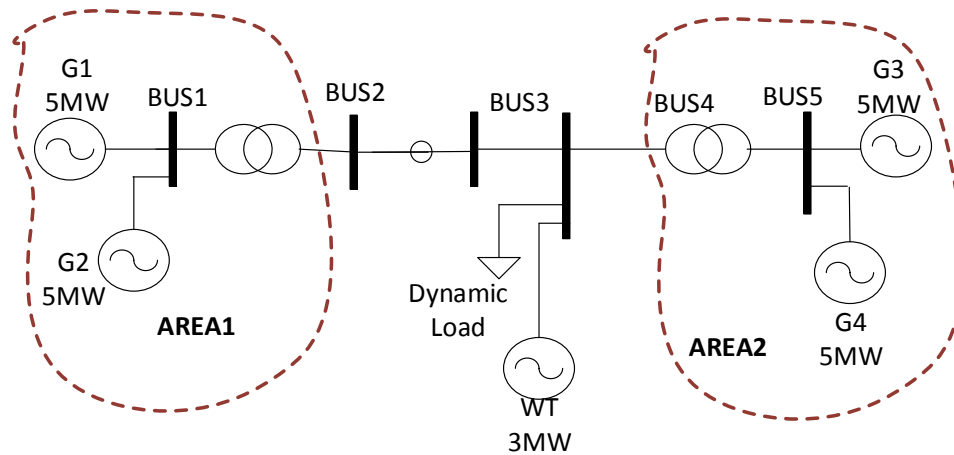


Figure 4.5: One Line Diagram of Reduced Two Area Test System

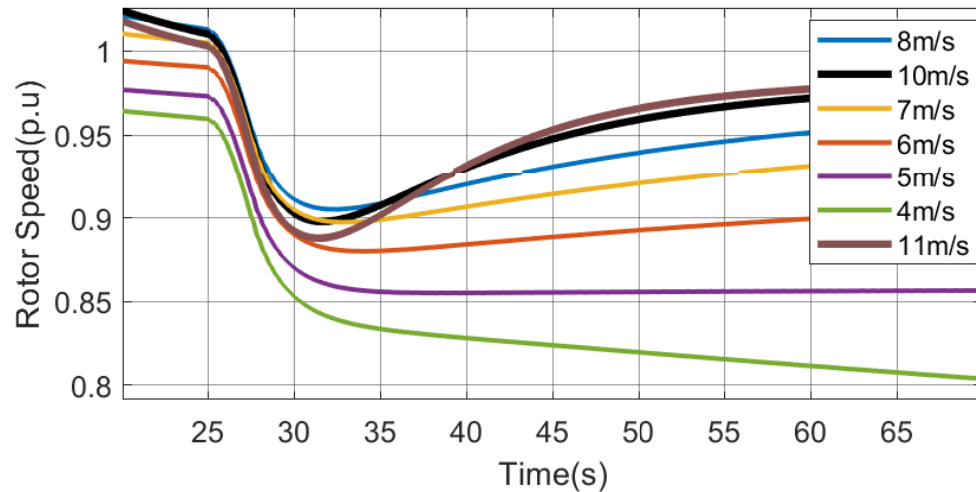


Figure 4.6: Rotor Speed for Different Wind Velocities with Kinetic Energy Control

4.3.1 Test1: Analysis of Kinetic Energy Control

4.3.1.1 Test A: Performance of Kinetic Energy Control for Different Wind Velocity

The effect of kinetic energy control is analysed for a range of wind velocities. The objective of this test is to understand the issues of kinetic energy control and to identify the best range of wind velocity for which the frequency regulation works better with kinetic energy control.

From Figure 4.6 it is clear that during inertial control, kinetic energy of the rotor is converted to support additional power. As a result of which the rotor speed declines. This is clearly depicted in Figure 4.6. For medium wind velocities like $10 - 11\text{m/s}$ the amount of energy released is higher and more is its ability to bring back the rotor speed due to additional power availability. But as wind speed reduces, the additional power reduces as in Figure 4.7. For lower wind speed $4 - 5\text{m/s}$, after the additional power support, the rotor speed starts declining due to the lower energy. This can sometimes lead to rotor stall as the speed falls below certain range which can lead to economic loss. Hence the test results concludes that it is not advantageous to opt for kinetic energy control based frequency regulation at lower wind velocities.

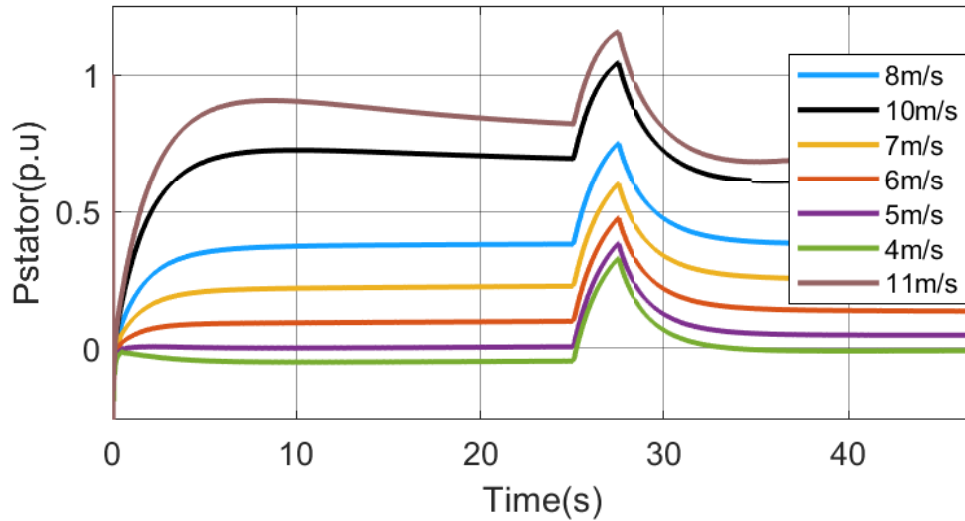


Figure 4.7: Active Power Output with Kinetic Energy Control

4.3.1.2 Test B: Effect of Inertial Constant on KE Control

Test B is performed to analyse the effect of inertial constant on KE control. Figure 4.8 compares the frequency of the system with KE control loop acting alone. KE loop improves the ROCOF of frequency curve by modulating the power output for first few seconds soon after a grid event as shown in Figure 4.9. The duration of the control loop action is determined by the inertial constant of the machine. Higher the inertial constant H more is the additional power that can be supported during the first few seconds. But around 35-40sec, as the frequency deviation reverses its sign, more power is absorbed with higher inertial constant. This can contribute towards a secondary dip which worsens the frequency nadir as show in Figure 4.8. Figure 4.10 shows that the more the inertial constant, the more is the kinetic energy released and the more is the droop in rotor speed. Figure 4.11 and Figure 4.12 analyse the performance for a wind velocity of 7m/s. The results shows that the KE loop when acting alone is ideal for medium wind velocities as active power absorption which causes secondary dip is not considerable higher. But for higher wind velocity it should be in combination with another loop that supports during primary response time. This in

turn to analyzes the need for variable kinetic loop gain for better performance.

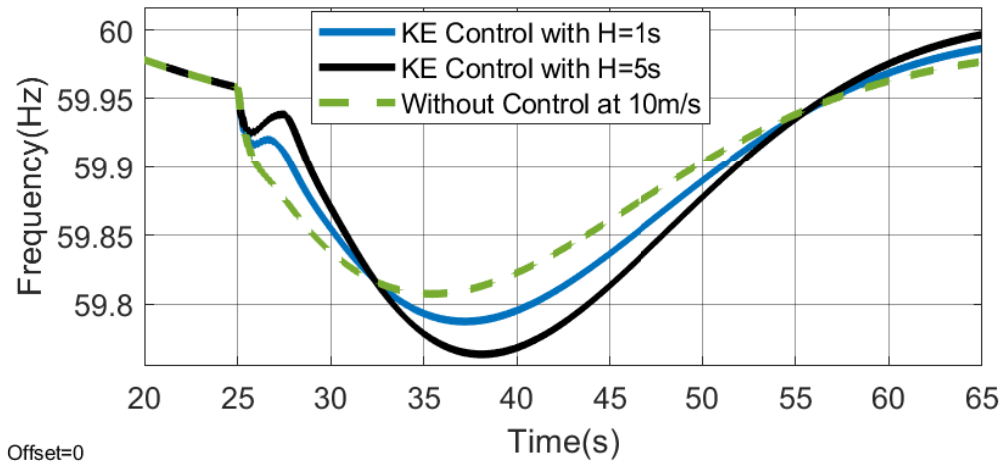


Figure 4.8: Frequency Improvement with Kinetic Energy Control with Different Inertial Constants at 10m/s

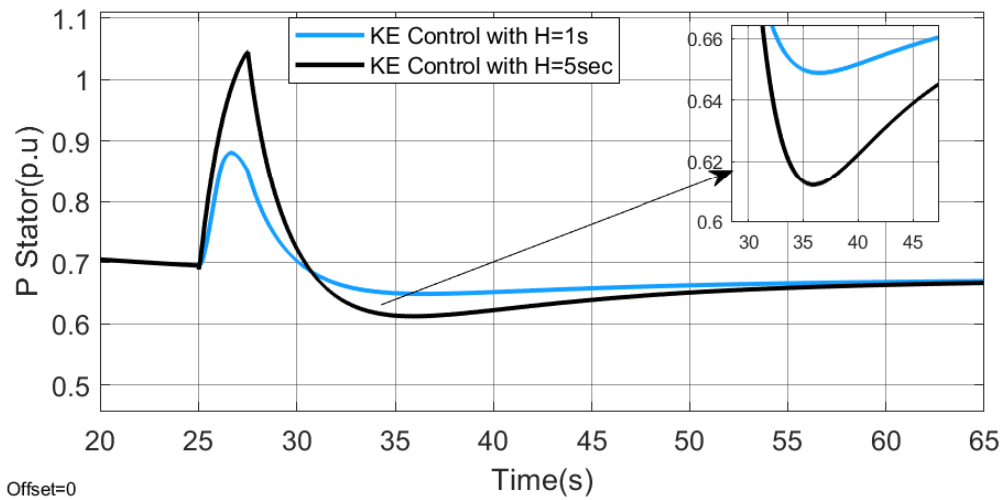


Figure 4.9: Active Power Output with Kinetic Energy Control with Different Inertial Constants at 10m/s

The Test A and Test B results can be concluded as,

- KE control performs better at medium wind velocity.
- At lower wind speed the rotor speed reduces too low. Also the available energy to absorb and come back to equilibrium point is less which lead to more worse secondary droop.

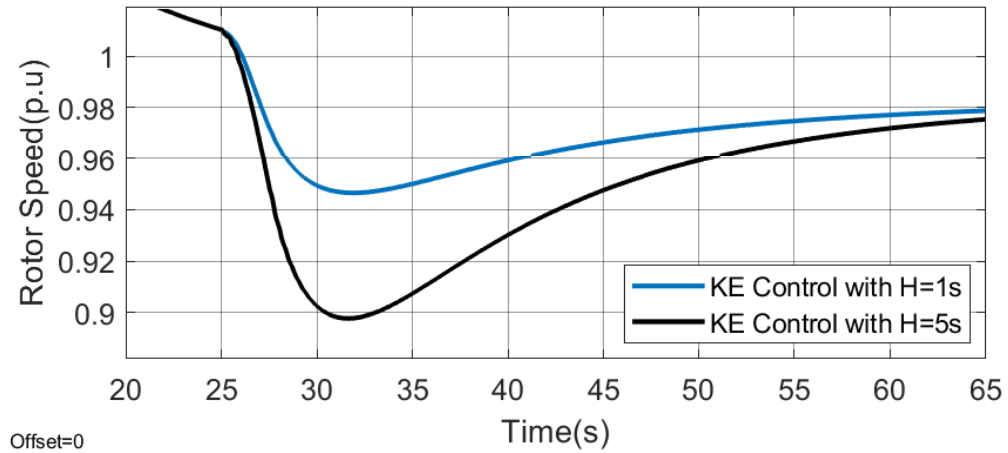


Figure 4.10: Rotor Speed with Kinetic Energy Control with Different Inertial Constants at 10m/s

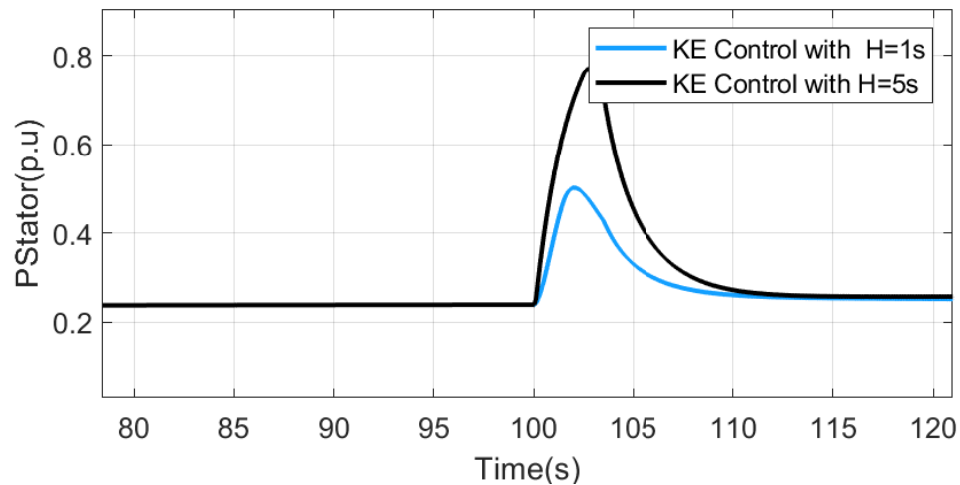


Figure 4.11: Active Power Output with Kinetic Energy Control with Different Inertial Constants at 7m/s

- At super synchronous wind velocity amount of available power is limited by mechanical limitation. Hence KE control is ideal during medium wind velocities.
- Combined control shows better performance.
- Concept of variable inertial constant can be considered. Keeping higher H value for higher wind speed is not advantageous.
- Higher the H, the more the time duration for which kinetic energy can be

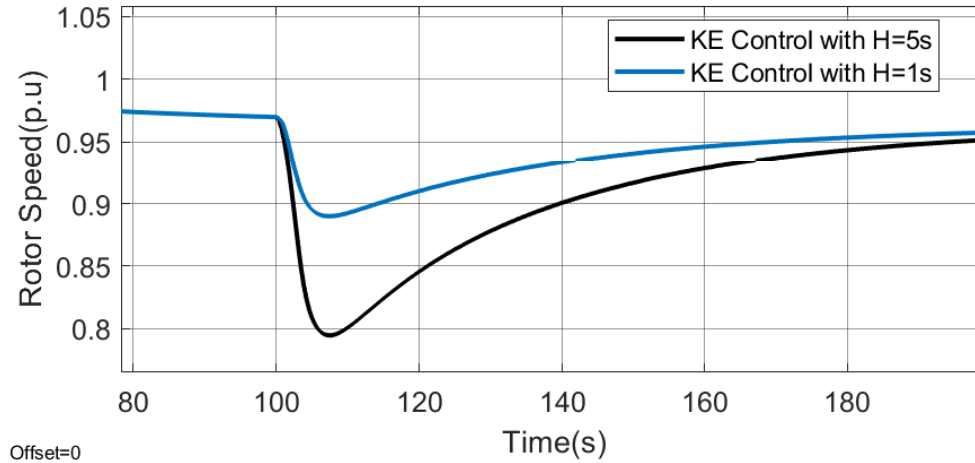


Figure 4.12: Rotor Speed with Kinetic Energy Control with Different Inertial Constants at 7m/s

released.

4.3.2 Test2: Analysis of Droop Control

Kinetic energy control alone can provide frequency support for only first few seconds during the inertial response period of the typical frequency response curve. In order to tackle with issues of secondary loop Test1 show cases the need for a support during primary response time frame. Droop control loop emulates the governor response as in a synchronous machine based generation thereby providing additional power support during the first 10sec duration soon after any frequency event. Figure 4.13 shows the frequency regulation capability of droop control loop analysed at 10m/s of wind velocity. A $0.1Hz$ improvement in nadir is observed with this control strategy. The additional power support provided by the droop loop during the frequency event is shown in Figure 4.14.

4.3.3 Test3: Analysis of Pitch Control Loop

The performance of pitch control loop is analysed for a super synchronous wind velocity of 13ms/s where 11.5m/s be the rated wind speed for the test system used. The system is tested with 30% deloading. Figure 4.15 shows the frequency improvement

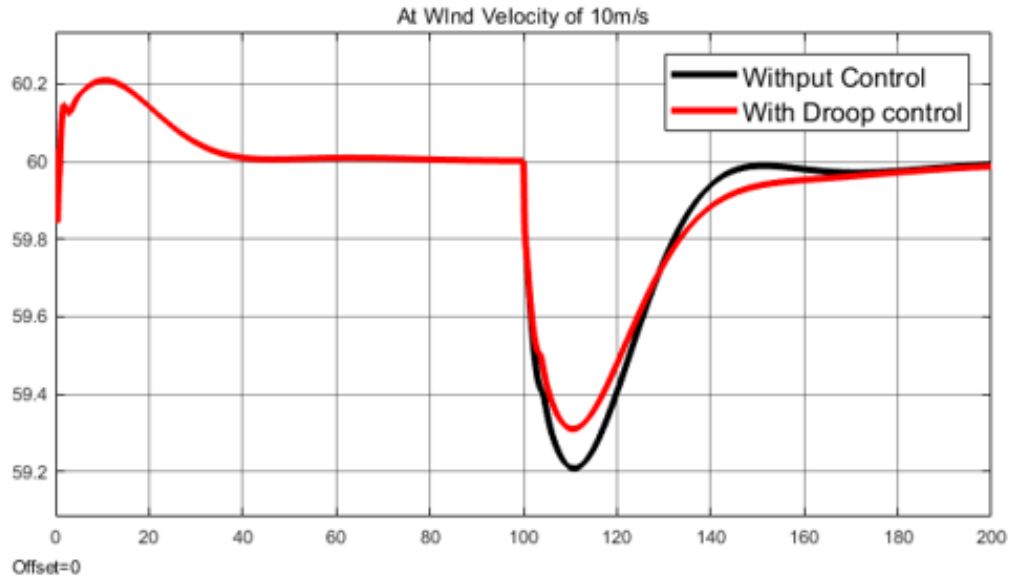


Figure 4.13: Frequency with Droop Control at 10m/s

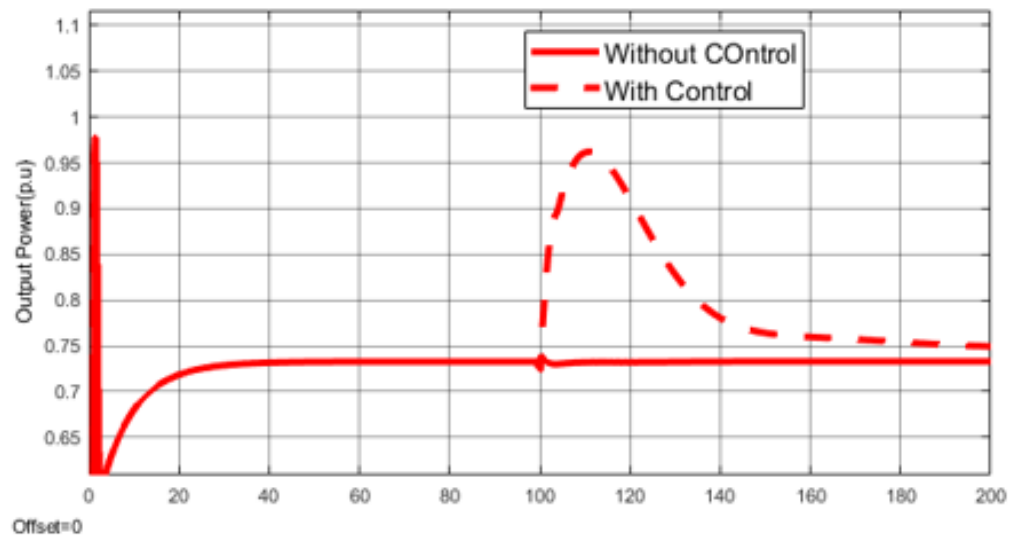


Figure 4.14: Active power with Droop Control at 10m/s

of 0.11Hz with the control loop. Figure 4.16 shows the modification in pitch angle from 12 deg to 4deg in response to the frequency event. The more the deloading, the more is the available power reserve to support during frequency deviation events. But this reduces the efficiency of WTCs resulting in large economic loss.

Based on these primary analysis following conclusions are made.

- Combined inertial+droop controller is ideal for medium wind velocity.

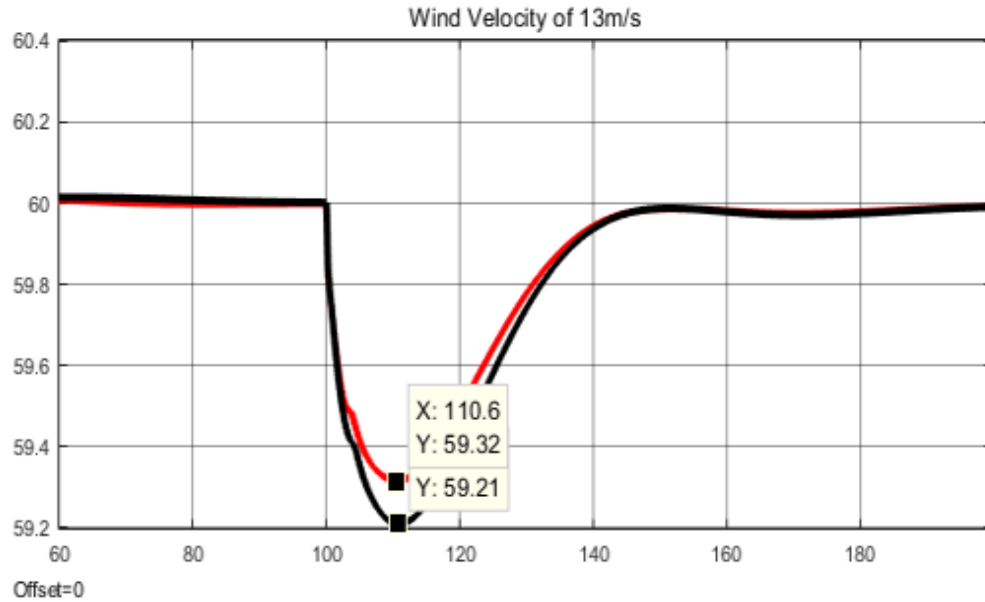


Figure 4.15: Frequency Improvement with Pitch Control at 13m/s

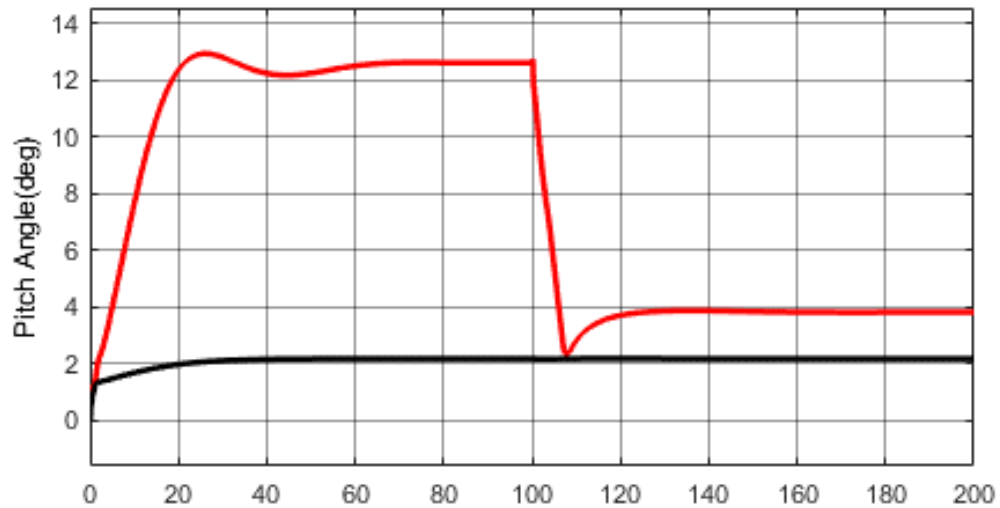


Figure 4.16: Pitch Angle Defined by the Loop at 13m/s

- Droop Control loop is ideal for low wind velocity.
- Modified pitch angle controller for super synchronous wind speeds.

The major challenges faced by conventional loop are summarized below,

- Not all control architecture is efficient at both sub and supersynchronous wind

speed.

- Rotor stall and rotor oscillations due to kinetic energy control.
- Consistent deloading of machine results in economic loss.

All these challenges demand the need for a coordinated control approach that can maximize the power output and provide excellent frequency regulation capability at both sub and supersynchronous wind speed.

4.4 MIMO Coordination Frequency Control Approach for Grid Connected DFIG

The different frequency control configurations need to be coordinated in a proper way to ensure excellent frequency regulation capability. The objective of this work is to consider the wind turbine mechanical and electrical dynamics which may be occurring at a different time frame to effectively coordinate these controllers. The effect of all these dynamics on frequency can be analysed using a multiple input multiple output identification approach. An overview of the proposed coordinated approach is shown in Figure 4.17

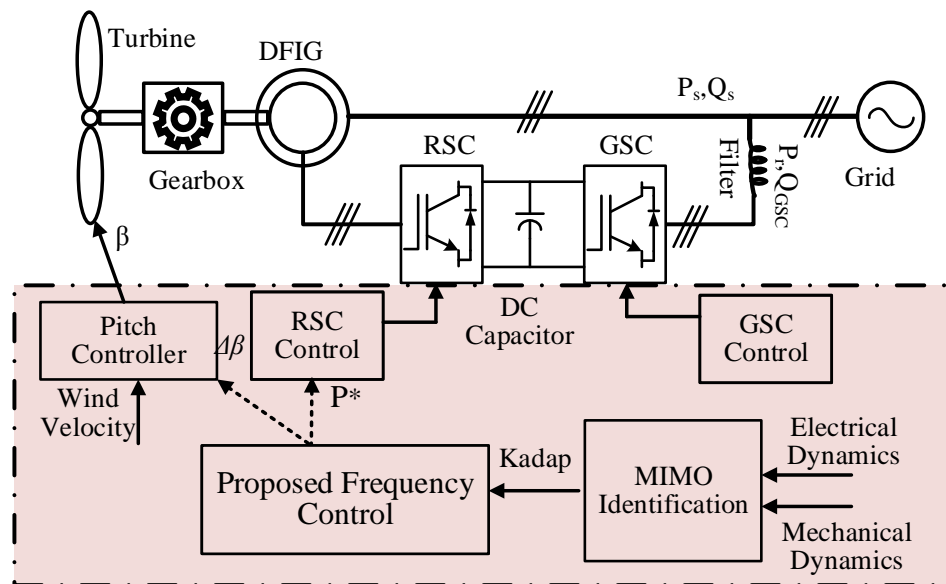


Figure 4.17: Schematic of Proposed Coordinated Control Architecture

4.4.1 Development of Mathematical Model for the Coordinated Approach

A complete non linear mathematical model of grid connected DFIG is developed based on dynamic equations. A general illustration of a DFIG based wind turbine system with the proposed modification is shown in Figure 4.17. The mathematical equations governing the operation of a DFIG in a synchronously rotating reference frame is presented here. The convention followed for modeling this work considers the outgoing current from the stator and the incoming current to the rotor-side as positive. The electrical equations of a DFIG based on a $d - q$ reference frame (rotating at synchronous speed) are given by,

$$\begin{aligned} v_{dqs} &= -r_s i_{dqs} + j \frac{\omega_e}{\omega_b} \Psi_{dqs} + p \frac{\Psi_{dqs}}{\omega_b} \\ v'_{dqr} &= -r'_r i'_{dqr} + j \frac{\omega_e - \omega_r}{\omega_b} \Psi'_{dqr} + p \frac{\Psi'_{dqr}}{\omega_b} \end{aligned} \quad (4.5)$$

$$\begin{aligned} \Psi_{dqs} &= -L_{ls} i_{dqs} + L_m (i_{dqs} + i'_{dqr}) \\ \Psi'_{dqr} &= -L'_{lr} i'_{dqr} + L_m (i_{dqs} + i'_{dqr}). \end{aligned} \quad (4.6)$$

The instantaneous value of real and reactive power output from the stator are given by,

$$\begin{aligned} P_{stator} &= v_{qs} i_{qs} + v_{ds} i_{ds} \\ Q_{stator} &= v_{qs} i_{ds} + v_{ds} i_{qs} \end{aligned} \quad (4.7)$$

where (P_{stator}) is active power and (Q_{stator}) is reactive power output from the stator.

The proposal made in this work is based on some assumptions, as described below:

- Synchronously rotating stator flux oriented reference (i.e., $\Psi_{ds} = \Psi_s$, $\Psi_{qs} = 0$ and $v_{qs} = V_s$, $v_{ds} = 0$).

- Negligible stator flux dynamics due to stronger grid (i.e., $p\Psi_{qs} = p\Psi_{ds} \approx 0$).

4.4.1.1 Model of RSC Control

RSC control based on dq transformation, allows independent control of P_{stator} and Q_{stator} output from the stator.

The electrical relationships that govern the design of RSC control is given by,

$$\begin{aligned} v'_{\text{dr}} &= r'_r i'_{\text{dr}} + p \frac{\sigma L'_r i'_{\text{dr}}}{\omega_b} - \omega_{\text{slip}} \left(\frac{\sigma L_s L'_r}{L_m} i_{\text{qs}} - \frac{r_s L'_r}{L_m} i_{\text{ds}} \right) \\ v'_{\text{qr}} &= r'_r i'_{\text{qr}} + p \frac{\sigma L'_r i'_{\text{qr}}}{\omega_b} - \dots \\ &\dots \omega_{\text{slip}} \left(\frac{\sigma L_s L'_r}{L_m} i_{\text{ds}} - \frac{L'_r}{L_m} (v_{\text{qs}} + r_s i_{\text{qs}}) \right) \end{aligned} \quad (4.8)$$

where $\sigma = \frac{L'_r L_s - L_m^2}{L_s L'_r}$. Equation (4.8) describes the rotor voltages in the d – q axis referred to the stator-side, where:

$$v'_{\text{dr}} = v''_{\text{dr}} + v'''_{\text{dr}} \quad (4.9)$$

$$v'_{\text{qr}} = v''_{\text{qr}} + v'''_{\text{qr}} \quad (4.10)$$

and

$$\begin{aligned} v''_{\text{dr}} &= \left(r'_r + p \frac{\sigma L'_r}{\omega_b} \right) i'_{\text{dr}} \\ v'''_{\text{dr}} &= -\omega_{\text{slip}} \left(\frac{\sigma L_s L'_r}{L_m} i_{\text{qs}} - \frac{r_s L'_r}{L_m} i_{\text{ds}} \right) \\ v''_{\text{qr}} &= \left(r'_r + p \frac{\sigma L'_r}{\omega_b} \right) i'_{\text{qr}} \\ v'''_{\text{qr}} &= -\omega_{\text{slip}} \left(\frac{\sigma L_s L'_r}{L_m} i_{\text{ds}} + \frac{L'_r}{L_m} (v_{\text{qs}} + r_s i_{\text{qs}}) \right). \end{aligned} \quad (4.11)$$

In (4.9) and (4.10),

- The first component is in proportion to the d and q axis rotor current dynamics, respectively.

- The second component represents the speed voltage that couples the d – q axis components with one another.

Using the stated assumptions, (4.7) can be written as,

$$P_s = \frac{L_m v_{qs}}{L_s} \left(\frac{v''_{qr}}{r_r + p \frac{\sigma L_r}{\omega_b}} \right) \quad (4.12)$$

$$Q_s = -\frac{v_{qs} \Psi_{ds}}{L_s} + \frac{L_m v_{qs}}{L_s} \left(\frac{v''_{dr}}{r_r + p \frac{\sigma L_r}{\omega_b}} \right).$$

Equation (4.12) shows that by properly defining the v''_{qr} and v''_{dr} components of rotor voltages, the control logic for the P_{stator} and Q_{stator} output of a DFIG can be defined.

Based on the conventional control architecture, inner loop current controllers and outer loop current controllers need to be included to represent the closed loop dynamic response of the DFIG model.

To include the dynamics of PI controller, integral of the error given to the PI as input is assumed as the state of the system. With x_{id} , x_{iq} , x_{ip} , x_{iv} as the integral error for the inner current control loop and outer power and voltage control loop respectively, the dynamic equations governing the PI can be represented as,

$$\frac{dx_{id}}{dt} = i_{dref} - i_d \quad (4.13)$$

$$\frac{dx_{iq}}{dt} = i_{qref} - i_q \quad (4.14)$$

$$\frac{dx_{ip}}{dt} = P_s - P_{MPPT} \quad (4.15)$$

$$\frac{dx_{iv}}{dt} = v_{ref} - v_{pcc} \quad (4.16)$$

where

$$i_{qref} = K_{pp}(P_s - P_{MPPT}) + K_{ip}x_{ip} \quad (4.17)$$

$$i_{dref} = K_{pv}(v_{ref} - v_{pcc}) + K_{iv}x_{iv} \quad (4.18)$$

The input voltage v_{dr} and v_{qr} are modified to include the contribution from controllers.

$$v_{qr} = K_{pq}(i_{qref} - i_{qr}) + K_{iq}x_{iq} \quad (4.19)$$

$$v_{dr} = K_{pd}(i_{dref} - i_{dr}) + K_{id}x_{id} \quad (4.20)$$

where K_{pq} , K_{pd} , K_{iq} , K_{id} being the proportional gain and the integral gain constant for inner loops and K_{pp} , K_{pv} , K_{ip} , K_{iv} for outer loop respectively.

4.4.1.2 Model of GSC Control

The GSC modification presented in Figure 4.17 focuses on maintaining a constant dc-link voltage. The GSC under a UPF mode of operation does not provide any additional reactive power support. However, in a non-UPF mode, the GSC control can regulate the reactive power flow between the converter and the stator/grid. Usually, the GSC control logic is designed based on a grid-voltage oriented reference frame. GSC control can regulate dc-link voltage with the d-axis current and reactive power for the q-axis.

$$\begin{bmatrix} V_{ai} \\ V_{bi} \\ V_{ci} \end{bmatrix} = R \begin{bmatrix} I_a \\ I_b \\ I_c \end{bmatrix} + pL \begin{bmatrix} I_a \\ I_b \\ I_c \end{bmatrix} + \begin{bmatrix} V_a \\ V_b \\ V_c \end{bmatrix} \quad (4.21)$$

In (4.21), R represents the line resistance and L is the line inductance. Using the parks transformation to convert an abc reference frame to a d – q frame rotating at the angular frequency of the supply voltage, ω_e (in units of rad/s), (4.21) can be

represented as,

$$\begin{aligned} v_{di} &= Ri_d + pLi_d - \omega_e Li_q + v_d \\ v_{qi} &= Ri_q + pLi_q - \omega_e Li_d + v_q \end{aligned} \quad (4.22)$$

where i_d and i_q are the $d - q$ axis currents from the inverter, v_d and v_q are the $d - q$ axis grid voltages, and v_{di} and v_{qi} are the $d - q$ axis output voltages of the inverter. Thus, the controller aims at generating the proper voltage sequence to maintain the DC link voltage and reactive power output.

4.4.1.3 Model of Turbine

The mechanical dynamics including turbine and rotor dynamics represented by two mass model along with the pitch controller dynamics is included to the developed mathematical model. The dynamic equations governing these mechanical dynamics in state space form is given below.

$$\begin{bmatrix} \dot{\omega}_t \\ \dot{\omega}_r \\ \dot{\theta}_{tw} \\ \dot{\beta} \end{bmatrix} = \begin{bmatrix} \frac{1}{2H_t}[-D\omega_b & D\omega_b & -Ksh & 0] \\ \frac{1}{2H_g}[D\omega_b & -D\omega_b & Ksh & 0] \\ \omega_b & -\omega_b & 0 & 0 \\ 0 & 0 & 0 & \frac{-1}{\tau_\beta} \end{bmatrix} + \begin{bmatrix} 0 & \frac{1}{2H_t} \\ 0 & 0 \\ 0 & 0 \\ 0 & \frac{1}{\tau_\beta} \end{bmatrix} \begin{bmatrix} T_m \\ \beta_{ref} \end{bmatrix} \quad (4.23)$$

where H_t is the turbine inertia, H_g is the generator inertia, K_{sh} is the frictional coefficient and D is the damping coefficient of the turbine. The turbine and rotor speed are denoted by ω_t and ω_r respectively and θ_{tw} represents the shaft twist. Since for the proposed work, the objective is to coordinate the controllers for frequency regulation based on wind speed, the dynamics of mechanical torque represented as input in the above state space model need to be analysed in detail. The reference mechanical torque is calculated on the basis of non linear $C_p - \lambda$ power equation

given by,

$$T_m = \frac{\frac{1}{2}\rho AV_w^2 C_p(\lambda, \beta)}{\omega_m} \quad (4.24)$$

Mechanical input T_m is represented as a $f(\omega, V_w, \beta)$ Where optimal tip speed ratio is $f(\omega, V_w)$. ρ is the air density, V_w is wind velocity, C_p is the optimum power coefficient.

$$\frac{d\omega_t}{dt} = \frac{1}{2H_t} \left(\frac{\frac{1}{2}\rho AV_w^2 C_p(\lambda, \beta)}{\omega_m} - K_{sh}\theta_{tw} - D(\omega_t - \omega_r)\omega_b \right) \quad (4.25)$$

Linearizing the above non linear equation,

$$\frac{d\omega_t}{dt} = \frac{1}{2H_t} \left(\frac{\partial T_m}{\partial \omega_t} \cdot \partial \omega_t + \frac{\partial T_m}{\partial \beta} \cdot \partial \beta + \frac{\partial T_m}{\partial V_w} \cdot \partial V_w + o(\omega, \beta, V_w) - K_{sh}\theta_{tw} - D(\omega_t - \omega_r)\omega_b \right) \quad (4.26)$$

where $o(\omega, \beta, V_w)$ represents the higher order non linear terms. The turbine speed dynamics are now modified to include the dynamics from wind speed and pitch angle.

4.4.2 Coordinated Control Approach

The detailed overview of the proposed approach is showcased in Figure 4.18. With the proposed approach the dynamics in q loop rotor current reference in eqn.(4.18) can be modified as,

$$i_{qref} = K_{pp}(P_s - (P_{MPPT} + \Delta P)) + K_{ip}x_{ip} \quad (4.27)$$

$$\Delta P = K_{adaptive} \Delta f \quad (4.28)$$

Similarly from pitch control loop , the eqn.(4.24) can be modified as,

$$T_m = \frac{\frac{1}{2}\rho AV_w^2 C_p(\lambda, \beta + \Delta\beta)}{\omega_m} \quad (4.29)$$

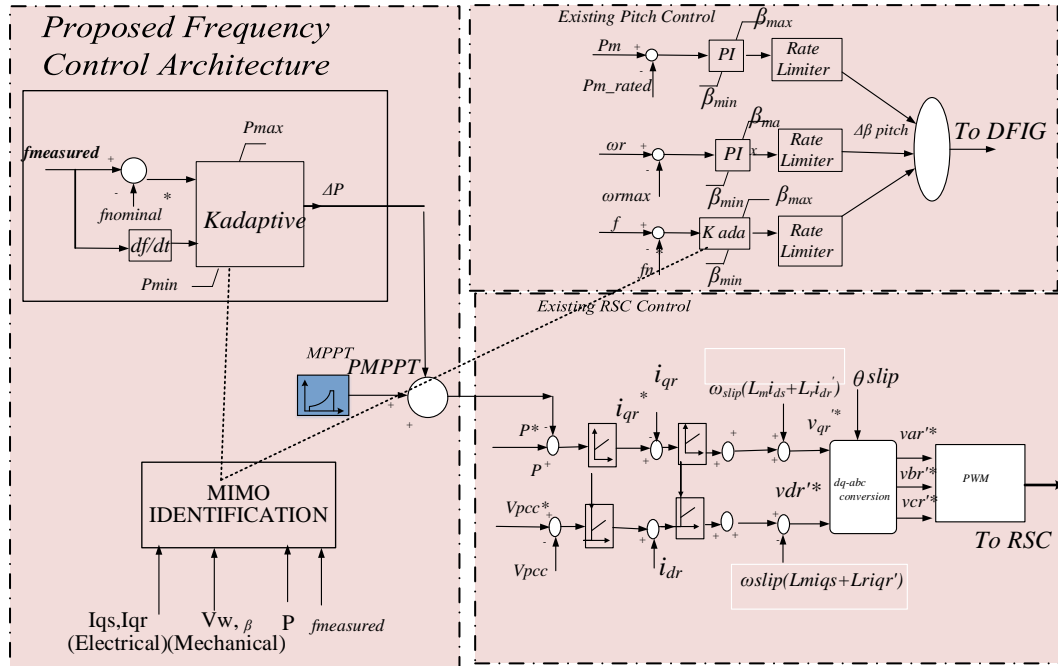


Figure 4.18: Detailed Overview of Proposed Coordinated Frequency Control Architecture

Based on the analysis, the variable gain frequency control architecture is proposed. The gain for the power modulation loop is developed by the adaptive logic based on the MIMO identification. Depending on the participation of different states during the frequency event, the gain is formulated for the frequency control architecture.

4.5 Preliminary Results

The coordinated control architecture with fixed gain is implemented. The droop and pitch based frequency control loops are coordinated based on wind velocity. The impact of the approach during different dynamic conditions is analyzed in the test scenarios is presented below.

4.5.1 Case A : Analysis for a Sub Synchronous Constant Wind Speed

This test scenario analyzes the proposed coordinated control for a sub synchronous constant wind velocity of 9m/s. Figure 4.19 shows the grid frequency deviation corresponding to the test scenario. Faster damping of the frequency deviations with

proposed control is visible from the results. The corresponding variation in stator power due to the proposed loop is shown in Figure 4.20. Since the wind velocity is below synchronous speed, the droop control loop will be dominant and the ΔP from droop loop is reflected in Figure 4.20. The detailed small signal analysis of the st scenario based on the developed mathematical test bed is summarized in Table 4.1. The damping and frequency of the dominant mode discussed in Table 4.1 shows a 64.9% improvement in damping with the proposed frequency control approach.

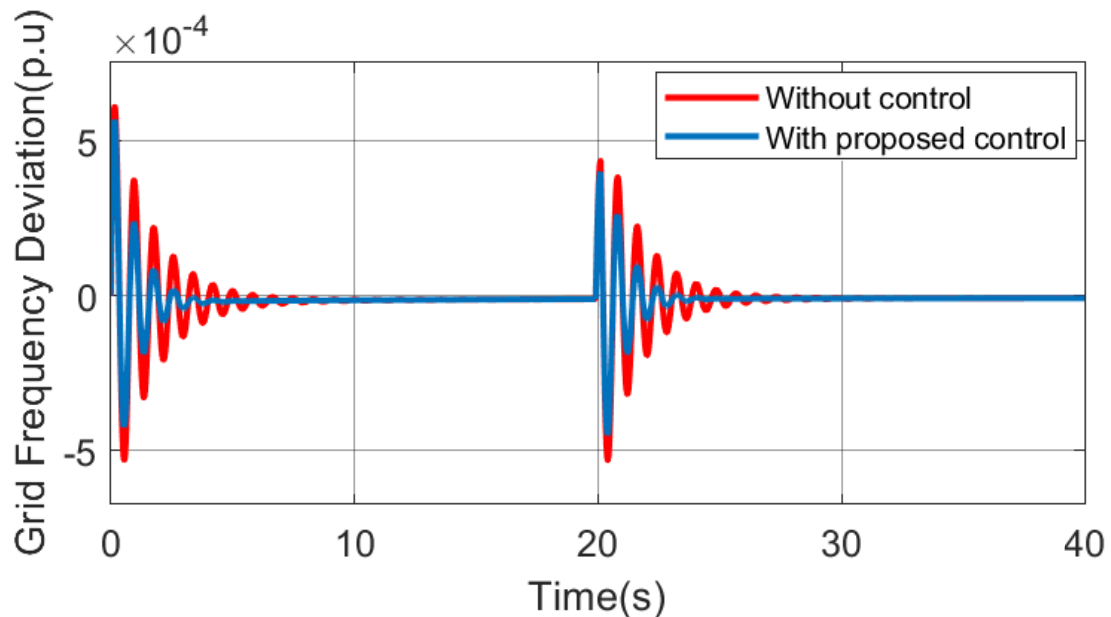


Figure 4.19: Grid Frequency Deviation with Proposed Coordinated Control Architecture for Case A

Table 4.1: Eigen Value Analysis and Participation of States for Case A

<i>Parameters</i>	<i>Without Control</i>	<i>With Proposed Control</i>
Eigenvalue	$-0.6105 \pm 7.855i$	$-0.997 \pm 7.764i$
Damping	7.7%	12.7%
Frequency	1.2502	1.235
Dominant States	'del2' 'sm2' 'psi2q2' 'psi1q2'	'del2' 'sm2' 'psi2q2' 'psi1q2'

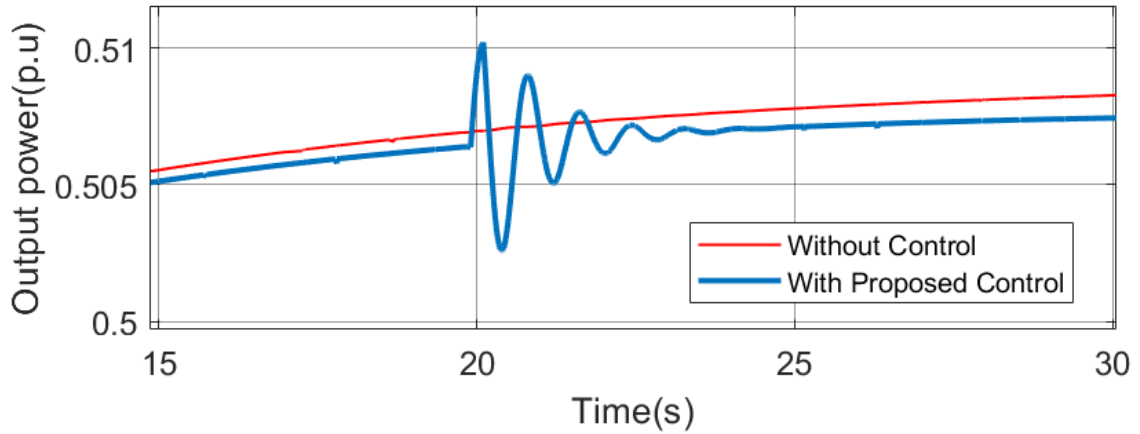


Figure 4.20: Output Power with Proposed Coordinated Control Architecture for Case A

4.5.2 Case B : Analysis for a Super Synchronous Constant Wind Speed

Case B analyzes the proposed approach for a super synchronous wind speed of 13m/s. Figure 4.21 and Figure 4.22 shows the grid grid frequency deviations and the corresponding $\Delta\beta$ by the pith frequency control loop. Table 4.2 highlights the frequency and damping of the dominant modes as the wind speed is above the synchronous value. A 10% improvement in damping is observed for this test scenario.

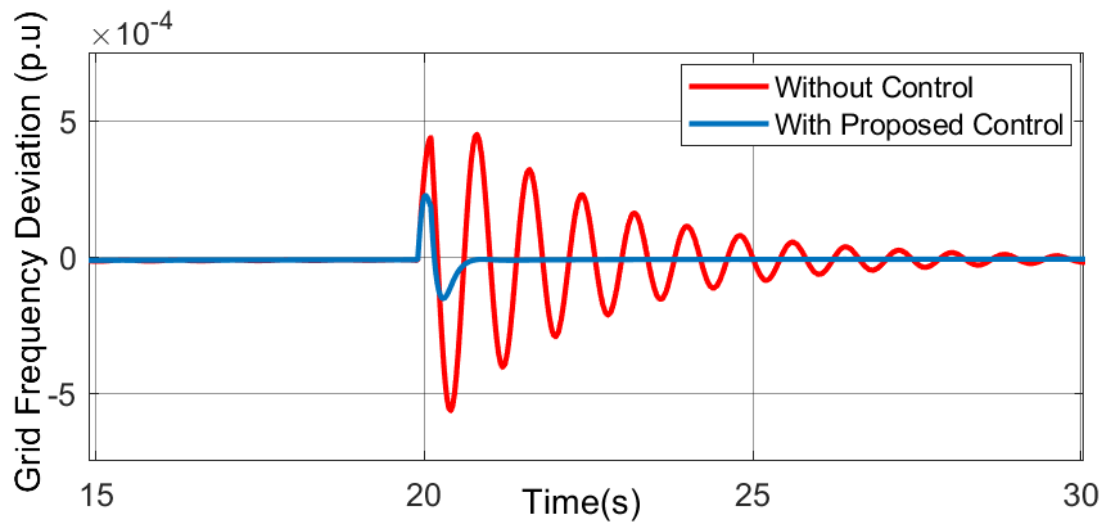


Figure 4.21: Grid Frequency Deviation with Proposed Coordinated Control Architecture for Case B

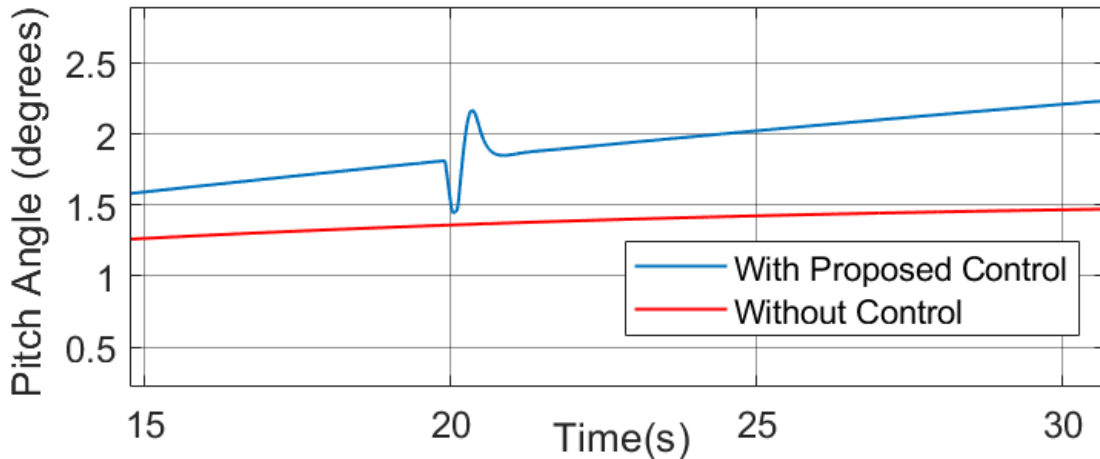


Figure 4.22: Output Power with Proposed Coordinated Control Architecture for Case B

Table 4.2: Eigen Value Analysis and Participation of States for Case B

<i>Parameters</i>	<i>Without Control</i>	<i>With Proposed Control</i>
Eigenvalue	$-0.434 \pm 7.907i$	$-0.4728 \pm 7.8943i$
Damping	5.4%	5.9%
Frequency	1.256	1.256
Dominant States	'del2' 'sm2' 'psi2q2' 'psi1q2'	'sm2' 'wt_d' 'del2' 'psi2q2'

4.5.3 Case C : Analysis for a Varying Wind Speed

In Case C the proposed coordinated approach is analyzed for a dynamically varying wind speed. Figure 4.23 shows the dynamic wind speed and the corresponding output power with and without the proposed control. The droop and pitch based controls are coordinated to bring considerable improvement in frequency deviation as shown in Figure 4.25. The contribution from pitch based frequency loop as the wind speed goes beyond the synchronous speed is showcased in Figure 4.26 and is compared with the conventional pitch loop. The ability of the proposed frequency loop to dynamically adjust the pitch to improve the grid frequency is depicted in the results. The corresponding ΔP calculated by the droop loop is shown in Figure 4.27. Table 4.3

highlights the frequency and damping of the dominant modes for the varying wind speed. A 79% improvement in damping is observed with the coordinated frequency control with constant gain.

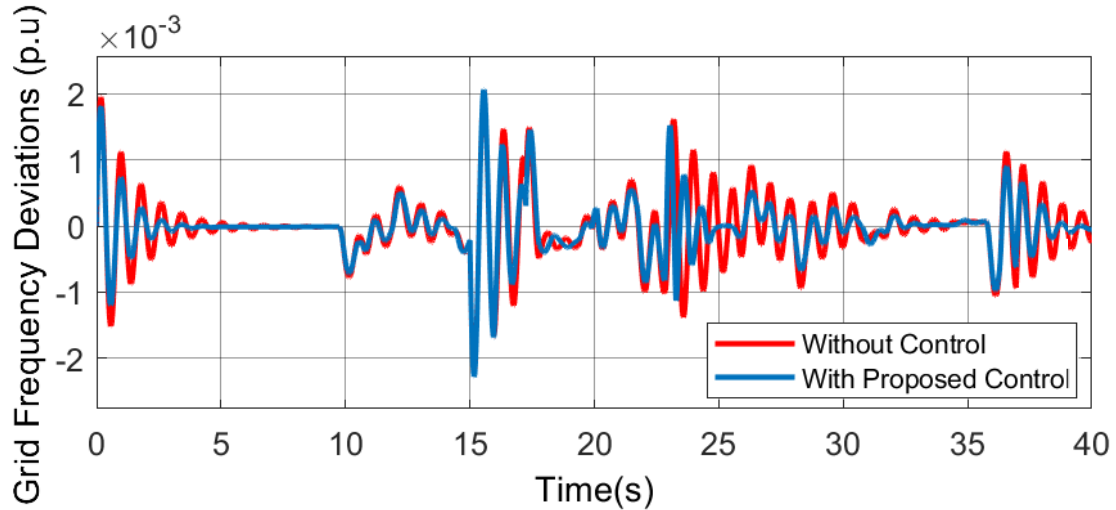


Figure 4.23: Grid Frequency Deviation with Proposed Coordinated Control Architecture for Case C

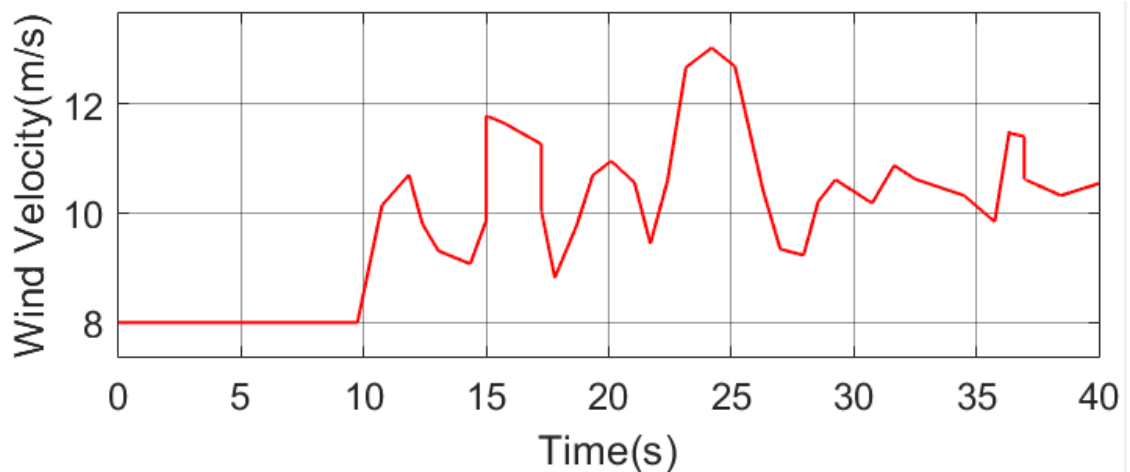


Figure 4.24: Wind Speed used for Analysis of Case C

4.6 Future Works

The preliminary results analyzed with constant gain coordinated control shows better damping in grid frequency deviations. The small signal analysis performed on the model identifies the dominant modes and the participating states and showcases

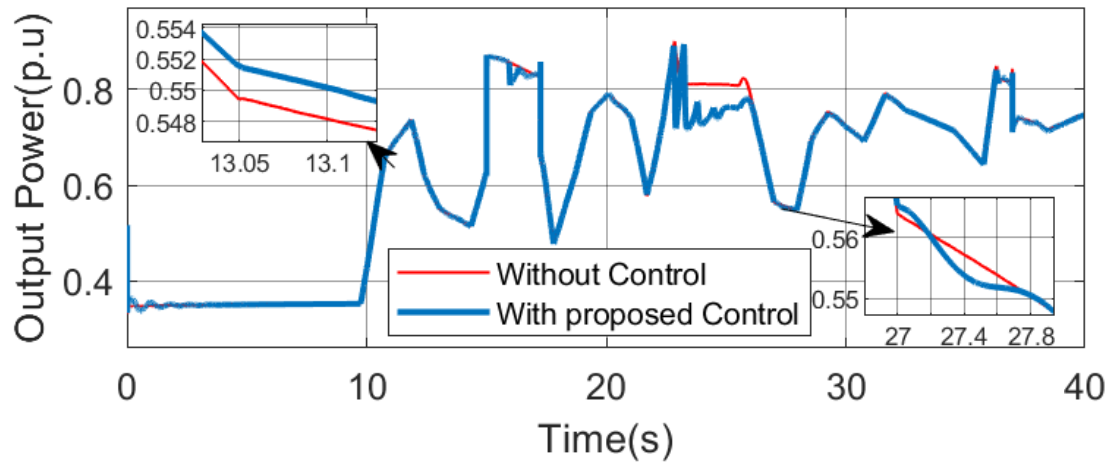


Figure 4.25: Stator Power with Proposed Coordinated Control Architecture for Case A

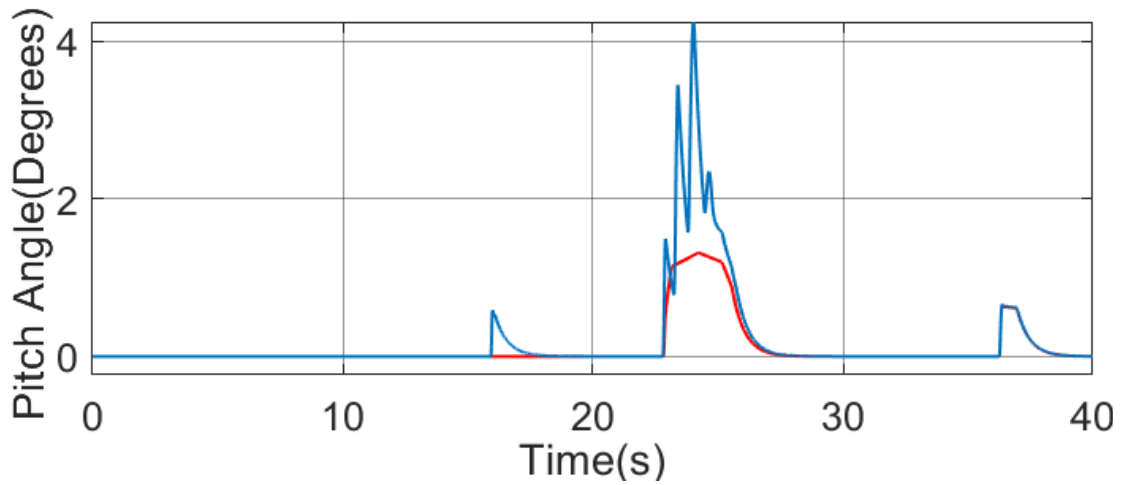


Figure 4.26: Pitch Angle Reference with Proposed Coordinated Control Architecture for Case C

Table 4.3: Eigen Value Analysis and Participation of States for Case C

<i>Parameters</i>	<i>Without Control</i>	<i>With Proposed Control</i>
Eigenvalue	$-0.4781 \pm 7.894i$	$-0.8527 \pm 7.7967i$
Damping	6.04%	10.87%
Frequency	1.256	1.2408
Dominant States	'del2' 'sm2' 'psi2q2' 'psi1q2'	'del2' 'sm2' 'psi2q2' 'psi1q2'

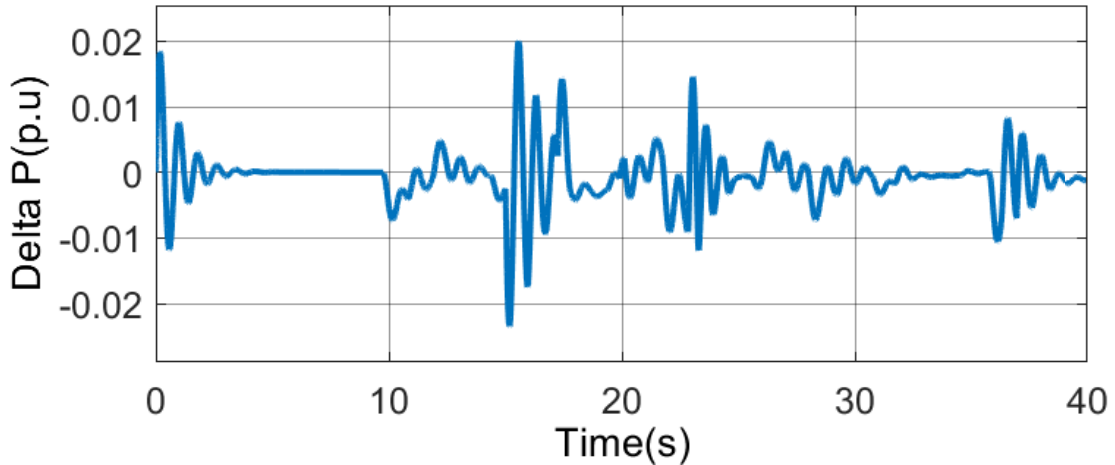


Figure 4.27: Delta P Calculated with Proposed Coordinated control Architecture for Case C

the improvement in damping and frequency with the proposed approach. In future, a MIMO identification approach that considers the mechanical and electrical dynamics will be implemented to dynamically adapt the gains of the frequency control loops based on the wind speed.

The future steps involved in proposing the control architecture for DFIG frequency regulation is summarized aelow.

- Complete the multiple input multiple output (MIMO) identification approach based on RLS algorithm.
- Develop a coordinated control architecture for frequency control of DFIG based on identified parameters.

A detailed block diagram of the proposed coordinated frequency control is shown in Figure.4.18.

4.7 Chapter Summary

The chapter analyses the different control logic that can make the WECS to actively participate in frequency regulation capability. The study presented here tries to analyse the best control logic based on the wind speed and then to develop coordina-

tion approach among these controllers which can efficiently participate in frequency regulation at the same time maximising the output from the WTG. The proposal aims at analysing the mechanical and electrical dynamics from different time frames to properly define the coordination among controllers. A RLS based MIMO approach identifying the participation of electrical and mechanical modes during a grid frequency event is proposed.

CHAPTER 5: MODELING OF DFIG INTEGRATED WEAK GRID AND DYNAMIC PERFORMANCE ANALYSIS WITH SYNCHRONOUS CONDENSER

This chapter discusses the issues and challenges faced by wind integrated into weak grid networks. The analysis is done with a Type4 wind turbine model integrated into a power grid represented by an aggregated synchronous generator model through a variable impedance network. The impedance of the network defines the strength of the grid. The work first analyses the issues with steady-state and transient stability during various grid strength and then proposes the importance of tuning the WTG grid side PLL and the effect of the synchronous condenser at PCC in improving the overall stability of the system during high power transfer. Detailed analysis of the effect of PLL bandwidth and gain values on stability has been presented. The effect of synchronous condenser parameters on-grid oscillations and stability has also been analyzed with various test scenarios. Finally the work proposes a modified control architecture for the exciter and PSS of synchronous condenser based on grid impedance to improve the overall stability of wind integrated to weak grid systems.

5.1 Introduction

Renewable energy-based electric power generation has gained considerable importance recently due to the increasing power demand and environmental concerns. The complexity of the power grid has also increased with this increased dependency on renewable energy sources like wind and solar. The increased integration and penetration have increased the challenges for solving grid problems like frequency regulation, voltage variation, low voltage ride through, power quality management, etc. Power electronics technology has gained a critical role in integrating renewable energy

sources to power grid. In some cases, the region with good wind conditions may be located far away from electrical loads, which create scenarios where WECS should try to transfer high power through a weak grid network. This paper first analyses the various issues faced by wind energy conversion system integrated to weak grid during high power transfer.

5.1.1 State-of-the-Art

A detailed analysis of the challenges and solution of integrating wind in weak grid is discussed in [87]. The paper analyzes the problem through detailed voltage stability, transient stability, and small-signal analysis using power flow, frequency, and time-domain simulations. Voltage stability is discussed as one crucial challenge to the stable operation of the wind power plant(WPP) to be discussed. Under such scenarios, the use of additional dynamic reactive power compensation techniques like STATCOM or synchronous condensers can ensure stability as the grid strength decreases which results in additional cost. [87] discusses a novel cost-effective integrated control strategy of wind power plant that reduces the size of the dynamic reactive power compensation requirement. Modern grid code requirements demand WPP to have certain control capabilities like the voltage, reactive power and power factor, etc. The ability of WPP to meet these requirements deteriorates as the grid impedance changes. The small-signal study and eigenvalue analysis performed shows that the PLL PI parameters has a greater impact on the stability of WPP. The work concludes that the PI control parameters of DC-link control block, PLL control block, voltage control block and communication time delay should be decreased, PI parameters of reactive power control block should be increased while PI parameters of inner current control should be optimized at some point in the middle. [87] proposes the coordinated control scheme of WPP as a solution to these problems. In this method WPP is made to acct like stiff voltage sources. But this proposed control makes WPP prone to shunt resonance between the voltage controller and the grid impedance.

Electromagnetic stability analysis of grid-connected DFIG in weak grid scenarios is analyzed in [88] using a reduced order small-signal model. The work also analyzes the effect of the RSC control loop and PLL loop on maintaining stability under weak grid scenarios. Eigenvalue comparison is done to ensure that the reduced model reflects the dominant oscillation modes of DC link voltage. Two dominant modes are observed during the analysis, out of which one of the dominant mod is affected by the grid strength. It is observed that as the grid strength reduces, the eigenvalue moves towards the right half of the s plane. This dominant mode is related to PLL for a short circuit ratio(SCR) of 4 while as grid strength reduces to SCR 1.5, this is related to RSC control. This shows the interaction between PLL and RSC control as the grid goes weaker. The effect of improving PLL bandwidth on stability has been proved in this work. The stability of the system reduces as the band width of the RSC active power control loop increases with grid strength.

Stability and power quality issues of variable speed permanent magnet-based WECS is discussed in [89]. The influence of load fluctuations on local voltage stability for high impedance grid connections has been discussed in detail. This can impose interconnection problems that limit the amount of wind power to be integrated. By participation factor analysis, the work tries to prove the influence of ac voltage control loop on unstable eigenvalues due to weak grid.

A feedback control strategy for type3 and type4 wind to enhance the overall stability during a weak grid is proposed in [90]. The coupling between the power delivery and voltage at the point of common coupling is identified as the root cause of stability issues using a linearized model. The proposed strategy involves two feedback that modulates the power order and the dc link voltage order thereby reducing this coupling effect to enhance the stability.

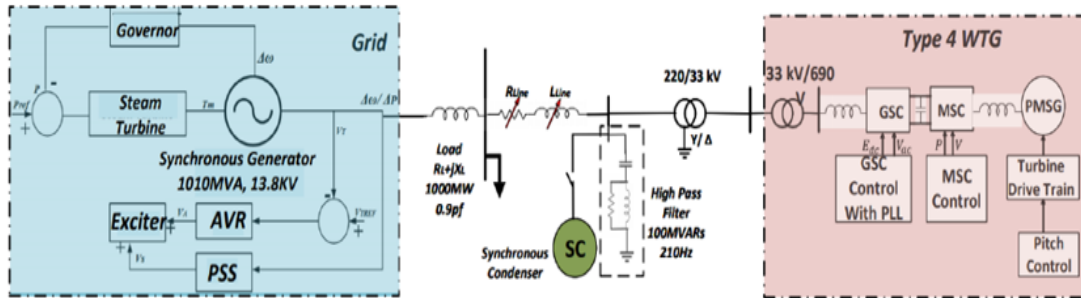


Figure 5.1: WTG Integrated Weak Grid Model.

5.1.2 Major Contributions

This work analyses the issues of the Type4 WTG model integrated to a weak grid. The effect of PLL bandwidth on improving the steady-state and transient stability has been discussed. Integrating a synchronous condenser at PCC as dynamic reactive power compensator is proposed for improving the stability as grid strength reduces. The effect of different SC parameters on-grid strength and damping of the oscillation frequencies has been discussed in detail. The work concludes by proposing the need for a modified synchronous condenser excitation controller to improve the stability under weak grid scenarios.

5.2 Mathematical Model of Weak Power Grid Model

An aggregated weak grid model to analyze the issues related to the weak grid has been developed in PSCAD based on CIGRE 671 report [91]. The schematic of the weak grid model developed is shown in Figure 5.1.

To reflect the variations in system frequency and impact on wind farms on stability the model representing the grid should reflect more dynamic behavior of the actual network. Hence a synchronous generator model is designed to represent the typical value of aggregated Australian thermal power plant. The 300MW Type 4 full-converter wind farm is modeled as one single lumped wind turbine generator (WTG). The Type 4 WTG model is integrated to the grid through variable impedance as

shown in Figure 5.1. This impedance value is varied to simulate different grid strength scenarios as shown in Table 5.1. The network impedance values are selected such that the SCR is simulated over a range of 7 (SCR>3, Strong grid) down to 1.149 (SCR<3, weak grid).

Table 5.1: Network Impedance for Different Test Cases

Test Case #	R_{Line} (Ω)	L_{Line} (H)	SCR
1	1.665	0.053	7.04
2	2.136	0.068	6.00
3	2.765	0.088	5.02
4	3.738	0.119	4.01
5	5.341	0.170	3.00
6	6.597	0.210	2.51
7	8.545	0.272	2.00
8	9.425	0.3	1.84
9	10.996	0.35	1.60
10	12.566	0.4	1.41
11	14.137	0.45	1.27
12	15.708	0.5	1.15

A high pass 3-phase harmonic filter of $210Hz$ is included near the PCC supporting additional reactive power. The aggregated transformer reactance between the wind farm and PCC is 21%, which does not change for different cases, only the line impedance is varied. The detailed mathematical model for each of these components are explained in this section.

5.2.1 Modeling of the Grid

The grid for the weak grid model is represented by a synchronous generator model whose rating is adjusted to represent the Australian thermal power plant as discussed in [91]. The architecture of the SG model is shown in Figure 5.2. The steam turbine governor system controls the synchronous generator. An IEEE T2 Automatic Voltage Regulator (AVR) controls the excitation current to the field winding thereby maintaining the terminal voltage and a Power System Stabilizer (PSS) for damping the oscillations. The PSS provides a supplementary input V_s to the AVR.

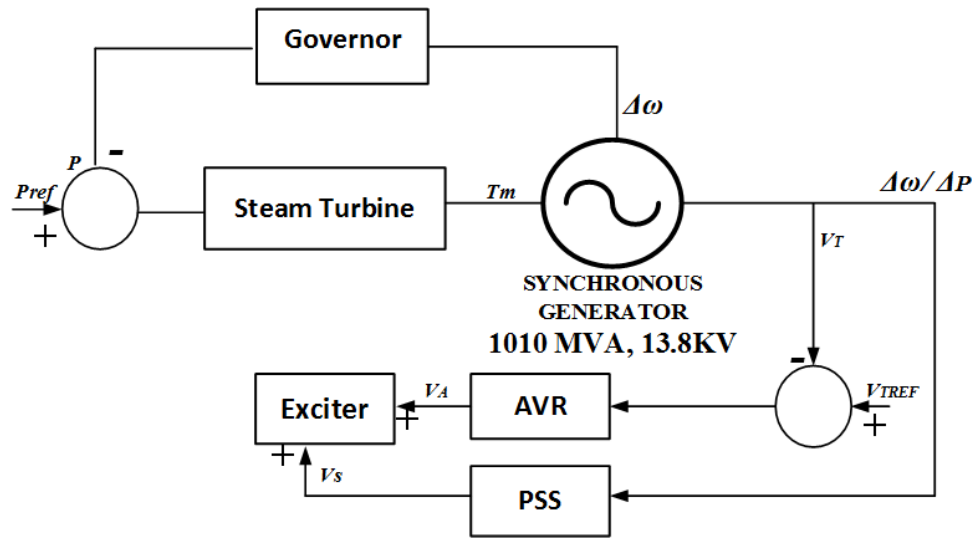


Figure 5.2: Structure of Synchronous Generator Model.

The parameters used for modeling the synchronous generator is given in Table.A.2.

5.2.2 Mathematical Modeling of Type4 Wind Farm

The general structure of a type 4 model is shown in Figure 5.3. In Type 4 Fully rated Converter models(FRC), the generator can be either electrical exciter or permanent magnet type or even induction generator based model. In our work, PMSG based models are developed. PMSG based wind model doesn't demand the need for slip rings and field excitation and reactive power compensation techniques as needed by other types. The generator is decoupled from the grid employing two back to back voltage source converters.

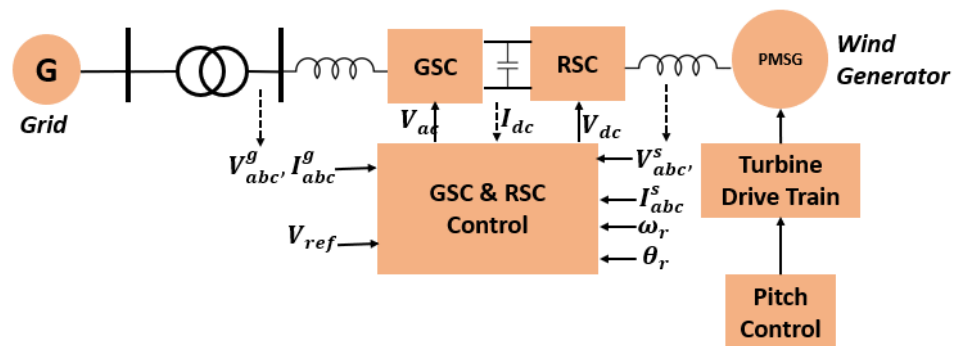


Figure 5.3: General Structure of Type 4 Wind Turbine Generator.

5.3 An Investigation of Grid Stability Based on Small Signal Analysis and Proposal of Adaptive PLL Control

In this section the small signal model of the weak grid model discussed in the earlier sections were developed. A detailed analysis of the effect of integral gain and the impact of optimal PLL bandwidth on system stability and oscillation is discussed. A detailed investigation of the influence that PLL parameters have on oscillation characteristics of the system under variable grid strength in terms of PLL bandwidth, damping, and natural oscillating frequency is also discussed in this chapter. Then a novel adaptive gain scheduling PLL is proposed and designed.

- A detailed analysis on the impact of the integral gain of the PLL on stability and oscillation.
- A small signal model of the wind integrated to a weak grid system, considering PLL dynamics.
- An adaptive PLL gain scheduling control architecture that dynamically adjusts the PLL control gains based on measurements.

5.3.1 Development of Small Signal Representation of the Power Grid Model with PLL

The linearized state space model of the developed weak grid test system is discussed in this section. The overall model is represented in the form of,

$$\Delta \dot{x} = A_{overall} \Delta x + B_{overall} \Delta u \quad (5.1)$$

where A is the state transition matrix of 33×33 , x is n-dimensional state vector (33×1) and u is the input vector. $A_{overall}$ is represented by considering the dynamics of synchronous generator representing the grid, WTG grid side converter, grid impedance and the PLL dynamics. The details of each of these are discussed below.

5.3.1.1 Model of synchronous generator

Synchronous generator is represented using 6th order state space model for electrical system along with second order model representing the mechanical side dynamics. Thus the overall 11th order state space representation of synchronous generator considering the exciter and Power System Stabilizer (PSS) representing the grid in the developed weak grid model is summarized as,

$$\Delta \dot{i} = -L^{-1}(R + \Delta\omega N) - L^{-1}\Delta v_{sys} \quad (5.2)$$

with resistance matrix R , inductance matrix L and N being the speed voltage terms.

L is given by,

$$L = \begin{bmatrix} L_d & kM_F & kM_D & 0 & 0 & 0 \\ kM_F & L_F & M_R & 0 & 0 & 0 \\ kM_D & M_R & L_D & 0 & 0 & 0 \\ 0 & 0 & 0 & L_q & kM_Q & kM_Q \\ 0 & 0 & 0 & kM_Q & L_{Q1} & kM_Q \\ 0 & 0 & 0 & kM_Q & kM_Q & L_{Q2} \end{bmatrix} \quad (5.3)$$

and $(R + \Delta\omega N)$ is,

$$R + \Delta\omega N = \begin{bmatrix} r & 0 & 0 & R_{14} & R_{15} & R_{16} \\ 0 & r_F & 0 & 0 & 0 & 0 \\ 0 & 0 & r_D & 0 & 0 & 0 \\ R_{41} & R_{42} & R_{43} & r & 0 & 0 \\ 0 & 0 & 0 & 0 & r_{Q1} & 0 \\ 0 & 0 & 0 & 0 & 0 & r_{Q2} \end{bmatrix} \quad (5.4)$$

$R_{14} = \Delta\omega L_q, R_{15} = \Delta\omega kM_{Q1}, R_{16} = \Delta\omega kM_{Q2}, R_{41} = -\Delta\omega L_d, R_{42} = -\Delta\omega kM_F, R_{43} = \Delta\omega kM_D.$

$x = \begin{bmatrix} \Delta id & \Delta iF & \Delta iD & \Delta iq & \Delta iQ1 & \Delta iQ2 & \Delta \omega_g & \Delta \delta \end{bmatrix}$,
 $u = \begin{bmatrix} \Delta vd & \Delta vF & 0 & \Delta vq & 0 & 0 \end{bmatrix}^T$. The second order mechanical dynamics are included, with ΔT_m being the torque input, L_d, L_f, kM_F, kM_Q , etc., being the synchronous machine parameters. The synchronous generator controller exciters and stabilizers are also considered.

$$\Delta \dot{v}_1 = \frac{\Delta v_t - \Delta v_1}{T_R} \quad (5.5)$$

$$\Delta \dot{v}_2 = \frac{K_s T_w (\Delta \dot{\omega}) - \Delta v_2}{T_w} \quad (5.6)$$

$$\Delta \dot{v}_s = \frac{\Delta \dot{v}_2 T_1 + \Delta v_2 - \Delta v_s}{T_2} \quad (5.7)$$

$$\Delta E_{fd} = K_A (\Delta v_{ref} - \Delta v_1 + \Delta v_s) \quad (5.8)$$

where K_A is the exciter gain, K_s is the stabilizer gain and T_1, T_2, T_R, T_w being the time constants, Δv_t being the terminal voltage change.

5.3.1.2 Model of Type 4 WTG

The Type 4 WTG model can be represented as the synchronous generator. The output generated from a synchronous generator is first rectified using a diode-bridge rectifier. Then a dc-dc boost converter converts this rectified dc voltage to different voltage levels. The boost converter control ensures MPPT, while the Grid Side Converter (GSC) is in dc-link control mode. The synchronous machine dynamics can be represented as discussed in Section 5.3.1.1. The dynamics of converter and WTG control are discussed below.

Grid Side Converter (GSC): Type 4 WTG has a grid side full converter, whose output is controlled using a conventional vector control strategy. The GSC converter controls the dc-link voltage and ac-side voltage output of the WTG. The dynamics of the inverter output current between the grid side converter and the PCC through

the filter inductance L_f and parasitic resistance R_f is represented as,

$$\Delta V_{d/qi} = R_f \Delta i_{L_{d/qi}} + L_f \frac{d\Delta i_{L_{d/q}}}{dt} + \Delta V_{pccd/q} \quad (5.9)$$

where $V_{d/qi}$ is the terminal voltage at the grid side inverter end and $i_{L_{d/qi}}$ is the inverter output current dynamics and $V_{pccd/q}$ is the PCC voltage. I_L and V_{pcc} is represented in dq domain components as, $I_L = I_{L_d} + jI_{L_q}$, $V_{pcc} = v_{pccd} + jv_{pccq}$, and ω is the PLL identified frequency.

GSC Control: The grid side current controller dynamics are represented as,

$$\Delta dV_{d/qi} = K_{pd/q}(\Delta i_{L_{d/qref}} - \Delta i_{L_{d/qi}}) + K_{id/q}x_{id/q} \quad (5.10)$$

$$\dot{x}_{id/q} = (\Delta i_{L_{d/qref}} - \Delta i_{L_{d/qi}}). \quad (5.11)$$

where $K_{pd/q}$ and $K_{id/q}$ represents the proportional and integral gains of outer and inner loop controllers. $i_{L_{d/qref}}$ is the current references for the inverter control loop, $\Delta dV_{d/qi}$ is the control voltage generated by the cascaded controller.

Grid Dynamics: Now considering the grid side dynamics,

$$V_{pcc} = V_g + Z_{line}I_L. \quad (5.12)$$

From this equation, v_{pccd} and v_{pccq} can be formulated as,

$$\Delta v_{pccd} = \Delta V_{gd} + R_{line}\Delta i_{L_d} - X_{line}\Delta i_{L_q} \quad (5.13)$$

$$\Delta v_{pccq} = \Delta V_{gq} + R_{line}\Delta i_{L_q} - X_{line}\Delta i_{L_d} \quad (5.14)$$

with $V_{gd/q}$ being the grid voltage and R_{line} and X_{line} being the variable grid impedance.

PLL Model: This section addresses the PLL dynamics on the stability of the wind integrated into a weak grid scenario. The PLL plays a critical role in adjusting the power flowing out of the WPP by adjusting the voltage phase and magnitude between the inverter output and the grid. The inverter output in the dq domain is converted to the corresponding abc domain based on phase and frequency information acquired by the PLL. As discussed in [95], a synchronous reference frame PLL [96, 97] is used in this test model.

Let the grid voltage vector represented as,

$$V_a = V_m \cos \omega t \quad (5.15)$$

$$V_b = V_m \cos\left(\omega t - \frac{2\pi}{3}\right) \quad (5.16)$$

$$V_c = V_m \cos\left(\omega t + \frac{2\pi}{3}\right) \quad (5.17)$$

PLL makes use of Park's transformation to convert the grid voltage vector from abc to dq reference frame,

$$\begin{bmatrix} v_d \\ v_q \end{bmatrix} = \frac{2}{3} \begin{bmatrix} T_{qd0} \end{bmatrix} \cdot \begin{bmatrix} V_a \\ V_b \\ V_c \end{bmatrix} \quad (5.18)$$

V_m represents the maximum amplitude of phase voltage and ωt is the grid voltage phase angle, θ is the angle between the grid voltage vector and d -axis of synchronous reference frame. Using trigonometric identities,

$$\begin{bmatrix} v_d \\ v_q \\ 0 \end{bmatrix} = \begin{bmatrix} \cos(\omega t - \theta) \\ \sin(\omega t - \theta) \\ 0 \end{bmatrix} \cdot V_m. \quad (5.19)$$

From (5.19), the q – axis component of the grid voltage is given by $V_m \sin(\omega t - \theta)$. For small differences between ωt and θ , V_q can be approximated as $V_m(\omega t - \theta)$. If the grid voltage vector is aligned ideally with the d component, then V_q will be zero. The

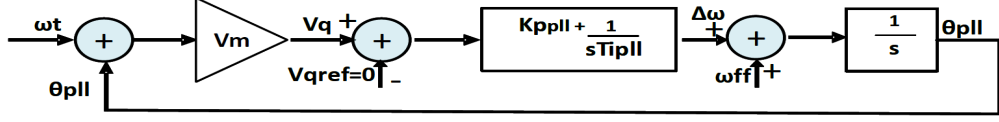


Figure 5.5: Small Signal Model of a Synchronous Reference Frame PLL.

second-order closed-loop transfer function for the phase-locked loop from Fig. 5.5 can be derived as,

$$\frac{\theta_{pll}}{\omega_t} = \frac{V_m K_{ppll} s + V_m \frac{1}{T_{ipll}}}{s^2 + V_m K_{ppll} s + V_m \frac{1}{T_{ipll}}}. \quad (5.20)$$

The dynamics equation of PLL can be represented as,

$$\frac{d\theta_{pll}}{dt} = K_{ppll} v_q + K_{ipll} \dot{\theta}_{pll}, \quad \frac{d\dot{\theta}_{pll}}{dt} = v_q \quad (5.21)$$

where $\dot{\theta}_{pll} = \omega_{pll}$, K_{ppll} is the proportional control gain of PLL loop filter and $K_{ipll} = \frac{1}{T_{ipll}}$ is the integral gain of the loop filter. Now substituting these v_{pccd} and v_{pccq} in (5.9) and upon linearization, the overall model of GSC considering PLL and grid dynamics can be represented as,

$$A = \begin{bmatrix} A_{11} & A_{12} & A_{13} & 0 & A_{15} & 0 \\ A_{21} & A_{22} & 0 & A_{24} & 0 & A_{26} \\ 0 & 0 & -K_{ppl} & K_{ipl} & 0 & 0 \\ 0 & 0 & -1 & 0 & 0 & 0 \\ 1 & 0 & 0 & 0 & 0 & 0 \\ 0 & 1 & 0 & 0 & 0 & 0 \end{bmatrix} \quad (5.22)$$

$$B = \begin{bmatrix} -1/L_f & -K_{pd}/L_f & 0 \\ 1/L_f & 0 & -K_{pq}/L_1 \\ 0 & K_{ppl} & 0 \\ 0 & 0 & 0 \\ 0 & 1 & 0 \\ 0 & 0 & 1 \end{bmatrix} \quad (5.23)$$

where $A_{11} = (K_{pd} - R_f - R_{line})/L_f$, $A_{12} = (\omega_{pll} - L_{line}\omega_{pll})/L_f$, $A_{13} = -(iq - L_{line}Iq)/L_f$, $A_{24} = -(id + L_{line}Id)/L_f$, $A_{15} = -K_{id}/L_f$, $A_{21} = (-\omega - L_{line}\omega_{pll})$, $A_{22} = (K_{pq} - R_f - R_g)/L_f$, $A_{26} = -K_{iq}/L_f$, with states,

$$x = \begin{bmatrix} \Delta i_{L_d} & \Delta i_{L_q} & \theta & \dot{\theta}_{pll} & x_{id} & x_{iq} \end{bmatrix} \quad (5.24)$$

and input vector,

$$u = \begin{bmatrix} \Delta V_d & \Delta V_q & \Delta i_{dref} & \Delta i_{qref} \end{bmatrix}. \quad (5.25)$$

5.3.2 Stability Analysis Based on the Small Signal Model and the Impact of PLL

Stability analysis of the power grid with WPP and the impact of PLL control gains on stability has been discussed in this section. First, a detailed analysis of grid stability using nominal PLL gains as a function of grid short circuit ratio (SCR) is presented. Then, the interaction of PLL bandwidth and control gains has been analyzed based on the closed-loop PLL bode plot.

5.3.2.1 Analysis of Grid Stability

A steady-state analysis of the test model is performed for all 12 test cases described in Table 5.1, which cover the identified SCR range. The analysis is performed with the nominal PLL gain value $K_p = 2$ and $K_i = 2$. Using small-signal analysis, the variation in voltage at PCC and the reactive power supplied is being analyzed. Figure 5.6a show the decrease in PCC voltage as the grid strength reduces. The terminal voltage pattern first increases as grid strength reduces, to which the reactive power support correspondingly reduces. However, as the grid moves to a weak grid region with an SCR below 3, the voltage starts dropping. The WTG tries to push more reactive power to the PCC to maintain the terminal voltage to meet the grid code requirements. However, as the grid strength drops below 1.41, the voltage drops drastically, resulting in grid instability. Figure 5.6b shows the impact of power grid strength

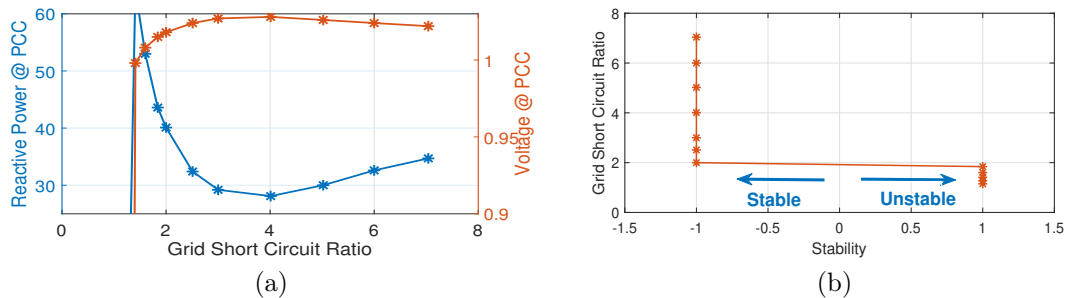


Figure 5.6: a) PCC Voltage Variations with Grid Strength. b) PCC Reactive Power Variations with Grid Strength.

on stability. In Figure 5.6b stable cases are represented with the $x - axis = -1$,

while unstable cases are represented in the right plane with the $x - axis = 1$. It is observed that up to Case 10, for an SCR ≥ 1.4 , the system is stable. However, as the grid strength drops below 1.4, sustained undamped oscillations are observed in PCC power. The PLL bandwidth also plays an important role in transient stability. Figure 5.7 shows that as the grid strength declines lower bandwidth PLL improves the overall stability.

TRANSIENT STABILITY BASED ON PLL BANDWIDTH

K_p	K_i	Grid Short Circuit Ratio					
		3	1.836	1.597	1.413	1.267	1.149
0.5	0.5	Yes	Yes	Yes	Yes	Yes	Yes
1	1	Yes	Yes	Yes	Yes	No	No
1	2	Yes	Yes	Yes	No	-	-
2	1	Yes	Yes	No	No	No	No
2	2	Yes	Yes	No	No	No	-
3	3	Yes	No	No	No	-	-
15	20	Yes	No	-	-	-	-
60	65	Yes	No	-	-	-	-
60	300	No	-	-	-	-	-

Figure 5.7: Impact of PLL Bandwidth on Transient Stability

5.3.2.2 Impact of Varying PLL Control Gains on Bandwidth and Grid Stability

The relation between the PLL control gains and bandwidth can be derived based on the small-signal model of the PLL, as shown in Figure 5.5. Comparing (20) with the second-order canonical representation given in (5.26) we get (5.27), (5.28), (5.29) for the PLL gains and bandwidth.

$$G_{cf}(s) = \frac{2\zeta\omega_{pll}s + \omega_{pll}^2}{s^2 + 2\zeta\omega_{pll}s + \omega_{pll}^2} \quad (5.26)$$

$$K_{pll} = \frac{2\zeta\omega_{pll}}{V_m} \quad (5.27)$$

$$T_{i_{pll}} = \frac{V_m}{\omega_{pll}^2} \quad (5.28)$$

$$\omega_{BW} = \omega_{pll} \cdot \sqrt{(1 + 2\zeta^2) + \sqrt{\zeta^4 + 4\zeta^2 + 2}} \quad (5.29)$$

where ω_{pll} is the PLL's natural frequency of oscillation and ζ is the damping ratio.

Interaction between PLL Bandwidth and Control Gains

This section provides insight regarding the impact of different PLL gains on bandwidth. The study seeks to identify the best combination of PLL gain values (K_p and K_i) that can change the bandwidth, which in turn affect the dynamic performance of the system. For instance, there are several combinations of PI gains that can give one unique bandwidth. For example, a bandwidth of 9.7Hz is seen with a PLL gain of [60, 65] and [20, 700]. Therefore, it is very important to understand the changes in bandwidth or damping that are contributed by various K_p or K_i combinations and identify which controller design is the most favourable. The dynamic performance of the system changes based on the bandwidth and PLL gains. It is reported that as the PLL gain value changes, the system stability conditions changes. This is because of PLL bandwidth and its changes with respect to its gain margin and phase margin. So a detailed analysis of the PLL bandwidth with control gain variations and their impact of PLL gain margin and phase margin is discussed below.

Varying K_p and Varying K_i : The impact of a set of selected PLL parameters has been tested on the weak grid model developed. The Bode plot is used to understand the impact of PLL control gains K_p and K_i on its parameters, such as bandwidth and phase margin of the PLL operating in the closed-loop. The magnitude plot depicts the decrease in the 3db bandwidth of the loop filter with PLL gain values. The phase plot shows the closed-loop system stability represented as the decrease in phase margin with PLL gain values.

Constant K_i and Varying K_p : Figure 5.9 shows the Bode diagram of PLL closed-loop transfer function with different K_p values with $K_i = 65$ kept as constant. It can be seen that as the PLL gain values drop, the phase margin drops. Since phase margin is the measure of system stability, this shows the need for an optimal PLL K_p

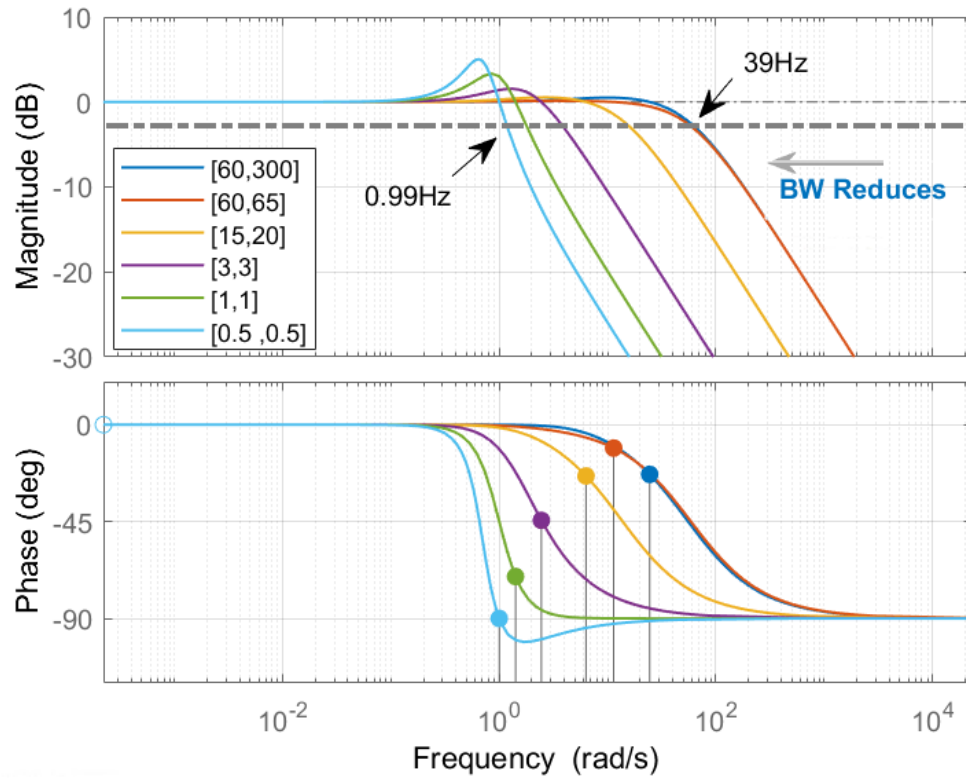


Figure 5.8: Bode Diagram of Closed Loop PLL Model.

value based on grid strength.

Constant K_p and Varying K_i : Figure 5.10 shows the Bode diagram of the of PLL closed-loop transfer function with different K_i values with K_p kept as constant at 60. It can be seen that as integral gain reduces, the phase margin is improved and varying integral gain does not bring a considerable reduction in PLL bandwidth. Therefore, varying K_i alone to reduce bandwidth keeping K_p constant is not a feasible solution as the grid strength drops beyond a certain point.

Proof of Impact of Control Gains on System Stability

During unbalanced conditions or distorted grid voltage harmonics, the PLL bandwidth has to be reduced to ensure that it will not lock faster with the varying grid frequency.

The impact of PLL gain on steady-state stability is shown in Figure 5.11. In Figure 5.11 stable cases are represented with $x - axis = -1$, while unstable cases are

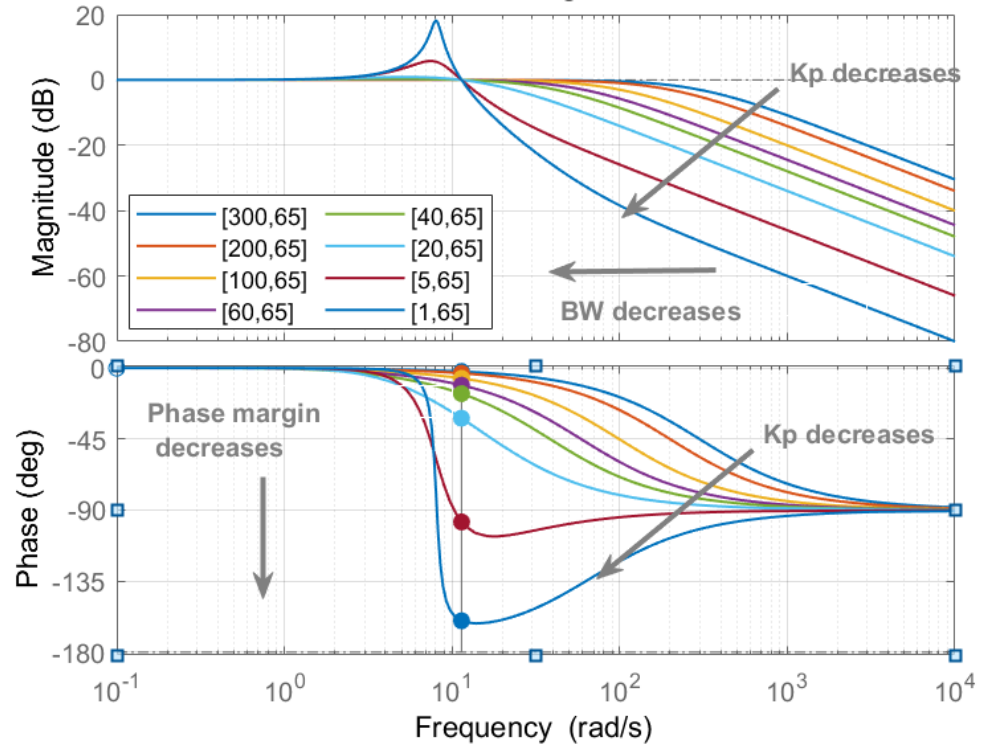


Figure 5.9: Bode Diagram to Explain the Influence of Proportional Gain K_p on Stability, Bandwidth and Oscillation Frequency with K_i as 65.

represented in the right plane with $x - axis = 1$. It can be seen that WPP remains stable for SCR as low as 1.4 as the PLL gains values are reduced to [3, 3].

The impact of control gains on stability can be proved using Lyapunov's stability theory. Consider the overall linear closed loop system represented by (5.22). The PLL gain values $K_{p_{pll}}$ and $K_{i_{pll}}$ in the state matrix indicate that the gains values can affect the stability of the system. Consider the quadratic Lyapunov function candidate given by,

$$V = x_k^T P x_k \quad (5.30)$$

where P is a symmetric positive definite matrix and V is the Lyapunov energy func-

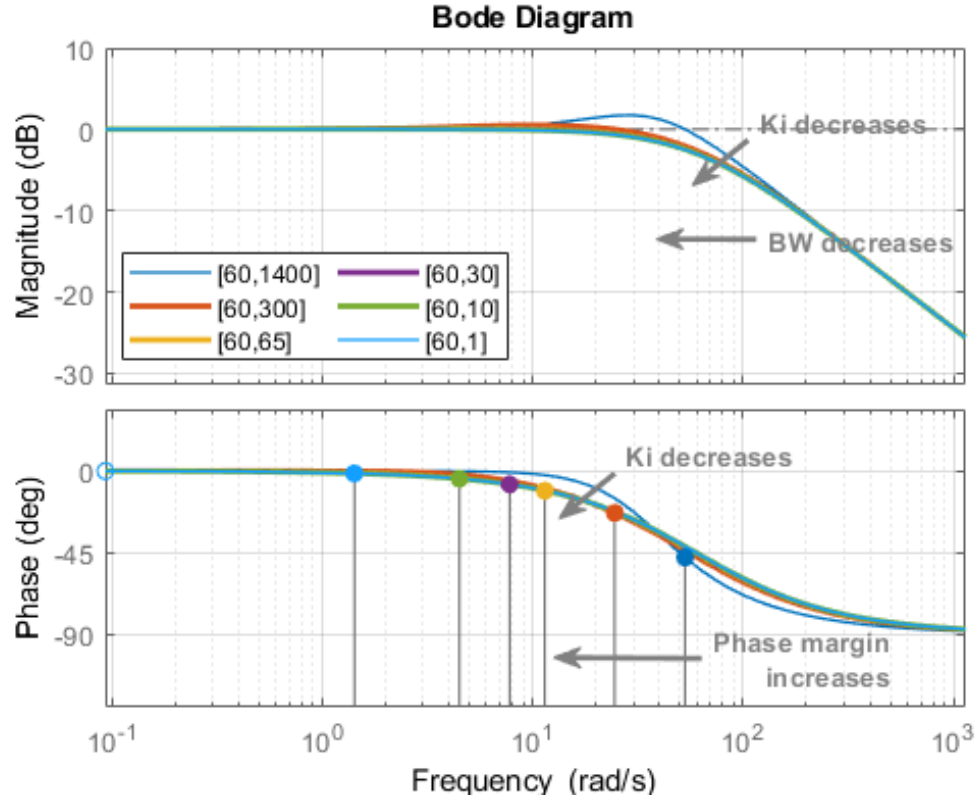


Figure 5.10: Bode Diagram to Explain the Influence of Integral Gain K_i on Stability, Bandwidth and Oscillation Frequency.

tion. The change in energy can be represented as,

$$\begin{aligned}
 \Delta V_k &= V_{k+1} - V_k \\
 &= x_{k+1}^T P x_{k+1} - x_k^T P x_k \\
 &= (A_{\text{overall}} x_k)^T P (A_{\text{overall}} x_k) - x_k^T P x_k \\
 &= x_k^T (A^T P A - P) x_k \\
 &= x_k^T (-Q) x_k
 \end{aligned} \tag{5.31}$$

According to Lyapunov theory, if there exist a positive definite Q that satisfies this equation, then the system is said to be stable (i.e., for the system to be stable ΔV_k should be negative definite or negative semidefinite). ΔV_k will be negative definite if the eigenvalues of $\Delta V_k \leq 0$.

$$|\lambda I - \Delta V_k| < 0 \tag{5.32}$$

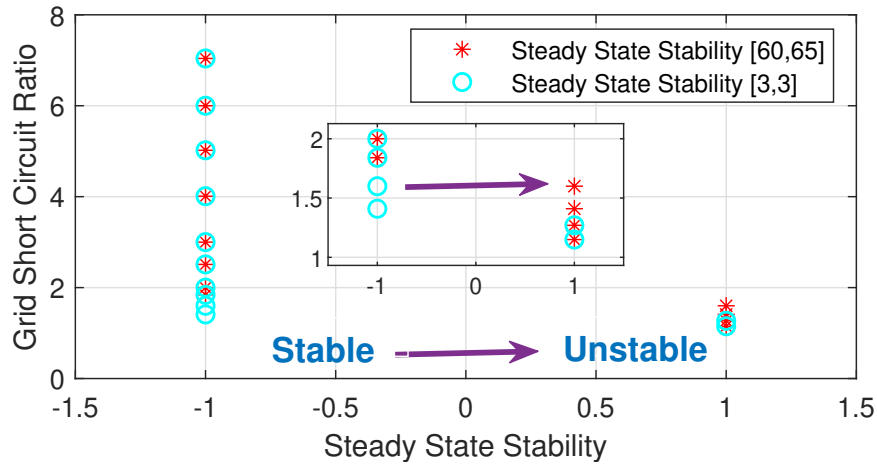


Figure 5.11: Impact of PLL Gain on Steady-State Stability.

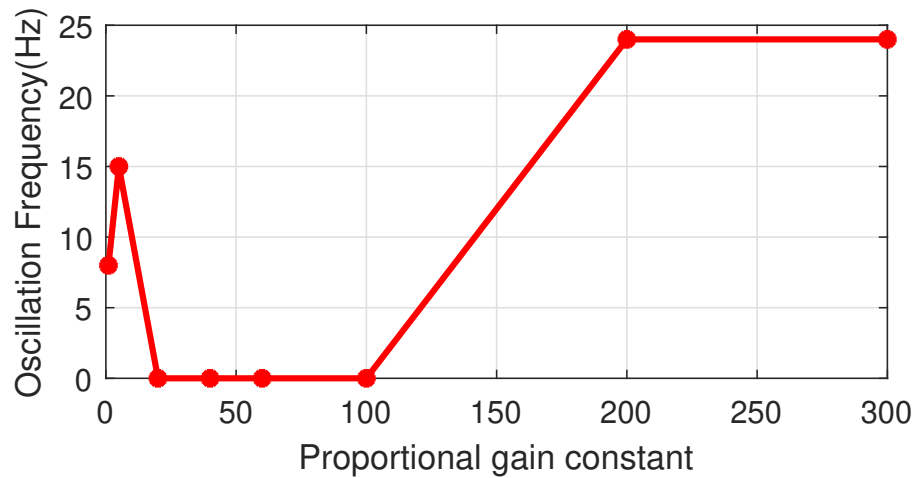


Figure 5.12: Variation in Oscillation Frequency with Proportional Gain Constant based on Simulation.

This results in an equation defined by the inner loop control gains, the PLL gain values, and other system parameters defined by the $A_{overall}$ matrix. Constraints for the loop filter gain for ensuring stability under varying grid conditions can be derived using this relationship, such that all eigenvalues will be negative. An example that is defined by the loop filter gains of the PLL is given below,

$$\frac{K_{i_{pll}}}{K_{p_{pll}}^2} + \frac{K_{p_{pll}}^2}{K_{i_{pll}}} + \frac{K_{i_{pll}} * K_{pd}}{K_{pll}^2} < 0 \quad (5.33)$$

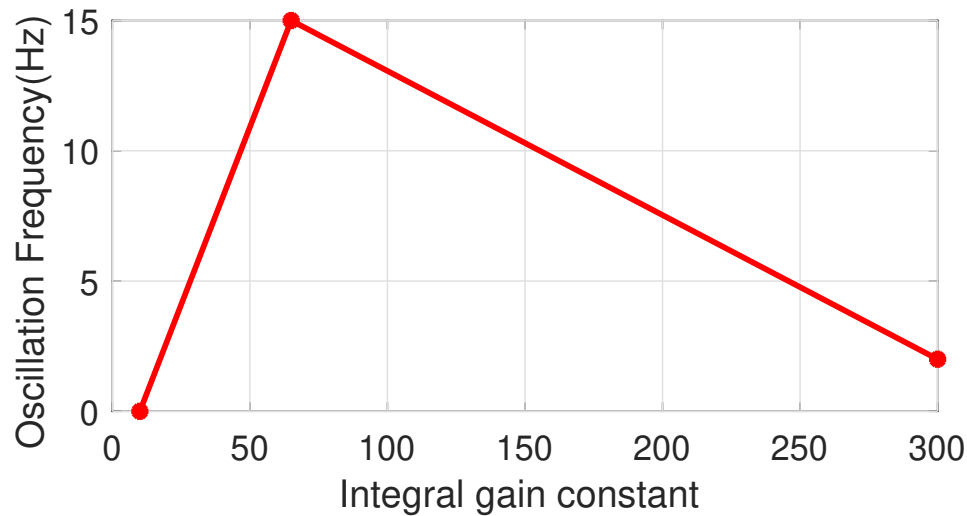


Figure 5.13: Variation in Oscillation Frequency with Integral Gain Constant.

This shows the contribution of both $K_{i_{pll}}$ and $K_{p_{pll}}$ on defining the stability and oscillations of the system.

The grid frequency oscillations based on the PLL gains using the small-signal model are presented in Figure 5.12. The results presented showcase the relation between the oscillation frequency and the proportional constant with a constant integral gain of $K_i = 65$. From Figure 5.12 it can be observed that as the grid strength reduces, during high power transfer the grid voltage distorts, low-frequency dominant oscillations are present in the grid voltage. To ensure stability, the PLL bandwidth of the GSC controller should be reduced, so that the PLL will not get locked to the oscillating frequency. As seen in Figure 5.9, as the PLL gain drops for a constant K_i , the stability margin drops. Moreover, we can observe a region of K_p where the oscillation are nearly zero, beyond which the oscillation increases. This is accounted by the K_i value of the PLL that defines the stability region over which K_p affects the oscillation. This is further supported by Figure 5.13, where for the same $K_p = 5$ that results in $15Hz$ oscillation in Fig.8, as the integral gain reduces to 10, the oscillation dies out and system stability is improved.

The Need for Adaptive PLL Gains

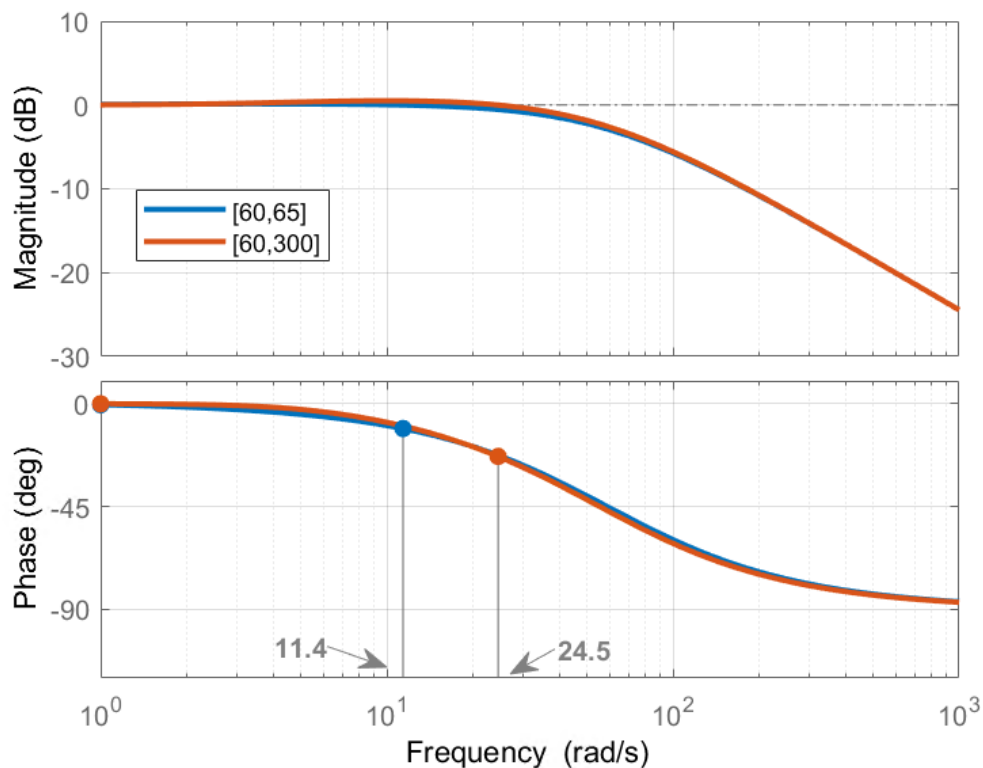


Figure 5.14: Bode diagram to Explain the Influence of Integral Gain K_i on Stability, Bandwidth and Oscillation Frequency with K_p as 60.

It is observed that even though the bandwidth does not change with varying K_i , there is a margin of stability determined by the integral gain of the PLL. For example, Figure 5.14 shows the bode diagram of varying K_i for an proportional gain of 60. It can be seen that the PLL integral gain falls into the unstable region resulting in an oscillation frequency of 24Hz as shown in Figure 5.12 and Figure 5.13 . This shows the need to find an optimal integral gain value of PLL that makes the system stable and then adjusts the proportional gain to modify the oscillations characteristics of the closed-loop system based on grid strength. Thus, without an argument, it is evident that an adaptive PLL is a requirement for wind integrated weak power grid.

5.3.3 Proposed Control Architecture With Adaptive Grid Model

Consider the basic diagram of a WTG grid side converter with PLL, as shown in Figure 5.16 with V_{pcc} as the PCC and V_g as the grid voltage, L_f as the inverter side filter inductance, and R_f as the parasitic resistance for the filter inductance and R_{line} and L_{line} as line resistance and inductance. I_L represents the inverter current. The PLL identifies the grid voltage angle and then generates the reference current for the inner current loop to synchronize the inverter output with the grid voltage.

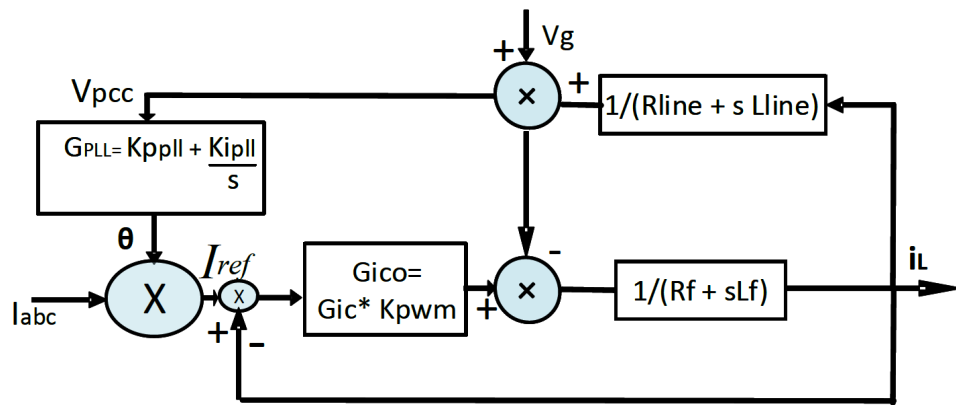


Figure 5.15: Block Diagram of the WTG Grid Side Converter with the PLL.

Based on Figure 5.16, the block diagram of the GSC in the s domain can be represented as shown in Figure 5.15. G_{PLL} represents the PLL transfer function, G_{ico} represents the overall inverter current control transfer function considering the PWM gain, inner loop current control gains [?]. The relation between V_{pcc} and the reference current to the inner control loop is defined by the PLL transfer function, while the relation between the reference current input to GSC with GSC output current I_L is defined by the inner control loop transfer function. Thus, the GSC output current i_L from Figure 5.15 is obtained as follows,

$$i_L = \frac{G_{ico} \frac{1}{R_f + sL_f}}{1 + G_{ico} \frac{1}{R_f + sL_f}} i_{abc} (G_{PLL}) V_{pcc} - \frac{\frac{1}{R_f + sL_f}}{1 + G_{ico} \frac{1}{R_f + sL_f}} V_{pcc} \quad (5.34)$$

Based on the impedance based stability analysis approach discussed in [?], (5.34) can be rewritten as,

$$i_L = Y_{PLL}V_{pcc} + Y_{ic}V_{pcc} \quad (5.35)$$

where Y_{PCC} is the first part of (5.34), which represents the admittance offered by the PLL loop in Figure 5.15, and Y_{ic} is the second part of the (5.34), which represents the admittance offered by the inner current control loop in Figure 5.15.

$$\frac{i_L}{V_{pcc}} = Y_{invo} = Y_{PLL} + Y_{ic} \quad (5.36)$$

where Y_{invo} represents the overall output admittance from GSC side of the WTG. Considering the grid side impedance as well,

$$\frac{i_L}{V_g} = \frac{1}{\frac{1}{Y_{invo}} + \frac{1}{Y_{line}}} \quad (5.37)$$

where $Y_{line} = \frac{1}{R_{line} + jL_{line}}$ is the variable line impedance as mentioned in Fig. 5.16. Upon further modification, the characteristic equation (*c.e.*) of (5.37) can be represented as,

$$c.e.(s) = 1 + \frac{Y_{invo}}{Y_{line}}. \quad (5.38)$$

Based on the overall linearized dynamic model of the grid side converter in (5.22), the relation between grid impedance and the PLL on stability has been analyzed.

Equation (5.22) shows that the eigenvalues are dependent on L_{line} , L_f and ω_{pll} given by the relationship $\frac{L_{line}\omega_{pll}}{L_f}$. This shows the ratio of the grid impedance to the GSC output impedance. The output impedance calculated using (5.35)-(5.38) can be further used to analyze the stability of the grid tied inverters. Based on [98], the stability of grid tied inverters under weaker grid scenarios can be guaranteed based on the Nyquist stability criterion per the ratio of the grid impedance to the inverter

output impedance. [98] also discusses the sufficient condition for stability based on Routh-Hurwitz criterion as $2\omega_n$ being the maximum PLL bandwidth for 1p.u. of grid inductance with ω_n being the fundamental frequency of oscillation. Considering the above condition,

$$\omega_{pll} \leq \frac{2\omega_n L_f}{L_{line}}. \quad (5.39)$$

Equation (5.39) also indicates the as grid goes weaker or as grid impedance goes higher, lower PLL bandwidth is desirable. Based on the varying grid impedance condition, the ideal ω_{pll} is identified and is then used to derive the PLL gain values as given by (5.27) and (5.28).

5.3.3.1 Proposed adaptive PLL Controller Architecture

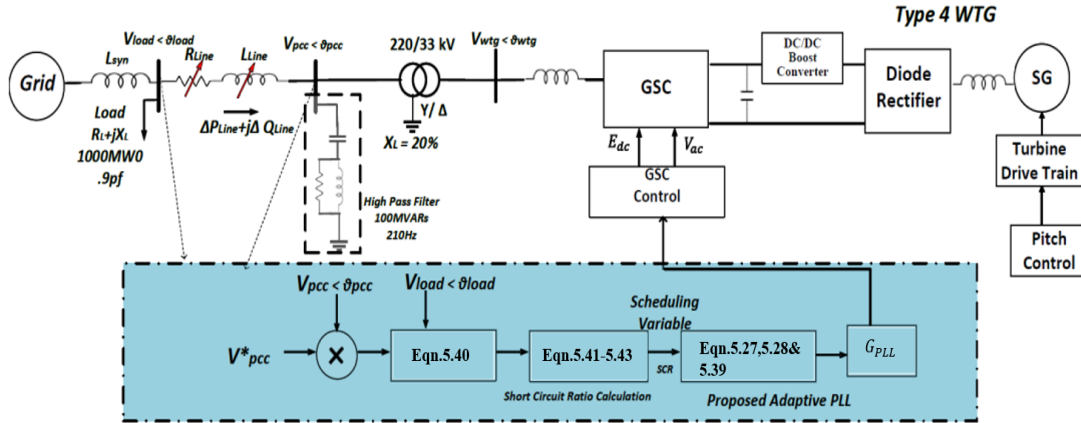


Figure 5.16: Proposed PLL Auto-Tune Control Architecture with a Type-4 WTG Integrated Weak Grid Model.

The proposed adaptive PLL is based on gain scheduling controllers with grid impedance or SCR as the scheduling variable. The detailed small signal model, considering the WTG and PLL dynamics described in the previous sections, utilizes the measurements to identify the natural frequency of oscillation, as defined in (5.39), which is further used by the proposed gain scheduling architecture to adapt the PLL gain values based on the grid dynamics. In practice, grid impedance may change with time and grid operating conditions. Consequently, online measurement of grid

impedance is very important and is attempted by many researchers developing adaptive control of grid-connected inverters. There are several existing measurement-based online grid impedance calculation techniques based on impulse perturbation, Fourier analysis, maximum-length binary sequence (MLBS) injection, etc. Different practical methods of online grid impedance measurement and challenges have been discussed in [99, 100, 101]. Accurate measurements are possible with filters and signal analysis. As these measurements are local (at the windfarm PCC, there is no need to communicate this to a central controller. The control diagram of the proposed architecture is shown in Figure 5.16. Gain scheduling controllers are preferred when the designed controller is not able to provide the desired performance or stability for the entire operating range. In this technique, the control gains are adjusted with plant operating conditions, thereby, ensuring the potential to respond to the changing operating conditions [102]. The scheduling variable for the proposed control is grid impedance or SCR, which can be calculated based on measurements, as shown below,

$$Z_{\text{line}} = \frac{V_{pcc}\angle\theta_{pcc} - V_{load}\angle\theta_{load}}{\Delta P_{\text{line}} + j\Delta Q_{\text{line}}}. \quad (5.40)$$

The grid SCR at the point of interconnection (POI) is calculated per [91],

$$\text{SCR}_{\text{POI}} = \frac{S_{\text{POI}}}{P_{\text{WF}}} \quad (5.41)$$

where S_{POI} is the short circuit level in MVA at the POI before integrating WPP of the P_{WF} rating. With the WPP rating as the base MVA, the SCR_{POI} is expressed as shown below,

$$\text{SCR}_{\text{POI}} = \frac{S_{\text{POI}}}{P_{\text{WF}}} = S_{\text{POI,PU}} = \frac{V_{\text{POI}}^2}{Z_{\text{sys,PU}}}. \quad (5.42)$$

With per unit voltage at the POI as 1.0 p.u., the SCR at the POI can be calculated as

the inverse of the per-unit impedance seen at the POI. This impedance should reflect the maximum impedance under which the WPP should operate.

$$Z_{\text{sys}} = \sqrt{R_{\text{Line}}^2 + (X_{\text{Line}} + X_{\text{syn}})^2} \quad (5.43)$$

where X_{Line} is the line reactance, X_{syn} is the line reactance between the generator and the load that can be obtained in a practical scenario using online impedance measurement techniques, as discussed in [99, 100, 101, 103, 104, 105], and Z_{sys} is the p.u. impedance at the point of interconnection. Thus, the inverse of (5.43) will provide the grid strength, which can be used as a scheduling variable for the gain scheduling control-based PLL architecture. A detailed algorithm of the proposed gain scheduling PI-based adaptive PLL is presented in Algorithm 1. The adaptive algorithm predicts the PLL control gain value until the measured PCC voltage change from 1p.u. represented as $\Delta V(k)$ is very small (typically 10^{-3}).

Algorithm 1 Proposed Adaptive PLL Control Algorithm

- 1: Measure the PCC and load (towards the grid side) voltage magnitudes and angles.
 - 2: Compute the line impedance between the PCC and the grid, as shown in (5.40).
 - 3: Calculate the overall system impedance seen by the WPP prior to its interconnection per (5.43).
 - 4: Calculate the grid SCR for a 1 p.u. voltage at the interconnection point per (5.42).
 - 5: Feed in this calculated SCR as the scheduling variable for the gain scheduling controller based PLL.
 - 6: Update the optimal PLL gains for the corresponding operating point represented by the SCR derived based on (5.27), (5.28), (5.39) from the small signal model.
 - 7: Calculate the $\Delta V(k)$ at each measurement instant.
 $\Delta V(k) \leq \epsilon$ Exit
 Go to Step: 1
 Return the PLL Gains for instant k
-

The overall flow diagram of the online process is illustrated in Fig. 5.17.

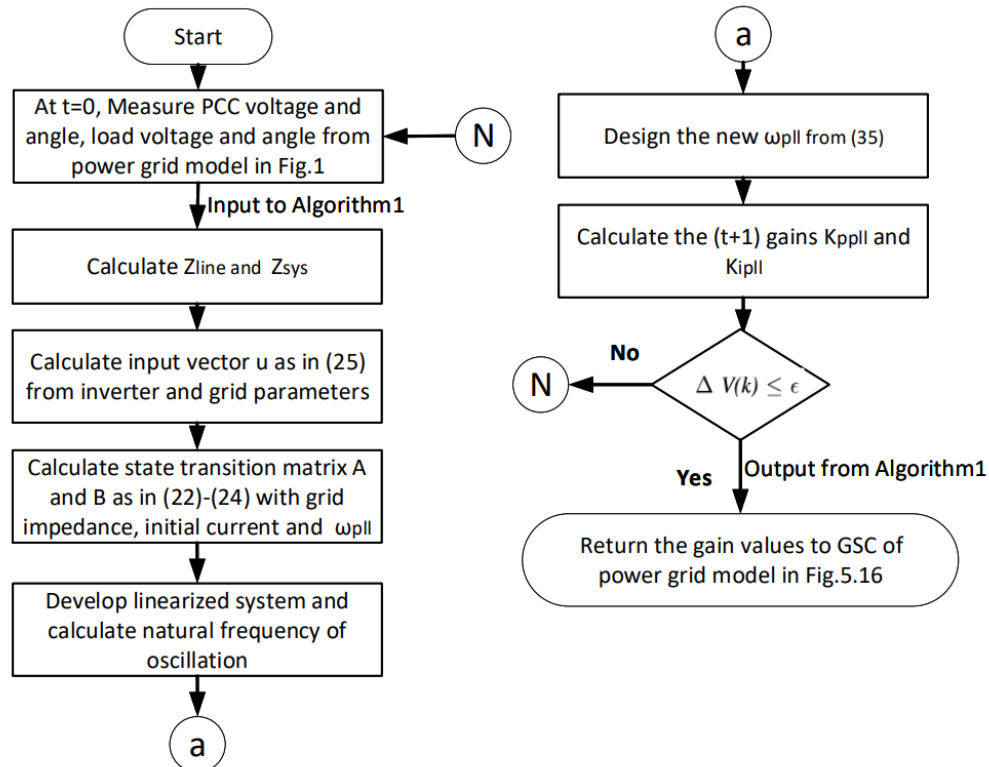


Figure 5.17: Proposed Adaptive PLL Control Flow Architecture.

5.3.4 Simulation Results

The weak grid model with the proposed adaptive gain scheduling PLL, as shown in Figure 5.16, is developed and first compared with the CIGRE model using MATLAB/Simulink with a 300MW Type-4 WTG model integrated at the PCC. For testing, grid impedance variations representing real-life wind integrated system are performed to validate the proposed adaptive PLL model (see Table 5.1). For the experimental results, we use a GE 1.5MW wind turbine model in the real-time simulator (OPAL-RT platform) and a 2 KW WTG (4 quadrant DC motor drive and a wound rotor induction machine- Lab-Volt 8013-A, [106]) for the hardware-in-the-loop (HIL) test set up that characterizes the GE 1.5 MW model. The specifications are included in Table A.3, respectively. The models and the hardware WTG is integrated with the simulator. The RSC and GSC are also integrated into the controller that is designed using the real-time simulator. For sensing, a data acquisition kit (OP 8660) is used.

The details are shown in Figure 5.18. Three tests are performed using the experi-

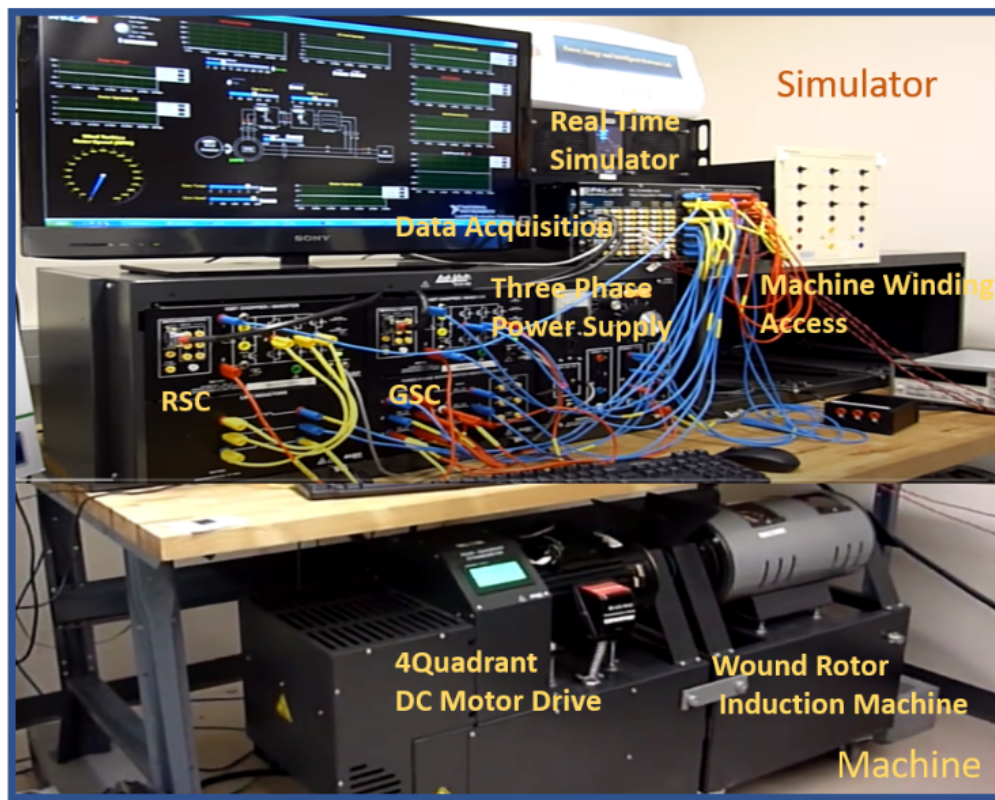


Figure 5.18: Schematic of HIL Real-Time Simulations Performed with OPAL-RT.

mental set-up. Test A provides an analysis of the proposed adaptive PLL method considering step variations in grid strength. Test B provides an analysis of the adaptive PLL with random changes in grid strength. Test C analyzes the performance of the adaptive PLL for a ramp change in grid strength with varying wind profile and grid fault.

5.3.4.1 Test A: Analysis of adaptive PLL for a step-change in grid strength

In this case, grid impedances are changed from Case 1 to Case 6 (as shown in Table 5.1) at 100s and then from Case 6 to Case 10 at 200s.

The PCC voltage corresponding to the test is shown in Figure 5.19. The drop in PCC voltage with grid strength can be seen in Figure 5.19, which is supported by the reactive power flow between the PCC and load point shown in Figure 5.20. The

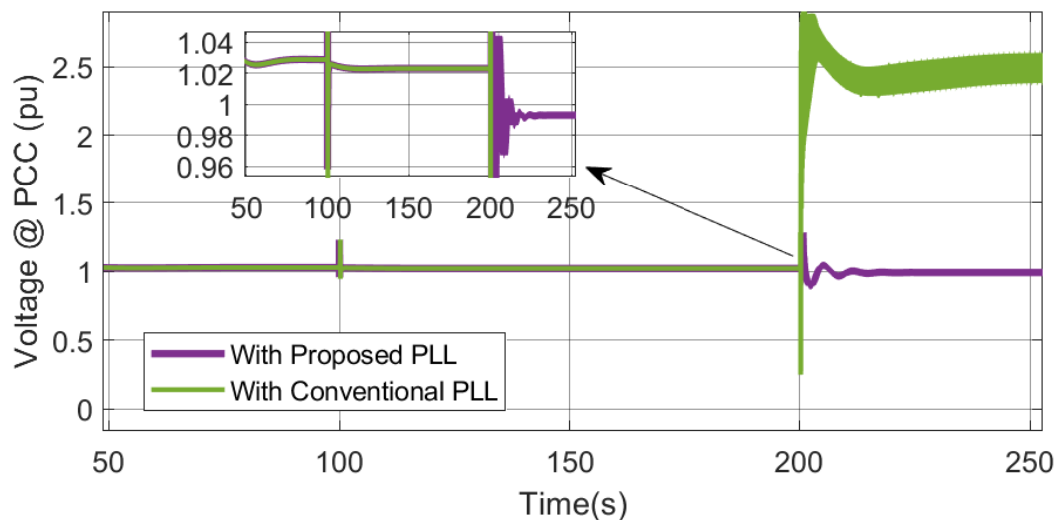


Figure 5.19: Test A: PCC Voltage.

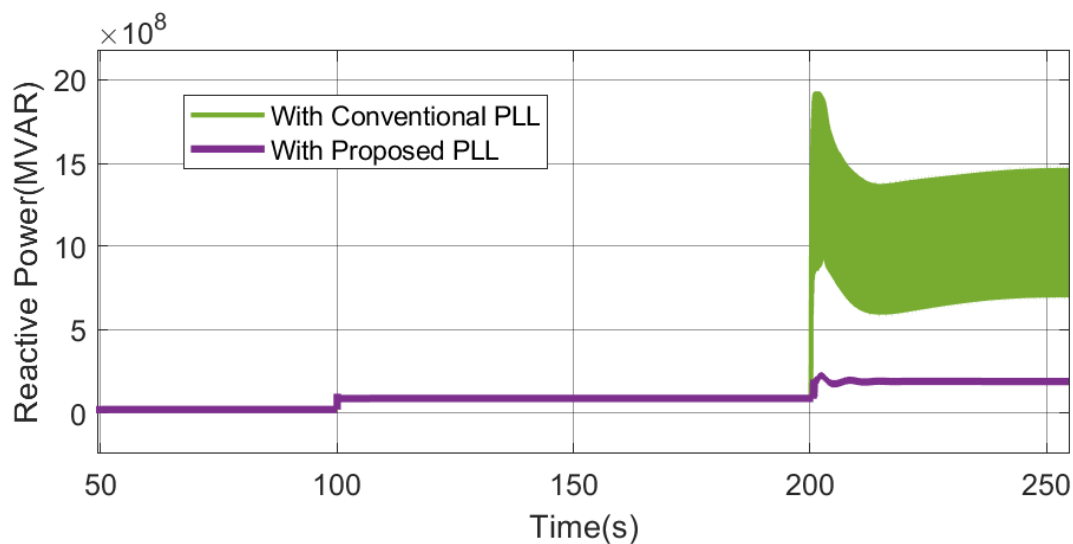


Figure 5.20: Test A: Reactive Power Flow between PCC and Load Point in Fig. 5.16.

wind power plant tries to push more reactive power, as the grid strength reduces, to maintain the PCC voltage at the desired value. The impedance calculated from measurements is shown in Figure 5.21. The increases in line impedance with the drop in grid strength is visible from the calculated impedance. The corresponding PLL gain values (derived by the proposed controller) are shown in Figure 5.22. The graphs depict the adaptation of PLL gain values based on the identified grid impedance. The corresponding PLL frequency as shown in Figure 5.23 shows that with the proposed adaptive PLL, the identified frequency for grid synchronization is not diverging when

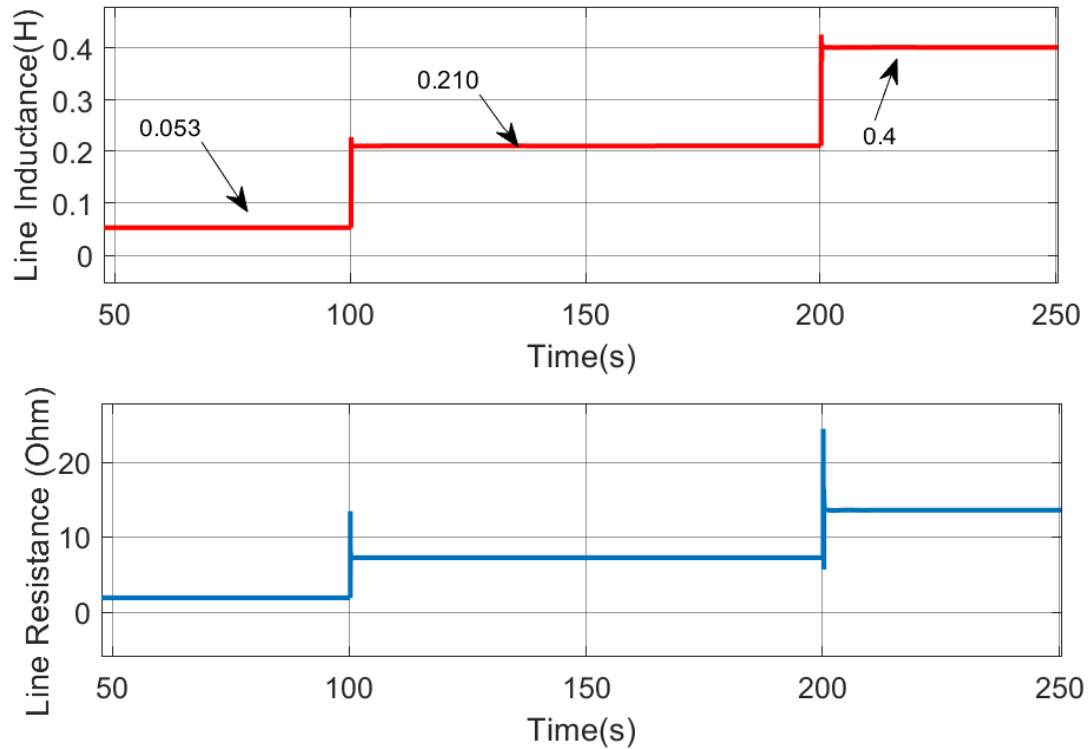


Figure 5.21: Test A: Calculated Line Impedance between PCC and Load Point in Fig. 5.16.

compared to the conventional PLL during the low grid strength condition (Case 10) triggered at 200s. Figure 5.24a and Figure 5.24b are presented to highlight the ability of the proposed adaptive control loop to consider the stability of the inner control loops. The figures compare the behavior of the inner loop control for the proposed PLL as the impedance changes from Case 1 to Case 6 at 100s, as discussed in Test A. The results of the adaptive PLL are compared with the conventional PLL using specific PLL gains [5,1530] and a bandwidth of 9.7Hz, which is similar to the bandwidth obtained by the adaptive PLL (with gains of [60,65] at 100s, as shown in Figure 5.22). The results highlight that the proposed control can adapt the PLL bandwidth and choose appropriate gain values, thereby improving the overall stability of the system considering the inner loop dynamics.

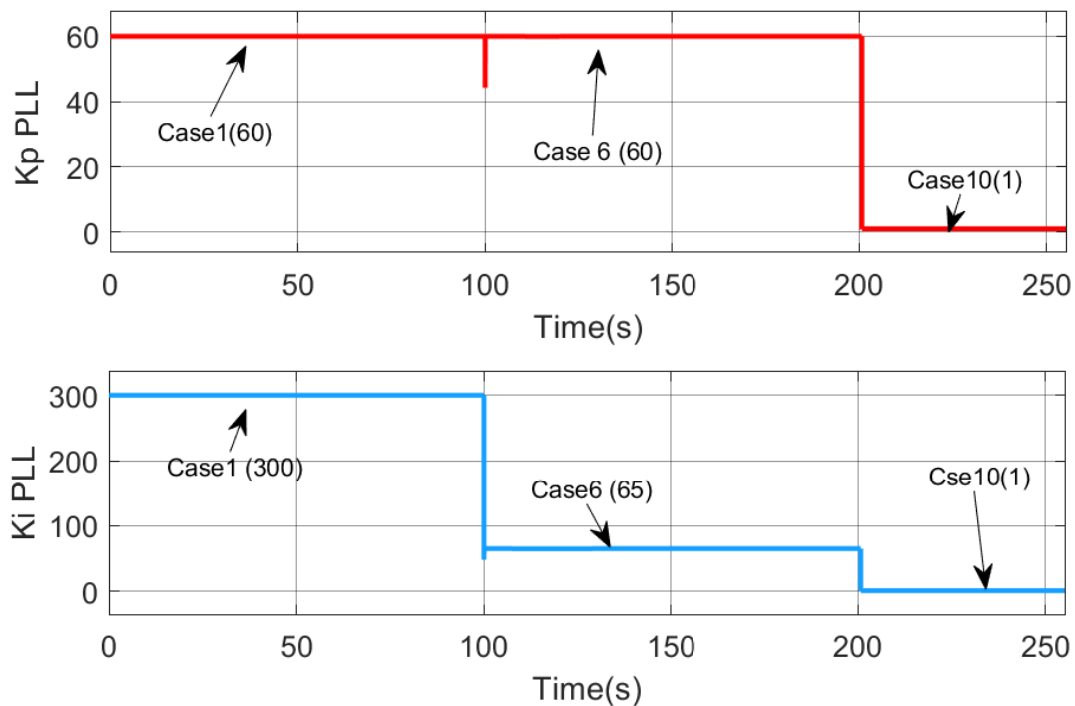


Figure 5.22: Test A: PLL Gain Values Calculated by the Algorithm.

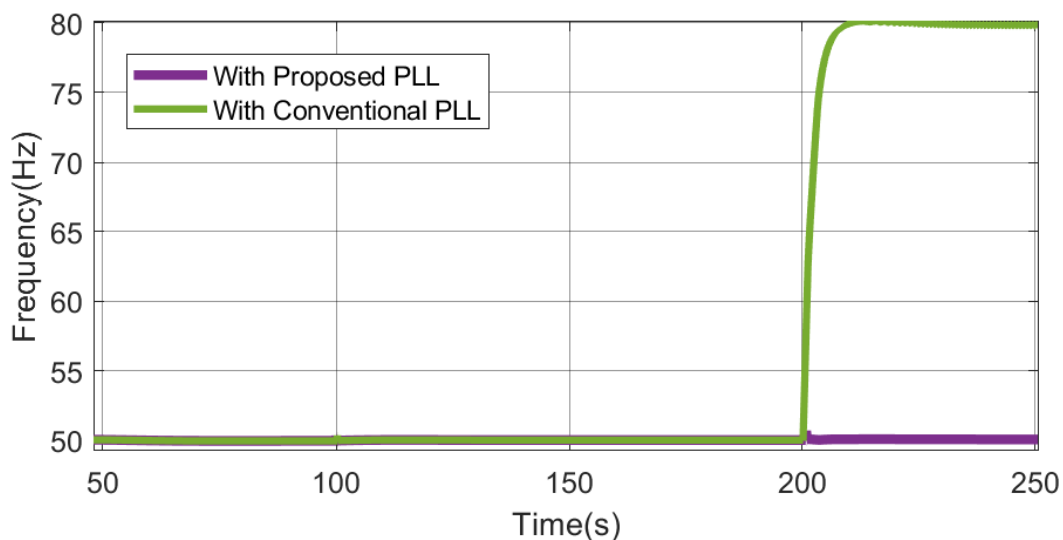


Figure 5.23: Test A: Identified System Frequency with the Proposed PLL.

5.3.4.2 Test B: Analysis of Adaptive PLL for Random Change in Grid Strength

Test B validates the proposed PLL with randomly varying grid impedance. The ability of the proposed PLL to accurately lock to the grid impedance is depicted in Figure 5.25. The PCC voltage corresponding to the test is shown in Figure 5.26.

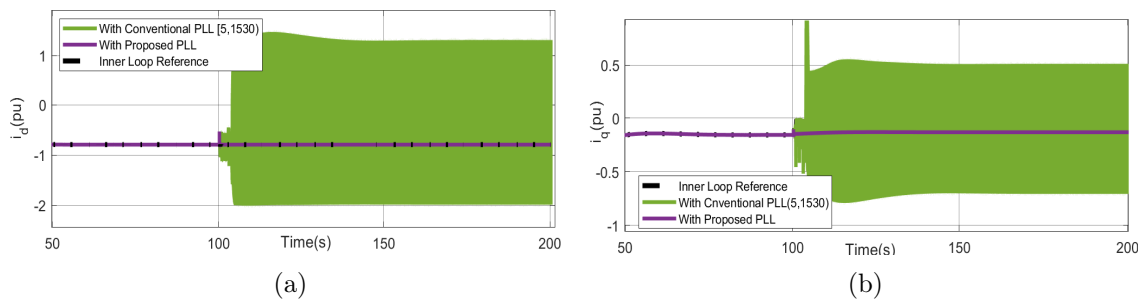


Figure 5.24: a) Test A: Comparison of the Inner d -Loop Behavior between the Proposed Control and Conventional Control with a Specific PLL Gain. b) Test A: Comparison of the Inner q -Loop Behavior between the Proposed Control and Conventional Control with a Specific PLL Gain.

The PCC voltages are very well maintained within the acceptable limit with the proposed method, even during dynamic variations in grid impedance. The active and reactive power flow at the PCC corresponding to these dynamic impedance variations is illustrated in Figure 5.27. With the proposed approach, the system can maintain the desired active power flow, even during the weakest grid conditions. The change in reactive power support offered by the WTG in maintaining the PCC voltage to the desired range is illustrated in Figure 5.27. Figure 5.28 shows the grid impedance calculated from the measurements. The corresponding dynamic PLL gain values derived from the proposed adaptive PLL architecture are shown in Figure 5.29.

Figure 5.30a and Figure 5.30b show the behavior of the inner current loop during dynamically varying PLL gains, as shown in Figure 5.29, corresponding to the dynamic grid impedance of Test B. The results show that with the adaptive PLL approach, the inner loop stability is maintained. This is accounted for by the adaptive nature of the control law, which derives the PLL bandwidth based on the closed loop measurements that include the dynamics of the inner loop control. The simulation results show that with the proposed adaptive PLL, the system can maintain the PCC voltage within the desired range, even during dynamically varying grid impedance conditions. This assures that the WTG is not disconnected from the grid, as grid

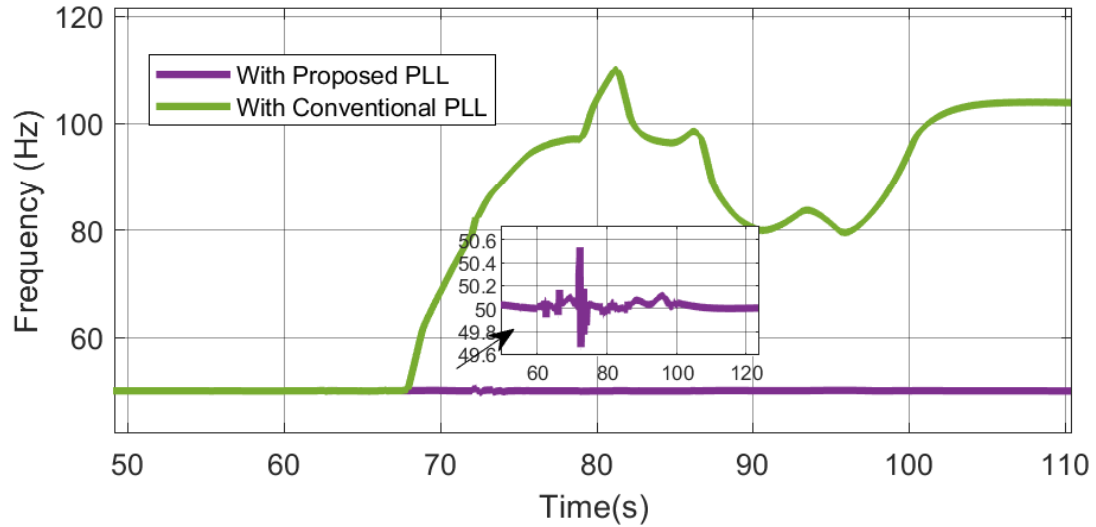


Figure 5.25: Test B: Identified Grid Frequency during Random Grid Impedance.

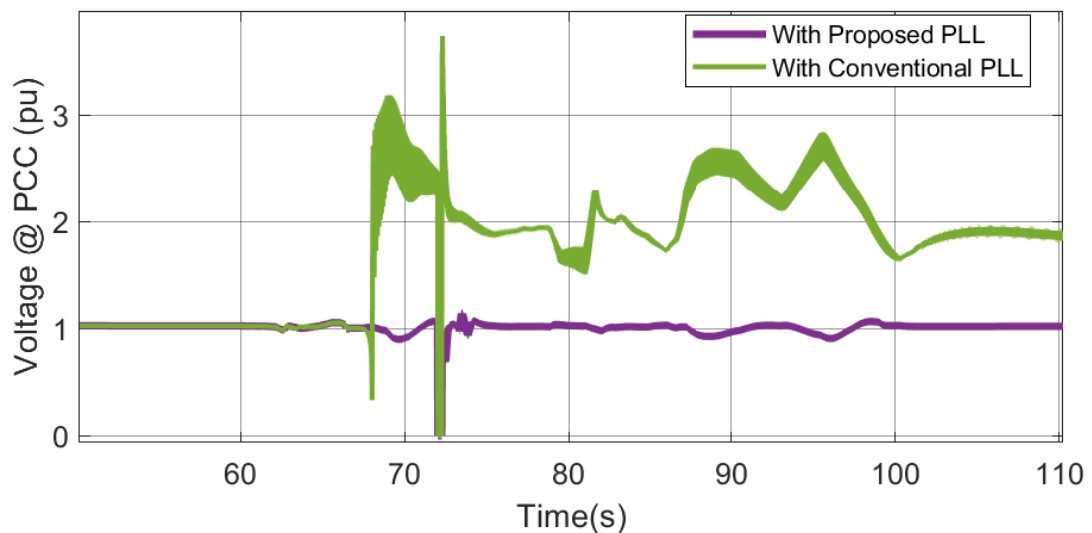


Figure 5.26: Test B: PCC Voltage during Random Change in Grid Impedance.

impedance increases. Thereby, maintaining the high power flow from the WTG, even during weaker grid scenarios.

5.3.4.3 Test C: Analysis of the proposed adaptive PLL for ramp change in grid strength with varying wind profile and grid fault

Test C analyses the sensitivity of the proposed adaptive PLL to varying wind profiles with a ramp change in grid impedance and grid fault simulated at 97sec for a

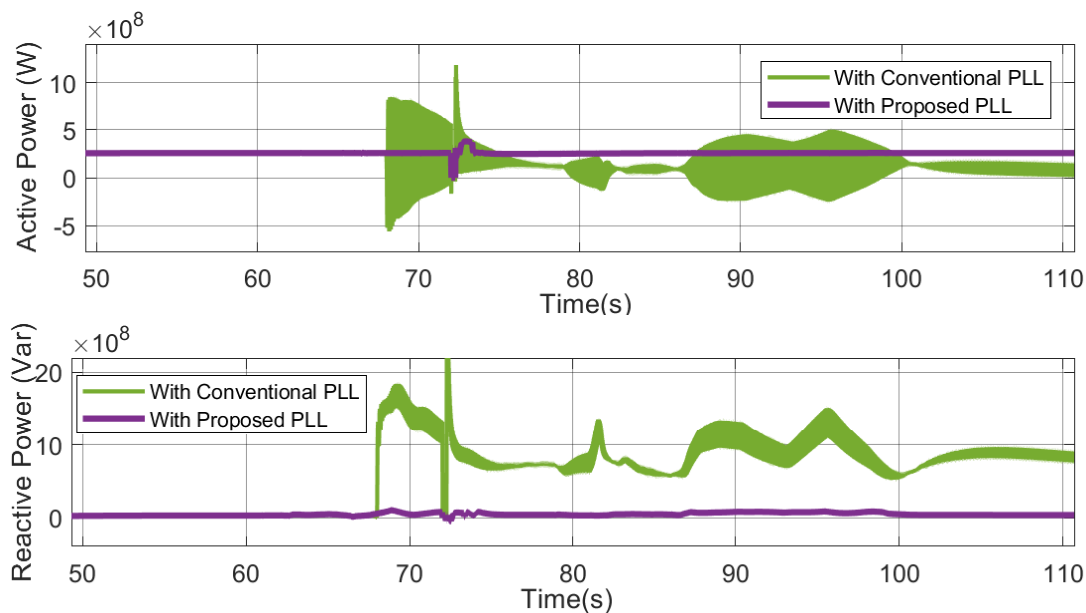


Figure 5.27: Test B: Power Flow at PCC during Random Grid Impedance Variations.

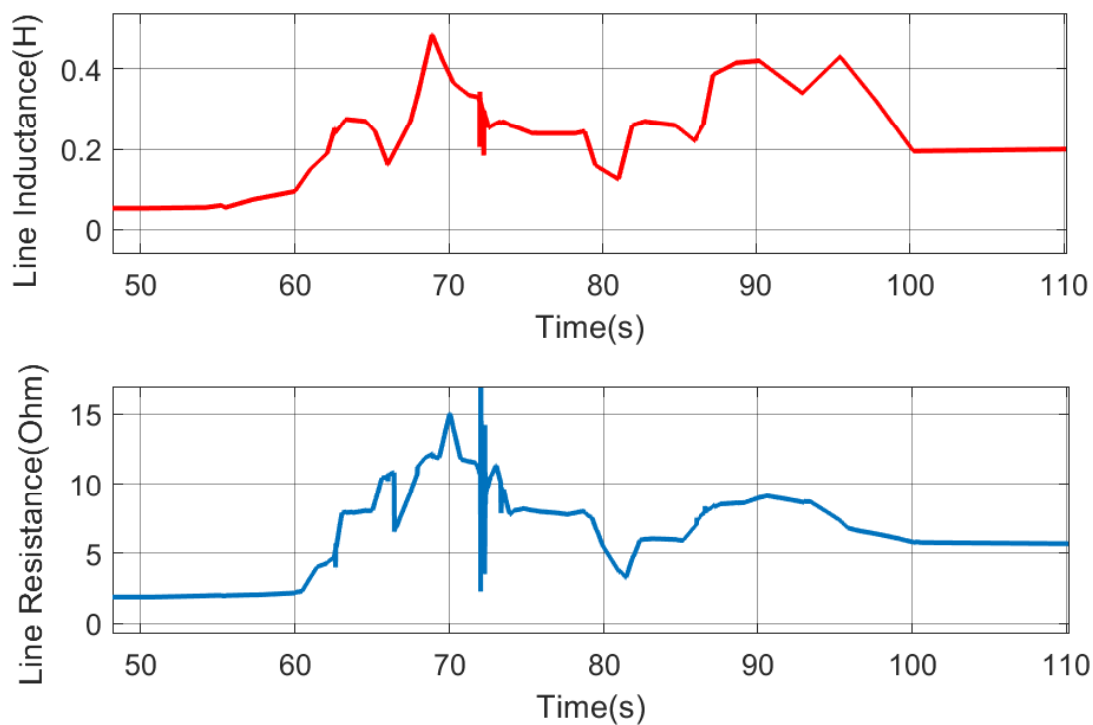


Figure 5.28: Test B: Identified Grid Impedance.

duration of 250ms. Figure 5.31 shows the variable wind profile used for analysis and Figure 5.32 shows the ramp variation in the grid impedance profile. The performance

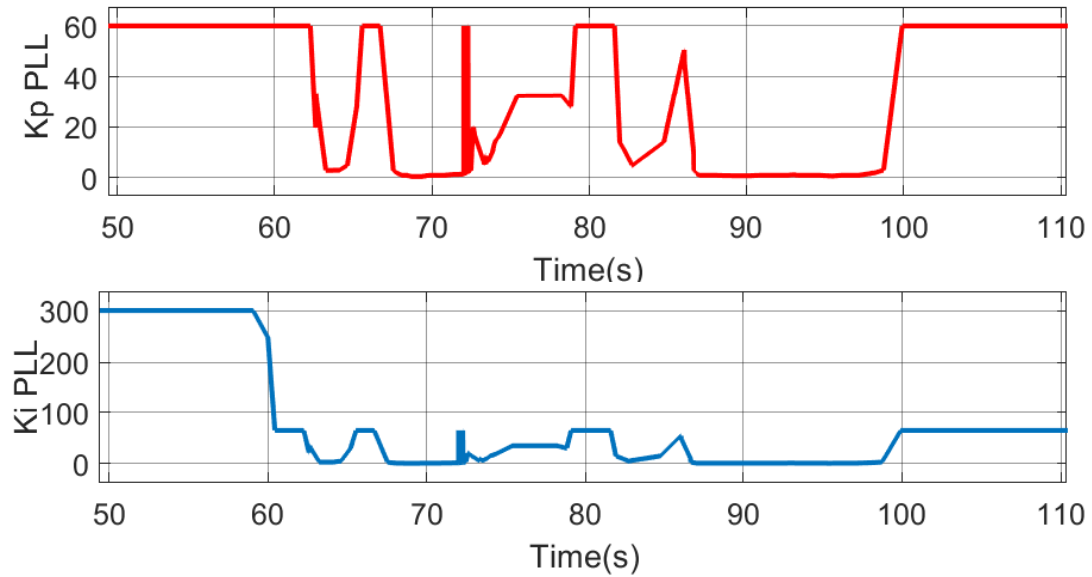


Figure 5.29: Test B: PLL Gains Derived by the Proposed PLL for the Given Impedance Variation.

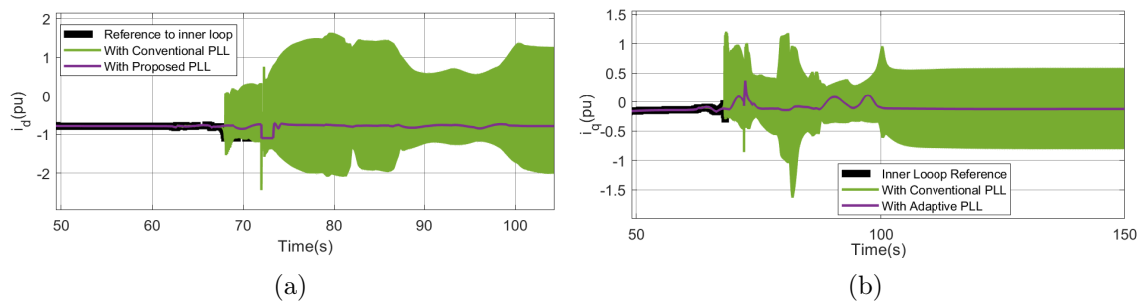


Figure 5.30: a) Test B: Behavior of Inner d -Loop for Test 2. b) Test B: Behavior of Inner q -Loop for Test 2.

of the proposed PLL architecture is validated using Figure 5.33 which shows that with the proposed architecture stable PCC voltage profile is maintained within the acceptable limit. It can be seen that with the proposed architecture, active power flow is maintained and the system is transient stable. The corresponding frequency identified by PLL is shown in Figure 5.34. The power output for the given wind profile and the derived integral gain values is shown in Figure 5.35 and Figure 5.36, respectively. Table 5.2 shows a comparison of the different test cases, which indicate the advantages of the proposed architecture.

Table 5.2: Comparison of Simulation Results

Parameter	PLL Architecture	Case A	Case B	Case C
% deviation in V_{pcc} from 1p.u.	Conventional	150 %	210 %	120 %
	Proposed	2.8 %	10 %	8 %
Δf from nominal	Conventional	30Hz	60Hz	70Hz
	Proposed	0.08 Hz	± 0.5 Hz	± 0.5 Hz

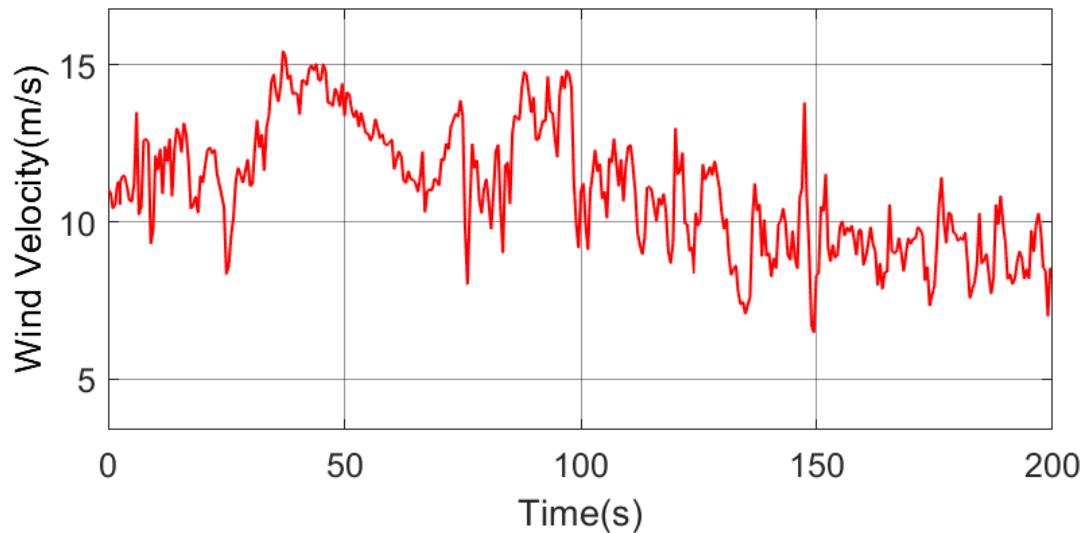


Figure 5.31: Test C: Variable Wind Profile used for Analysis.

The section presents a detailed analysis of the challenges faced by the wind on a weak grid system. The importance of PLL parameters under varying grid strength conditions and the effect of PLL parameters has been studied in detail. The study shows the need for an adaptive PLL controller to maintain grid stability with varying grid strength conditions. Towards this end, the paper also designs an adaptive PLL controller which is tested using a real-life grid model. It is observed that the proposed architecture provides grid stability during steady-state and transient operations when compared to the conventional PLL controller.

The section presents a detailed analysis of the challenges faced by the wind on a weak grid system. The importance of PLL parameters under varying grid strength

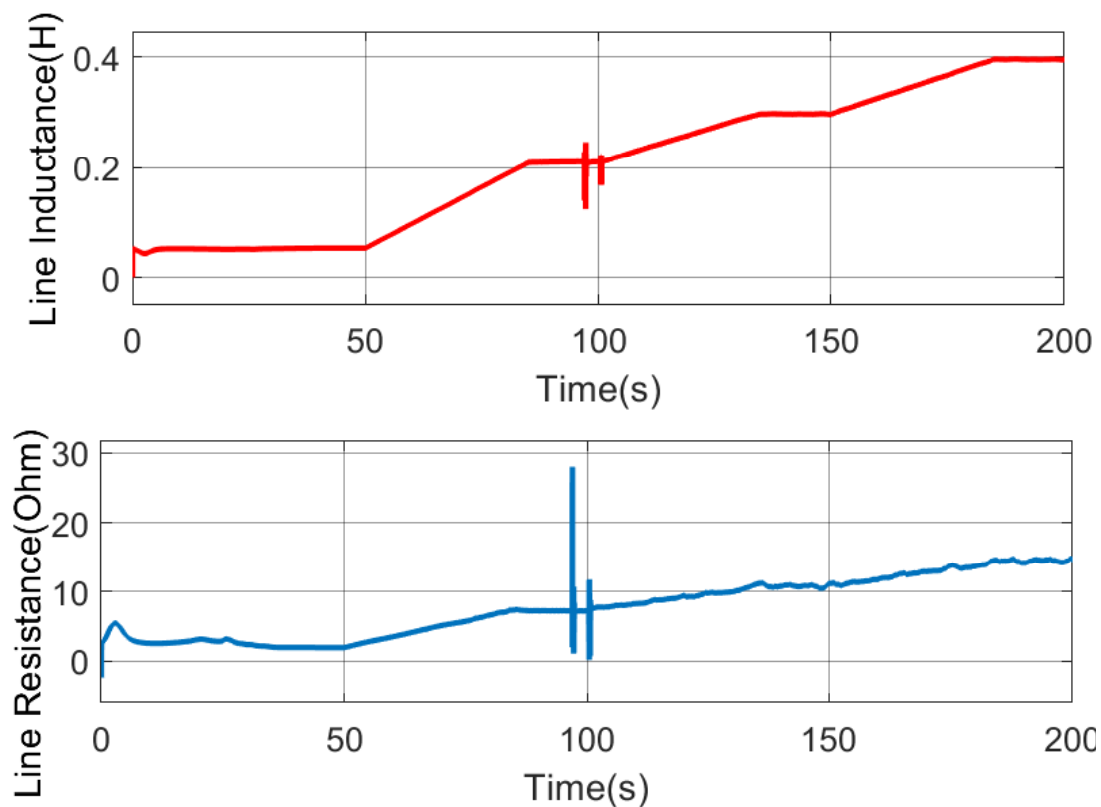


Figure 5.32: Test C: Identified Grid Impedance.

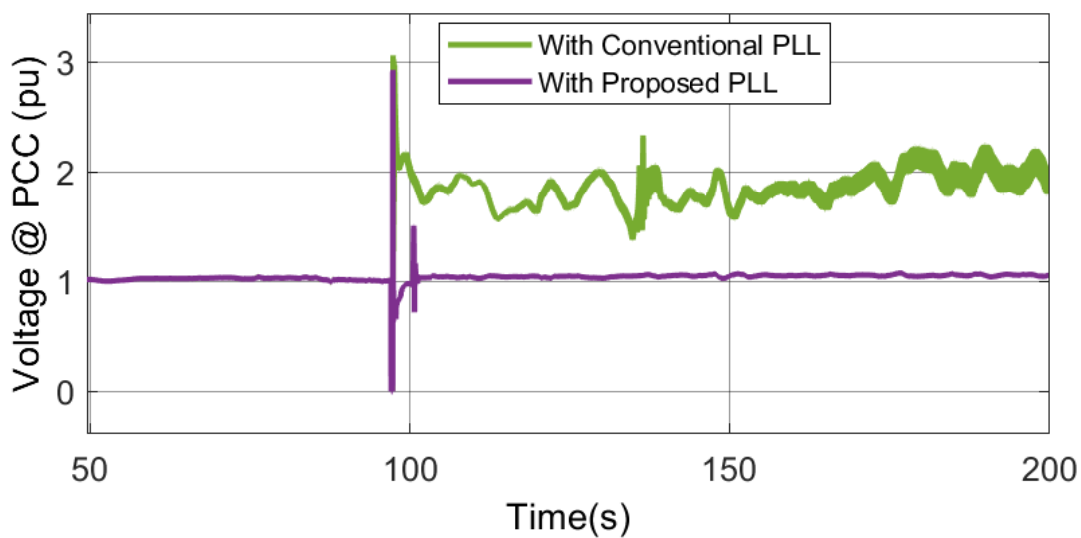


Figure 5.33: Test C: PCC Voltage during Ramp Change in Grid Impedance with Variable Wind Profile.

conditions and the effect of PLL parameters has been studied in detail. The study shows the need for an adaptive PLL controller to maintain grid stability with varying

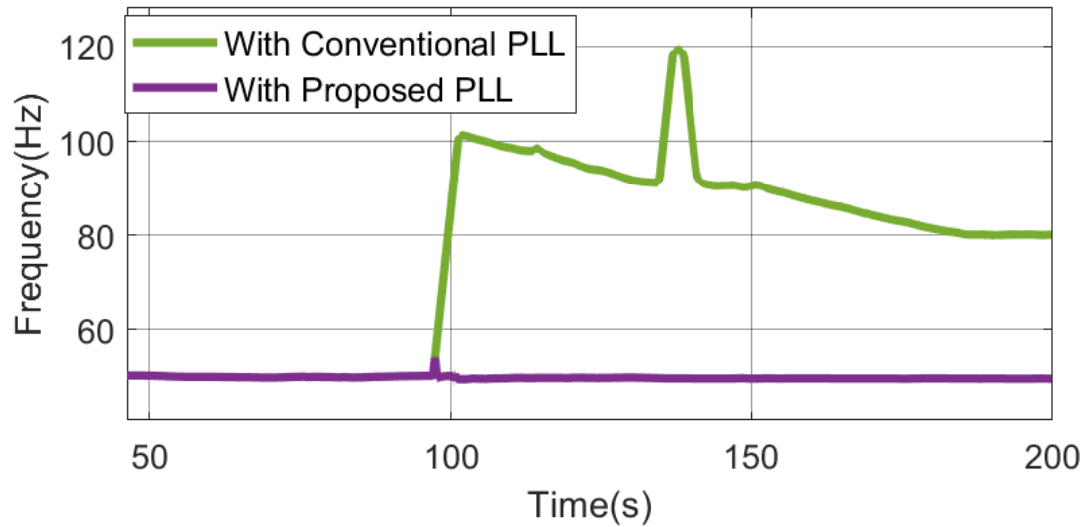


Figure 5.34: Test C: Identified Grid Frequency with and without Proposed PLL.

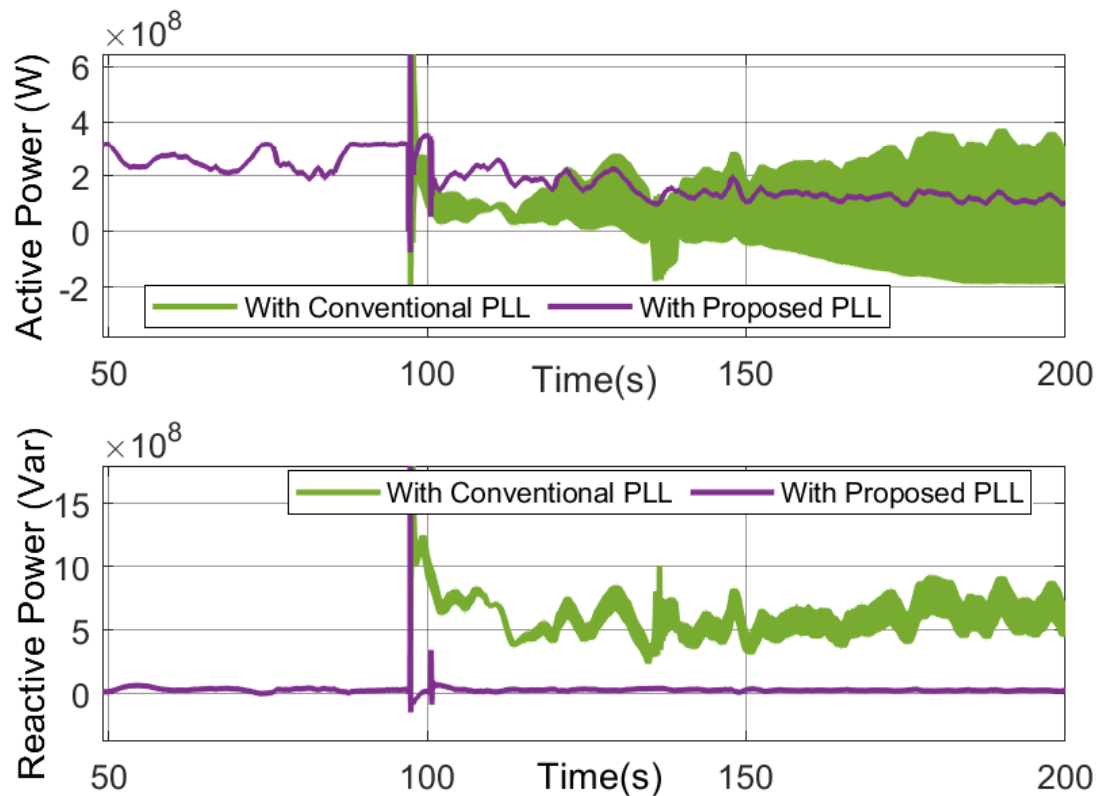


Figure 5.35: Test C: Power Flow at PCC during Ramp Change in Grid Impedance Variations with Variable Wind Profile.

grid strength conditions. Towards this end, the chapter also designs an adaptive PLL controller which is tested using a real-life grid model. It is observed that the proposed

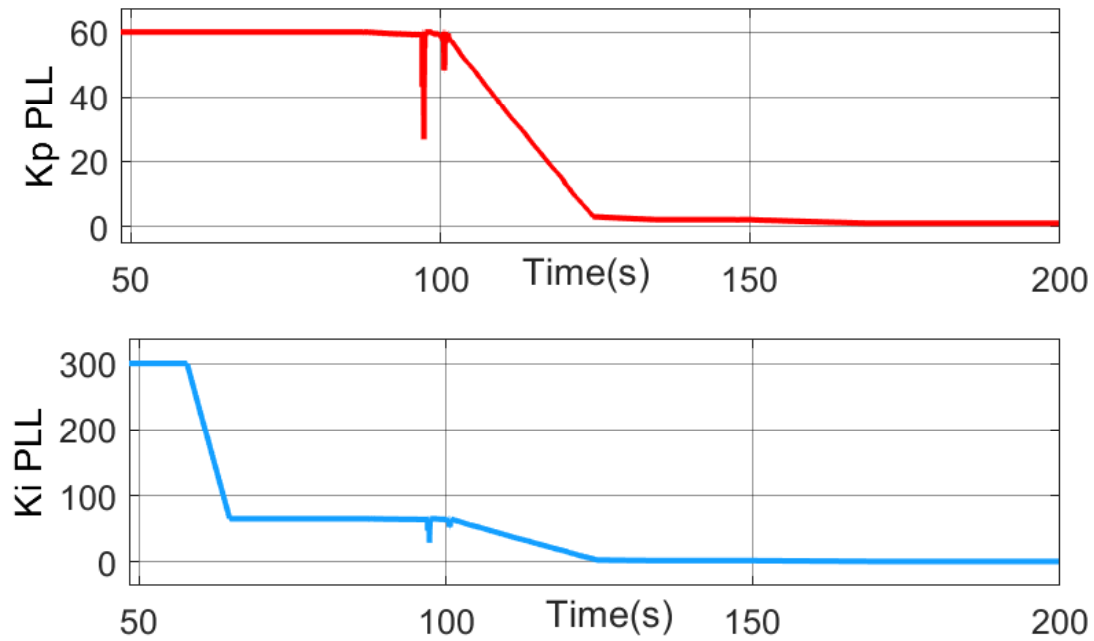


Figure 5.36: Test C: PLL Gains Derived by the Proposed PLL for the Given Impedance Variation.

architecture provides grid stability during steady-state and transient operations when compared to the conventional PLL controller.

An analysis of the above discussions shows that the phasing out of conventional generations with renewable penetration is the root cause for the decline of grid strength. This reduces the overall inertia and short circuit capacity of the grid. Moreover, the power electronic devices used to interface the renewable based generations with the grid will decouple the rotor frequency from grid frequency and also limits the short circuit power due to the limitations in the maximum current carrying capacity of these power electronic components. This results in several poorly damped or undamped oscillations during high power transfer which are one of the biggest challenge faced by current renewable penetrated grid.

5.4 Possible Solutions to Improve Stability of Wind on Weak Grid

Several different possible solutions to mitigate the stability issues due to wind on the weak grid have been discussed in the literature [91]. The most popular of those

include,

- A synchronous condenser at PCC to provide additional reactive power support.
- Adding a power electronic based compensators like static synchronous compensator (STATCOM) or static var compensators (SVCs)
- Modifying the PLL references using Phasor Measurement Unit(PMU)
- Modifying the WTG decoupled control using local synchronizing reference.

Compared to other compensations devices like SVCs, condenser provides added functionalities like improving grid inertia and short circuit power and short term overload capacity on top on reactive power support. Moreover, the maximum obtainable capacitive current from SVCs decreases linearly with the system voltage. Hence synchronous condenser is overviewed as a promising solution to maintain the stability of the renewable penetrated transmission network.

In this section, the effect of synchronous condenser on stability has been analyzed in detail. The rating of the condenser, location, and the impact of grid oscillations which are critical parameters for improve grid stability is studied in details. The results are validated and the performance is compared with SVC to highlight the advantages of using SCs.

5.5 Impact of Synchronous Condenser on Wind Integrated Weak Grid Systems

5.5.1 Mathematical Modeling of SC

Synchronous condenser is a synchronous generator with mechanical input set to zero. The synchronous machine used in the grid model is derated to 50MVA with a disabled turbine governor system to represent the reactive power compensator. The compensator has an inertial constant of 3s and the excitation control based on IEEE T2 exciter of which is set to control its terminal voltage to 1p.u.

5.5.2 Steady State Analysis

Aggregated grid model shown in Figure 5.1 is analyzed for varying grid strength simulated by adjusting the line impedance values. 12 different test case scenarios were formulated based on reference from [91]. The SCR values are ranging from 7 (case 1, representing a stronger grid) to 1.15 (case 12, representing a weaker grid). The line impedance parameters used for the different test cases are summarized in Table 5.1.

The model is first validated and analysed for steady state results. The summary of steady state analysis is shown in Table 5.3. As grid impedance increases from case 1 through case 12, grid strength quantified as Short Circuit Ratio(SCR) reduces. WTG is able to transfer power upto grid strength as low as 1.64. As the grid strength further reduces the WTG losses its stability and it fails to transfer high power to the grid. As grid strength reduces from 7 to 3, WTG tries to push more reactive power resulting in an increase in PCC voltage. As the grid strength further goes low from 3 down 1.15, WTG tries to push more and more reactive power, but still it is not able to maintain the PCC voltage. The voltage drops as the grid strength reduces further the system stability is lost.

Table 5.3: Summary of the Steady State (S.S) Analysis

Case No.	SCR at PCC	S.S Stable	Voltage (pu) at PCC	Phase (deg) at PCC	Phase (deg) at WTG	Q(MVAR) at PCC
1	7.004	Y	1.015	4.83	14.78	66
2	5.91	Y	1.02	6.06	15.63	68.17
3	5.09	Y	1.024	7.77	17.42	62.56
4	4.08	Y	1.025	10.68	20.37	55.5
5	3.00	Y	1.027	15.88	24.85	53.17
6	2.51	Y	1.027	19.78	28.72	53.41
7	2.00	Y	1.024	25.31	35.14	58.55
8	1.84	Y	1.02	28.46	38.29	61.46
9	1.60	Y	1.012	34.12	44.20	69.9
10	1.41	N	-	-	-	-
11	1.27	N	-	-	-	-
12	1.15	N	-	-	-	-

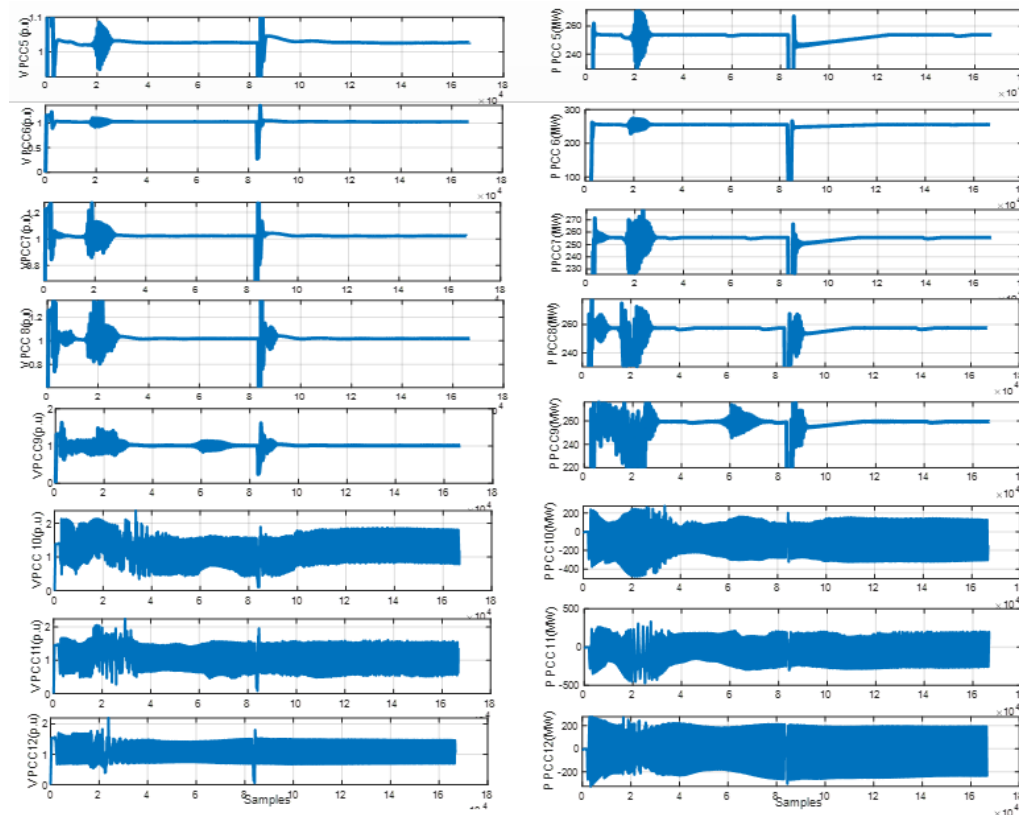


Figure 5.37: Fault Ride through Behavior for Three Phase to Ground Fault for Cases 5-12 of Table 5.1.PCC Voltage(left), PCC Power(right)

5.5.3 Transient Analysis

The transient response of the system to weak grid is analysed for a three phase to ground fault applied at PCC at 25sec for a duration of 250ms. A successful fault ride-through behavior, where the WTG is able to recover from the fault and to re-synchronize to the grid, is only obtained up to case 9. The PCC voltage and active power flow during dynamic analysis is shown in Figure 5.37.

5.5.4 Effect of Synchronous Condenser at PCC

To analyze the effect of synchronous condenser on improving stability, the condenser modeled as described in Section 5.5.1 was integrated at PCC. Fault ride through performance with SC at PCC is tested for a three phase to ground fault applied at 60sec for a duration of 250ms. From Figure 5.38, it can be seen that the stability

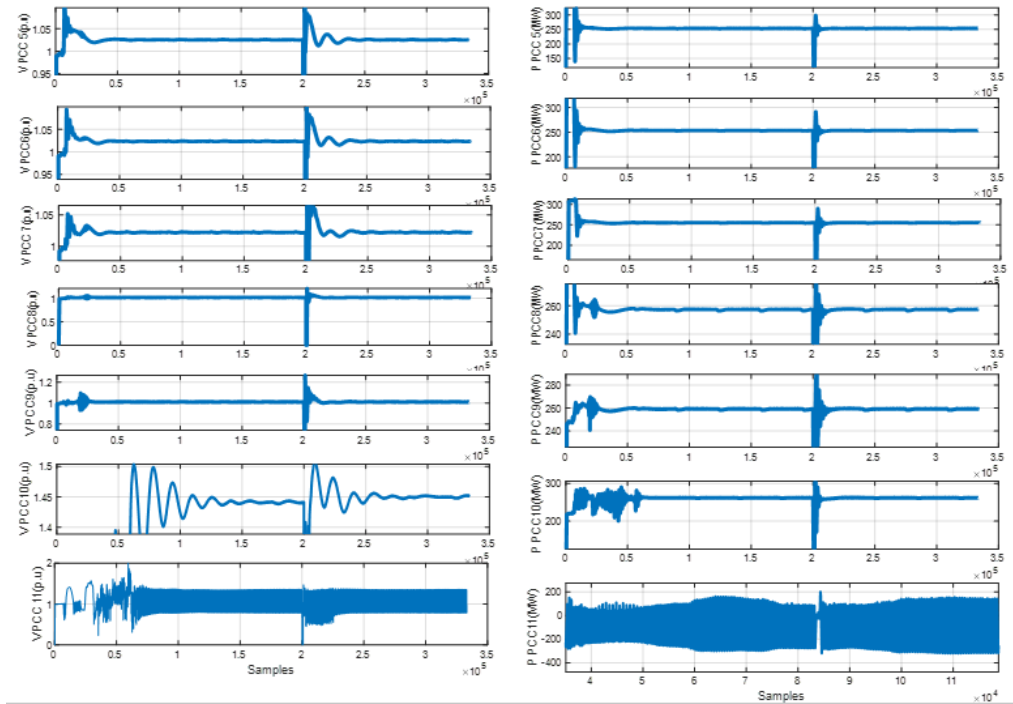


Figure 5.38: Fault Ride through Behavior for Three Phase to Ground Fault with SC at PCC for Cases 5-11 of Table 5.1. PCC Voltage(left), PCC Power(right)

during FRT has improved as grid strength reduces. With SC at PCC the WPP can maintain a stable operation upto a grid strength as low as 1.41. This is achieved with a 50MVA SC at PCC. This response will be still better with higher rated SC due to increased dynamic reactive power support offered. Steady state analysis also shows better stability with SC at PCC as the grid impedance increases.

5.5.5 Effect of Synchronous Condenser Parameters on Stability and Oscillation

The effect of different synchronous condenser parameters on stability and oscillation frequencies have been analyzed in this test case. As discussed in literature [107, 108, 109], a low frequency oscillation is noticed as the grid strength reduces. Various SC parameters like excitation limit, transient and sub transient reactance, reference voltage to AVR, exciter gain value etc has been considered for this test. The summary of the analysis is shown in Table 5.4 and Table 5.5 respectively. Transient reactance and exciter gain seems to have considerable effect on both stability and oscillation

frequencies.

Table 5.4: Analysis of Different SC Parameters on Stability

Parameter	Effect on Stability for $SCR \leq 1.83$
Machine Transient reactance	Increases as the transient reactance reduces
Exciter Gain	Increases with increase in the gain values
Sub-transient reactance	Increases as the sub-transient reactance reduces

Table 5.5: Analysis of Different SC Parameters on Oscillations Frequencies

Parameter	Effect on oscillation frequency
Excitation Limit	Considerable effect is not observed
Machine Transient reactance	Reduces as reactance reduces
Exciter Gain	Reduces with exciter gain within a limit
Reference voltage	Lowering Vref increases the oscillation frequency while higher Vref leads to instability

Table 5.6: Analysis of Exciter Gain Effect on Low Frequency Oscillation for a 50MVA SC

Exciter $Gain(K_E)$	Oscillation Frequency(Hz)
0.1	4.13
1	4.34
2	4.34
25	8.9
50	9.09

5.5.5.1 Effect of Synchronous Condenser Excitation Gain And Limit

The results shows that lower gain results in lower oscillation frequency. Study performed to analyse the effect of excitation gain and limit on the stability concludes the relation of excitation limit of improving the system stability as grid strength reduces. This is mainly because of the improved reactive power compensation with the synchronous condenser as the excitation limit changes. Figure 5.39 and Figure 5.40 shows that at grid strength as low as 1.14, lower excitation limit has improved the stability. Based on the analysis, it is understood that the rating of SC, the grid strength

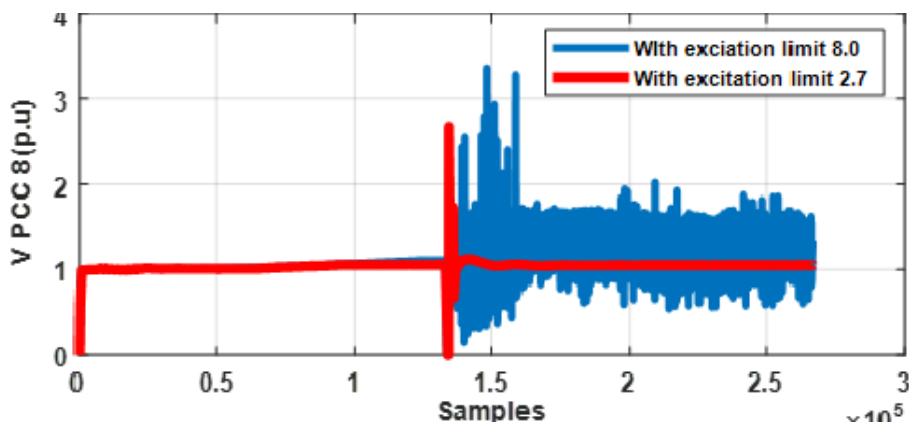


Figure 5.39: PCC Voltage for Case8 with Different Excitation Limit.

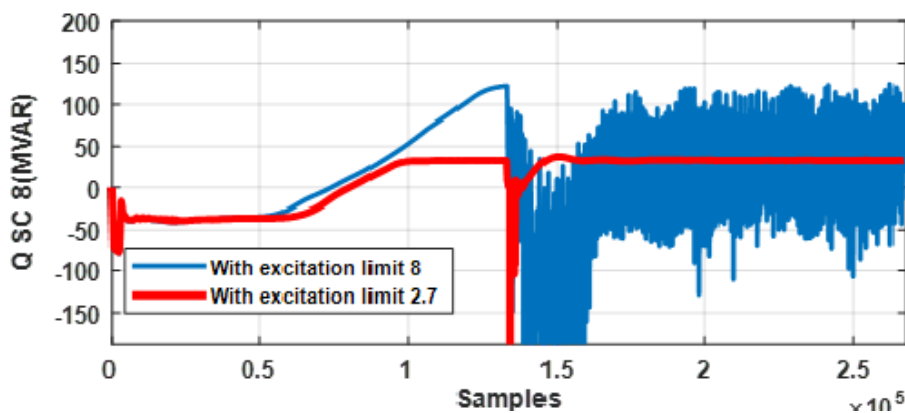


Figure 5.40: Reactive Power for Case8 with Different Excitation Limit.

and the dynamic reactive power requirement are the factors that can impact stability. The synchronous condenser has the ability to absorb or provide reactive power to maintain the PCC voltage to desired level. But when the condenser is operating with a negative excitation to reduce the PCC voltage, the stability is maintained upto certain level but further reduction in excitation voltage makes the voltage to fall drastically thereby reversing the polarity of the poles. This results in voltage build up phenomenon. The literature discusses that this effect of voltage rise can not be limited even with a voltage regulator of rapid time element.

Figure 5.41 and Figure 5.42 shows the analysis of excitation voltage on stable case5 with strong grid. As the excitation voltage lower limit is increased from -1 p.u to -3.5p.u, the reactive power of +45MVARs is supplied to the grid as be seen in

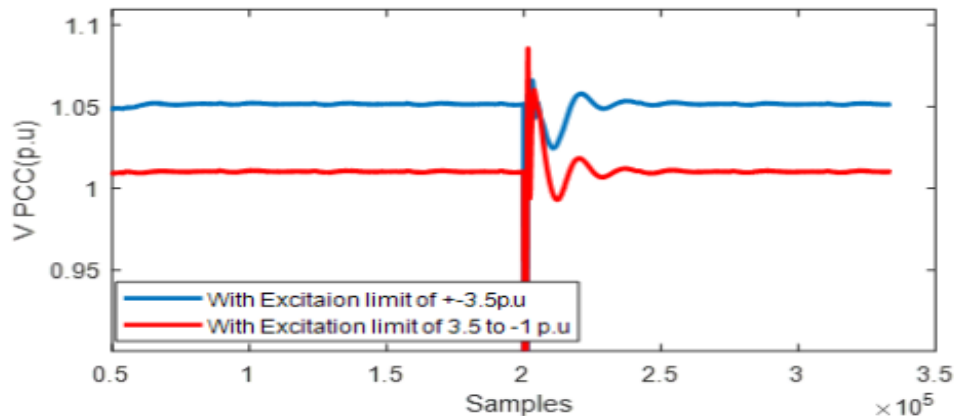


Figure 5.41: Effect of Lower Excitation Limit on PCC Voltage for Case5.

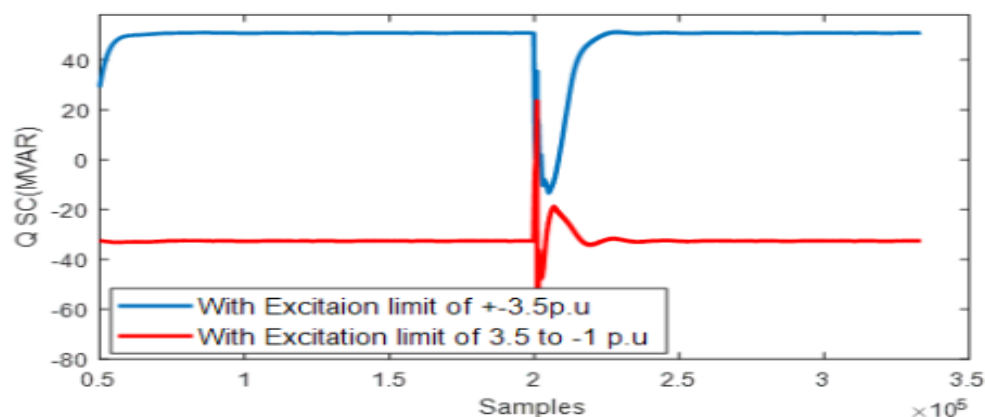


Figure 5.42: Reactive Power for Case5 with Different Excitation Limit.

Figure 5.42. This is due to the reverse polarity operation of synchronous condenser with the increase in lower excitation limit. This causes the field excitation voltage to hit the limit and makes the condenser push reactive power leading to a rise in PCC voltage. But as the condenser rating increases, a lower excitation of -3.5 provides excellent voltage regulation capability. This is clearly depicted in Figure 5.43.

For higher rated condenser, excitation limit as low as -3.5 absorbs around 52MVARs of reactive power maintaining the PCC voltage to desired level. This proves the need to derive an optimal lower excitation limit considering the grid strength and condenser rating. This proves the importance of optimal excitation limit for synchronous condenser.

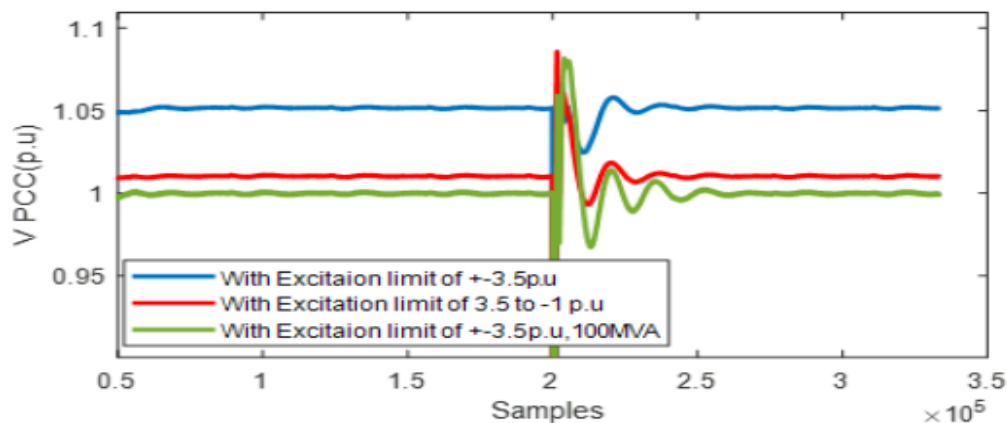


Figure 5.43: Effect of Lower Excitation Limit and Condenser Rating on PCC Voltage for Case5.

5.5.5.2 Impact of Transient Reactance on System Stability and Oscillation

The impact of transient reactance on oscillation frequency can be clearly seen from Table 5.7. As grid goes weaker lower the transient reactance improves stability as discussed in Table 5.4 and Table 5.5. Lower reactance results in lower oscillation. This indicates that synchronous condensers with lower transient reactance would be ideal for a grid with SCR below 1.83.

The effect of transient reactance change in stability has been analyzed with a 30% increase and a decrease in reactance. As the transient reactance reduces the voltage rise after fault is maximum and so is the reactive power support offered by SC during a fault. But as the grid goes weaker, analysis of a marginal case shows that, with an increase in transient reactance, the fault current and the reactive power support during fault reduces. This reduces the PCC voltage which in turn triggers the reverse operation of SC. These effects are visible from the PCC voltage and reactive power support showcased in Figure 5.44 and Figure 5.45 respectively for a marginal grid strength scenario. As grid goes weaker, lower reactance will improve the overall stability as discussed in Figure 5.46.

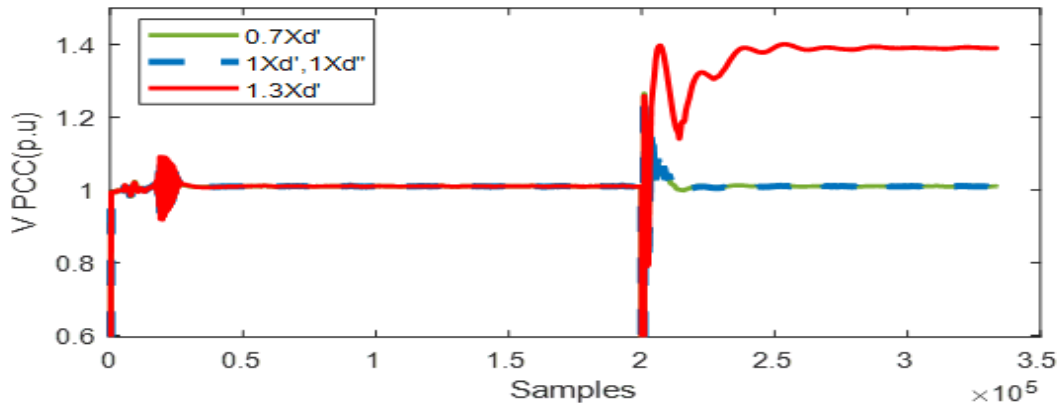


Figure 5.44: Effect of Transient Reactance on Stability for Marginal Grid Strength Scenario

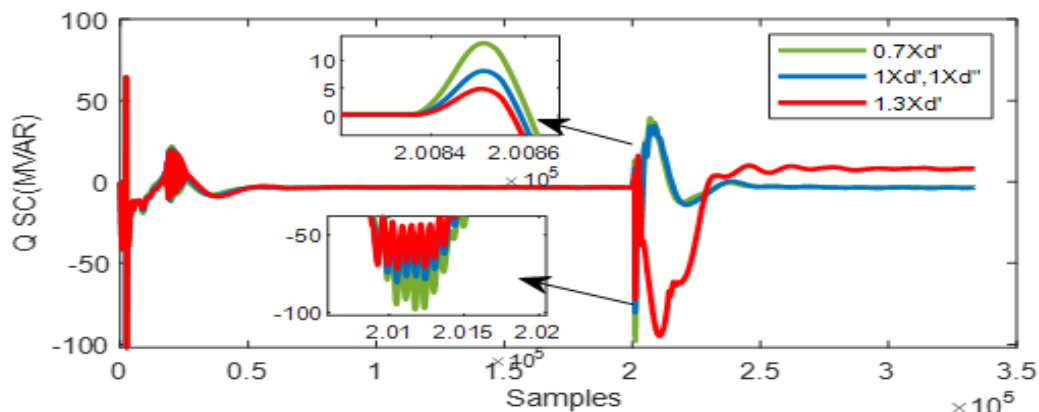


Figure 5.45: Reactive Power Support from SC during Different Transient Reactance for Marginal Grid Strength Scenario

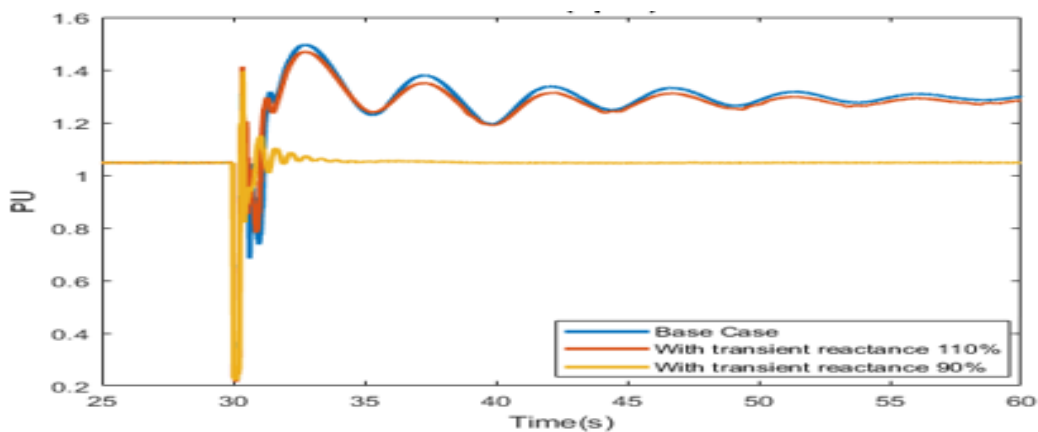


Figure 5.46: Effect of Transient Reactance on PCC Voltage for a Weak Grid Scenario

Table 5.7: Analysis of Transient Reactance Effect on Low Frequency Oscillation for a 50MVA SC

Transient reactance (X'_d)	Oscillation Frequency(Hz)
$0.37X'_d$	1.20
$0.8X'_d$	4
X'_d	4
$1.5X'_d$	4.76

5.5.5.3 Impact of SC inertia on system stability

The impact of SC inertia on overall system stability is discussed in this section. The test case is performed for a range of inertia varying from 3s to 8s for different grid strength. Figure 5.47 shows the improvement in grid strength during three phase to ground fault with higher inertial constant. This showcases the importance of SC over other compensation techniques due to this additional feature for improving system inertia, thereby improving the overall frequency stability and Rocof.

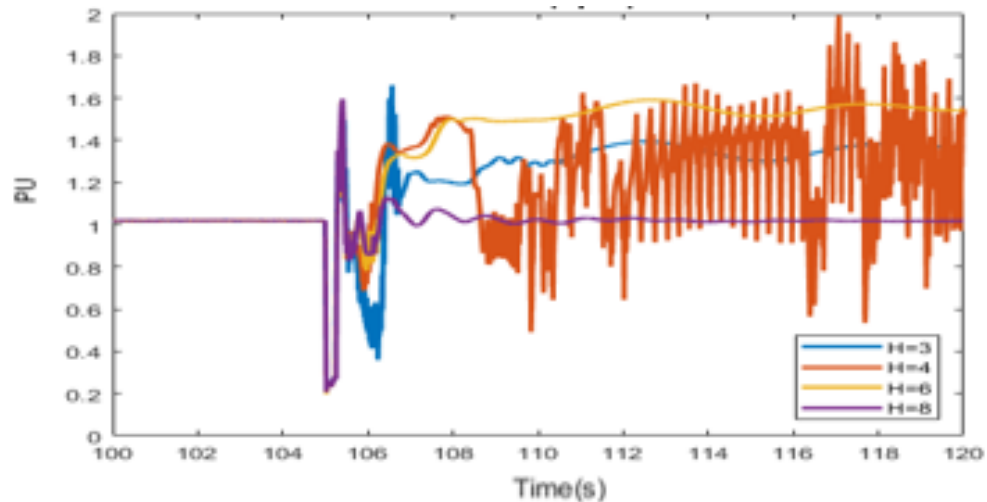


Figure 5.47: PCC Voltage Variations with Different Inertial Constant for Case10.

5.5.6 Performance Comparison of Different Compensation Techniques

In this section the performance of synchronous condenser with static exciter is compared with another conventional SC with IEEE T2 exciter and static var compensators

(SVC). The rating of compensation techniques compared is 340 MVA. The SVC is comprised of a 80MVARs Thyristor Controlled Reactor(TCR) and three 110MVARs Thyristor Switched Capacitors (TSC). As the grid strength drops and grid becomes sensitive, a harmonic filter is also included in the SVC model. The filter removes the odd harmonics that can arise due to the thyristor switching.

5.5.6.1 Performance comparison of different compensation techniques for a weak grid

The performance of Siemens SC is compared with SVC and another conventional SC. The two condensers used for analysis differ in their parameters and excitation system used. The performance is compared for a weak grid scenario with $SCR \leq 1.41$. The results are showcased in Figure 5.48 and Figure 5.49.

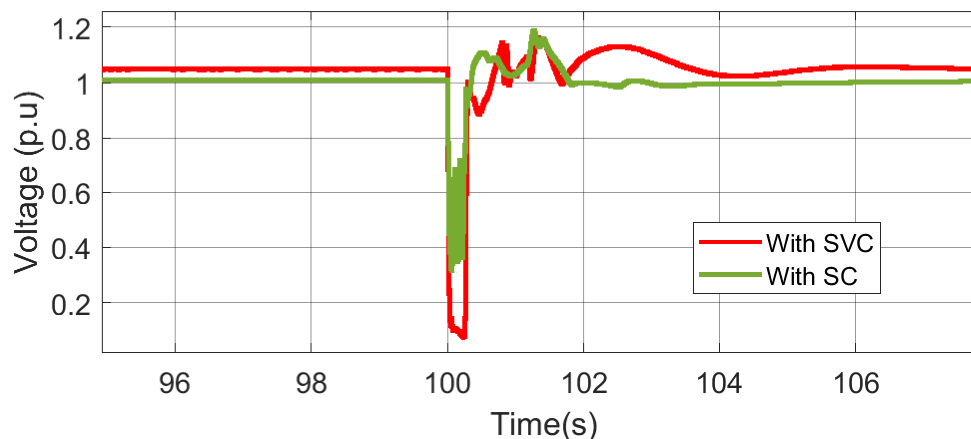


Figure 5.48: PCC Voltage during Fault in a Weak Grid Scenario

The results in Figure 5.49 shows that the reactive power support offered by the SC during fault is superior compared to SVC. This is because the reactive support offered by SVC is proportional to the square of the terminal voltage. Hence during fault as the terminal voltage drops to very low value, the reactive power support from SVC is lower compared to SC.

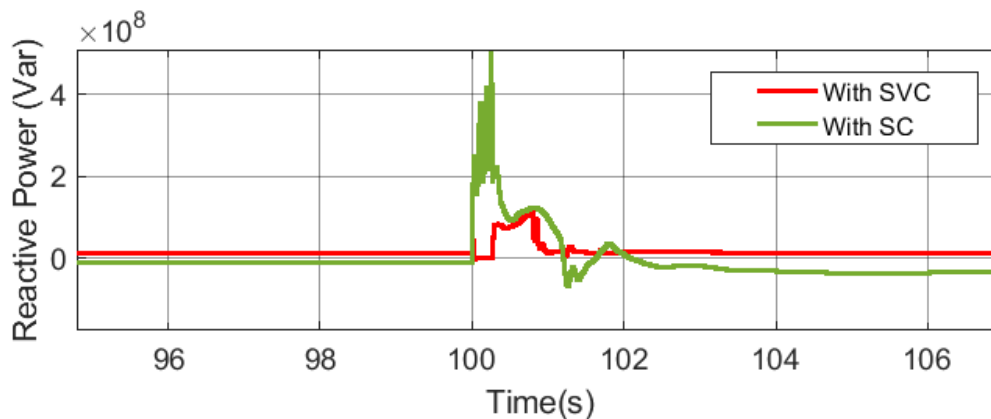


Figure 5.49: Reactive Power Support during Fault in a Weak Grid Scenario

5.5.6.2 Performance Comparison of Different Compensation Techniques for a Weak Grid for Different Fault Types

As discussed in previous section, since the reactive power support offered by SVC depends on the magnitude of terminal voltage, it is really important to analyze the performance during different fault types. A comparison of PCC voltage and fault current for a weak grid scenario during different fault conditions (Single phase, two phase to ground and three phase fault) are analyzed in this section.

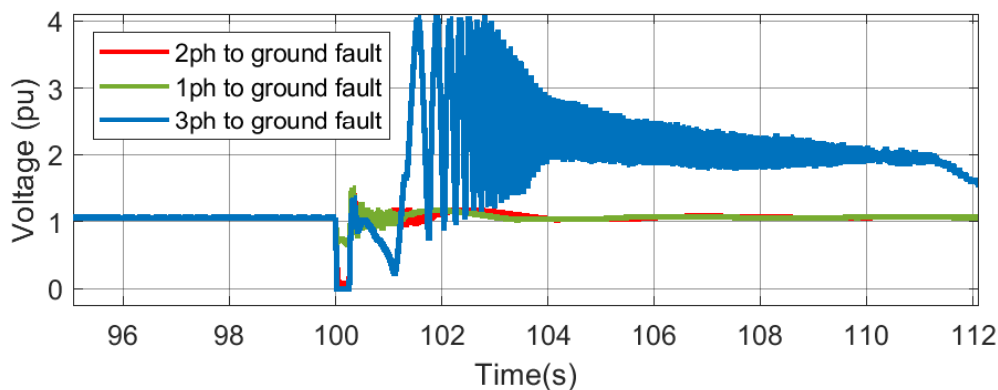


Figure 5.50: Comparison of PCC Voltage with SVC for Different Fault Types in a Weak Grid Scenario

Figure 5.50 shows that with SVC as the intensity of fault increases, the more is the drop in the PCC voltage. This can further drop as grid strength declines. Hence a

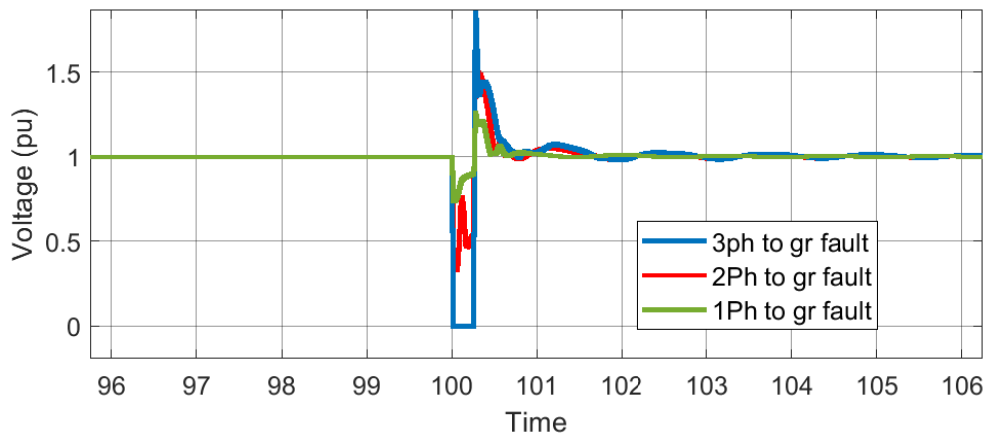


Figure 5.51: Comparison of PCC Voltage with SC for Different Fault Types in a Weak Grid Scenario

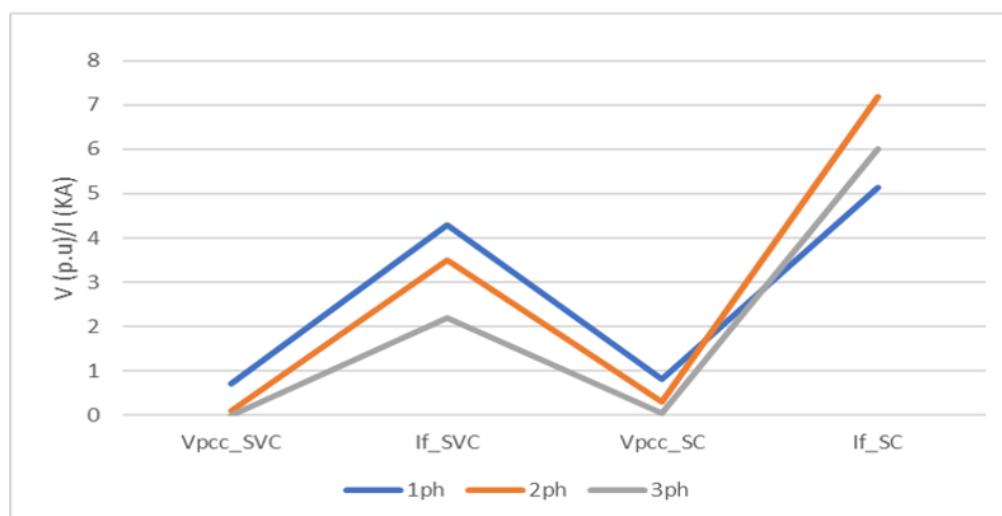


Figure 5.52: Comparison of Minimum PCC Voltage and Fault Current for SVC with SC.

comparison of PCC voltage in Figure 5.51 and Figure 5.50 shows the superior nature of condenser in maintaining the overall stability during weak grid scenario even during the most severe three phase to ground fault. A similar increasing trend is observed in fault current contribution from SVC. But for SC the fault current contribution for two phase fault is more compared to three phase. Based on the above analysis, the performance of SVC is ideal for a single phase to ground fault. Hence a comparison of SVC with SC for single phase to ground fault is presented below in Figure 5.53.

The result showcases the ability of condenser to settle back faster to the nominal voltage following the event. This can be accounted due to the superior and faster control offered by static excitation control of SC. The corresponding reactive power support offered is compared in Figure 5.54.

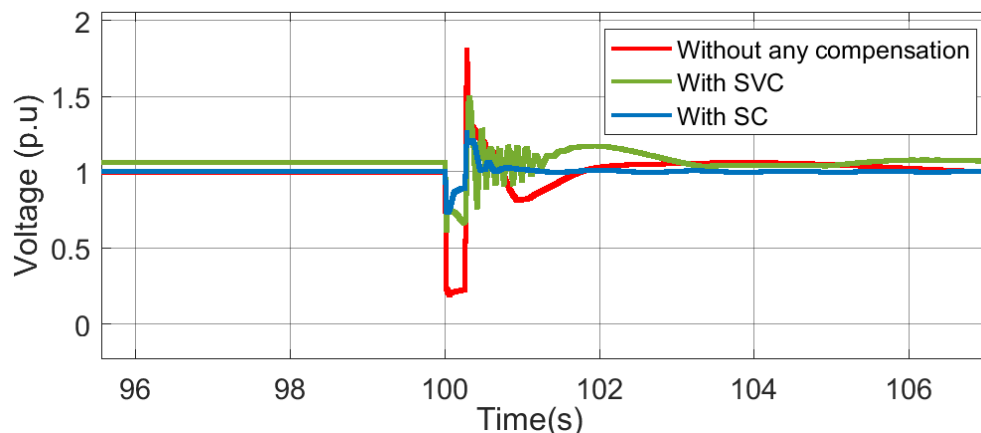


Figure 5.53: Comparison of PCC Voltage during Single Phase to Ground Fault.

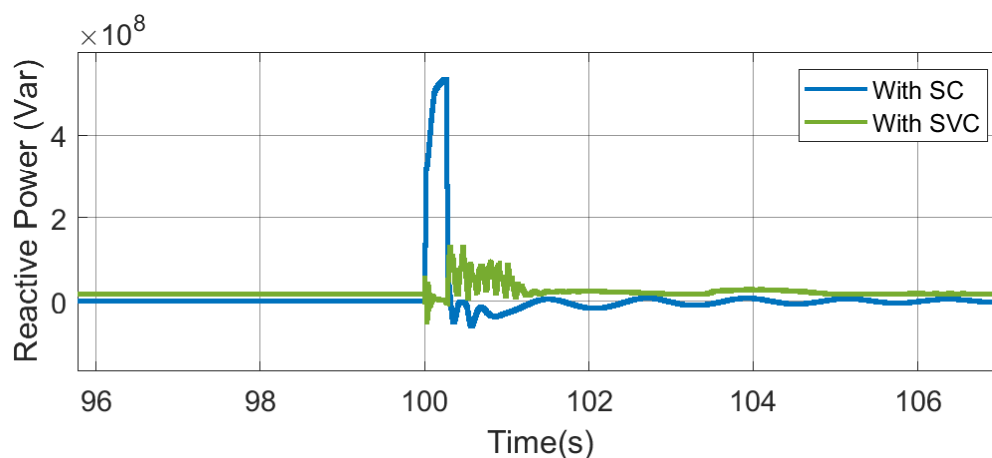


Figure 5.54: Comparison of Reactive Power Offered during Single Phase to Ground Fault.

5.5.6.3 Performance Comparison of Different Compensation Techniques for a Weak Grid for different Grid Frequency Dynamics

The presence of low and sub synchronous oscillations in a weak grid scenario has been discussed by many researchers. The work in [110] identifies the co-existence of

low frequency and subsynchronous oscillation in weak grid and the impact of PLL bandwidth that decides the dominant modes. The idea of lowering the PLL bandwidth as the grid strength declines to improve the overall stability has been discussed. The impact of PLL bandwidth on stability with and without synchronous condenser has been discussed in our earlier work [95]. A comparison of different compensation techniques with grid dynamics due to PLL is studied in this section. Figure 5.55 and Figure 5.56 shows the PCC voltage and reactive power support offered by weak grid condition with 9Hz bandwidth. The results shows that the system goes unstable without any device, which demands lowering the PLL bandwidth to improve stability. The addition of reactive compensation with SC can improve the overall stability but cannot be maintained with SC at PCC. This show st sensitiveness of SVC to grid dynamics due to PLL. The comparison presented here shows that superior performance can be assured from SC compared to SVC. The analysis presented in Section 5.5.6

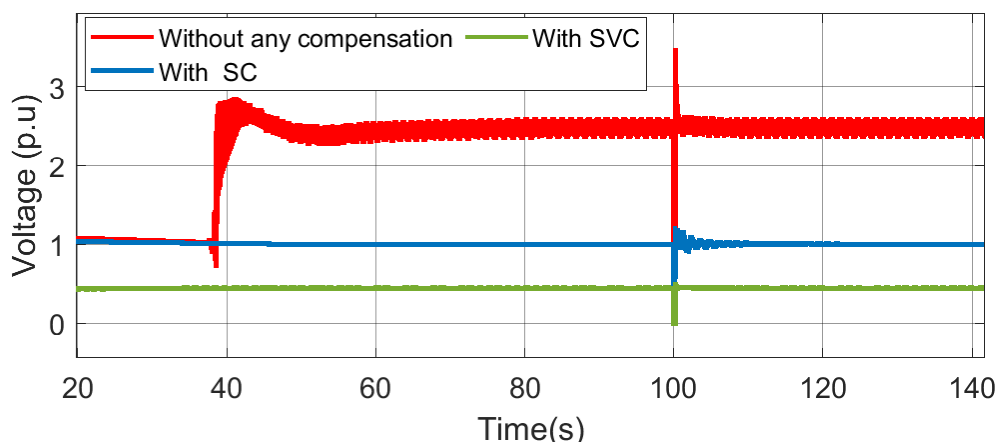


Figure 5.55: Comparison of PCC Voltage during Single Phase to Ground Fault.

shows that SC offers superior compensation behavior and improves the overall stability over a wider range as the grid strength declines and grid dynamic conditions due to fault and PLL changes. These results combined with the additional advantages offered by SC involving rotational inertia, short circuit current capability etc makes SC a better choice over power electronics based solutions in the current grid with

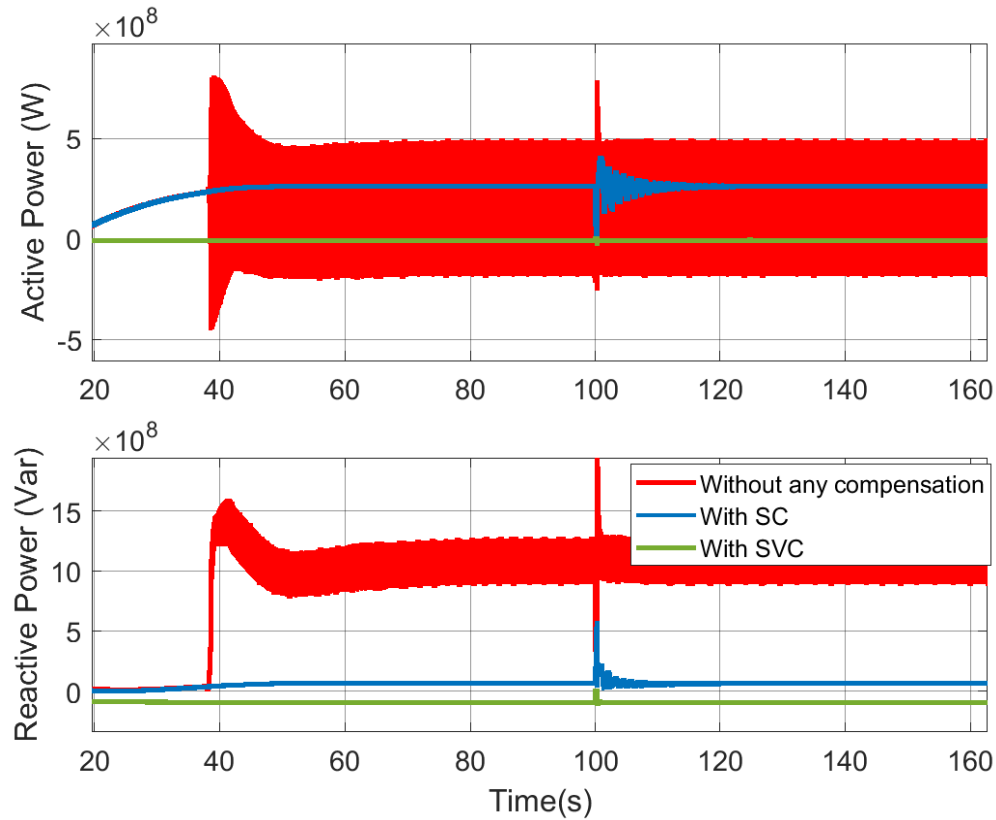


Figure 5.56: Comparison of Reactive Power Offered during Single Phase to Ground Fault.

highly penetrated renewable resources.

5.6 Future Works

Based on the study presented in this paper, the influence of the PLL parameters and synchronous condenser parameters on improving the stability with reduction in grid strength is very well show cased. Dynamically modifying these parameters can be one possible solution approach for these weak grid issues. The proposed overview of the control architecture of SC integrated wind farms on a weak grid is shown in Figure 5.57.

The proposed controller includes,

Excitation Limit Control: The study presented in the previous section clearly depicts the need for ideal field excitation limit for the synchronous condenser. During

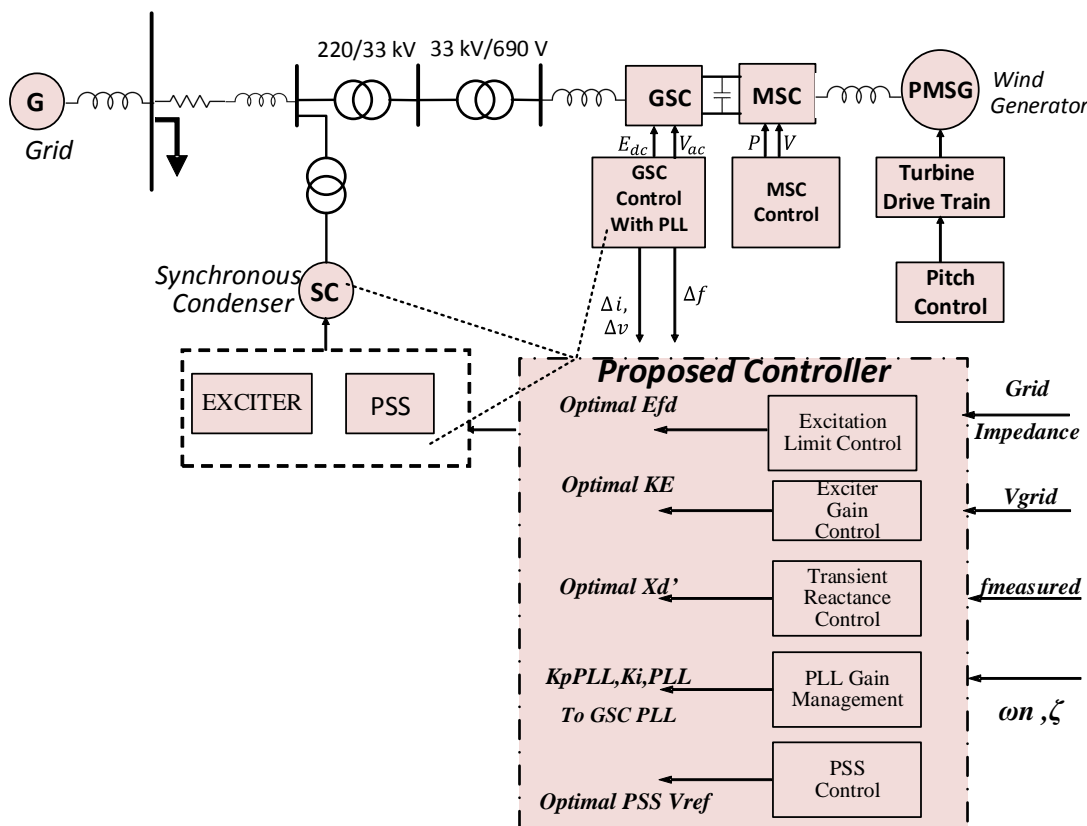


Figure 5.57: Proposed Control Architecture for Improving Stability as Grid Strength Reduces.

reactive power absorption, with negative excitation the chances of reverse polarity operation of synchronous condenser is a challenging issue to be taken care. Hence the proposed control aims a suggesting a optimal excitation limit based on the grid impedance and PCC voltage which defines the reactive power requirement from the condenser.

Exciter Gain and Transient reactance Control: The effect of exciter gain and transient reactance on improving the low frequency oscillations noticed in weak grid is analysed in the previous sections. This suggests the need for ideal value for gain as well as transient reactance for the machine. The proposed controller aims at deriving an optimal value for mitigating the low frequency oscillations thereby improving the overall stability of the system.

PLL Gain Management based on the Grid Impedance: Based on the test results discussed in previous sections, reducing the PLL gains or reducing the PLL bandwidth has improved the stability. For example, for an SCR of 3, PLL bandwidth of 31Hz could give stable system. But as the SCR reduces to 1.84, PLL bandwidth has to be further reduced to 1Hz. But reducing bandwidth is a trade off for settling time or phase noise. Hence finding an optimal PLL bandwidth that offers stability and at the same time should ensure that the phase noise is within the limit is one the design challenge attempted in this proposal. The proposed system should be able to identify the optimal maximum bandwidth at any particular grid impedance without affecting the system stability.

PSS Input Control: The controller aims at deriving an optimal control input voltage to PSS that damps the oscillations that arises as the grid strength decreases. A detailed analysis of the effect of grid impedance on oscillation frequency and the effect on PSS will be done in future. Based on the study results, a proper control logic will be derived to identify the input voltage to PSS that damps the oscillations to improve overall stability of wind on the weak grid.

5.7 Chapter Summary

This paper presents a detailed analysis of issues related to wind on weak grid during high power transfer. The effect of GSC converter side PLL and synchronous condenser as dynamic reactive power compensator is studied. Different test scenarios are performed to analyse the effect of condenser parameters on stability and reducing oscillation frequencies. The need for optimal excitation limit for condenser to prevent it from reverse polarity operation is discussed. Based on the study a possible control architecture is proposed to optimally define the lower excitation limit for the condenser and input to the PSS that will mitigate these issues due to weak grid.

CHAPTER 6: A COORDINATED OPTIMAL FEEDBACK CONTROL FOR MITIGATION OF MOTOR STARTING VOLTAGE SAGS IN DER INTEGRATED DISTRIBUTION NETWORKS

This chapter proposes a coordinated optimal feedback control approach to mitigate the induction motor (IM) starting voltage sag and support the transient restoration in distribution networks. The proposed technique is expected to reduce the starting high current to maintain the network voltage using neighboring voltage supporting distributed generation (VSDG). An optimal feedback based coordinated controller has been designed to estimate the reactive power to be injected at different locations of the network based on the motor loads. The coordinated controller on top of the existing local controller uses motor voltage feedback signals thereby adjusting the reactive power support based on the voltage sag.

6.1 Introduction

The high inrush of current during Direct-On-Line(DOL) starting of induction motor, short circuit faults, interconnection of heavy loads etc. are the common causes of voltage dip. etc[111]. Voltage sags affect the power quality badly resulting in voltage flickers or disconnection of frequency dependent loads. The performance of the supply system has been bench-marked by many utilities. IEEE defines voltage dip as the reduction of rms voltage between 0.1 pu and 0.9 pu for a duration of 0.5 cycle to 1 minute[66]. The characteristics of these voltage sag changes with the operating conditions. In industrialized countries about 60% of generated electrical energy is consumed for running IM in domestic appliances, driving pumps, fans, compressors, elevators and industrial machinery of various types [111, 67]. In industrial sector the

voltage sag caused by DOL starting of IM can cause severe loss in production due to unadvertised tripping of switch gear. The following section discusses the issues due to voltage sags and the need for proper voltage sag mitigation techniques in distribution networks.

6.1.1 State-of-the-Art

During the starting of induction motor the initial high current persists as long as the motor reaches the synchronous speed. As the starting torque is a function of starting voltage, a sudden dip in this voltage fails to accelerate the motor to rated full speed. This can create an impact on the local as well as remote loads connected to the network. Motor starting voltage dip is lower in magnitude [111] and longer in duration compared to fault induced voltage sag. The sag duration is usually more than 30 cycles [112] when a large sized motor with high inertia load is connected to a weak power system. Such long duration sags can lead to a wide range of sensitive equipment to drop out [113]. The motor starting voltage sag problem is more severe in rural areas where voltage profile is always very low and most of the agricultural pumps are driven by IM [114]. Besides IMs are the most extensive electrical power application in industrialized countries as they are frequently switched-on into the supply system which may arise voltage flicker because of frequent or sporadic motor starting [115]. Frequent switching incidents of IM and longer recovery time increase the cost of mitigation and cost of damage of sensitive equipment.

The proposed voltage sag mitigation strategy is tested in both 12.4kV network and 123 bus larger distribution networks containing single and multiple motor and DG units. From simulation results, it is revealed that the proposed coordinated optimal feedback control of VSDGs can provide a fast restoration of the motor starting transient voltage dip.

6.1.2 Major Contributions

In this chapter, a coordinated optimal feedback control methodology for VSDGs to overcome the dips at the motor terminal and provide voltage support during motor starting has been proposed. The proposed control determines the level of reactive power support required from VSDGs to the network based on intensity of the voltage dip. The main contribution (or the novelty) of this paper is that the proposed architecture uses a measurement based multiple input multiple output (MIMO) identification framework for the control. The main advantages of this architecture are:

- The coordinated control approach uses a measurement based identification that provides an optimal framework.
- The changes are captured using a Multi-Input-Multi-Output (MIMO) identification which provides simultaneous identification thus ensuring the coupling effect of system voltage and frequency.
- The architecture provides a smooth transition of multiple DG control, and also provide optimal reactive power support from each DG.
- The coordinated control architecture seamlessly interfaces with local controller.
- The algorithm is very efficient (reduction in voltage change by up to 10%) even with locational changes in the IM.

6.2 Proposed Control Architecture

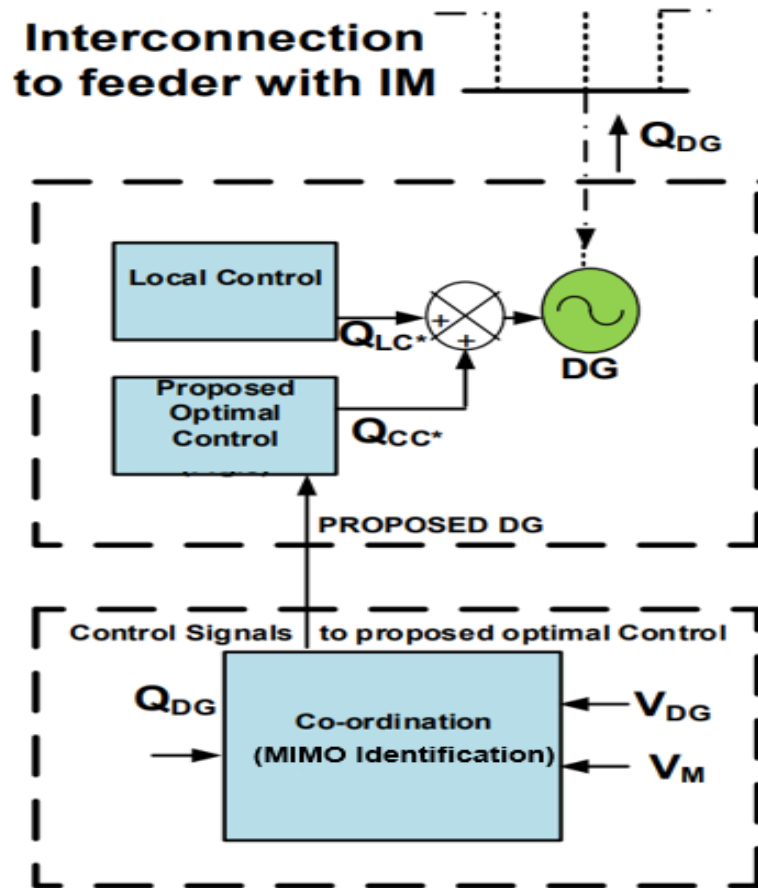


Figure 6.1: Proposed Overall Coordinated Control Architecture

The objective of this paper is to design an optimal coordinated controller to improve voltage sag. Figure 6.1 shows the proposed coordinated control approach for multiple DGs supporting reactive power. The architecture includes a local controller, proposed optimal feedback controller which coordinates among multiple DGs and IMs connected to the system. Figure 6.2 shows the proposed optimal controller that relies on system information represented using state matrices. System parameters are identified using motor point of common coupling (PCC) voltage as input and reactive power output of DG as output. Coordinated approach demands the need for multiple input multiple output identification technique. The identified state ma-

trices along with input and output is given to state estimator that makes sure that all states of the system can be observed. Linear quadratic regulator tries to derive a optimal feedback control input to the system based on a quadratic minimization function. Theoretical framework of the proposed architecture is explained in detail in the following subsections.

6.2.1 MIMO Identification for Coordinated control

Robust subspace identification algorithm is used to identify the system behavior for multiple input multiple output system. This algorithm is a solution for combined deterministic-stochastic identification problems. Controllable modes of deterministic system can be either stable or unstable while controllable modes are assumed stable for stochastic system. Robust combined algorithm is explained in detail [116].

The combined subspace identification algorithms compute state space models from given input-output data. The combined identification problem can be represented by an unknown combined system of order n given by,

$$\begin{aligned}x_{k+1} &= Ax_k + Bu_k \\y_k &= Cx_k + Du_k\end{aligned}\tag{6.1}$$

where x_k , u_k and y_k represent the states, input and output of the system. A , B , C , D are the state matrices. The goal is to determine the order n of the unknown system and system matrices A , B , C , D up to within a similarity transformation and the covariance matrices Q , S and R so that the second order statistics of the output of the stochastic subsystem and of the stochastic part of the given output are equal. B and D matrices are determined through minimization of prediction error which lead to an increase in the computational complexity. The algorithm is implemented based on QR decomposition. The algorithm depends not only on R factor but also on the original data.

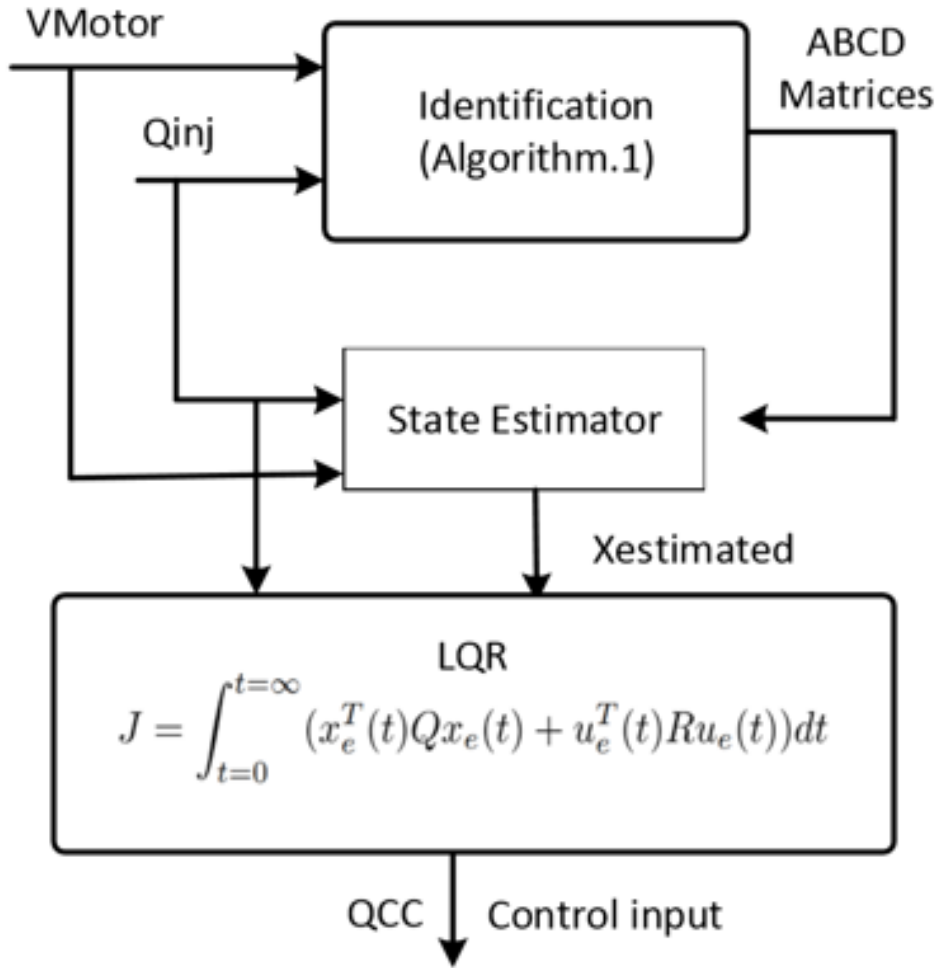


Figure 6.2: Proposed Control Architecture

Subspace identification problems are based on geometric concepts. These geometric operations can be easily represented using a QR decomposition. Orthogonal projection involves projecting the row space of a matrix on to the row space of another matrix. Oblique projection involves non orthogonal projection of a matrix as a linear combination of two non orthogonal matrices. With Y_f as the future output and W_p as the block Hankel matrix containing past inputs and outputs, the oblique projection o_i is calculated as,

$$o_i = Y_f/W_p \quad (6.2)$$

While the orthogonal projections are computed based on future output and Hankel

matrices by,

$$Z_i = Y_f / \begin{pmatrix} W_p \\ U_f \end{pmatrix} \quad (6.3)$$

where z_i is the projected matrix which can be computed from given data without knowing system matrices, Y_f is the future output and W_p is the past input and output data.

$$Z_{i+1} = Y_f - / \begin{pmatrix} W_{p+} \\ U_{f-} \end{pmatrix} \quad (6.4)$$

where U_{f-} is matrix defined by shifting the border between past and future one block row down from U_f , W_{p+} is the block Hankel matrix defined by adding the one block row around the border between past inputs and future outputs. This algorithm calculates the singular value decomposition of the geometric projections and partition those to unitary matrix and singular values as,

$$o_i \pi_{U_f} = US(V^T) \quad (6.5)$$

where U and V are the left and right singular vectors and S is the singular value. π_{U_f} is the geometric operator that projects the row space of matrix U_f on to the orthogonal component of the row space of matrix U_f . The extended observability matrix can be calculated as,

$$\Gamma_i = U_1 S_1^{1/2} \quad (6.6)$$

$$\Gamma_{i-1} = \underline{\Gamma}_i \quad (6.7)$$

where Γ_i represents the extended observability matrix. Γ_{i-1} is obtained by stripping the last l rows of the extended observability matrix, Γ_i and $\underline{\Gamma}_i$ represents the extended observability matrix without the last l rows. State matrices A and C are calculated

using

$$\frac{\Gamma_{i-1}^\dagger Z_{i+1}}{Y_{i|i}} = \frac{A}{C} \Gamma_{i-1}^\dagger Z_i + \mathcal{K}U_f + \frac{\rho_w}{\rho_v} \quad (6.8)$$

where $Y_{i|i}$ is the block Hankel matrix with only one row of outputs, Γ_{i-1}^\dagger represents the Moore-Penrose pseudo inverse of matrix Γ_{i-1} . while B and D matrices are determined through minimization of prediction error and are given by,

$$B, D = \arg \min_{B, D} \left\| \begin{pmatrix} \Gamma_{i-1} Z_{i+1} \\ Y_{i|i} \end{pmatrix} - \begin{pmatrix} A \\ C \end{pmatrix} \Gamma_i Z_i - \mathcal{K}(B, D)U_f \right\|_F^2 \quad (6.9)$$

where $\mathcal{K}(B, D)$ represents the linear matrix function. This linear nature of $\mathcal{K}(B, D)$ makes the overall optimization function convex resulting in unique minimum. Covariance matrix can be calculated as,

$$\begin{pmatrix} Q & S \\ S^T & R \end{pmatrix} = E_j \left[\begin{pmatrix} \rho_w \\ \rho_v \end{pmatrix} \cdot \begin{pmatrix} \rho_w^T & \rho_v^T \end{pmatrix} \right] \quad (6.10)$$

An overview of the combined robust deterministic stochastic identification algorithm is shown below.

Algorithm 2 Robust Deterministic Stochastic MIMO Identification Algorithm

- 1: Calculate the oblique and orthogonal projections.
 - 2: Calculate the SVD of weighted oblique function.
 - 3: Determine the order by inspecting the singular values in S and partition the SVD accordingly to obtain U_1 and S_1
 - 4: Determine Γ_i and Γ_{i-1} .
 - 5: Solve for linear equations for A and C.
 - 6: Recompute Γ_i and Γ_{i-1} from A and C.
 - 7: Solve for B and D.
 - 8: Finally determine the covariance matrices Q,S,R.
-

6.2.2 Linear Quadratic Regulator

LQR is a state feedback based optimal controller. It uses linear system model in the form of state space equations and quadratic objective function relating the states

function given by,

$$J = \lim_{T \rightarrow \infty} \frac{1}{T} \int_0^T (x^T Q x + u^T R u) dt \quad (6.12)$$

where Q and R are the co variance matrices. Q and R are usually diagonal matrices and should be positive definite. Proper choice of Q and R matrices defines the optimal control generation. The optimal control input is calculated by solving Ricatti equation given by,

$$A^T P_c + P_c A + Q - P_c R^{-1} B^T P_c = 0 \quad (6.13)$$

subject to the condition A and B are stabilizable. The optimal control input is given by,

$$u = -Kx \quad (6.14)$$

where u is the optimal control input, x is the estimated state and K is the linear quadratic gain given by,

$$K = R^{-1} B^T P_c \quad (6.15)$$

where P_c is the unique solution of Ricatti equation.

6.2.2.2 Kalman Filter Design

The optimal control input in equation 6.14 requires state of the system. A kalman filter is used as an estimator to estimate the states of the system. Kalman filter estimates the states based on the measured output [120]. Th predictor step for state

vector is given by,

$$\dot{x} = A\hat{x} + Bu \quad (6.16)$$

The covariance P is given by,

$$P = APA^T + Q \quad (6.17)$$

where P is the covariance of the state vector estimate and Q is the process noise covariance. L is the kalman gain that minimizes the objective function. It is given by,

$$L = PC^T(CPC^T + R)^{-1} \quad (6.18)$$

where C is the observation matrix and R is the measurement noise covariance. The corrector step is given by,

$$\dot{x} = A\hat{x} + Bu + L(y - C\hat{x}) \quad (6.19)$$

$$P = P - LCP \quad (6.20)$$

6.3 Proposed Coordinated Control Approach

DGs are operated in Q mode during motor starting to the maximum DG kVA capacity. For steady state voltage support, DG can be operated in P-Q mode at the optimum P and Q ratio. The control action can be implemented by a Proportional Integral (PI) controller as discussed in [114].

6.3.1 Design of DG Local Controller (LC)

In this approach, the reference values for P and Q are determined proportional to the variation of PCC voltage from its reference. The decision of generating P and Q can be made based on the level of voltage sag measuring at the instant of the motor starting and can be updated at every instant of time. The control mechanism designed with PI controller is shown in Figure 6.4.

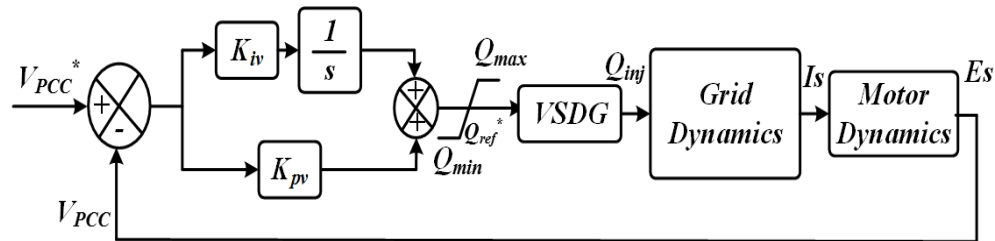


Figure 6.4: Local Controller of DG

While designing the PI control for the system, the network is assumed to be balanced and is represented by a set of algebraic equations. The major assumption made here is by regulating the starting current drawn by the motor; the terminal voltage sag can be regulated as well. The terminal voltage of the motor is considered as the output voltage used as the feedback for the controller design. Once this loop is completed, the PI gains were tuned to achieve a desired response following a voltage. The control action using local controller will be more challenging when a DG is trying to support voltage sag due to multiple motors connected near it. The number of DG and motor loads can vary dynamically in real life scenario. This emphasizes the need for a coordination among the control strategy to define the optimal reactive power support from each of the DGs to better improve the recovery characteristics of motor starting voltage dip.

6.3.2 Design of Coordinated Controller (CC)

The coordinated control for a system with multiple DGs and multiple motors can be achieved using Linear Quadratic Gaussian (LQG) control [120, 114]. This optimal

control aims to define an output feedback law by minimizing a quadratic cost function. LQG is a combination of Linear quadratic estimator (kalman) in association with a Linear quadratic regulator(LQR). In this approach, the states of the system is estimated based on the system output and input by the estimator, which is then utilized in the optimal control law ($u = -K.x_e$) defined by minimization of cost function for control of the overall system. In this paper, considering reactive power injection of DGs as the system input and the voltage deviation at the motor connected nodes as system output, the online system transfer function is identified using MIMO identification techniques. The derived system parameters are then used by LQR to update the control law . Figure 6.5 represents the implementation approach for proposed coordinated control approach for VSDG.

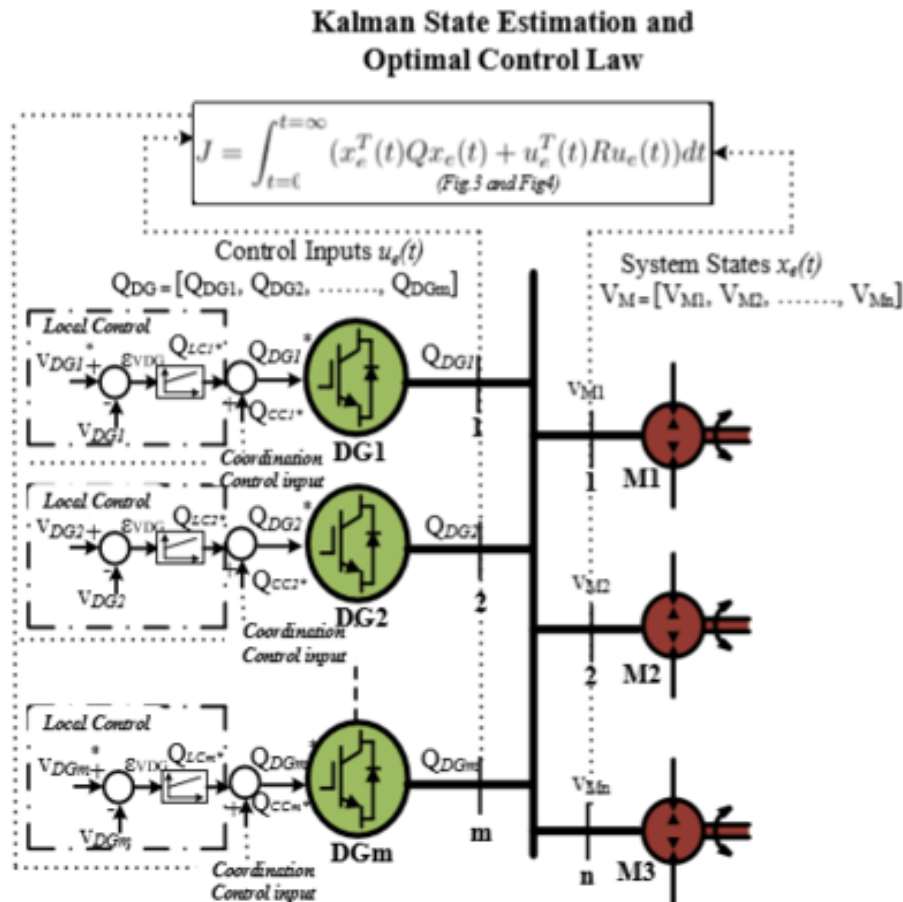


Figure 6.5: Proposed Coordinated Control Approach for VSDG

In Figure 6.5, based on the system states (terminal voltages of motor PCC) and system input (reactive power injected), the objective function associated with optimal control law is minimized. When the optimal control law is minimized, the net reactive power that is required to be produced by various DGs to mitigate the voltage sag is estimated. Once the net reactive power is obtained, the reactive power reference is to be divided to the various DGs available. This has been achieved using various droop gains K_1, K_2, \dots, K_m . The droop gains for multiple DGs case are optimized based on their capacity and their proximity on the feeder with respect to the motor.

6.4 Implementation of Proposed Coordinated Controller

The main goal of the paper is to utilize VSDG for mitigating motor starting transient voltage dip as opposed to currently available voltage regulating equipment, e.g. voltage regulator, tap changer etc. Implementation of the proposed architecture is shown in Figure 6.6.

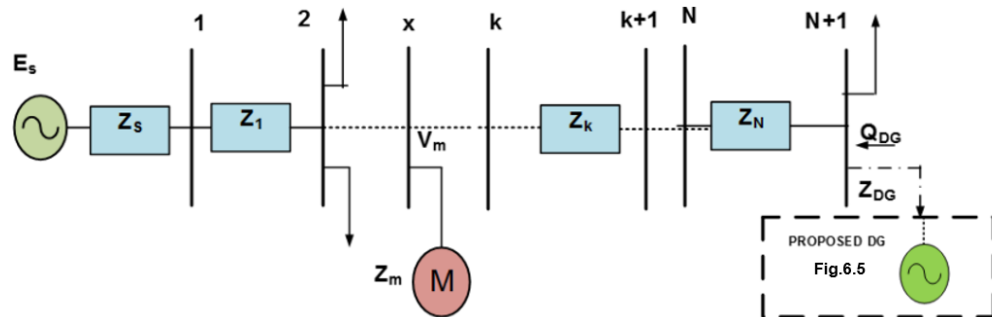


Figure 6.6: One Line Diagram of Test System with Proposed Architecture

Power distribution network shown in Figure 6.6 has N buses where the IM is connected at the bus x . Expressions of voltage dips at motor terminal can be derived as,

$$\Delta V_m = V_{std} - \frac{E_s}{1 + \frac{(Z_{xN} + Z_m)}{(Z_{xN} Z_m)}} \quad (6.21)$$

where E_s represents the grid voltage. Z_{xN} is the impedance of line between the IM at bus x and N buses of the system. Z_m is the starting impedance of the motor given by [111],

$$Z_m(t) = (R_e + \frac{R_2}{S(t)}) + j(X_e + X_2) \quad (6.22)$$

where $S(t)$ is the starting slip of the IM, R_e and X_e are the equivalent impedance on stator side, X_m is the magnetising reactance between stator and rotor, R_2 and X_2 are the rotor side impedance. To investigate the effect of VSDG on starting voltage dip, a DG is connected at the $N+1$ bus. The equations of voltage dip at the motor terminal derived using the superposition theorem is given by,

$$\Delta V_m = V_{std} - \frac{Z_m E_s (Z_{xN} + Z_{DG}) + E_{DG} (Z_s + Z_{1x})}{(Z_m (Z_s + Z_{1x}) + (Z_s + Z_{1x} + Z_m) (Z_{xN} + Z_{DG}))} \quad (6.23)$$

The IM starting transient power can be calculated from starting voltage and starting current as,

$$S_m = P_m + jQ_m = 3V_m I_m \quad (6.24)$$

where P_m is the motor starting power and Q_m is the motor starting reactive power. The identification process will analyse the system parameters based on variation of this motor terminal voltage with the reactive power injected by the DG. The reactive power output of DG is given by,

$$Q_{inv} = v_d i_q + v_q i_d \quad (6.25)$$

where v_q is zero when the reference frame is oriented along the stator voltage position.

The voltage along d axis is given by,

$$v_{di} = Ri_d + L \frac{di_d}{dt} - \omega_e Li_q + v_d \quad (6.26)$$

where v_d is the d axis grid voltage and v_{di} is the d axis output voltage of DG, i_d and i_q are the d and q axis current output of DG.

6.5 Simulation Results

In this section the effect of proposed controller of VSDG on motor starting voltage dips has been discussed. Test 1, 2 and 3 are performance tests to analyze the efficiency of the proposed controller. One-line diagram of test feeder with motors and VSDGs used for Test 1 is shown in Figure 6.7. The following tests results discussed in this section is based on offline identification of multiple input multiple output system.

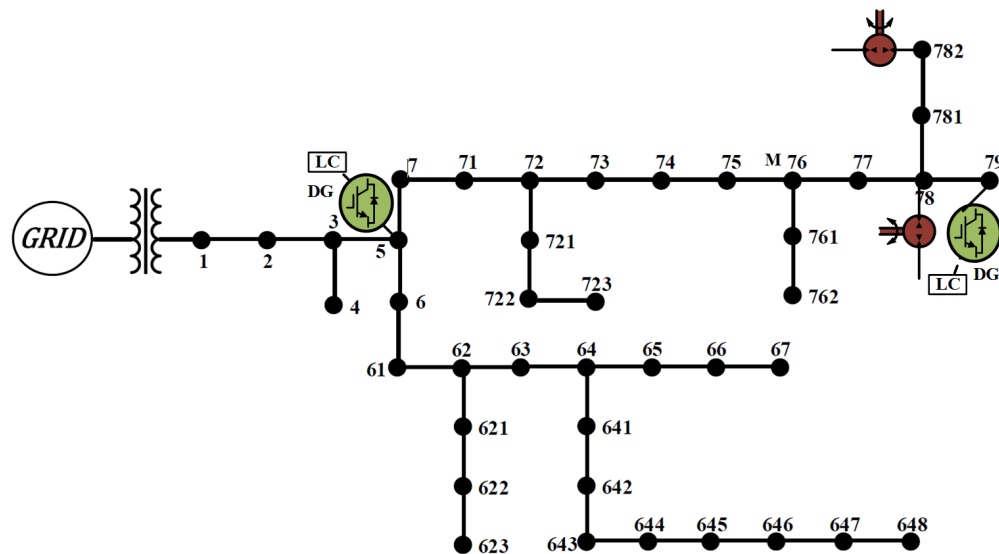


Figure 6.7: Test 1-Test 3: One Line Diagram of System used for Performance Test

6.5.1 Test 1: Performance Analysis with One Motor Two DG

For the test case 1, DGs are connected at bus 79 and bus 5. For Test.1.a an induction motor is connected to bus 78 close to DG at bus 79. Test.1.b is conducted with induction motor connected to bus 7 close to DG at bus 5. The objective of this test is

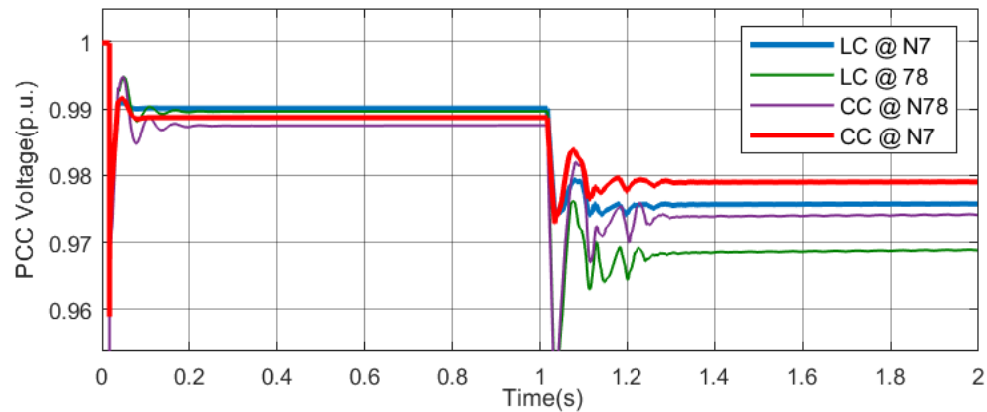


Figure 6.8: Test 1: VPCC for One motor Two VSDG with Local controller(LC)

to compare and understand the coordination among the DGs as the location of motor changes. Figure 6.8 shows the voltage restoration and recovery characteristics of the motor PCC voltage at node 78 and node 7 with both DGs coordinated to provide reactive power support. The improvement in voltage dip with Local Controller(LC) and Coordinated Controller(CC) has been compared and is shown in Table 6.1. It can be observed that with the proposed voltage support technique the voltage sag and recovery following the DOL starting of IM has been improved. Figure 6.9 and Figure 6.10 shows the reactive power support offered by both DGs with local control and coordinated control. For test.1.a where motor is close to DG at bus 79, there is a 9% increase in reactive power support offered by DG at bus 79 compared to DG at bus 5 as a results of coordination. Similarly for test.1.b where motor is close to DG at bus 5, there is a 12.45% increase in reactive power support offered by DG at bus 5 compared to DG at bus 79 as a results of coordination. The optimal gain derived as a results of minimisation of the objective function is shown in Figure 6.11. The rate of change of gain for DG at bus 5 is higher for Test.1.b while is it higher for DG at 79 for Test.1.a. This clearly depicts the effect of coordination among DGs as the location of motor changes.

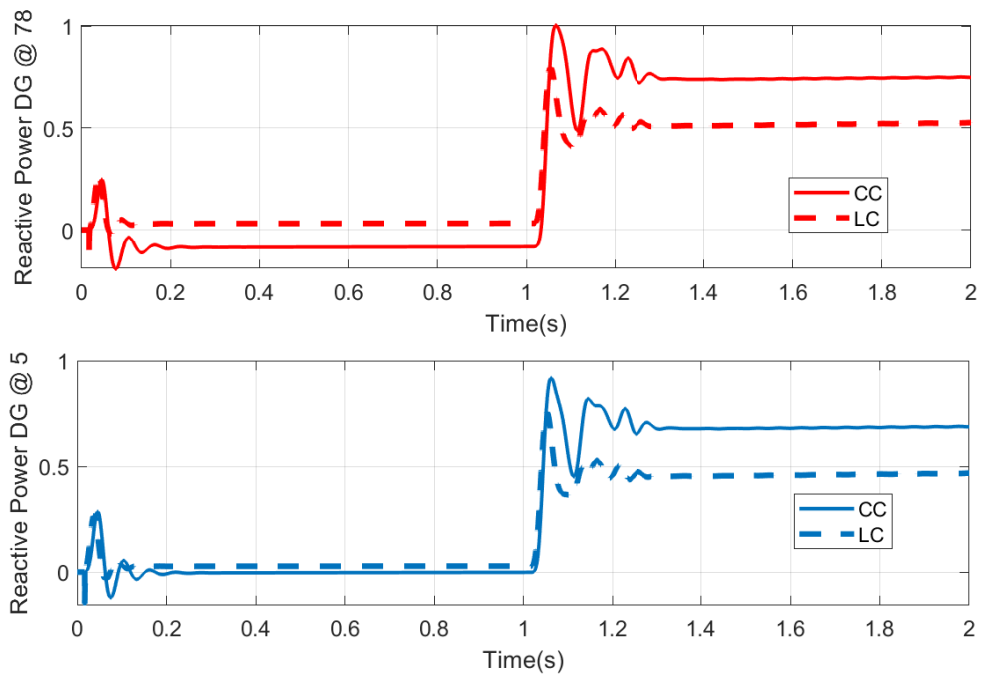


Figure 6.9: Test.1.a: Reactive Power Support for Motor at Bus 78

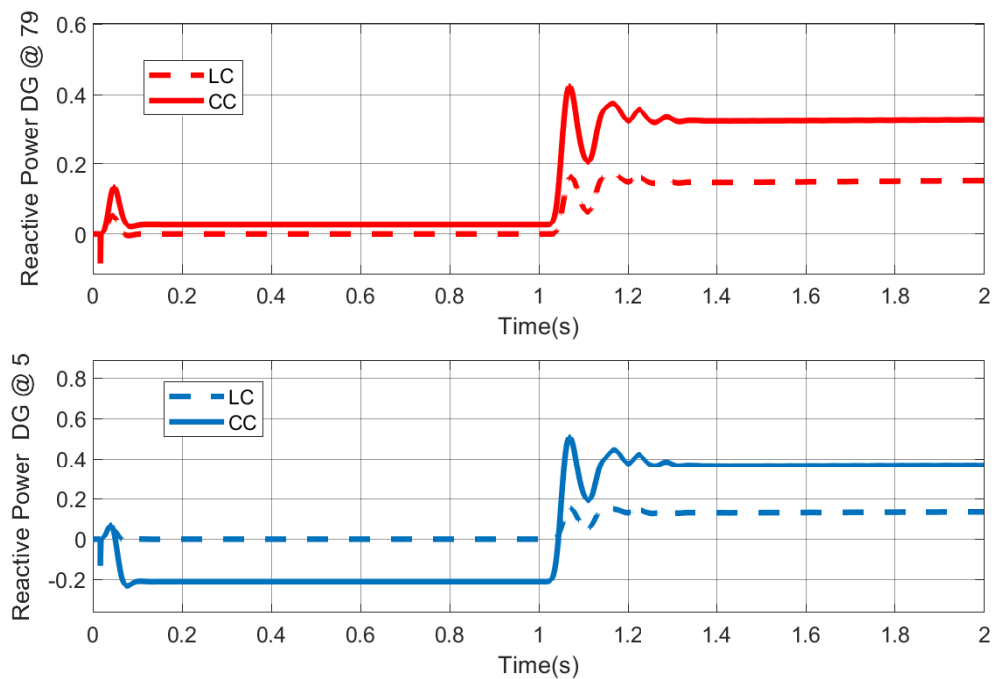


Figure 6.10: Test.1.b: Reactive Power Support for Motor at Bus 7

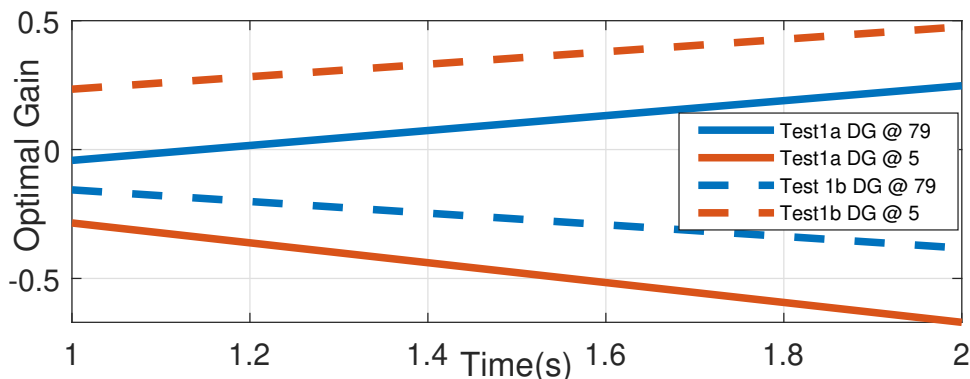


Figure 6.11: Test 1: Optimal Gain for DGs as the Cost Function is Minimised

Table 6.1: Performance Analysis of Test1 Result with Proposed VSDG

Control	Steady State Voltage	%SteadyState Improvement
Test.1.a:No VSDG	0.9468p.u	
Test..1a:LC	0.9688p.u	2.32 % w.r.t No VSDG
Test.1.a:CC	0.9741p.u	2.88 % w.r.t No VSDG
Test.1.b:No VSDG	0.9734p.u	
Test.1.b:LC	0.9757p.u	0.236 % w.r.t No VSDG
Test.1.b:CC	0.979p.u	0.575 % w.r.t No VSDG

6.5.2 Test 2: Performance Analysis with Two Motor Two DG with Motor Close to DG at Bus 79

In this test, induction motor is located at node 76 and node 782 and DG at node 79 and node 5. Motor is close to DG at node 79. Both the DGs coordinate together to improve the PCC voltage at motor terminals.

Figure 6.12 and Figure 6.13 shows the improvement in motor PCC voltage with proposed VSDG. Figure 6.13 and Figure 6.14 shows the coordinated reactive power injected by DG at node 5 and node 79 based on minimisation of objective function given by optimal control law. Table 6.2 shows the performance analysis of proposed control approach based on test2. The percentage contribution of DG at bus 79 has increased by 207% compared to DG at bus 5 due to the coordination effect.

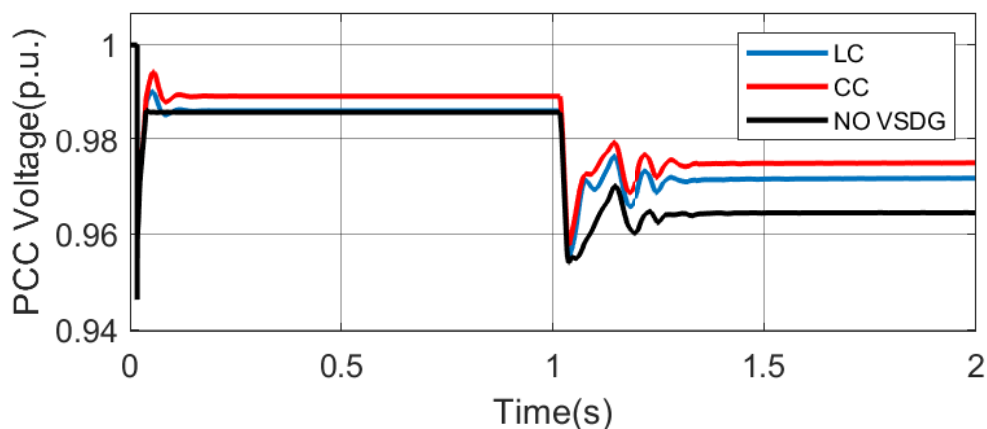


Figure 6.12: Test 2: PCC Voltage for Motor at Bus 76 for Local Control and Coordinated Control

Table 6.2: Performance Analysis of of Test 2 Result using the Proposed Control

Control	Steady State Voltage	%SS Improvement
Motor at Bus 782		
No VSDG	0.9559p.u	
With LC	0.9646p.u	0.9 % w.r.t NoVSDG
With CC	0.9688p.u	1.34 % w.r.t No VSDG
Motor at Bus 76		
No VSDG	0.9645p.u	
With LC	0.9716p.u	0.736 % w.r.t No VSDG
With CC	0.975p.u	1.08 % w.r.t No VSDG

The motor terminal voltage obtained above with the coordinated control input can be proved optimal by analysing the value of cost function. A test has been performed for different values of control input other than that given by coordinated controller. Figure 6.15 shows that cost function is optimal for the control input given by coordinated approach for Test2. The motor terminal voltage corresponding to this is 0.975p.u. for motor at Node 76 as shown in Figure 6.12. Figure 6.16 shows the interaction of local controller with coordinated controller. The local controller (LC) and coordinated controller (CC) continuously interact with each other and updates the

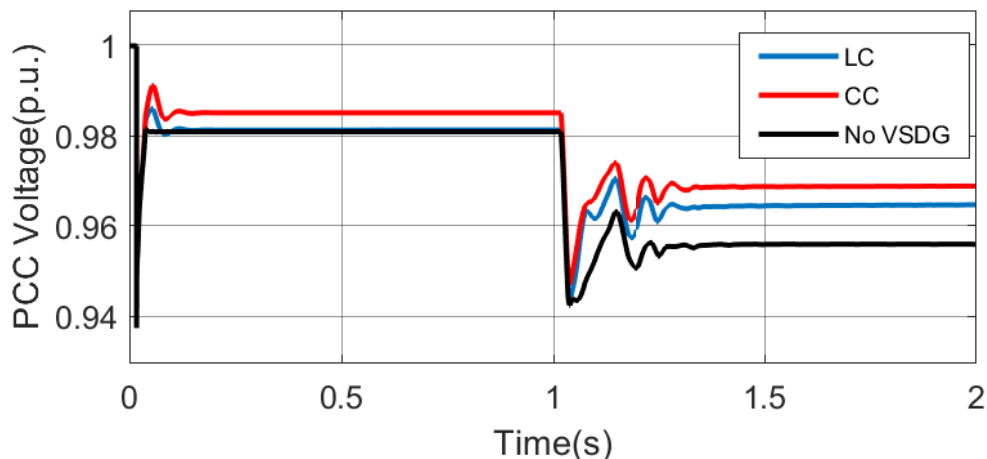


Figure 6.13: Test 2: PCC Voltage for Motor at Bus 782 with Local Control and Coordinated Control

inputs and outputs. The LC sets the PQ (Real Reactive Power) reference level based on voltage sag measuring at the instant of the motor starting. The CC communicates with all DGs and Motor connected buses and update the reference input based on minimization of optimization function. Figure 6.16 shows how the coordination effect changes the Q reference as the local controller contribution is varied manually. For the test case2 as the Qref from LC is increased, correspondingly there is a reduction in Qref from CC. This clearly depicts the coordination effect and interaction between two controllers. The results of test2 performance analysis has been tabulated in Table 6.2. The percentage performance improvement with proposed control is clearly compared without any VSDG case.

6.5.3 Test 3: Performance Analysis with Two Motor Two DG with Motor Close to DG at Bus 5

In this test, induction motor is located at node 6 and node 7 and DG at node 79 and node 5. Both the DGs coordinate together to improve the PCC voltage at motor terminals. Figure 6.17 and Figure 6.18 show the improvement in motor PCC voltage with proposed VSDG. Figure 6.19 shows the coordinated reactive power injected by DG at node 5 and node 79 based on minimization of objective function given by

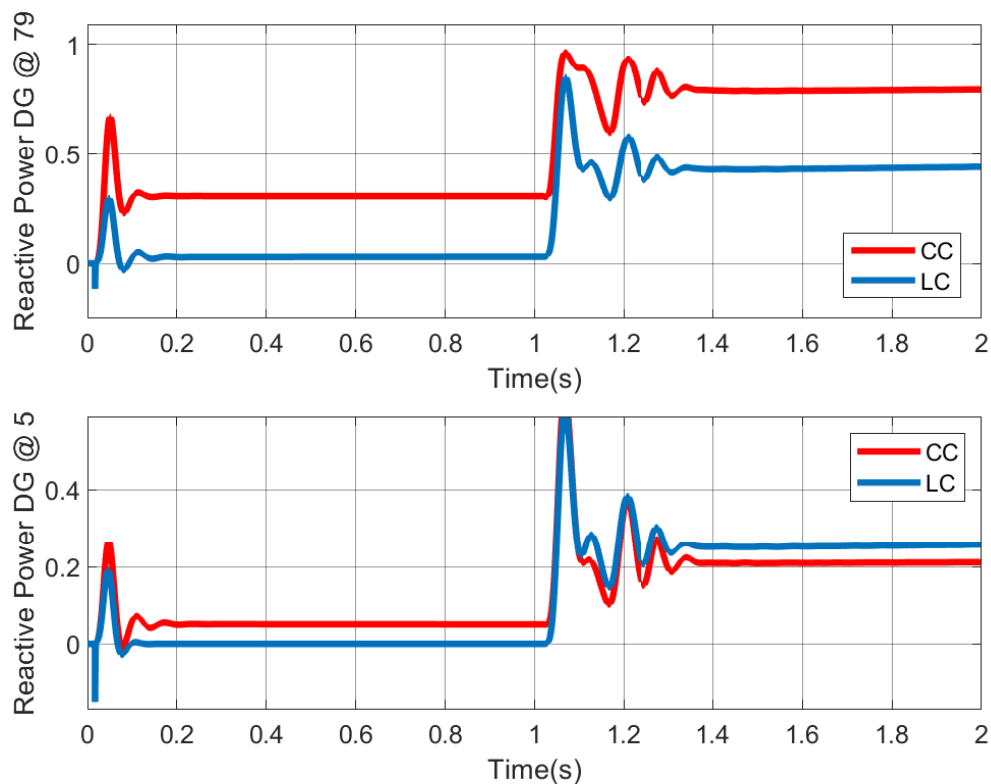


Figure 6.14: Test 2: Coordinated Reactive Power Support with DG at Bus 5 and Bus 79

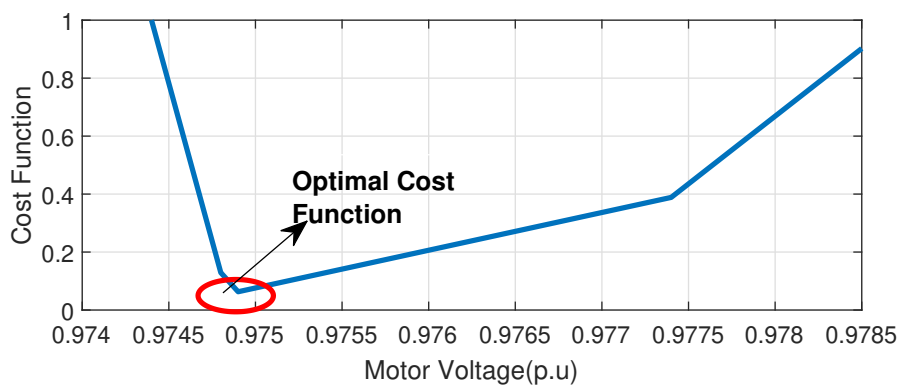


Figure 6.15: Test 2: Cost Function for Different Control Inputs

optimal control law. DG at bus 5 provided 55% more reactive power than DG at bus 79. The rate of change of optimal gain is higher for DG at bus 5 there by providing more percentage contribution from DG closer to the motor. Table 6.3 shows the performance analysis of proposed control approach based on Test 3.

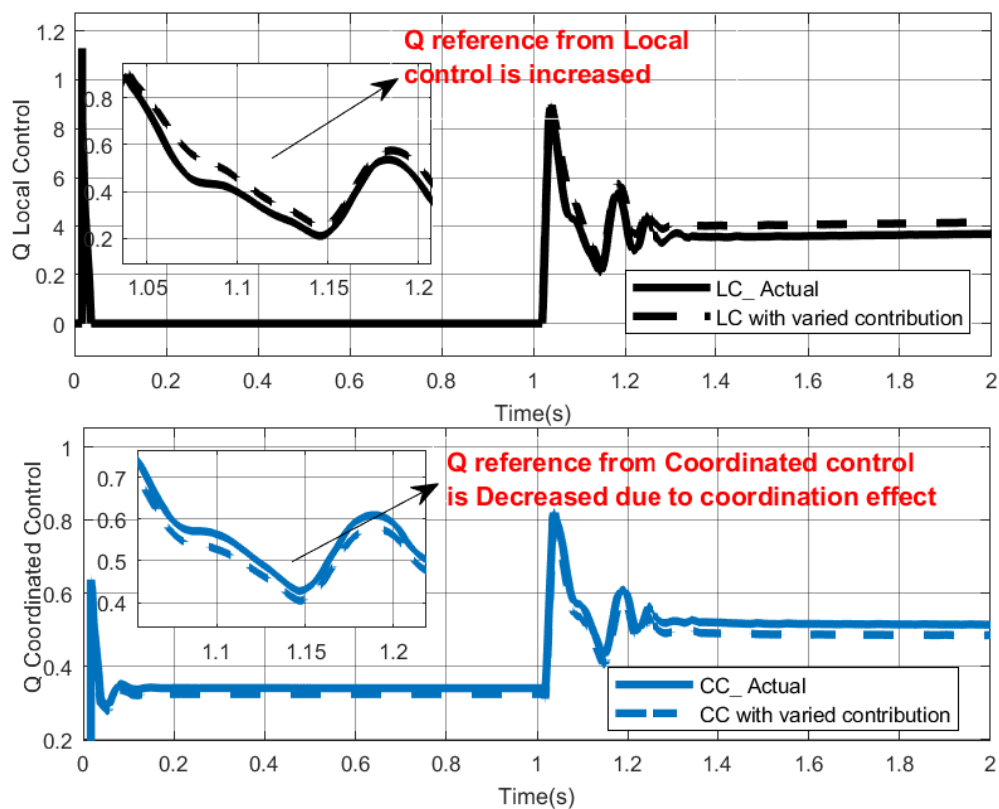


Figure 6.16: Test2: Interface between Local Controller and Coordinated Controller

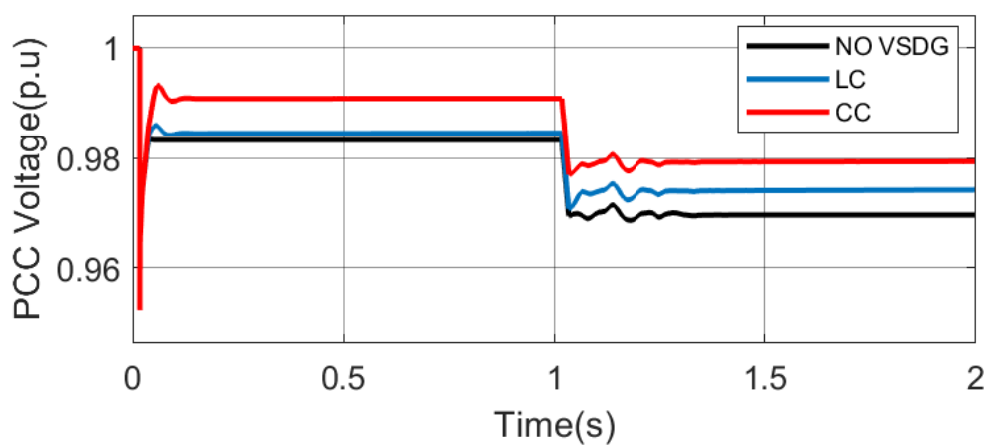


Figure 6.17: Test 3: VPCC for Motor at Bus 6 for Local Control and Coordinated Control

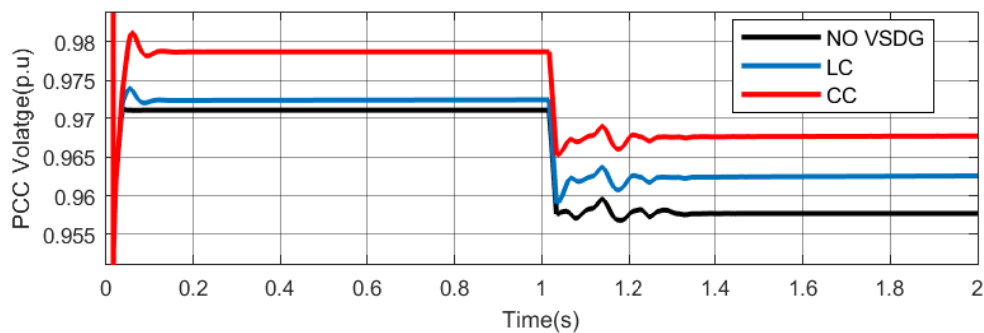


Figure 6.18: Test 3: VPCC for Motor at Bus 7 with Local Control and Coordinated Control

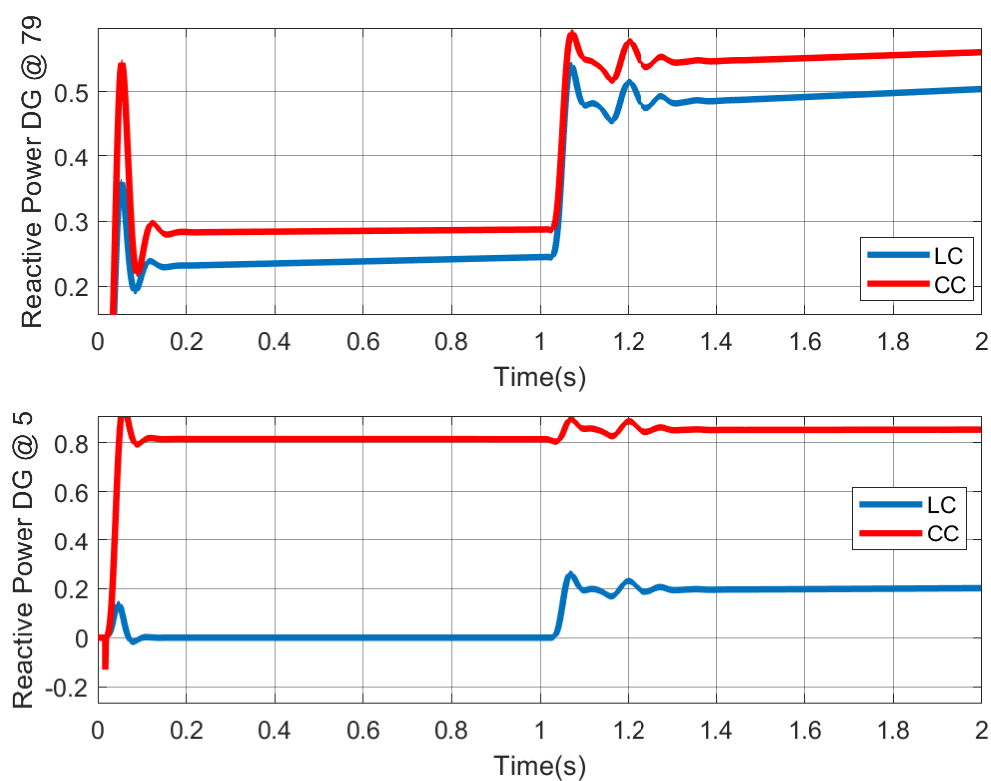


Figure 6.19: Test 3: Coordinated Reactive Power Support with DG at Bus 5 and Bus 79

6.5.4 Test 4: Scalability Test on 123 Bus Distribution System with Single and Multiple VSDG

The reliability of the proposed architecture is tested for scalability on a larger 123 bus system. Test 4 and Test 5 are conducted to analyze the scalability of the

Table 6.3: Performance Analysis of Test 3 Result with the Proposed VSDG

Control	Steady State Voltage	%SS Improvement
Motor at Bus 7		
No VSDG	0.9577p.u	
With LC	0.9625p.u	0.501 % w.r.t No VSDG
With CC	0.9677p.u	1.044 % w.r.t No VSDG
Motor at Bus 6		
No VSDG	0.9696p.u	
With LC	0.9741p.u	0.464 % w.r.t No VSDG
With CC	0.9793p.u	1.00 % w.r.t No VSDG

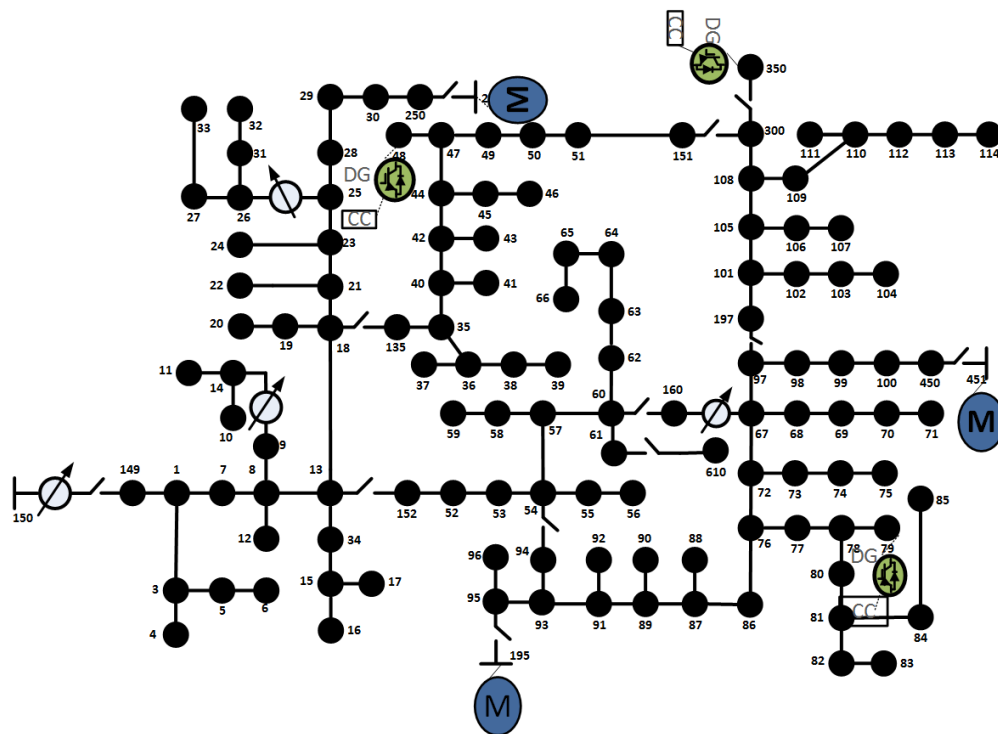


Figure 6.20: Test 4 and Test 5: One Line Diagram of 123 Bus System used for Scalability Test.

proposed architecture. One-line diagram of test feeder with a larger system (123 bus) as shown in Figure 6.20. A motor is connected to bus 451. The improvement in motor PCC voltage drop due to motor starting is analyzed with one VSDG connected to bus 350 and multiple VSDG at bus 350 and bus 48. Figure 6.21 shows that the

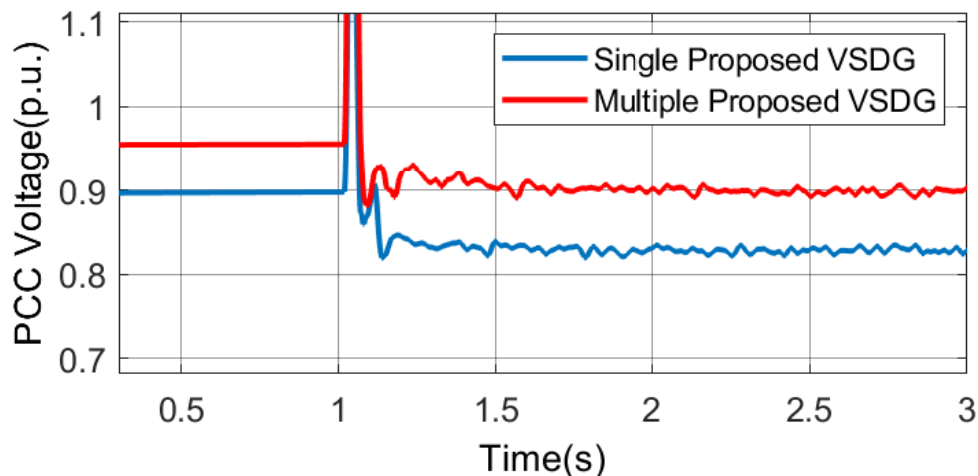


Figure 6.21: Test4: Comparison of VPCC for Motor at Node 451 with Single and Multiple VSDG

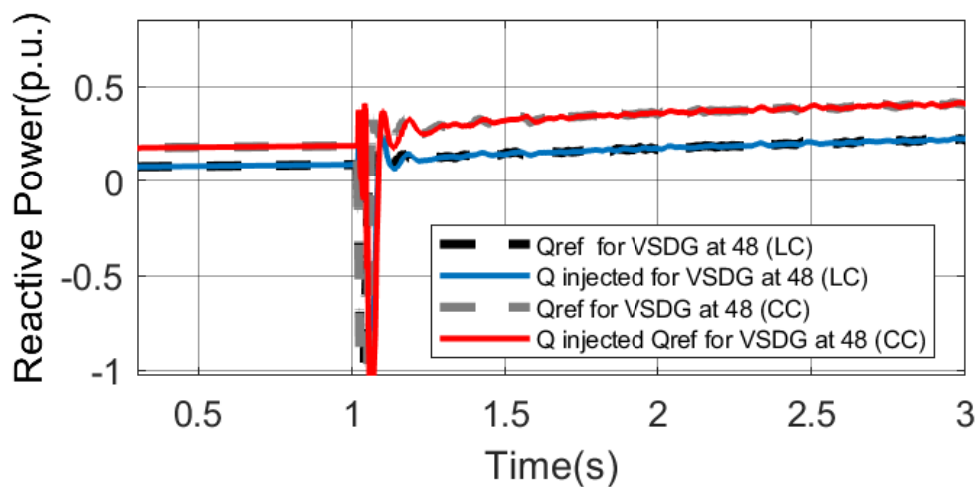


Figure 6.22: Test 4: Coordinated Reactive Power Support for DG at Node 48

PCC voltage has improved by 8.8% with multiple VSDG compared to single VSDG scenario. Figure 6.22 and Figure 6.23 shows the reactive power reference and reactive power injected by two VSDGs with local controller and proposed coordinated control. The increased reactive power injected with the coordinated control approach accounts for the improved PCC voltage.

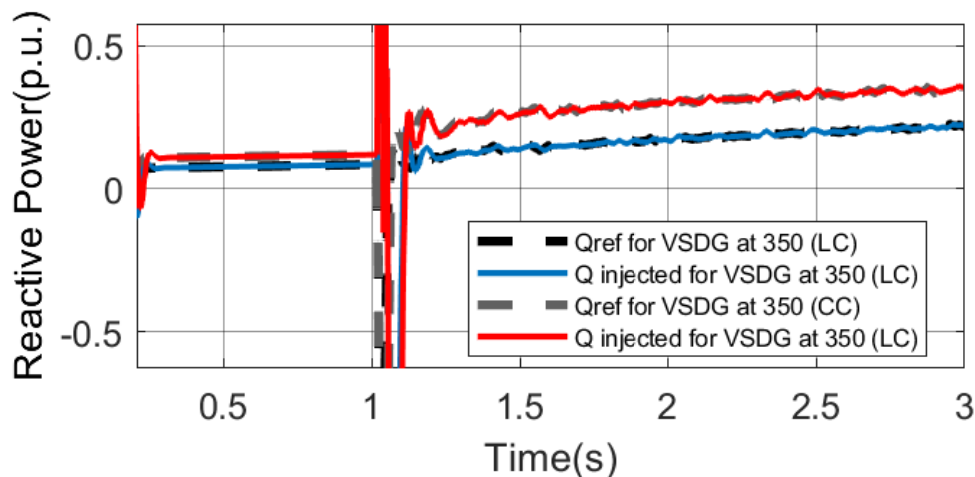


Figure 6.23: Test 4: Coordinated Reactive Power Support for DG at Node 350

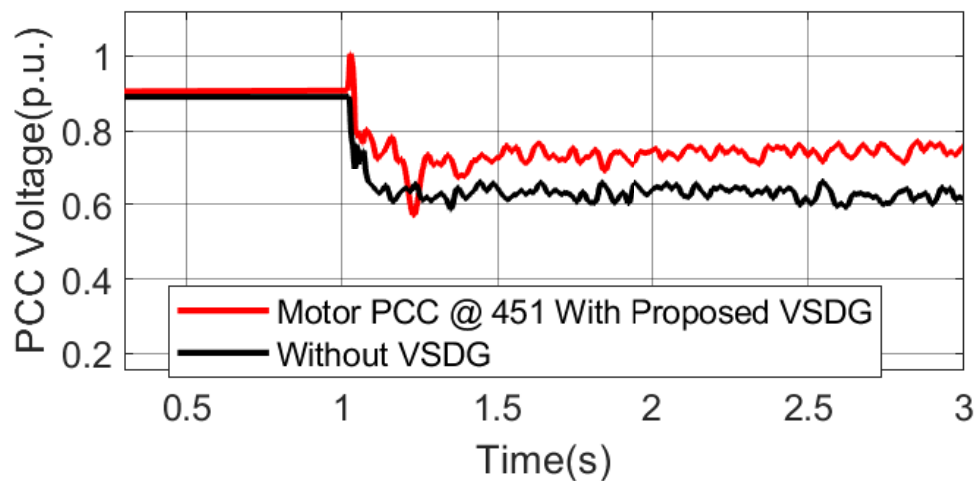


Figure 6.24: Test 5: VPCC for Motor at Node 451

6.5.5 Test 5: Scalability Test on 123 Bus Distribution System with Multiple VSDG and Motor

In this test case, the performance of proposed architecture is analyzed for multiple VSDG connected to bus 350, 48 and 79 and multiple motor connected to bus 451, 251 and 195 of the test bus. Figure 6.24, Figure 6.25, and Figure 6.26 show the improvement in motor PCC voltages with the proposed VSDG. The PCC voltage has increased by 17% for motor at bus 451, 20% for motor at bus 195 and 12.6% for motor at bus 251 with the proposed coordinated control compared to without any VSDG

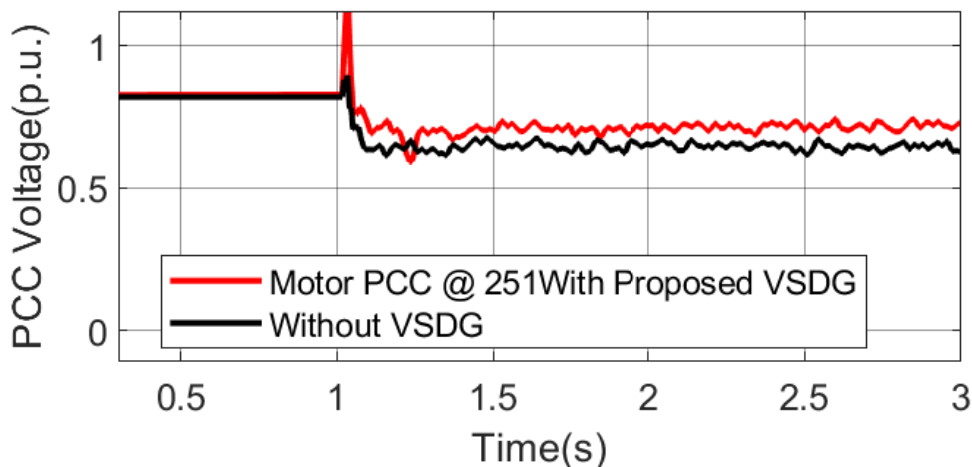


Figure 6.25: Test 5: VPCC for Motor at Node 251

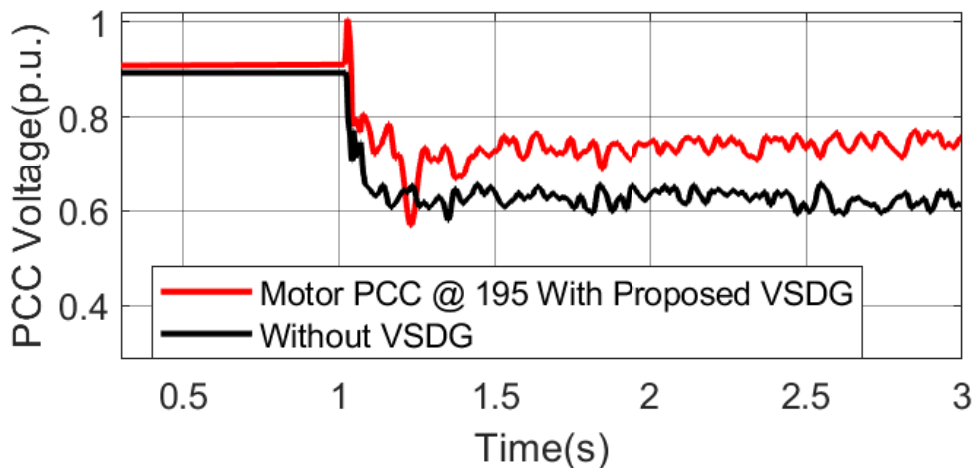


Figure 6.26: Test 5: VPCC for Motor at Node 195

motor voltage. Figure 6.27. It is clear from the results that DG at 79 which is close to motor at bus 451 and bus 195 contributes the maximum reactive power support. The rate of change of optimal gain is also higher for this DG at bus 79. Table 6.4 shows the performance analysis of proposed control approach based on Test 4 and Test 5.

The scalability test results above shows the performance of the proposed controller in a real system where the actual number of DGs and motors will be larger. Larger the amount of DGs in the system, the more is the net reactive power input to the

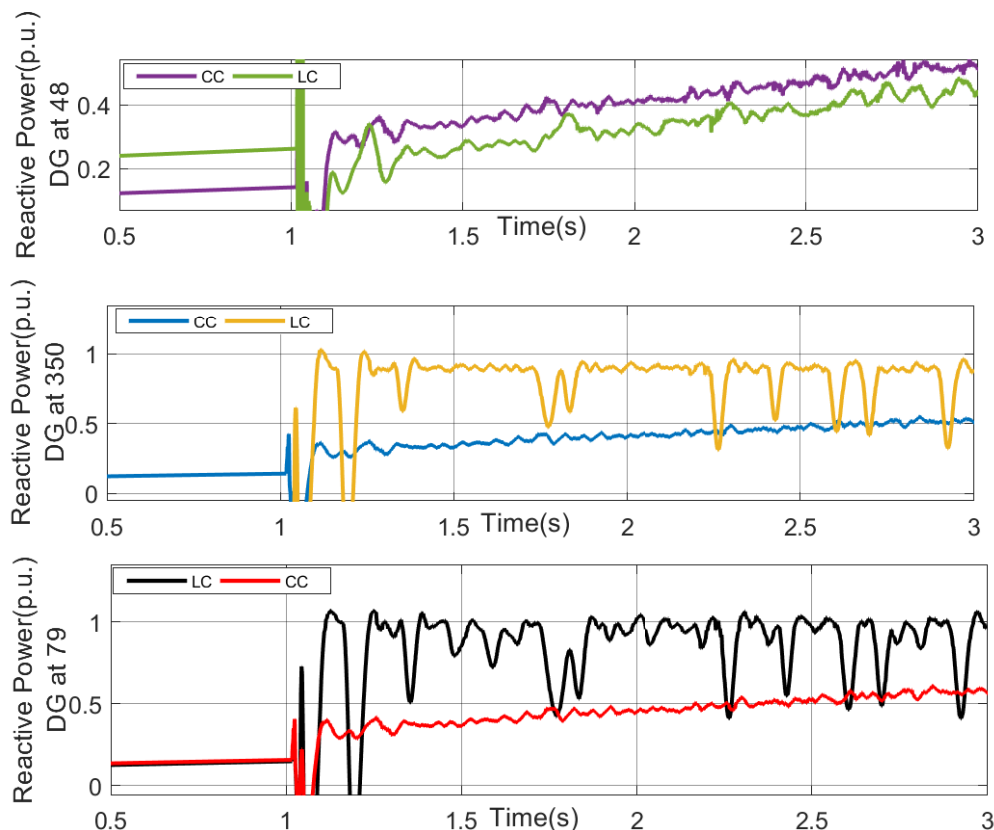


Figure 6.27: Test 5: Coordination of Reactive Power Support Offered by DGs

Table 6.4: Results of Scalability Test 4 and Test 5 with the Proposed VSDG

Control	%Steady State Improvement
Test 4: Motor at Bus 451 and Multiple DG	8.8% w.r.t Single VSDG
Test 5: Motor at Bus 451	17% w.r.t No VSDG
Test 5: Motor at Bus 195	20% w.r.t No VSDG
Test 5: Motor at Bus 251	12.6% w.r.t No VSDG

system. Hence the contribution of reactive power from each DGs reduces. Table 6.5 shows that the percentage steady state error is less for all cases with two DGs connected to network compared to single DG. The rate of improvement is dependent on the number and location of the DGs and motor. Percentage steady state error in voltage with all three DGs connected to the network is the lowest of all the cases. Eventhough, there is no communication with the motor controller, the coordinated

Table 6.5: Relation of Percentage Steady State Error to Number of DGs

No of DGs	%Steady State Improvement
DG at Node 79	5.33%
DG at Node 5	4.87%
DG at Node 10	4.83%
DG at Node 79 and Node 5	4.66%
DG at Node 79 and Node 10	3.97%
DG at Node 10 and Node 5	4.17%
DG at Node 79, Node 10 and Node 5	3.43%

control system relies on the motor terminal voltage measured at PCC. In practical scenario the motor and DGs will be at different locations. In case if there is a delay in sensing and communication of motor terminal voltage due to the poorly performed motor controller or communication techniques used, it can impact the operation of proposed coordinated controller. A test is performed with delayed motor terminal voltage for Test2 described above.

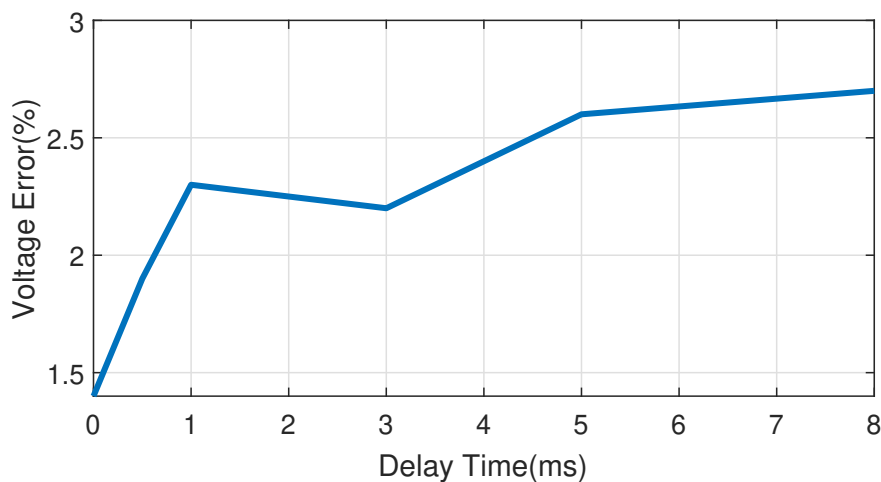


Figure 6.28: Percentage Voltage Error with Delayed Input

Figure. 6.28 shows the percentage error in steady state motor voltage with delayed motor input. It can be clearly seen that the percentage voltage error increases with delay.

6.6 Chapter Summary

This chapter proposes a coordinated optimal feedback control of VSDGs for mitigation and fast restoration of IM starting voltage sag transients. The proposed scheme is tested for several network conditions in MV distribution networks. The results conclude that integration of VSDG with the proposed control architecture contributes to the improvement in the steady state voltage as well as transient conditions. The proposed coordinated control strategy can be implemented to mitigate any types of voltage sags. The proposed topology tested for scalability in a 123 bus system also shows satisfactory results. In this study, multiple VSDGs and multiple motors are used for testing and the results show considerable improvement with integration of proposed coordinated control of VSDGs. In future, the application of the proposed coordinated control will be extended to a large practical system.

CHAPTER 7: AN OPTIMAL POLICY-DRIVEN INTEGRATED CONTROL FRAMEWORK FOR GRID-TIED INVERTERS BASED ON FREQUENCY DECOMPOSITION METHODOLOGY

This chapter presents a novel integrated control architecture for grid connected inverters. The proposed method augments an identification-based adaptive control approach with vendor-provided static controllers, thereby widening the operating range of the controller for dynamic grid operating conditions. The respective contribution from each of the controllers is determined by the optimal control policy, which is derived considering the nonlinear system dynamics that are represented as energy signals at the inverter terminals. A frequency mode decomposition algorithm, formulated based on a discrete transform, acts on these dynamic energy signals to convert them into a physically meaningful signal representing the dynamics that impact the power quality of the inverter output. The integrated architecture acts on these decomposed signals to remove these unwanted high-frequency components, ensuring improved power quality and overall stability for a wider range of grid operating conditions. Proposed architecture overrides the issues in conventional proportional integral controller due to variable operating points in the network without demanding much of the structural changes. The proposed system will be relevant for the current scenario where the new grid code demands the DERs to provide additional ancillary services like power smoothing, frequency regulation etc.

7.1 Introduction

Renewable energy sources are integrated to wind through power electronic devices like inverters and converters. Recent grid code demands these devices to supply ac-

tive power while at the same time absorb and supply reactive power. The increased integration and penetration has increased the challenges for solving grid problems like frequency regulation, voltage variation, low voltage ride through, power quality management etc. Several studies has been done on control of these Distributed Energy Resources (DERs) to operate in a wider dynamic range to provide added functionalities (e.g., voltage and frequency regulation, smoothing, etc.) as demanded by IEEE 1547 code.

7.1.1 State-of-the-Art

The importance of maintaining the stability of grid-connected inverters during dynamic conditions is discussed in [1],[121]. The papers emphasize that stability is ensured if the ratio between the grid impedance and inverter output impedance satisfies the Nyquist stability criterion. Decentralized power balance control of grid-connected inverters is proposed in [122]. The proposed control is not based on any communication between the individual inverter modules. Conventional inverter topology follows higher switching frequencies to reduce the THD in output current but is limited in high power applications. The requirements for GCI control in a distributed environment has been discussed in detail in [123]. With such architectures, the control of inverters should be based on available local information and thus communication becomes more complex as the distance between inverters increases. To reduce the complexity and yet maintain the stability, inverter control should be solely based on terminal quantities. Towards this goal, good control over real and reactive power is needed for the stable operation of the power systems. The control architecture should be able to capture the grid dynamics at the inverter terminals and at the same time, it should allow augmentation to conventional inverter control architectures.

Direct energy function approach based stability analysis in power system has a long history. Utilisation of energy function based approach for transient analysis has been discussed in [124]. Ways to improve the transient stability of DER integrated

power grid by analysing the potential energy absorbing capability of the network are explained in [125]. These energy function-based approaches that defines the relation between the accumulated energy in system and its dynamics is formulated and is utilized to study the power system stability in the perspective of system energy considering the nonlinear relationship of the variable during the transient process in power systems. A system is considered stable if its energy is continuously decreasing until it reaches an equilibrium state [126]. This depicts the importance of optimization of energy for improving system stability.

Moreover, the challenges imposed as a result of the high-frequency components in an inverter output, due to different filter configurations and its parameter changes, are not considered in our earlier work. The high-frequency components in the inverter output are eliminated by the proper design of filters, such as L or $L - C - L$ filters. However, these filter parameters can change as a result of atmospheric conditions or the interaction of these filters with grid impedance, which can result in higher-order harmonics in the inverter output [127, 128, 129]. This can seriously impact the power quality of the inverter output. Recent IEEE standards have recommended practice and requirements for harmonic control in the power system as discussed in [130]. According to this, the harmonic component in inverter output current above the 35th harmonics needs to be limited to 0.3% of the fundamental value in weak grid systems. Thus, to comply with the grid codes under such unpredictable grid operating conditions, the use of an advanced control method is needed for an inverter that considers the nonlinear operating behavior of the grid connected inverter (GCI) and offers a wider operating range, improves overall grid stability, and efficiently eliminates the higher-order frequency components on the inverter output.

7.1.2 Major Contributions

The main contributions of the proposed framework are:

- Robustness to filter parameter variations.

- Efficiency in removing high-frequency dynamics from output, thereby improving overall stability and power quality.
- Wider operating range compared to static controllers.
- Dynamically adapting control policy that weights the participation from each controller based on grid conditions.
- Optimal policy derivation considering the nonlinear behavior of the system.
- Frequency decomposition approach extracts the targeted frequency range from measured inverter output and derives the control policy to effectively eliminate those high frequency dynamics.
- Online identification approach that does not demand prior knowledge of complex system parameters.
- Optimized control approach considering the nonlinear system behavior.

7.2 Three Phase Inverter Model in $d - q$ Reference Frame

General configuration of a three phase inverter that integrates the renewable based energy resource like Wind Energy Conversion Systems (WECS) or Photo Voltaic (PV) farms to grid [1] is shown schematically in Figure 7.1. In PV farms the available output DC power is then converted to AC using an inverter, while WECS utilizes a back to back configuration of converter and inverter with a DC link at the middle. The DC link voltage is maintained constant by control techniques thereby assuring a stable AC power at the output. Thus in both cases an inverter to convert the DC power to AC is mandatory. The inverter vector control architecture focuses on maintaining the (a) active power output or DC link voltage on the renewable energy side and (b) reactive power output of the inverter.

The conventional vector utilizes reference frame theory for independent control of the output of grid connected inverters. Similar to a WECS, reference frame in grid

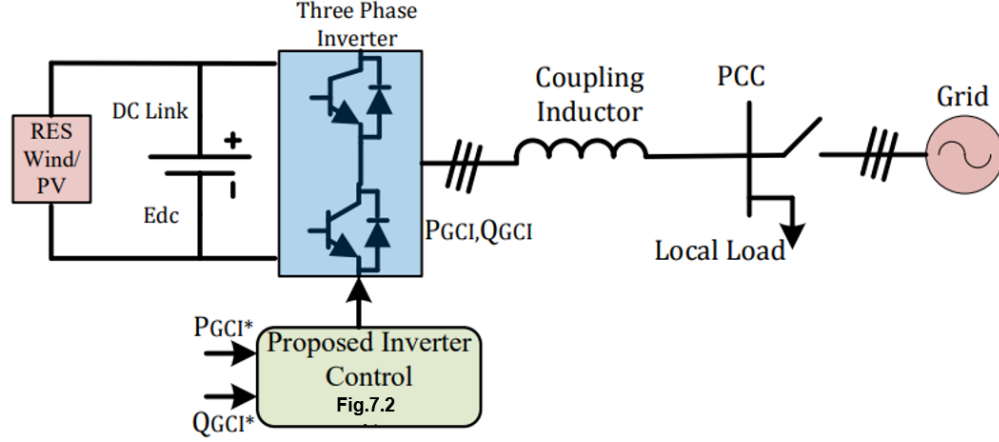


Figure 7.1: Typical Configuration of Three Phase Inverters with RES [1].

connected inverter control is oriented along the grid voltage vector. Generally, grid connected inverters are current regulated with d-axis current, i_d controlling the active power flow or DC link voltage and the q-axis current, i_q controls reactive power flow. With R and L are the line inductance and resistance electrical relation that connects the output voltage for inverter across the line parameters are given by [1],

$$\begin{bmatrix} V_{inva} \\ V_{invb} \\ V_{invc} \end{bmatrix} = R \begin{bmatrix} I_{inva} \\ I_{invb} \\ I_{invc} \end{bmatrix} + L \frac{d}{dt} \begin{bmatrix} I_{inva} \\ I_{invb} \\ I_{invc} \end{bmatrix} + \begin{bmatrix} V_{ga} \\ V_{gb} \\ V_{gc} \end{bmatrix} \quad (7.1)$$

where $V_{inva,b,c}$ represents the inverter output voltage, $V_{ga,b,c}$ is the grid voltage and $I_{inva,b,c}$ is the inverter output current. Eqn.(7.1) in synchronously rotating dq reference frame rotating at angular frequency, ω_e rad/s using Parks transformation can be represented as,

$$\begin{aligned} v_{di} &= Ri_d + L \frac{di_d}{dt} - \omega_e Li_q + v_d \\ v_{qi} &= Ri_q + L \frac{di_q}{dt} + \omega_e Li_d + v_q \end{aligned} \quad (7.2)$$

where i_d and i_q is the d-axis and q-axis current from inverter respectively, v_d and v_q is the d-axis and q-axis grid voltage respectively, and v_{di} and v_{qi} is the d-axis and

q-axis output voltage of the inverter.

The v_{di} and v_{qi} in eqn (7.2) can be separated into two components: Thus,

$$\begin{aligned} v_{di} &= ((R + pL) i_d) + (v_d - \omega_e L i_q) = V'_{dic} + V''_{di} \\ v_{qi} &= ((R + pL) i_q) + (v_q + \omega_e L i_d) = V'_{qic} + V''_{qi} \end{aligned} \quad (7.3)$$

The first term V'_{dqic} is the input sequence generated by the conventional control loop. The second term represents, V''_{dqic} , compensates the coupling between the d and q -axis components and p is the derivative operator ($\frac{d}{dt}$). The controller generates proper sequence of input voltage (v'_{di} and v'_{qi}) for the inverter PWM to control inverter output current i_d and i_q respectively.

abc to dq transformation is done based on the angular frequency of the supply voltage given by,

$$\theta_e = \int \omega_e dt = \tan^{-1} \left(\frac{v_\beta}{v_\alpha} \right) \quad (7.4)$$

where v_α and v_β are the alpha and beta components of the grid voltage vectors.

Reference frame d-axis is aligned along the stator voltage position obtained from (7.4) and v_q is zero. The active and reactive power output of the grid connected inverter is then given by [131],

$$\text{Activepower, } P = v_d i_d \quad \text{Reactivepower, } Q = v_d i_q \quad (7.5)$$

i_d defines the active power output and i_q defines the reactive power output which in turn is controlled by v'_{di} and v'_{qi} respectively.

7.3 Overview of Proposed Methodology

The proposed architecture showcased in Figure 7.1, and detailed in the overall control architecture shown in Figure 7.2, consists of two parts. The first part is the

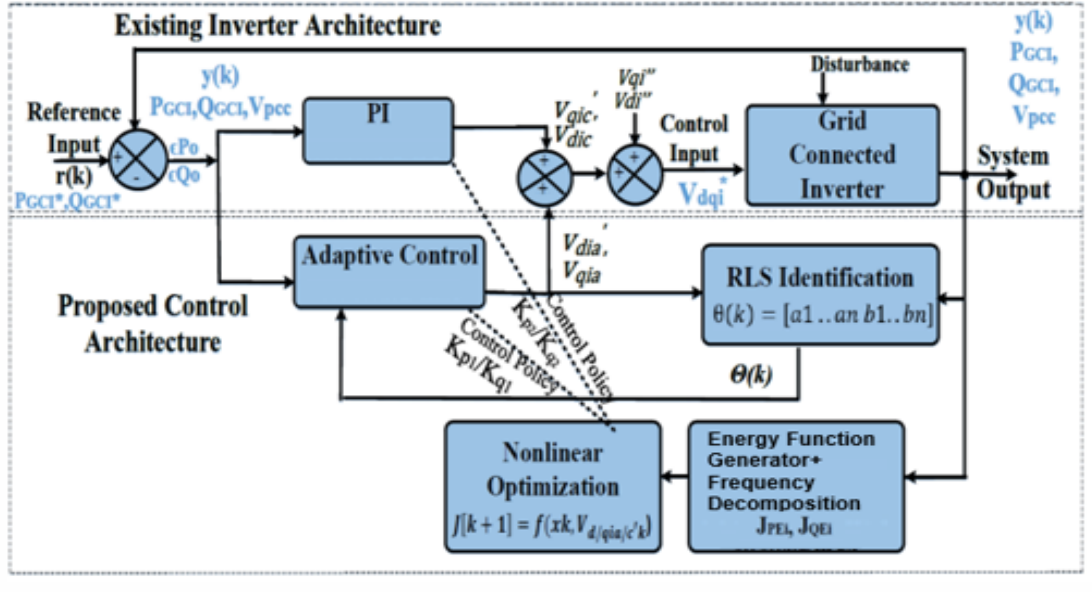


Figure 7.2: Schematic of the Proposed Hybrid Control Architecture

policy generation and the second part is the hybrid control architecture. The policy generation process is discussed next.

7.3.1 Policy Generation

7.3.1.1 Energy Function Generator

The structure preserving energy function based approach, described in [132], represents the energy on a system in terms of change of energy at the terminals of the system. In this approach, if the post disturbance energy of a system is gradually declining and is always with the critical energy limit, then the system is considered stable. In this work, the dynamics in the grid are represented as energy signals formulated based on measurements, as shown in (7.6) and (7.7). The energy calculation due to the active power flow is,

$$J_{PEi} = \sum_{k \in N_j} B_{ig} V_{inv} V_g (\cos(\delta_{ig}) - \cos(\delta_{ig}^*)) + P_{inv}^* \Delta \delta_{inv} \quad (7.6)$$

where i represents the inverter end point and g represents grid point, V_{inv} represents voltage at the inverter point of common coupling (PCC) and V_g represents grid volt-

age, δ_{ig} represents the corresponding voltage angles between the inverter and grid point, P_{inv}^* represents the inverter active power, and B_{ig} represents the line susceptance between the inverter and grid point.

Similarly, the reactive power energy is,

$$J_{Q_{Ei}} = - \sum_{k \in N_j} 0.5 B_{ig} \Delta V_{inv} V_g \cos(\delta_{ig}) - \int_{V_{inv}^*}^{V_{inv}} \frac{Q_{inv}^*}{V_{inv}} dV_{inv} \quad (7.7)$$

where Q_{inv}^* represents the inverter reactive power, and B_{ig} represents the line susceptance. Since dq domain control is employed, $J_{P_{Ei}}$ is further used to derive the control policy for the d -loop and $J_{Q_{Ei}}$ for the q -loop, respectively.

7.3.1.2 Energy Function Frequency Decomposition

The frequency decomposition of energy signals is discussed in Algorithm 3.

J_{PQ} is defined as a vector of energy signals representing active and reactive power as,

$$J_{PQ}(k) = \begin{bmatrix} J_{P_{Ei}} & J_{Q_{Ei}} \end{bmatrix}. \quad (7.8)$$

The energy signal $J_{PQ}(k)$ is represented in terms of the frequency components as $j[n]$ with ‘ N ’ different frequency components. The desired frequency components is now extracted to $j_{desired}[n]$.

The detailed algorithm for decomposition is discussed in Algorithm 3.

The frequency spectrum of the energy signal $J_{PQ}[k]$ can be calculated using Fast Fourier Transform (FFT) shown in (7.9) per [?, ?].

$$J_{PQ}[k] = \sum_{n=0}^{N-1} j[n] \cdot \exp\left(\frac{-i2\pi kn}{N}\right) \quad (7.9)$$

$$0 \leq k \leq N - 1$$

In this work, the DCT shown in (7.10) is used to compute the frequency spectrum of the energy signal $J_{PQ}[k]$ per [133, 134]. DCT is based on only real components and

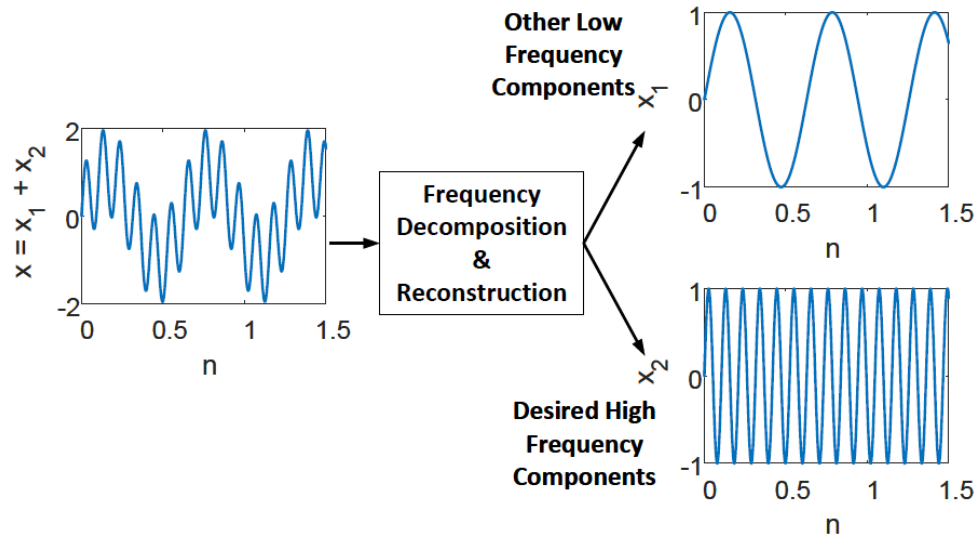


Figure 7.3: Frequency Decomposition and Signal Reconstruction.

hence reduces the computation complexity with greater efficiency. The corresponding imaginary components are obtained using the DST [134, 135], shown in (7.11). Then, the complex frequency domain signal can be obtained, as shown in (7.12).

$$J_c[k] = 2 \sum_{n=0}^{N-1} j[n] \cdot \cos\left(\frac{\pi k (2n + 1)}{2N}\right) \quad (7.10)$$

$$0 \leq k \leq N - 1$$

$$J_s[k] = \sum_{n=0}^{N-1} j[n] \cdot \sin\left(\frac{\pi k (2n + 1)}{2N}\right) \quad (7.11)$$

$$J_{PQ}[k] = J_c[k] + i \cdot J_s[k] \quad (7.12)$$

The spectrum magnitude, $P[k]$, is shown in (7.13), where N is the length of $J_{PQ}[k]$. The energy signal frequency spectrum, $X[k]$, can then be expressed in terms of fre-

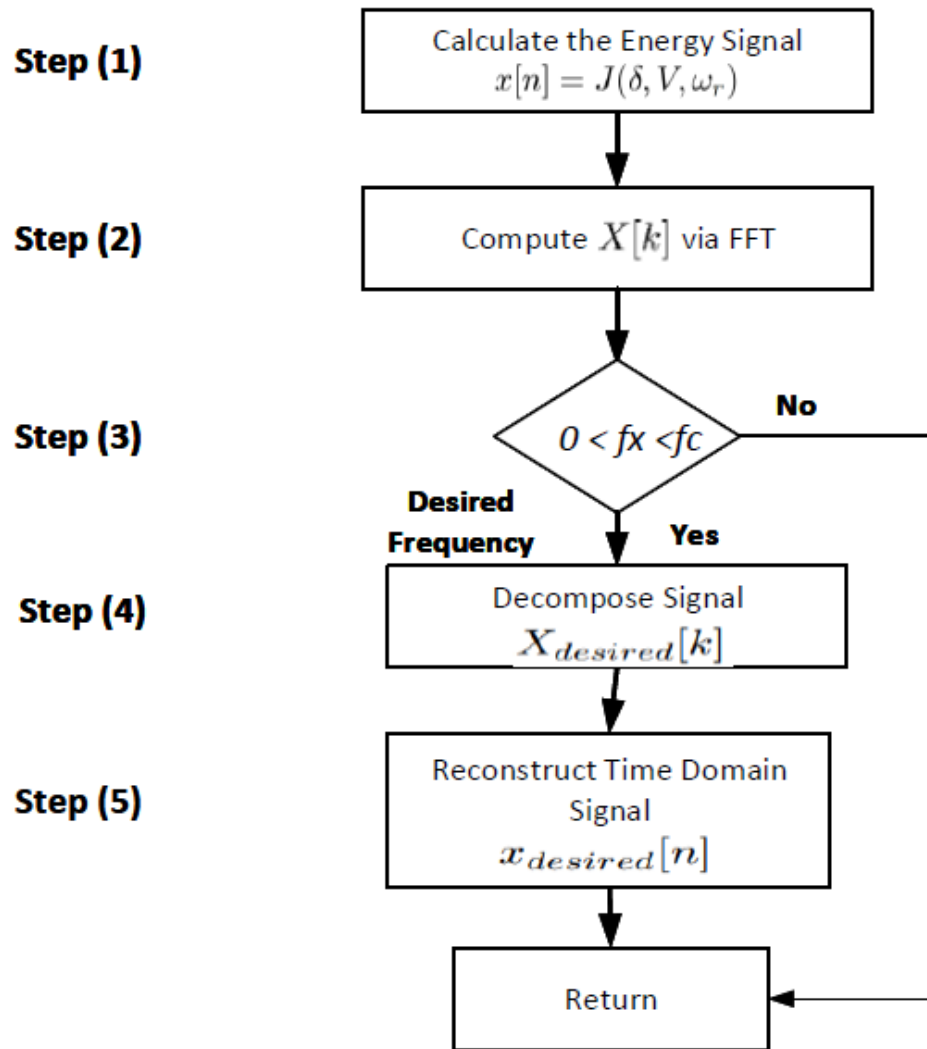


Figure 7.4: Frequency Decomposition and Signal Reconstruction Flow Chart.

quency, f_x , and the corresponding magnitude, $P[k]$, such that $X[k] \rightarrow [f_x, P[k]]$.

$$P[k] = \frac{2 \cdot |J_{PQ}[k]|}{N} \quad (7.13)$$

The frequency spectrum $[f_x, P[k]]$ is then sorted, such that the frequency components in the desired range ($f_1 \leq f_x \leq f_c$) are extracted based on the cutoff frequency,

f_c , per (7.14).

$$J_{desired}[k] = J_{PQ}[k], \forall f_1 < f_x < f_c \quad (7.14)$$

To reconstruct the time domain signal, the inverse DCT (IDCT) is used, as shown in (7.15) per [133]. This approach is used to reconstruct the extracted time domain ($j_{desired}[n] = [j_{pdesired}[n], j_{qdesired}[n]]$) from their corresponding frequency domain signals, $J_{desired}[k]$.

$$j_{desired}[n] = \frac{1}{N} \sum_{k=0}^{N-1} \beta[k] \cdot J_{desired}[k] \cdot \cos\left(\frac{\pi k (2n + 1)}{2N}\right) \quad 0 \leq n \leq N - 1 \quad (7.15)$$

$$\beta[k] = \begin{cases} \frac{1}{2}, k = 0 \\ 1, 1 \leq k \leq N - 1 \end{cases}$$

Algorithm 3 Energy Signal Frequency Decomposition

- 1: Compute the energy signal, $j[n] = J_{PQ}$.
 - 2: Compute the frequency spectrum of the energy signal, $J_{PQ}[k]$ (via the DCT (7.10), DST (7.11), and combined complex signal (7.12)).
 - 3: Obtain the spectrum magnitude $P[k]$ via (7.13) and corresponding frequencies $[f_x, P[k]]$. [133, 134, 135]
 - 4: Decompose $J_{PQ}[k]$ to identify the key frequency components.
 - 5: Extract the frequency spectrum signal into the desired range $J_{desired}[k]$, where $J_{desired}[k]$ is selected in range $f_1 < f_x < f_c$ per (7.14).
 - 6: Reconstruct the desired time domain signal $j_{desired}[n]$ from $J_{desired}[k]$ per the IDCT (7.15), respectively.
-

7.3.1.3 Optimal Policy Generation using Nonlinear Optimization

A control policy that coordinates both controllers in the integrated architecture is derived by optimizing the extracted energy signal from Section 7.3.1.2. This is done considering the nonlinear behavior of the system and its dynamics. The performance of linear optimization techniques on nonlinear systems depends on the extend of

nonlinear behavior exhibited by the system and on how often the feedback gain matrix can be updated. The nonlinear dynamics are assumed to be linear for a small region in and around the equilibrium point.

The nonlinear behavior of the frequency decomposed energy signal, representing the system dynamics discussed in Section 7.3.1.2, can be shown as,

$$j_{desired}[n + 1] = f(x_n, V'_{iac}(n)) \quad (7.16)$$

where $j_{desired}[n]$ is the extracted energy signal of the desired frequency range, x_n is the observed state and $V'_{iac}(n)$ is the input from the augmented control architecture represented as,

$$V'_{iac}(n) = \begin{bmatrix} V'_{dia}(n) & V'_{qia}(n) & V'_{dic}(n) & V'_{qic}(n) \end{bmatrix} \quad (7.17)$$

$$x_n = \begin{bmatrix} x_{p1}(n) & x_{p2}(n) & x_{q1}(n) & x_{q2}(n) \end{bmatrix}. \quad (7.18)$$

The system can be maintained at the desired equilibrium state $x^* = [x_{p1}^*, x_{p2}^*, x_{q1}^*, x_{q2}^*]$ if,

$$\forall V'_{iac} s.t, x^* = f(x^*, V'_{iac}) = j_{desired}^*. \quad (7.19)$$

Linearizing the dynamics around the x^* gives,

$$\begin{aligned} \begin{bmatrix} x_{p1}(n+1) & x_{p2}(n+1) & x_{q1}(n+1) & x_{q2}(n+1) \end{bmatrix} &\approx \\ j_{desired}^* + \frac{\partial j_{desired}^*}{\partial x}(x^*, V'_{iac})(x_n - x^*) & \\ + \frac{\partial j_{desired}^*}{\partial V'_{iac}}(x^*, V'_{iac})(V'_{iac}(n) - V'_{iac}) &. \end{aligned} \quad (7.20)$$

This can be equivalently represented as,

$$\begin{aligned}
x[n+1] - x^* &\approx \frac{\partial j_{desired}}{\partial (x_n - x^*)} (x_n - x^*) + \\
&\frac{\partial j_{desired}}{\partial (V'_{iac}(n) - V'^*_{iac})} (V'_{iac}(n) - V'^*_{iac})
\end{aligned} \tag{7.21}$$

where $A = \frac{\partial j_{desired}}{\partial (x_n - x^*)}$ and $B = \frac{\partial j_{desired}}{\partial (V'_{iac}(n) - V'^*_{iac})}$. Let $(x_n - x^*) = z_n$ and $(V'_{iac}(n) - V'^*_{iac}) = v_n$.

$$z[n+1] - x^* = Az_n + Bv_n \tag{7.22}$$

Now the nonlinear system dynamics are represented as linear dynamics around the operation point (x^*, V'^*_{iac}) . The cost function J_{cost} for this linearized representation can be derived as a standard linear optimization problem,

$$J_{cost} = (z_n)^T Q z_n + (v_n)^T R v_n \tag{7.23}$$

where Q and R are the respective covariance matrices. Q defines the weight of the state on the cost function, with $Q = A^T A$. Additionally, R is selected based on the control input weight.

The P_k is found iteratively by solving the discrete Riccati equation given by,

$$\begin{aligned}
P_k &= Q_{H+k} + K_k^T R_{H+k} K_k + \\
&(A_{H+k} - B_{H+k} K_k)^T P_{k+1} (A_{H+k} - B_{H+k} K_k)
\end{aligned} \tag{7.24}$$

subject to the condition that A and B (i.e., the state and input matrices) are stabilizable. Then, based on the solution of the Riccati equation, the optimal control gain, K , for the linear time varying system representation with a k -step horizon is,

$$\begin{aligned}
K_k &= -[R_{H+k} + B_{H+k}^T P_{k+1} B_{H+k}]^{-1} \\
&B_{H+k}^T P_{k+1} A_{H+k}.
\end{aligned} \tag{7.25}$$

The optimal control input is given by,

$$\begin{aligned}
 v_n &= K_k z_n \\
 (V'_{iac(n)} - V'^*_{iac(n)}) &= K_k (x_n - x^*) \\
 V'_{iac(n)} &= V'^*_{iac(n)} + K_k (x_n - x^*)
 \end{aligned} \tag{7.26}$$

where K is the optimal control policy for the d and q loops of the control loop. K_{p1} and K_{q1} correspond to the optimal policy for the adaptive control loop, and K_{p2} and K_{q2} correspond to the optimal policy for the vector control loop, corresponding to input V'_{iac} and $V'_{qia'}$, respectively. The overall gain changes based on the changing dynamics of the energy function with respect to the control input.

7.3.2 Proposed Integrated Control Architecture

The overall control architecture consists of an integration of adaptive control framework with an online identifier and conventional control with a dynamic control policy generation mechanism that allows augmentation of the device level controller.

7.3.2.1 Online Model Identification and Modeling of Adaptive Controller

The hybrid architecture makes use of online identification techniques. An RLS algorithm produces the transfer function coefficient (i.e., for a second order system the coefficients are a_1, a_2, b_1, b_2), as shown in (7.29) and (7.31), which are updated at every time step.

Let $\epsilon_{P_o}(k)$ and $\epsilon_{Q_o}(k)$ be the dynamic change in active and reactive power measured at the PCC from the reference.

$$\epsilon_{PQ_o}(k) = \begin{bmatrix} \epsilon_{P_o}(k) & \epsilon_{Q_o}(k) \end{bmatrix} \tag{7.27}$$

The control input for the adaptive control loop is,

$$V'_{ia}(k) = \begin{bmatrix} V'_{dia}(k) & V'_{qia}(k) \end{bmatrix} \tag{7.28}$$

$$\frac{\epsilon_{PQ_o}(k)}{V'_{ia}(k)} = \frac{b_1 z^{-1} + b_2 z^{-2}}{1 + a_1 z^{-1} + a_2 z^{-2}} \tag{7.29}$$

When the model output, $\epsilon_{PQ_{om}}(k)$, equals the actual output (within an acceptable range of deviation), the identified transfer function represents the actual system at that time step given by,

$$\begin{aligned}\epsilon_{PQ_{om}}(k) = & -a_1\epsilon_{PQ_o}(k-1) - a_2\epsilon_{PQ_o}(k-2) \\ & + b_1V'_{ia}(k-1) + b_2V'_{ia}(k-2)\end{aligned}\quad (7.30)$$

$$\epsilon_{PQ_o}(k) = X\Theta \quad (7.31)$$

where $\Theta = \begin{bmatrix} a_1 & a_2 & b_1 & b_2 \end{bmatrix}$. The identified coefficients are further utilized by the Minimum Variance Control (MVC) algorithm-based adaptive control loop. From (7.27), the second order transfer function of the model considering the error is represented as,

$$\epsilon_{PQ_o}(k) = \frac{B^*(z^{-1})}{A^*(z^{-1})}z^{-d}V'_{ia}(k) + \frac{C^*(z^{-1})}{A^*(z^{-1})}\eta(k) \quad (7.32)$$

where η represents the error in the model. Predicting the system output ‘ d ’ steps into the future produces,

$$\begin{aligned}\epsilon_{PQ_o}(k+d) &= \frac{C^*(z^{-1})}{A^*(z^{-1})}\eta(k+d) + \frac{B^*(z^{-1})}{A^*(z^{-1})}V'_{ia}(k) \\ &= F^*(z^{-1})\eta(k+d) + \frac{G^*(z^{-1})}{A^*(z^{-1})}\eta(k) + \frac{B^*(z^{-1})}{A^*(z^{-1})}V'_{ia}(k)\end{aligned}\quad (7.33)$$

where $F^*(z^{-1})$ and $G^*(z^{-1})$ are linked with $C^*(z^{-1})$ through the Diophantine equation:

$$C^*(z^{-1}) = A(z^{-1})F(z^{-1}) + z^{-d}G(z^{-1}). \quad (7.34)$$

MVC develops a control sequence $u(k)$ (i.e., V'_{ia}) in such a way that the objective function,

$$J_{obj} = E\{[\epsilon_{PQ_o}(k+d) - \epsilon_{PQ_{or}}]^2\} \quad (7.35)$$

is minimized. In (7.35), E represents the expected value of the deviation of the estimated

process output ‘ d ’ steps into the future and the system reference input $\epsilon_{PQ_{or}}$.

The optimal control sequence derived after minimization is then represented as (7.36),

$$V'_{ia}(k) = \frac{C^*(z^{-1})\epsilon_{PQ_{or}} - G^*(z^{-1})\epsilon_{PQ_o}(k)}{B^*(z^{-1})F^*(z^{-1})} \quad (7.36)$$

7.3.2.2 Modeling of Integrated Control

In the proposed hybrid architecture, the input control sequence is determined by the augmented control architecture comprised of both vector control and adaptive control. Let V_{di}^* and V_{qi}^* represent the final control voltage sequence,

$$\begin{aligned} V_{di} &\propto V_{di}^* \\ V_{qi} &\propto V_{qi}^* \end{aligned} \quad (7.37)$$

The overall input sequence, V_{di}^* and V_{qi}^* can be derived as,

$$\begin{aligned} V_{di}^* &= (V'_{dia} + K_{p1}V'_{dia}) + (V'_{dic} + K_{p2}V'_{dic}) + V''_{di} \\ V_{qi}^* &= (V'_{qia} + K_{q1}V'_{qia}) + (V'_{qic} + K_{q2}V'_{qic}) + V''_{qi} \end{aligned} \quad (7.38)$$

where K_{p1} , K_{q1} , K_{p2} , and K_{q2} the respective control gains per the control policy defined by (7.25), and the control input sequence V_{dqi}^* and inverter output V_{dqi} are linearly related.

Based on the reference frame alignment $V_q = 0$ and V_d is a constant. Therefore, the active and reactive power output of the grid connected inverter (P_{GCI} , Q_{GCI}) are then given by [131],

$$P_{GCI}(k) = V_d i_d \quad Q_{GCI}(k) = V_d i_q \quad (7.39)$$

where i_d defines the active power output of the inverter and i_q defines the reactive power output of the inverter, which in turn is controlled by V_{di}^* and V_{qi}^* , respectively. Based on the grid dynamics represented by the energy signal, the augmented controller generates a proper sequence of input voltage (V_{di}^* and V_{qi}^*) for the inverter pulse width modulation (PWM) to

control the inverter output current i_d and i_q , respectively. As the frequency components in the grid dynamics change, the optimization function derives the control policy, such that the contribution from each of the controllers in the hybrid architecture is varied to ensure minimal change in energy.

7.4 Simulation Results

The proposed control methodology is tested and validated on a real-world power grid integrated with the inverter model in the real-time simulator. Initially the system is tested on a small-scale aggregated power grid feeder (IEEE 13 bus system). The inverter is integrated into bus 680. For the experimental results, the models and the hardware are integrated with the simulator. The inverter is integrated into the controller that is designed using the real-time simulator OPAL-RT. For sensing, a data acquisition kit (OP8660) is used. A three-phase power supply integrated with the simulator is controlled via an external signal derived from the real-time grid model (IEEE 13 bus system) designed in the real-time simulator. The details are shown in Figure 7.24. Finally, the performance in real-world scenarios is validated based on the test cases performed on the IEEE 123 bus test system.

7.4.1 Analysis on IEEE 13 bus system

The proposed architecture is validated using a standard IEEE 13 bus system (see Figure 7.5). The inverter is integrated into bus 680. Five cases are discussed in this paper for the IEEE 13 bus system. Case A analyzes the performance of the proposed hybrid control architecture during grid faults, Case B analyzes the performance during sudden load change, Case C focuses on the robustness of the proposed architecture to high frequency dynamics introduced as a result of filter parameter variations, Case D verifies the performance during ancillary services like power smoothing, and Case E verifies the wider operating range provided by the proposed control method during high frequency dynamics. The test results are quantified and compared in Table 7.1.

7.4.1.1 Case A: Performance validation for grid faults

The performance of the integrated control architecture is tested for a three-phase to ground fault applied at bus 692 for a duration of 150ms.

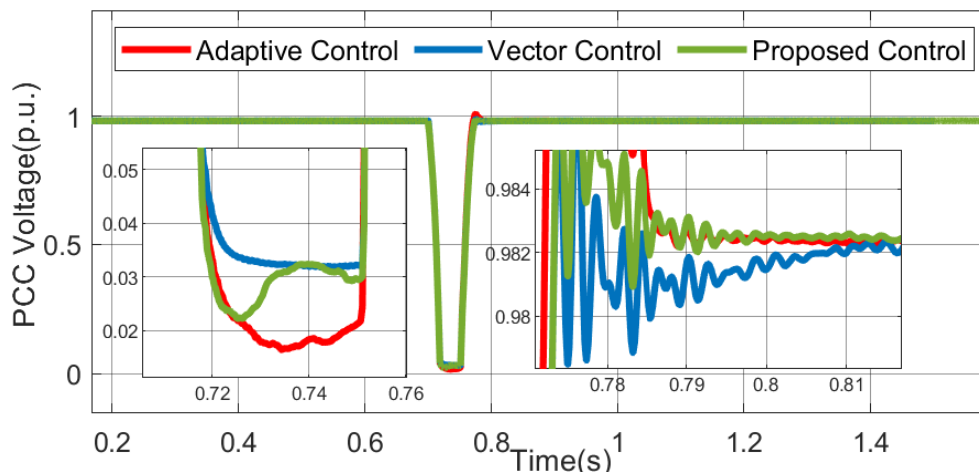


Figure 7.6: Case A: PCC Voltage at Inverter Terminals during Fault.

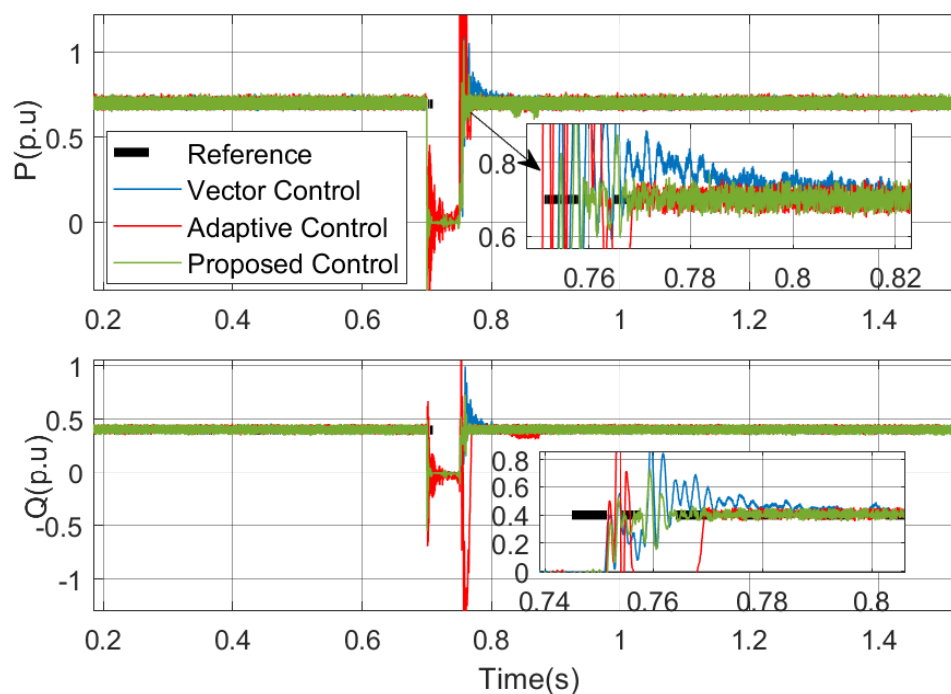


Figure 7.7: Case A: Power Output of Inverter.

7.4.1.2 Case B: Performance validation for load change

The proposed architecture is validated for a sudden load change initiated at 0.7s on bus 690. Figure 7.12 shows the ability of the proposed architecture to meet the sudden demand change faster than the conventional control. The PCC voltage shows that the terminal quantities settle faster to their respective nominal values. This is further supported by the

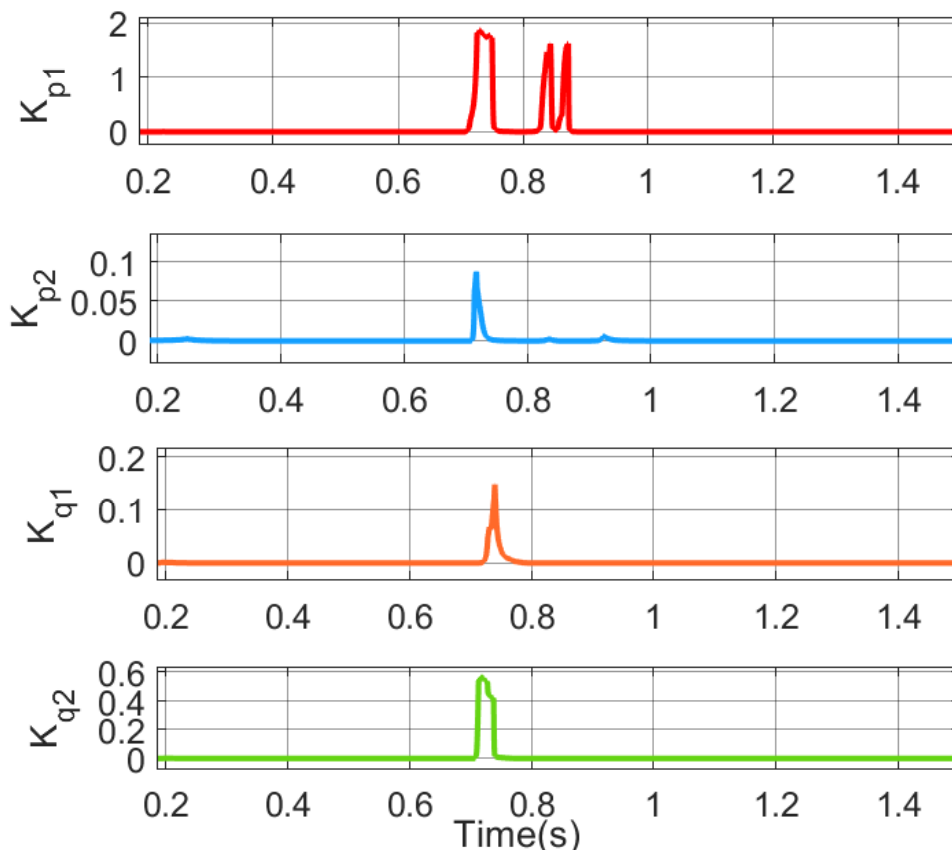


Figure 7.8: Case A: Control Policy Generated for Test Case A.

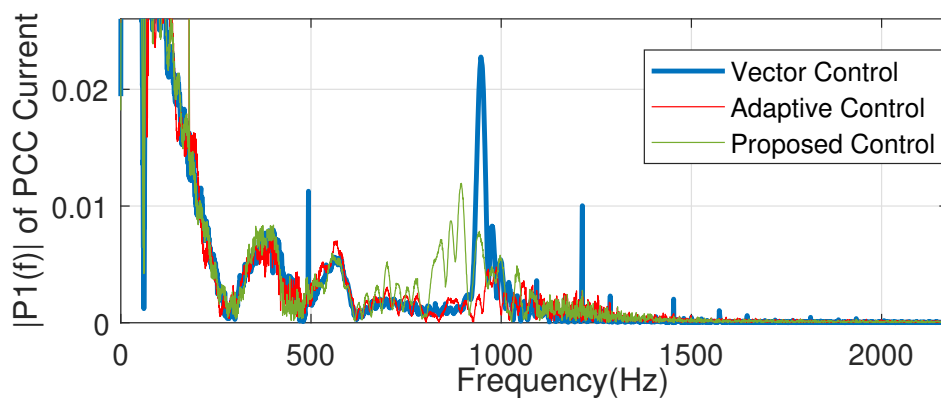


Figure 7.9: Case A: Frequency Spectrum of Inverter Output Current.

inverter output shown in Figure 7.13. The optimization policy adjusts the contributions from the controller as the energy changes during the event triggered at 0.7s. The corresponding derived control policy is shown in Figure 7.14.

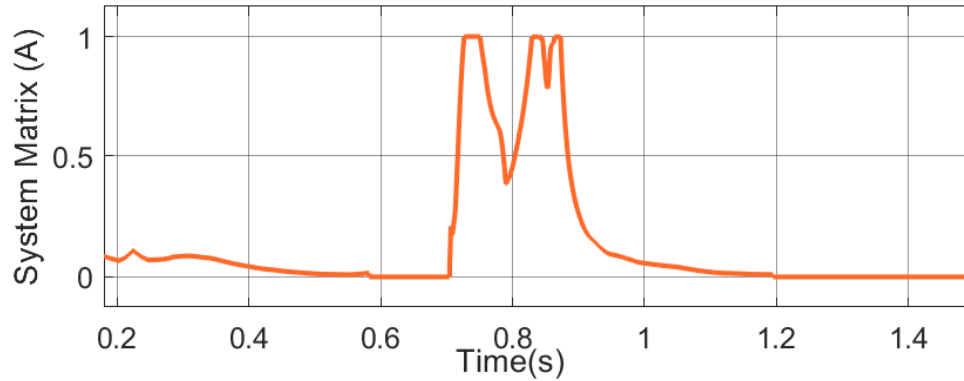


Figure 7.10: Case A: Dynamic System Matrix Derived using Nonlinear Optimization.

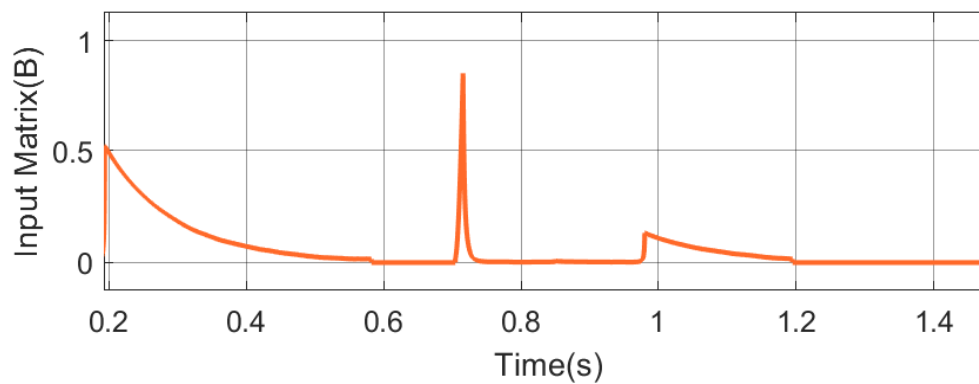


Figure 7.11: Case A: Dynamic Input Matrix Derived using Nonlinear Optimization.

Table 7.1: Comparison of Test Results
VC: Vector Control, PC: Proposed Control

Case	Parameter	VC	PC	% Reduction
A	V_{pcc} Settling time, T_s (s)	0.08	0.035	56.25
A	Inverter Power T_s (s)	0.07	0.02	71.42
B	V_{pcc} Settling time T_s (s)	0.09	0.018	80
B	Inverter Power T_s (s)	0.05	0.002	96
C	PCC Voltage T_s (s)	0.2	0.035	82.5
C	PCC Power tracking T_s (s)	0.1	0.007	3
D	Δ Frequency (Hz)	± 0.2	± 0.05	75

7.4.1.3 Case C: Performance validation with change in filter parameters

The robustness of the proposed control method for parameter variations is tested and validated in this test case. The inverter is operated under the reference tracking mode with a 50% change in filter parameters.

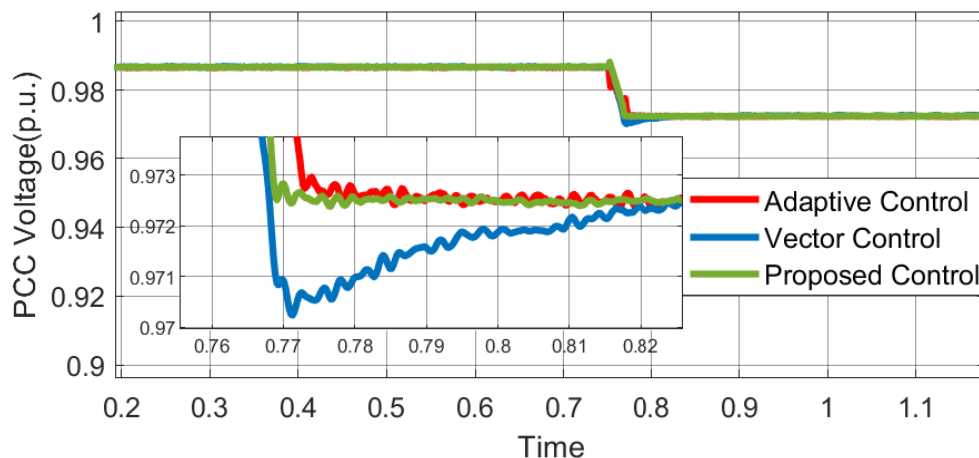


Figure 7.12: Case B: PCC Voltage at Inverter Terminals during Load Change.

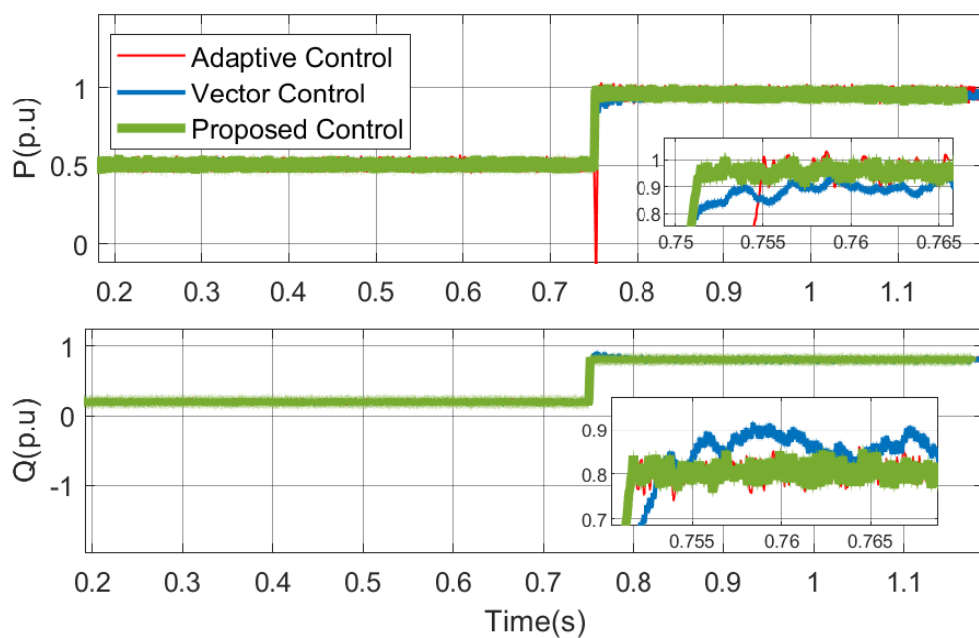


Figure 7.13: Case B: Power Output of Inverter during Load Change.

The PCC voltage and inverter power output displayed in Figure 7.16 and Figure 7.17 shows that the performance efficiency of conventional control drops as the filter parameters change. The advantages of the proposed architecture in terms of faster control action and maintaining the power quality with less oscillations can be seen from the test results. The control input derived by policy regulator that defines the participation from each controller is depicted in Figure ??.

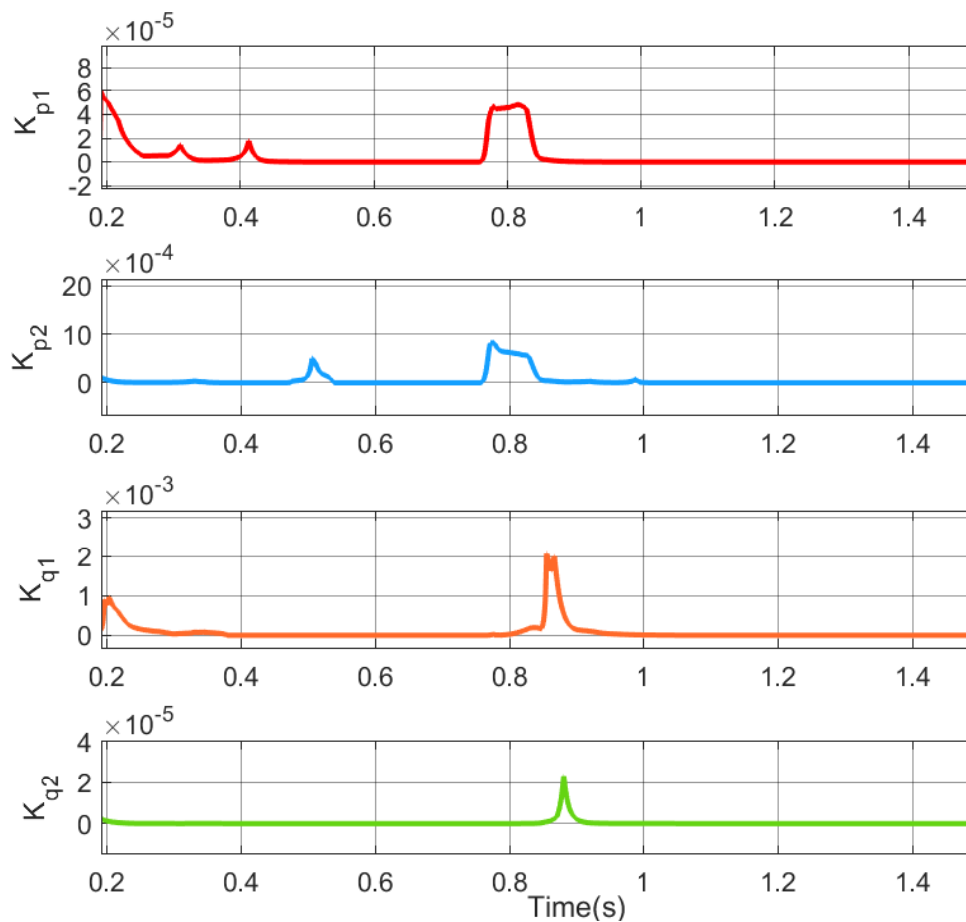


Figure 7.14: Case B: Control Policy Derived by Optimization Function during Load Change.

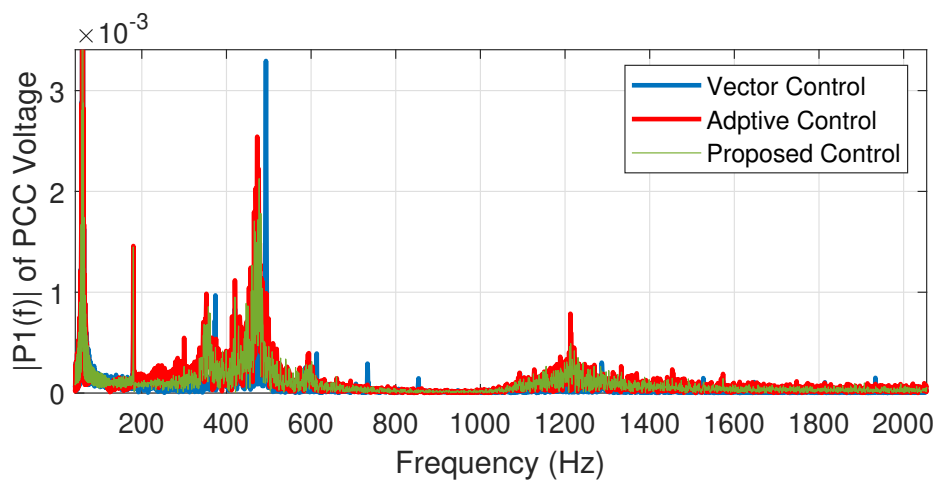


Figure 7.15: Case B: Frequency Spectrum of PCC Voltage during Load Change.

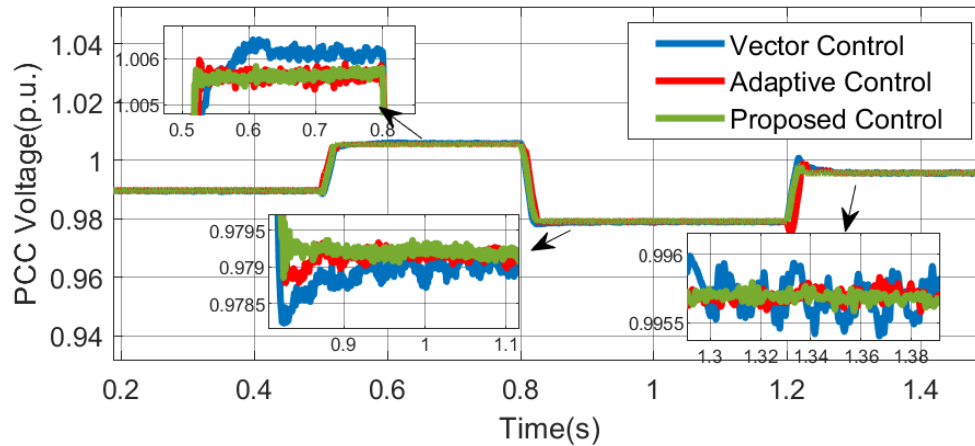


Figure 7.16: Case C: PCC Voltage at Inverter Terminals during Parameter Variations.

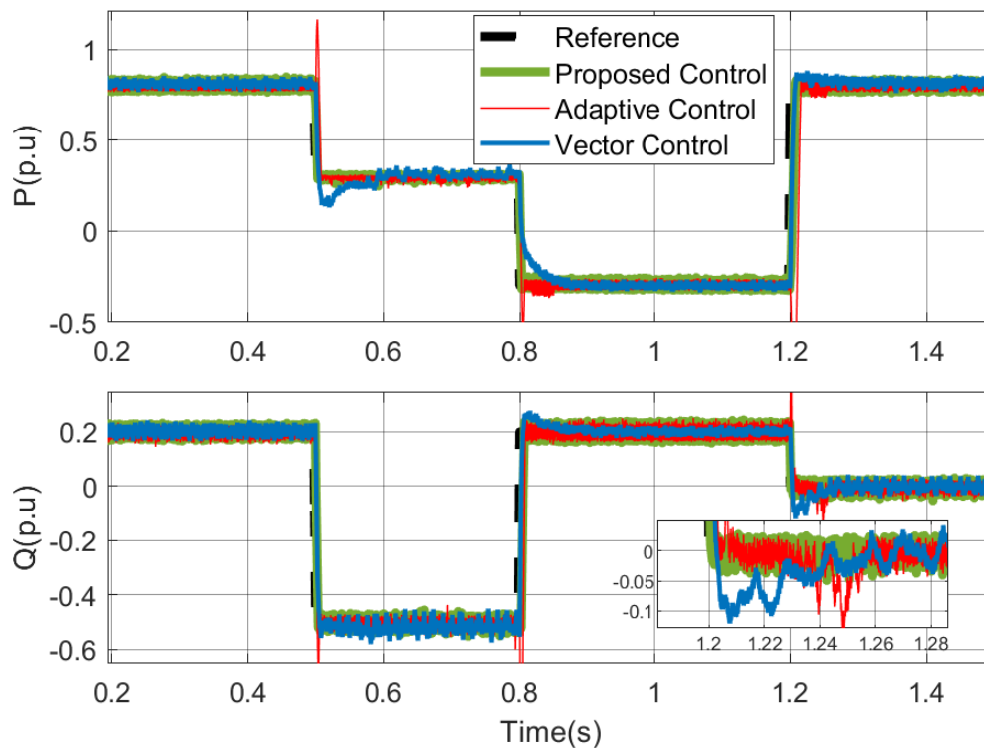


Figure 7.17: Case C: Power Output of Inverter during Parameter Variations.

7.4.1.4 Case D: Performance validation during ancillary services

The performance of the proposed augmented control while rendering ancillary services (power smoothing application) is analyzed in this test case scenario. The output of the inverter during highly varying power demand, while offering a power smoothing service, is

shown in Figure 7.18. The ability of the proposed architecture to tightly maintain the frequency within $\pm 0.05Hz$ from nominal compared to $\pm 0.2Hz$ with the conventional approach for the same power demand is showcased in Figure 7.19.

The corresponding control policy derived by the optimization function and frequency spectrum of the inverter output current is shown in Fig. 7.21.

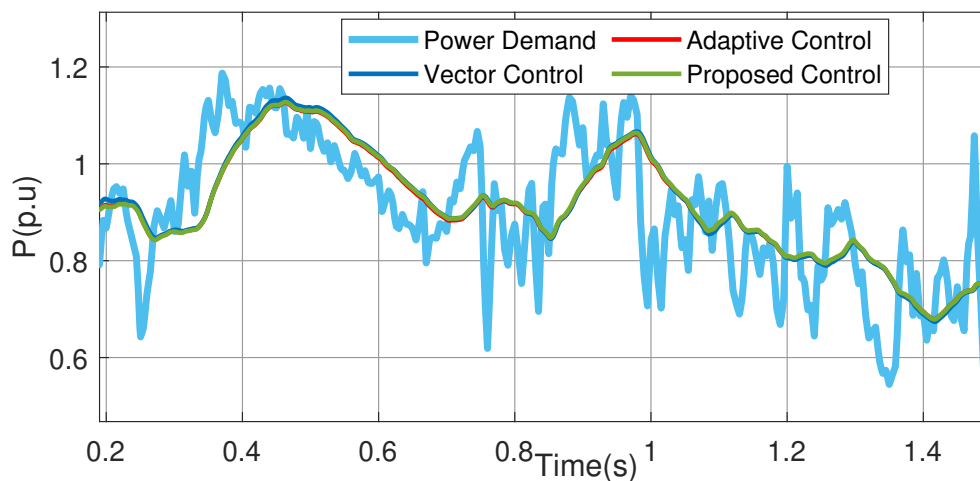


Figure 7.18: Case D: Inverter Output during Case D.

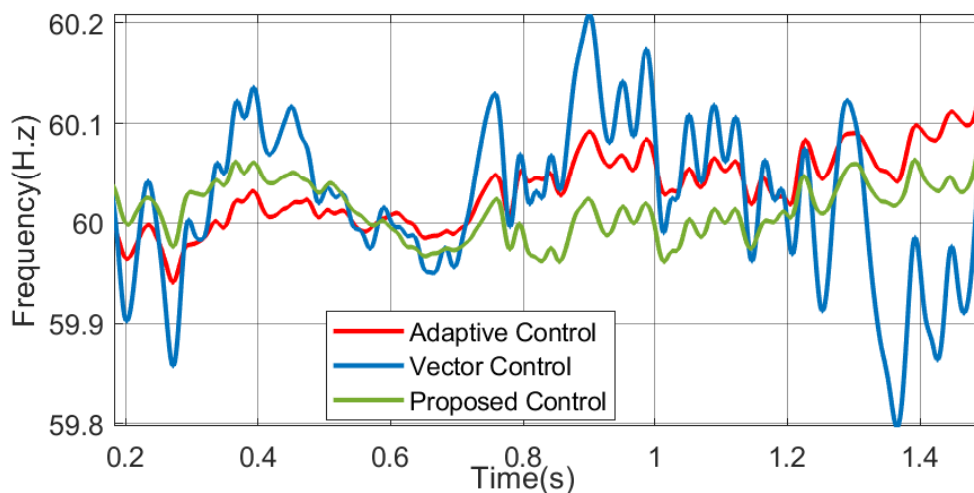


Figure 7.19: Case D: Frequency Deviation from Nominal during Highly Varying Power Demand.

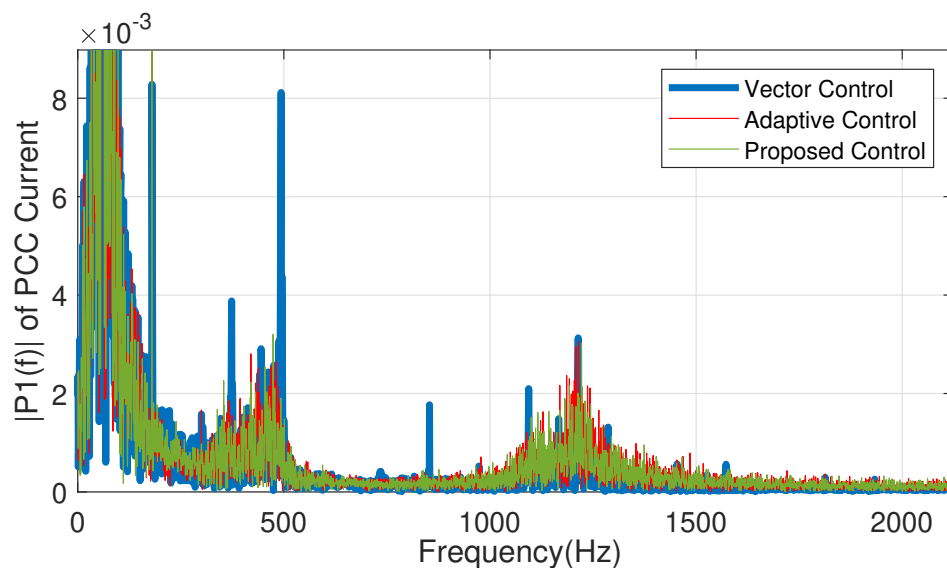


Figure 7.20: Case D: Frequency Spectrum of Inverter Output Current.

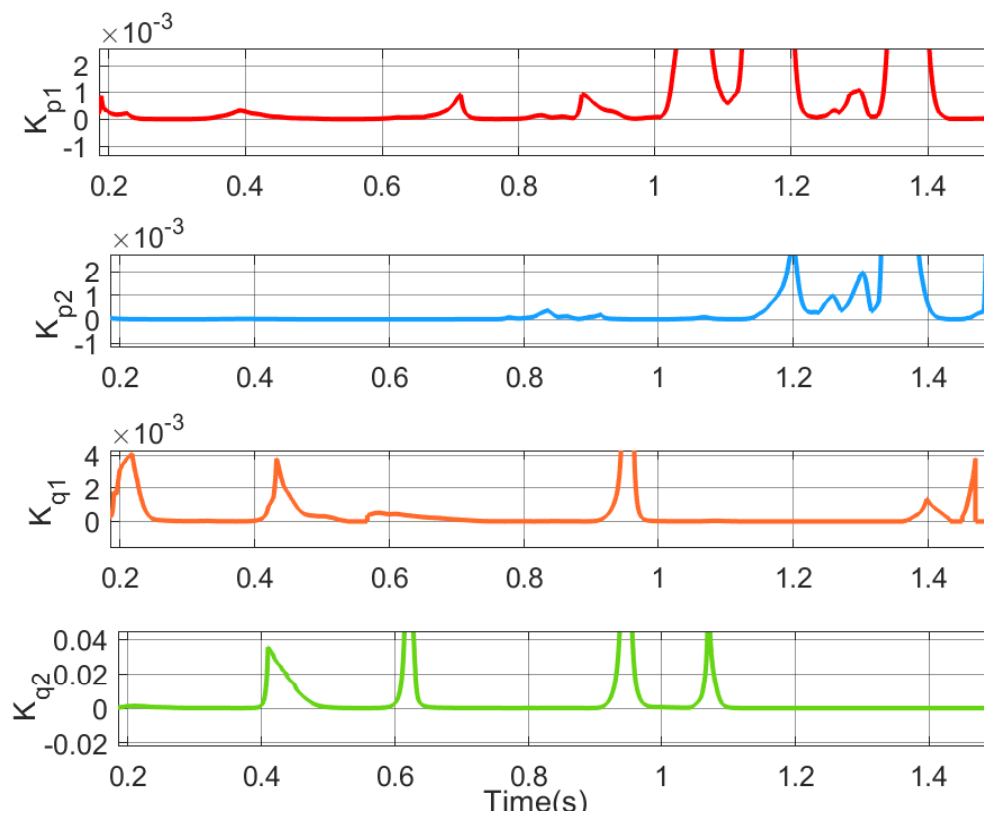


Figure 7.21: Case D: Control Policy Derived for Case D.

7.4.1.5 Case E: Performance validation during high frequency dynamics

The performance of the proposed augmented control during high frequency dynamics introduced by a malfunctioning filter or as a result of interaction between filter parameters with grid impedance is validated in this test scenario. Figure 7.22 shows the power output for the inverter during such an instance. The results depicts the ability of the proposed control to maintain power quality and meet the demand set by the reference during the extreme dynamic conditions, where the conventional control fails. This showcases the wider operating range offered by the proposed integrated control loop.

The frequency spectrum of the inverter output and the corresponding input control sequence for Case E is showcased in Fig. ??.

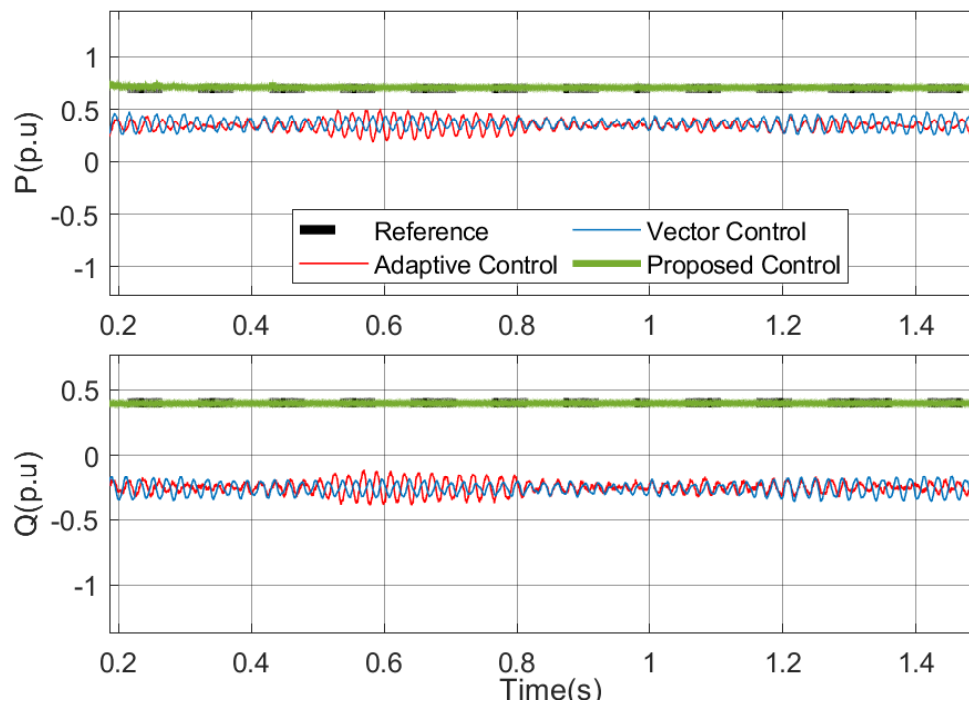


Figure 7.22: Case E: Inverter Output Corresponding to Case E.

7.4.2 Scalability Test

The discussions presented in the above section, based on the analysis on a small system, shows the need for improve control performance and the advantages of proposed methodology. Furthermore, the performance of the proposed control method in a real world scenario

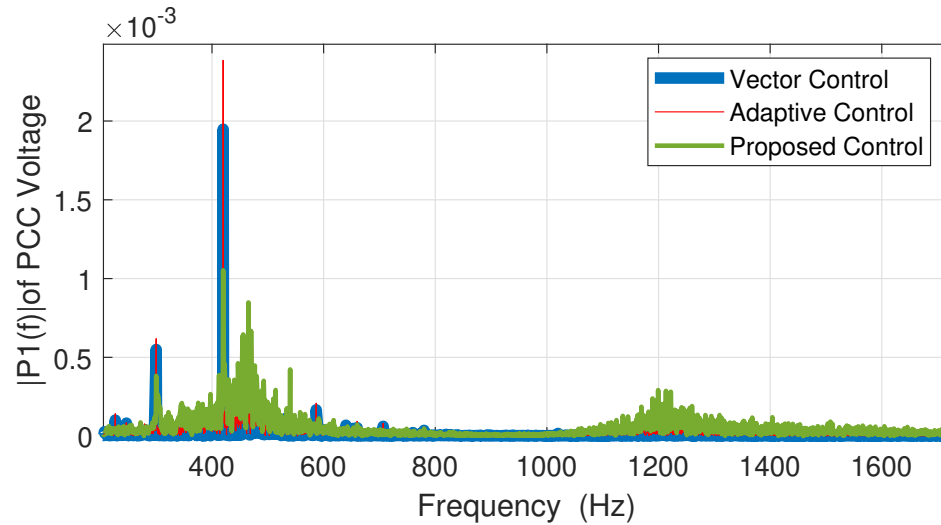


Figure 7.23: Case E: Frequency Spectrum of Inverter Output Corresponding to Case E.

can be demonstrated by analyzing it on a representative scaled system. In this section the proposed architecture is validated based on its performance on an IEEE 123 bus test system, which is shown in Figure 7.24. Two tests cases are presented. Case 1 analyzes the performance during a grid fault and Case 2 during a load change. As shown in Figure 7.24, the proposed inverter is integrated to bus 48 of the 123 bus system.

7.4.2.1 Case 1: Performance validation during grid fault

The performance of the proposed approach to a grid fault is validated on the scaled system with a three phase to ground fault applied at 0.7s on bus 47. The PCC voltage corresponding to the grid fault initiated at 0.7s is shown in Figure 7.25. The voltage rise phenomenon that occurs due to error accumulation is reduced with the proposed control compared to the conventional control.

The faster control action of the proposed control is depicted in Figure 7.26.

The control input sequence discussed in Figure 7.27 shows the coordination between the controllers in integrated control during the grid dynamics. Figure 7.27 shows that the contribution from adaptive control is higher compared to conventional during the instant of the dynamics.

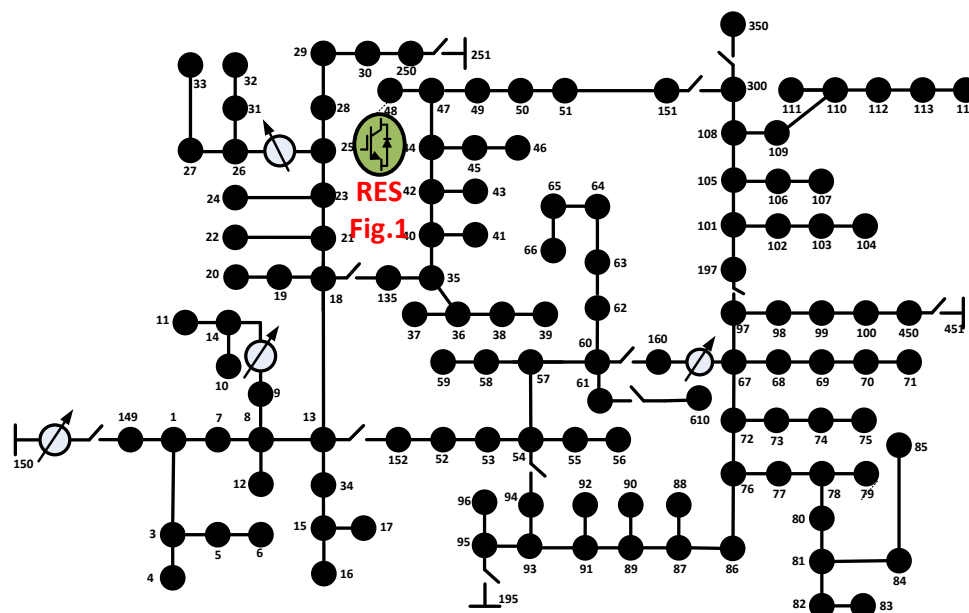


Figure 7.24: One Line Diagram of IEEE 123 Bus System used for Scalability Test.

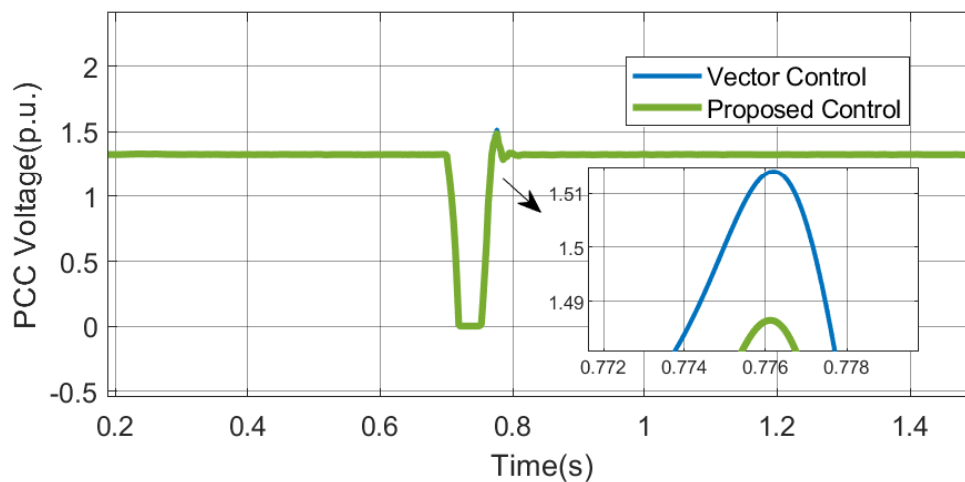


Figure 7.25: Case 1: PCC Voltage of Inverter Corresponding to Grid Fault.

7.4.2.2 Case 2: Performance validation during reference tracking

The superiority of the proposed control compared to static controllers, resulting from its faster control action, is validated on the scaled system using Case 2. The ability of the proposed controller to track the reference faster than conventional control is showcased in

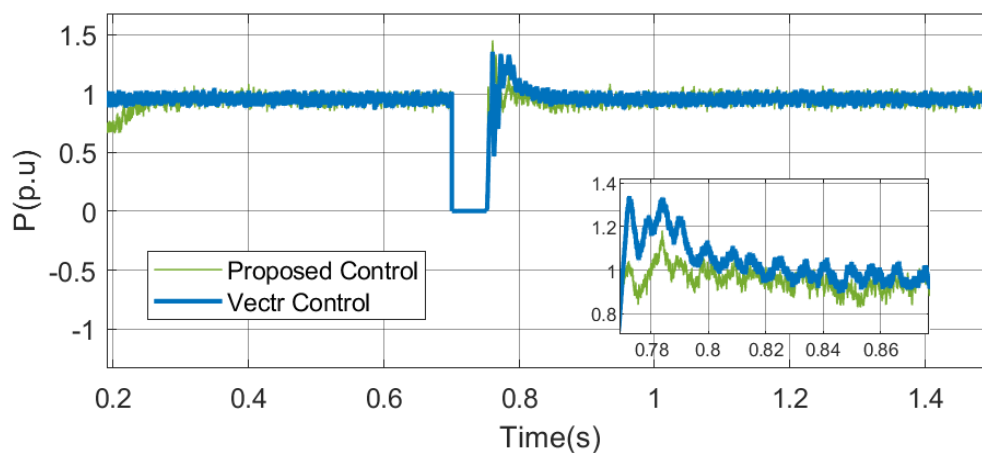


Figure 7.26: Case 1: Inverter Output Power during Grid Fault.

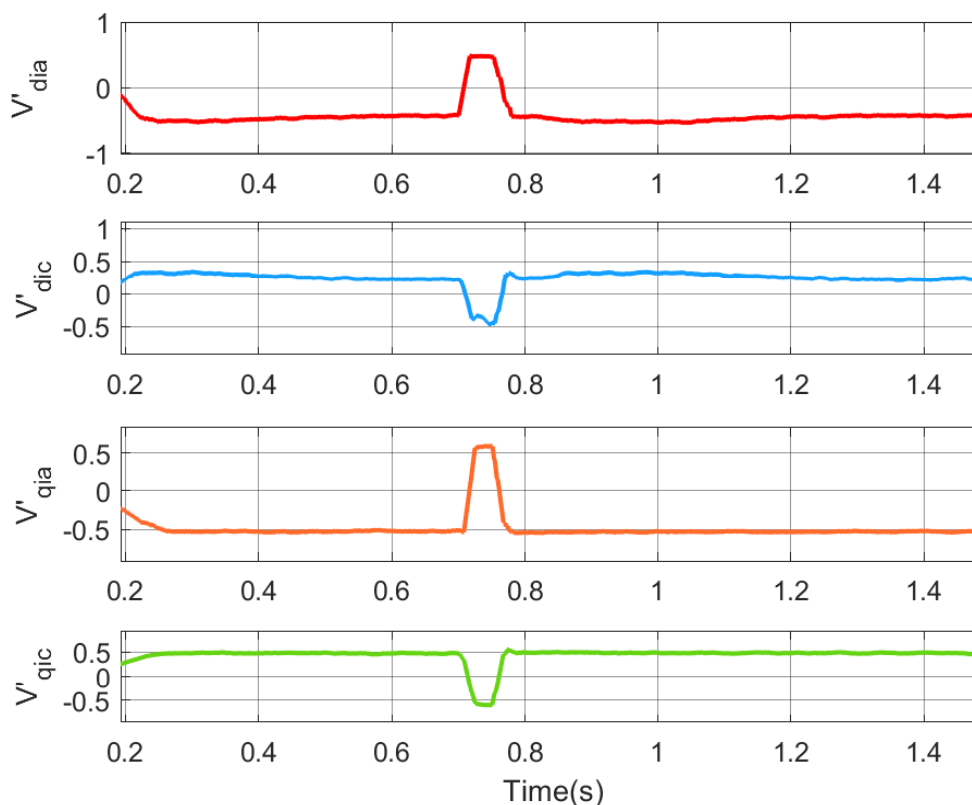


Figure 7.27: Case 1: Control Sequence Developed by the Proposed Control for Grid Fault.

Figure 7.28.

The steady state error with the proposed controller is 84% reduced compared to the conventional control with the control input sequence shown in Figure 7.29.

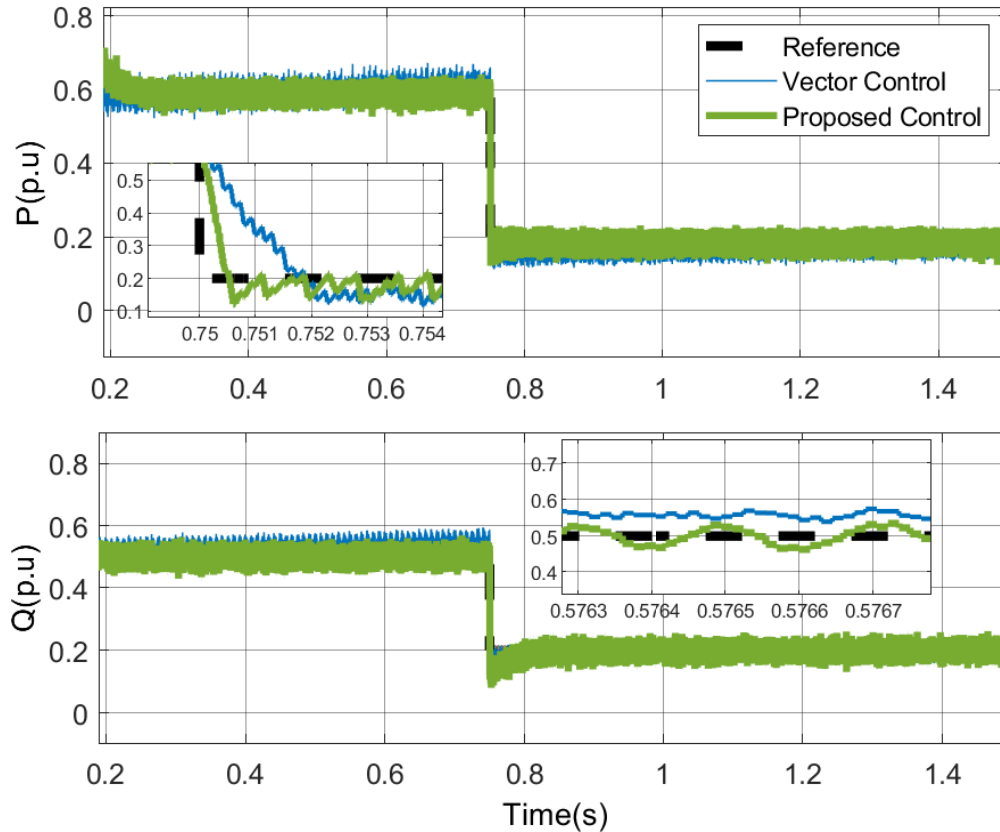


Figure 7.28: Case 2: Inverter Output Power during Grid Fault.

Table 7.2: Comparison of Scalability Test Results
VC: Vector Control, PC: Proposed Control

Case	Parameter	VC	PC	% Reduction
Case 1	V_{pcc} overshoot (%)	1.52	1.485	2.30
Case 1	V_{pcc} settling time T_s (s)	0.08	0.03	62.5
Case 2	P_{pcc} settling time T_s (s)	0.02	0.00054	97
Case 2	P_{pcc} steady error (p.u.)	0.05	0.008	84

7.5 Chapter Summary

A frequency decomposition based integrated control architecture for grid connected inverters is discussed in this work. The proposed architecture augments the conventional control with an adaptive identification based control loop. An energy function-based approach that represents the grid dynamics as a function of the change in energy at the inverter terminals is discussed in this paper. The control policy for coordinating the controllers is derived

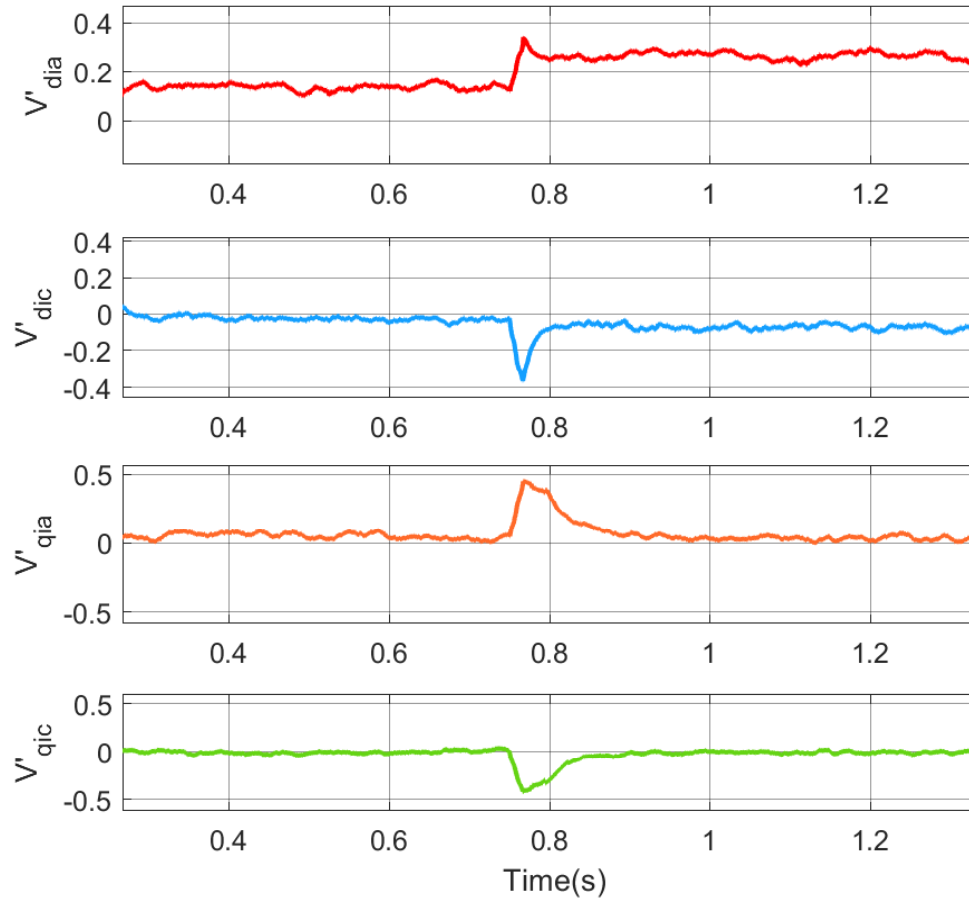


Figure 7.29: Case 2: Control Input Sequence Developed by Proposed Control during Case 2.

using an optimization function that acts considering the nonlinear behavior of the system dynamics. The ability of the proposed approach to reduce the oscillation frequencies in the inverter output, thereby improving the overall power quality of the output, is validated. The experimental and scalability test results discussed in this paper showcase the faster control performance of the proposed control architecture with a wider operating region, as compared with conventional control.

CHAPTER 8: CONCLUSIONS AND FUTURE WORK

In this dissertation, an advanced control framework for DFIG based WECS and inverter-based DER have been designed and demonstrated. The main purpose of this dissertation is to provide solutions to improve the overall stability and reliability of the grid even with the high penetration of renewable-based resources. The advanced control approaches discussed in this dissertation can be seamlessly interfaced with the existing architecture thereby assuring their ability to provide ancillary services to the grid as demanded by the grid code. The merits of the proposed control approach are highlighted by comparing it with the existing architecture. The performance and application of these in real-world scenarios is supported by performing real-time simulations based on OPAL-RT and scalability test performed on 123 bus system. Further, the complexity of the control approaches and their possibility of practical implementation by realization using commercialized digital signal controllers is also discussed. The proposed control approach enhances the overall operational range and reliability of the RES integrated power system.

- Chapter 1 discusses the challenges and issues faced by the RES integrated power system.
- A modified speed sensorless adaptive framework for DFIG robust to current sensor failure which ensures excellent dynamic performance has been discussed in Chapter 2 and Chapter3.
- An efficiently coordinated control approach that ensures excellent frequency regulation capability and overall stability improvement in the weak grid is discussed in Chapter4 and Chapter5.
- Finally, Chapter 6 and 7 proposes a control architecture for RES based generation that improves the overall performance at the distribution level.

The dissertation also proposes a future work to develop a coordinated control framework for frequency regulation based on the MIMO identification approach. The mathematical framework for this has been developed and some preliminary results has been discussed. Furthermore, a coordinated control framework for synchronous condenser based stability enhancement for a wind integrated to a weak grid is proposed for future work.

Some potential future research plans includes,

- MIMO based coordinated approach can be extended to large wind farms to coordinated among wind farms considering the wind speed and wake effect to efficiently utilize the variable wind power to improve stability of RES integrated power grid network.
- A modified grid side control architecture to take care of the low frequency and sub-synchronous oscillations that occur in a weak grid can be a future research plan to consider.

LIST OF PUBLICATIONS

Refereed Journals

1. S. Hasan, A. R. Nair, R. Bhattarai, S. Kamalasan and K. M. Muttaqi, "A Coordinated Optimal Feedback Control of Distributed Generators for Mitigation of Motor Starting Voltage Sags in Distribution Networks," in *IEEE Transactions on Industry Applications*, vol. 56, no. 1, pp. 864-875, Jan.-Feb. 2020.
2. A. Thakallapelli, A. R. Nair, B. D. Biswas and S. Kamalasan, "Frequency Regulation and Control of Grid-Connected Wind Farms Based on Online Reduced-Order Modeling and Adaptive Control," in *IEEE Transactions on Industry Applications*, vol. 56, no. 2, pp. 1980-1989, March-April 2020.
3. A. R. Nair, R. Bhattarai and S. Kamalasan, "Mutual Inductance Estimation Based Sensorless Adaptive Variance Controller for Doubly Fed Induction Generator," in *IEEE Transactions on Industry Applications*, vol. 56, no. 6, pp. 7166-7175, Nov.-Dec. 2020.
4. A. R. Nair, R. Bhattarai, M. Smith and S. Kamalasan, "Parametrically Robust Identification Based Sensorless Control Approach for Doubly Fed Induction Generator," in *IEEE Transactions on Industry Applications*, vol. 57, no. 1, pp. 1024-1034, Jan.-Feb. 2021.
5. A. R. Nair, R. Bhattarai, M. Smith and S. Kamalasan, "A Hybrid Adaptive Control Architecture for Grid Connected Inverter with Optimal Policy Generation," in *IEEE Transactions on Industry Applications*.

Refereed Conferences

1. A. R. Nair, R. Bhattarai and S. Kamalasan, "Parametrically Robust Mutual Inductance Estimation based Adaptive Control Architecture for Doubly Fed Induction Generator (DFIG)," 2019 IEEE Energy Conversion Congress and Exposition (ECCE), Baltimore, MD, USA, 2019, pp. 434-441.

2. A. R. Nair, R. Bhattarai and S. Kamalasan, "A Sensorless Adaptive Grid Side Control Approach for Doubly Fed Induction Generator (DFIG)," 2019 IEEE Industry Applications Society Annual Meeting, Baltimore, MD, USA, 2019, pp. 1-10.
3. J.Geis-Schroer, A. R. Nair, S.Patel, S. Kamalasan, "Modeling and Analysis of a Weak Grid Considering the Effects of Phase-Locked Loop and Synchronous Condenser Integration on Grid Stability".
4. A. R. Nair, M. Smith and S. Kamalasan, "Optimization based Integrated Adaptive Control Architecture for Grid Connected Inverter (GCI)," 2020 IEEE Energy Conversion Congress and Exposition (ECCE), 2020, pp. 3112-3118.
5. Ogundairo, A. R. Nair, M. Smith and S. Kamalasan, "Online Adaptive Damping Controller Architecture for Wind Integrated Power Grid," 2020 IEEE International Conference on Power Electronics, Drives and Energy Systems (PEDES), 2020, pp. 1-6.
6. A. R. Nair, R. Bhattarai, M. Smith and S. Kamalasan, "Energy Function Based Modified Integrated Control Architecture For Grid Connected Inverter," 2020 IEEE Industry Applications Society Annual Meeting, 2020, pp. 1-7.

REFERENCES

- [1] R. Bhattarai, N. Gurung, and S. Kamalasadana, "Dual mode control of a three-phase inverter using minimum variance adaptive architecture," *IEEE Transactions on Industry Applications*, vol. 54, pp. 3868–3880, July 2018.
- [2] H. Polinder, J. A. Ferreira, B. B. Jensen, A. B. Abrahamsen, K. Atallah, and R. A. McMahon, "Trends in wind turbine generator systems," *IEEE Journal of Emerging and Selected Topics in Power Electronics*, vol. 1, pp. 174–185, Sep. 2013.
- [3] R. Cardenas, R. Pena, S. Alepuz, and G. Asher, "Overview of control systems for the operation of dfigs in wind energy applications," *IEEE Transactions on Industrial Electronics*, vol. 60, pp. 2776–2798, July 2013.
- [4] G. Lalor, A. Mullane, and M. O'Malley, "Frequency control and wind turbine technologies," *IEEE Transactions on Power Systems*, vol. 20, pp. 1905–1913, Nov 2005.
- [5] R. Pena, J. C. Clare, and G. M. Asher, "Doubly fed induction generator using back-to-back pwm converters and its application to variable-speed wind-energy generation," *IEE Proceedings - Electric Power Applications*, vol. 143, pp. 231–241, May 1996.
- [6] S. Li, R. Chaloo, and M. J. Nemmers, "Comparative study of dfig power control using stator-voltage and stator-flux oriented frames," in *2009 IEEE Power Energy Society General Meeting*, pp. 1–8, July 2009.
- [7] L. Xu and P. Cartwright, "Direct active and reactive power control of dfig for wind energy generation," *IEEE Transactions on Energy Conversion*, vol. 21, pp. 750–758, Sep. 2006.
- [8] Y. Zhang, Z. Li, Z. Piao, W. Xie, X. Wei, and W. Xu, "A novel three-vectors-based predictive direct power control of doubly fed induction generator for wind energy applications," in *2012 IEEE Energy Conversion Congress and Exposition (ECCE)*, pp. 793–800, Sep. 2012.
- [9] M. Debouza and A. Al-Durra, "Grid ancillary services from doubly fed induction generator-based wind energy conversion system: A review," *IEEE Access*, vol. 7, pp. 7067–7081, 2019.
- [10] R. Billinton and W. Wangdee, "Reliability-based transmission reinforcement planning associated with large-scale wind farms," *IEEE Transactions on Power Systems*, vol. 22, pp. 34–41, Feb 2007.
- [11] B. Singh, G. K. Kasal, and S. Gairola, "Power quality improvement in conventional electronic load controller for an isolated power generation," *IEEE Transactions on Energy Conversion*, vol. 23, pp. 764–773, Sep. 2008.
- [12] N. Barberis Negra, O. Holmstrom, B. Bak-Jensen, and P. Sorensen, "Aspects of relevance in offshore wind farm reliability assessment," *IEEE Transactions on Energy Conversion*, vol. 22, pp. 159–166, March 2007.

- [13] A. P. de Moura, A. A. F. de Moura, and A. A. F. de Moura, "Analysis of injected apparent power and flicker in a distribution network after wind power plant connection," *IET Renewable Power Generation*, vol. 2, pp. 113–122, June 2008.
- [14] A. Petersson, T. Thiringer, L. Harnefors, and T. Petru, "Modeling and experimental verification of grid interaction of a dfig wind turbine," *IEEE Transactions on Energy Conversion*, vol. 20, pp. 878–886, Dec 2005.
- [15] and and F. Blaabjerg, "Flicker study on variable speed wind turbines with doubly fed induction generators," *IEEE Transactions on Energy Conversion*, vol. 20, pp. 896–905, Dec 2005.
- [16] S. T. Tentzerakis and S. A. Papathanassiou, "An investigation of the harmonic emissions of wind turbines," *IEEE Transactions on Energy Conversion*, vol. 22, no. 1, pp. 150–158, 2007.
- [17] Z. Chen, "Compensation schemes for a scr converter in variable speed wind power systems," *IEEE Transactions on Power Delivery*, vol. 19, pp. 813–821, April 2004.
- [18] S. Bozhko, G. Asher, R. Li, J. Clare, and L. Yao, "Large offshore dfig-based wind farm with line-commutated hvdc connection to the main grid: Engineering studies," *IEEE Transactions on Energy Conversion*, vol. 23, pp. 119–127, March 2008.
- [19] S. V. Bozhko, R. Blasco-Gimenez, R. Li, J. C. Clare, and G. M. Asher, "Control of offshore dfig-based wind farm grid with line-commutated hvdc connection," *IEEE Transactions on Energy Conversion*, vol. 22, pp. 71–78, March 2007.
- [20] and, J. R. Bumby, P. J. Tavner, and S. Yang, "Coordinated control of an hvdc link and doubly fed induction generators in a large offshore wind farm," *IEEE Transactions on Power Delivery*, vol. 21, pp. 463–471, Jan 2006.
- [21] F. Blaabjerg, , and S. B. Kjaer, "Power electronics as efficient interface in dispersed power generation systems," *IEEE Transactions on Power Electronics*, vol. 19, pp. 1184–1194, Sep. 2004.
- [22] P. C. Krause and C. H. Thomas, "Simulation of symmetrical induction machinery," *IEEE Transactions on Power Apparatus and Systems*, vol. 84, pp. 1038–1053, Nov. 1965.
- [23] S. Li, T. A. Haskew, K. A. Williams, and R. P. Swatloski, "Control of dfig wind turbine with direct-current vector control configuration," *IEEE Transactions on Sustainable Energy*, vol. 3, pp. 1–11, Jan 2012.
- [24] J. Mohammadi, S. Vaez-Zadeh, S. Afsharnia, and E. Daryabeigi, "A combined vector and direct power control for dfig-based wind turbines," *IEEE Transactions on Sustainable Energy*, vol. 5, pp. 767–775, July 2014.
- [25] and P. Cartwright, "Direct active and reactive power control of dfig for wind energy generation," *IEEE Transactions on Energy Conversion*, vol. 21, pp. 750–758, Sep. 2006.

- [26] A. Kadri, H. Marzougui, and F. Bacha, "Mppt control methods in wind energy conversion system using dfig," in *2016 4th International Conference on Control Engineering Information Technology (CEIT)*, pp. 1–6, Dec 2016.
- [27] R. Bibave and V. Kulkarni, "A novel maximum power point tracking method for wind energy conversion system: A review," in *2018 International Conference on Computation of Power, Energy, Information and Communication (ICCPEIC)*, pp. 430–433, March 2018.
- [28] I. John and B. Jayanand, "Voltage control and maximum power tracking of dfig based wind power generator," in *2015 International Conference on Power, Instrumentation, Control and Computing (PICC)*, pp. 1–6, Dec 2015.
- [29] R. Bibave and V. Kulkarni, "A novel maximum power point tracking method for wind energy conversion system: A review," in *2018 International Conference on Computation of Power, Energy, Information and Communication (ICCPEIC)*, pp. 430–433, March 2018.
- [30] D. Biswas, S. S. Sahoo, P. M. Tripathi, and K. Chatterjee, "Maximum power point tracking for wind energy system by adaptive neural-network based fuzzy inference system," in *2018 4th International Conference on Recent Advances in Information Technology (RAIT)*, pp. 1–6, March 2018.
- [31] Y. Han, R. Ma, W. Pan, and L. Xu, "Maximum power point tracking of dfig wind turbine system based on adaptive higher order sliding mode," in *2017 Chinese Automation Congress (CAC)*, pp. 2446–2451, Oct 2017.
- [32] A. Muneer and M. B. Kadri, "Pitch angle control of dfig using self tuning neuro fuzzy controller," in *2013 International Conference on Renewable Energy Research and Applications (ICRERA)*, pp. 316–320, Oct 2013.
- [33] A. Bakouri, H. Mahmoudi, M. Barara, A. Abbou, A. Bennassar, and M. Moutchou, "A complete control startegy of dfig connected to the grid for wind energy conversion systems," in *2015 3rd International Renewable and Sustainable Energy Conference (IRSEC)*, pp. 1–6, Dec 2015.
- [34] E. B. Muhando, T. Senjyu, A. Uehara, T. Funabashi, and C. Kim, "Lqg design for megawatt-class wecs with dfig based on functional models' fidelity prerequisites," *IEEE Transactions on Energy Conversion*, vol. 24, pp. 893–904, Dec 2009.
- [35] Y. Xiao and Y. Lv, "Pitch-controlled wind turbine synchronized cutting-in control and modeling-simulation," in *Proceedings of the 10th World Congress on Intelligent Control and Automation*, pp. 3113–3117, July 2012.
- [36] P. Li, W. Hu, R. Hu, and Z. Chen, "The integrated control strategy for primary frequency control of dfigs based on virtual inertia and pitch control," in *2016 IEEE Innovative Smart Grid Technologies - Asia (ISGT-Asia)*, pp. 430–435, Nov 2016.
- [37] B. E. Elnaghi, M. E. Dessouki, and F. A. Elkader, "Experimental investigation of pitch angle controller for dfig based wind energy conversion system," in *2017 Nineteenth International Middle East Power Systems Conference (MEPCON)*, pp. 1477–1482, Dec 2017.

- [38] L. Jianlin and X. Honghua, "Research on control system of high power dfig wind power system," in *2008 International Conference on MultiMedia and Information Technology*, pp. 669–672, Dec 2008.
- [39] G. Tapia, A. Tapia, and J. X. Ostolaza, "Proportional and integral regulator-based approach to wind farm reactive power management for secondary voltage control," *IEEE Transactions on Energy Conversion*, vol. 22, pp. 488–498, June 2007.
- [40] M. E. Moursi, G. Joos, and C. Abbey, "A secondary voltage control strategy for transmission level interconnection of wind generation," *IEEE Transactions on Power Electronics*, vol. 23, pp. 1178–1190, May 2008.
- [41] M. Kayikci and J. V. Milanovic, "Reactive power control strategies for dfig-based plants," *IEEE Transactions on Energy Conversion*, vol. 22, pp. 389–396, June 2007.
- [42] J. P. da Costa, H. Pinheiro, T. Degner, and G. Arnold, "Robust controller for dfigs of grid-connected wind turbines," *IEEE Transactions on Industrial Electronics*, vol. 58, pp. 4023–4038, Sep. 2011.
- [43] M. Alberdi, M. Amundarain, A. Garrido, I. Garrido, and F. J. Sainz, "Control for voltage dips ride-through of oscillating water column-based wave power generation plant equipped with doubly-fed induction generator," in *2011 19th Mediterranean Conference on Control Automation (MED)*, pp. 371–377, June 2011.
- [44] S. K. Sahoo, A. K. Sinha, and N. K. Kishore, "Low voltage ride-through of a grid-connected doubly-fed induction generator with speed sensorless vector control," in *2016 National Power Systems Conference (NPSC)*, pp. 1–6, Dec 2016.
- [45] S. Foster, L. Xu, and B. Fox, "Coordinated reactive power control for facilitating fault ride through of doubly fed induction generator- and fixed speed induction generator-based wind farms," *IET Renewable Power Generation*, vol. 4, pp. 128–138, March 2010.
- [46] R. Cardenas, R. Pena, J. Proboste, G. Asher, J. Clare, and P. Wheeler, "Mras observers for sensorless control of doubly-fed induction generators," in *2008 4th IET Conference on Power Electronics, Machines and Drives*, pp. 568–572, April 2008.
- [47] G. Iwanski, M. Szypulski, T. Luszczuk, and P. Pura, "Cross and dot product based mras observer of the rotor position of doubly fed induction machine," in *2014 Ninth International Conference on Ecological Vehicles and Renewable Energies (EVER)*, pp. 1–5, March 2014.
- [48] R. Bhattarai, N. Gurung, and S. Kamalasan, "Minimum variance controller based adaptive control for doubly fed induction generator," in *2016 North Amer. Power Symp. (NAPS)*, pp. 1–6, Sep. 2016.
- [49] R. Bhattarai, N. Gurung, S. Ghosh, and S. Kamalasan, "Parametrically robust dynamic speed estimation based control for doubly fed induction generator," *IEEE Transactions on Industry Applications*, vol. 54, pp. 6529–6542, Nov 2018.
- [50] R. Cardenas, R. Pena, J. Proboste, G. Asher, and J. Clare, "Mras observer for sensorless control of standalone doubly fed induction generators," *IEEE Transactions on Energy Conversion*, vol. 20, pp. 710–718, Dec 2005.

- [51] R. Pena, R. Cardenas, J. Proboste, G. Asher, and J. Clare, "Sensorless control of doubly-fed induction generators using a rotor-current-based mras observer," *IEEE Transactions on Industrial Electronics*, vol. 55, pp. 330–339, Jan 2008.
- [52] B. Shen and B. T. Ooi, "Parameter-insensitive sensorless decoupled p-q controller for doubly-fed induction machine," in *2007 IEEE Power Electronics Specialists Conference*, pp. 2102–2107, June 2007.
- [53] R. Datta and V. T. Ranganathan, "Direct power control of grid-connected wound rotor induction machine without rotor position sensors," *IEEE Transactions on Power Electronics*, vol. 16, pp. 390–399, May 2001.
- [54] A. Parida and D. Chatterjee, "A robust parameter non-sensitive rotor position and speed estimator for dfig," in *Proceedings of The 2014 International Conference on Control, Instrumentation, Energy and Communication (CIEC)*, pp. 12–16, Jan 2014.
- [55] M. Abdelrahem, C. Hackl, and R. Kennel, "Application of extended kalman filter to parameter estimation of doubly-fed induction generators in variable-speed wind turbine systems," in *2015 International Conference on Clean Electrical Power (ICCEP)*, pp. 226–233, June 2015.
- [56] K. Belmokhtar, H. Ibrahim, and A. Merabet, "Online parameter identification for a dfig driven wind turbine generator based on recursive least squares algorithm," in *2015 IEEE 28th Canadian Conference on Electrical and Computer Engineering (CCECE)*, pp. 965–969, May 2015.
- [57] A. Susperregui, J. Jugo, I. Lizarraga, and G. Tapia, "Automated control of doubly fed induction generator integrating sensorless parameter estimation and grid synchronisation," *IET Renewable Power Generation*, vol. 8, pp. 76–89, January 2014.
- [58] Y. Zhang, Y. Yuan, X. Chen, K. Qian, and B. Wu, "The optimization initial value and micro-variation search algorithm and its simulation in parameter identification of doubly fed induction generator," in *2009 International Conference on Sustainable Power Generation and Supply*, pp. 1–4, April 2009.
- [59] Yajun Rong, Hong Wang, Wei Yang, and Hanhong Qi, "Artificial neural network in the application of the doubly-fed type wind power generator parameter identification," in *2014 IEEE Conference and Expo Transportation Electrification Asia-Pacific (ITEC Asia-Pacific)*, pp. 1–5, Aug 2014.
- [60] K. Åström and B. Wittenmark, *Adaptive Control*. Addison-Wesley series in electrical engineering : control engineering, Addison-Wesley, 1995.
- [61] B. Lu, Y. Li, X. Wu, and Z. Yang, "A review of recent advances in wind turbine condition monitoring and fault diagnosis," in *2009 IEEE Power Electronics and Machines in Wind Applications*, pp. 1–7, June 2009.
- [62] R. Bhattarai, N. Gurung, A. Thakallapelli, and S. Kamalasan, "Reduced order state observer based feedback control methodologies for doubly fed induction machine," *IEEE Transactions on Industry Applications*, vol. PP, no. 99, pp. 1–1, 2018.

- [63] K. Rothenhagen and F. W. Fuchs, "Current sensor fault detection and reconfiguration for a doubly fed induction generator," in *2007 IEEE Power Electronics Specialists Conference*, pp. 2732–2738, June 2007.
- [64] R. Pena, R. Cardenas, J. Proboste, G. Asher, and J. Clare, "Sensorless control of doubly-fed induction generators using a rotor-current-based mras observer," *IEEE Transactions on Industrial Electronics*, vol. 55, pp. 330–339, Jan 2008.
- [65] R. Bhattarai, N. Gurung, S. Ghosh, and S. Kamalasadana, "Parametrically robust dynamic speed estimation based control for doubly fed induction generator," *IEEE Transactions on Industry Applications*, vol. 54, pp. 6529–6542, Nov 2018.
- [66] R. Pena, R. Cardenas, J. Proboste, G. Asher, and J. Clare, "Sensorless control of doubly-fed induction generators using a rotor-current-based mras observer," *IEEE Transactions on Industrial Electronics*, vol. 55, pp. 330–339, Jan 2008.
- [67] G. Iwanski and W. Koczara, "Sensorless stand alone variable speed system for distributed generation," in *2004 IEEE 35th Annual Power Electronics Specialists Conference (IEEE Cat. No.04CH37551)*, vol. 3, pp. 1915–1921 Vol.3, June 2004.
- [68] G. Iwanski and W. Koczara, "Sensorless direct voltage control of the stand-alone slip-ring induction generator," *IEEE Transactions on Industrial Electronics*, vol. 54, pp. 1237–1239, April 2007.
- [69] S. Li, T. A. Haskew, K. A. Williams, and R. P. Swatloski, "Control of dfig wind turbine with direct-current vector control configuration," *IEEE Transactions on Sustainable Energy*, vol. 3, pp. 1–11, Jan 2012.
- [70] R. Pena, R. Cardenas, J. Proboste, G. Asher, and J. Clare, "Sensorless control of doubly-fed induction generators using a rotor-current-based mras observer," *IEEE Transactions on Industrial Electronics*, vol. 55, pp. 330–339, Jan 2008.
- [71] R. Bhattarai, N. Gurung, S. Ghosh, and S. Kamalasadana, "Parametrically robust dynamic speed estimation based control for doubly fed induction generator," in *2017 IEEE Industry Applications Society Annual Meeting*, pp. 1–8, Oct 2017.
- [72] L. Ljung, *System Identification: Theory for the User*. Pearson Education, 1998.
- [73] N. Zhou, D. J. Trudnowski, J. W. Pierre, and W. A. Mittelstadt, "Electromechanical mode online estimation using regularized robust rls methods," *IEEE Trans. on Power Syst.*, vol. 23, pp. 1670–1680, Nov 2008.
- [74] K. Åström and B. Wittenmark, *Adaptive Control: Second Edition*. Dover Books on Electrical Engineering, Dover Publications, 2013.
- [75] J. Hetthéssy and L. Keviczky, "Minimum variance control a review and outlook," *Periodica Polytechnica Electrical Engineering*, vol. 21, no. 1, pp. 31–45, 1977.
- [76] "Wind speed profile."
- [77] X. Hua, X. Hongyuan, and L. Na, "Control strategy of dfig wind turbine in primary frequency regulation," in *2018 13th IEEE Conference on Industrial Electronics and Applications (ICIEA)*, pp. 1751–1755, May 2018.

- [78] S. Ghosh, S. Kamalasan, N. Senroy, and J. Enslin, "Doubly fed induction generator (dfig)-based wind farm control framework for primary frequency and inertial response application," *IEEE Transactions on Power Systems*, vol. 31, pp. 1861–1871, May 2016.
- [79] T. Wang, L. Ding, S. Yin, J. Jiang, F. Cheng, and J. Si, "A new control strategy of dfig-based wind farms for power system frequency regulation," in *2015 IEEE PES Asia-Pacific Power and Energy Engineering Conference (APPEEC)*, pp. 1–5, Nov 2015.
- [80] F. Yantao and X. Zhen, "Coordinated primary frequency regulation and inertia response based on dfig using over speed and torque reserve," in *2017 36th Chinese Control Conference (CCC)*, pp. 9141–9144, July 2017.
- [81] Z. Wang and W. Wu, "Coordinated control method for dfig-based wind farm to provide primary frequency regulation service," *IEEE Transactions on Power Systems*, vol. 33, pp. 2644–2659, May 2018.
- [82] C. Tu, J. Cao, L. He, and Y. Fang, "Combined active and reactive power control strategy to improve power system frequency stability with dfigs," *The Journal of Engineering*, vol. 2017, no. 13, pp. 2021–2025, 2017.
- [83] C. Zhangjie, W. Xiaoru, and T. Jin, "Control strategy of large-scale dfig-based wind farm for power grid frequency regulation," in *Proceedings of the 31st Chinese Control Conference*, pp. 6835–6840, July 2012.
- [84] Y. Cui, P. Song, X. S. Wang, W. X. Yang, H. Liu, and H. M. Liu, "Wind power virtual synchronous generator frequency regulation characteristics field test and analysis," in *2018 2nd International Conference on Green Energy and Applications (ICGEA)*, pp. 193–196, March 2018.
- [85] Z. Wang and W. Wu, "Coordinated control method for dfig-based wind farm to provide primary frequency regulation service," *IEEE Transactions on Power Systems*, vol. 33, pp. 2644–2659, May 2018.
- [86] F. Teng, M. Aunedi, D. Pudjianto, and G. Strbac, "Benefits of demand-side response in providing frequency response service in the future gb power system," *Frontiers in Energy Research*, vol. 3, p. 36, 2015.
- [87] Y. Zhou, D. D. Nguyen, P. C. Kjø̃r, and S. Saylor, "Connecting wind power plant with weak grid - challenges and solutions," in *2013 IEEE Power Energy Society General Meeting*, pp. 1–7, 2013.
- [88] J. Hu, Y. Huang, D. Wang, H. Yuan, and X. Yuan, "Modeling of grid-connected dfig-based wind turbines for dc-link voltage stability analysis," *IEEE Transactions on Sustainable Energy*, vol. 6, no. 4, pp. 1325–1336, 2015.
- [89] N. P. W. Strachan and D. Jovicic, "Stability of a variable-speed permanent magnet wind generator with weak ac grids," *IEEE Transactions on Power Delivery*, vol. 25, no. 4, pp. 2779–2788, 2010.
- [90] Y. Li, L. Fan, and Z. Miao, "Stability control for wind in weak grids," *IEEE Transactions on Sustainable Energy*, vol. 10, no. 4, pp. 2094–2103, 2019.

- [91] "Connection of wind farms to weak ac networks," technical brochure 671, CIGRE, 2016.
- [92] Z. Ali, N. Christofides, L. Hadjidemetriou, E. Kyriakides, Y. Yang, and F. Blaabjerg, "Three-phase phase-locked loop synchronization algorithms for grid-connected renewable energy systems: A review," *Renew. Sustain. Energy Rev.* vol. 90, pp. 434-452, 2018.
- [93] M. J. Korytowski, *Effects of the Phase-Locked Loop on the Stability of a Voltage Source Converter in a Weak Grid Environment*. PhD thesis, University of Pittsburgh, 2015.
- [94] F. Blaabjerg, R. Teodorescu, M. Liserre, and A. Timbus, "Overview of control and grid synchronization for distributed power generation systems," *IEEE Trans. Ind. Electron.* 53, 2006.
- [95] J. Geis-Schroer, A. R. Nair, S. Patel, and S. Kamalasan, "Modeling and analysis of weak grid considering phase locked loop and synchronous condenser effect on grid stability," in *2020 IEEE International Conference on Power Electronics, Smart Grid and Renewable Energy (PESGRE2020)*, pp. 1-6, 2020.
- [96] B. Liu, F. Zhuo, Y. Zhu, H. Yi, and F. Wang, "A three-phase pll algorithm based on signal reforming under distorted grid conditions," *IEEE Transactions on Power Electronics*, vol. 30, no. 9, pp. 5272-5283, 2015.
- [97] S. Golestan, M. Monfared, F. D. Freijedo, and J. M. Guerrero, "Advantages and challenges of a type-3 pll," *IEEE Transactions on Power Electronics*, vol. 28, no. 11, pp. 4985-4997, 2013.
- [98] M. Cespedes and J. Sun, "Adaptive control of grid-connected inverters based on online grid impedance measurements," *IEEE Transactions on Sustainable Energy*, vol. 5, no. 2, pp. 516-523, 2014.
- [99] T. Roinila, M. Vilkkko, and J. Sun, "Broadband methods for online grid impedance measurement," in *2013 IEEE Energy Conversion Congress and Exposition*, pp. 3003-3010, 2013.
- [100] A. V. Timbus, R. Teodorescu, F. Blaabjerg, and U. Borup, "Online grid measurement and ens detection for pv inverter running on highly inductive grid," *IEEE Power Electronics Letters*, vol. 2, no. 3, pp. 77-82, 2004.
- [101] Z. Liu, J. Liu, and Z. Liu, "Analysis, design, and implementation of impulse-injection-based online grid impedance identification with grid-tied converters," *IEEE Transactions on Power Electronics*, vol. 35, no. 12, pp. 12959-12976, 2020.
- [102] C. J. Bett, "9 - gain-scheduled controllers," in *The Electrical Engineering Handbook* (W.-K. CHEN, ed.), pp. 1107 - 1114, Burlington: Academic Press, 2005.
- [103] G. Hallak, C. Nie, and G. Bumiller, "Accurate low access impedance measurements with separated load impedance measurements on the power-line network," *IEEE Transactions on Instrumentation and Measurement*, vol. 67, no. 10, pp. 2282-2293, 2018.

- [104] M. Cespedes and J. Sun, "Adaptive control of grid-connected inverters based on online grid impedance measurements," *IEEE Transactions on Sustainable Energy*, vol. 5, no. 2, pp. 516–523, 2014.
- [105] L. Asiminoaei, R. Teodorescu, F. Blaabjerg, and U. Borup, "Implementation and test of an online embedded grid impedance estimation technique for pv inverters," *IEEE Transactions on Industrial Electronics*, vol. 52, no. 4, pp. 1136–1144, 2005.
- [106] "Opal-rt 2kw hil doubly-fed induction generator (dfig) demo."
- [107] L. Fan and Z. Miao, "An explanation of oscillations due to wind power plants weak grid interconnection," *IEEE Transactions on Sustainable Energy*, vol. 9, no. 1, pp. 488–490, 2018.
- [108] L. Fan and Z. Miao, "Wind in weak grids: 4 hz or 30 hz oscillations?," *IEEE Transactions on Power Systems*, vol. 33, no. 5, pp. 5803–5804, 2018.
- [109] Y. Li, L. Fan, and Z. Miao, "Wind in weak grids: Low-frequency oscillations, sub-synchronous oscillations, and torsional interactions," *IEEE Transactions on Power Systems*, vol. 35, no. 1, pp. 109–118, 2020.
- [110] L. Fan and Z. Miao, "An explanation of oscillations due to wind power plants weak grid interconnection," *IEEE Transactions on Sustainable Energy*, vol. 9, no. 1, pp. 488–490, 2018.
- [111] S. Hasan, N. Gurung, K. M. Muttaqi, and S. Kamalasan, "Electromagnetic field-based control of distributed generator units to mitigate motor starting voltage dips in power grids," *IEEE Transactions on Applied Superconductivity*, vol. 29, pp. 1–4, March 2019.
- [112] and, "Torque and reactive power control of a doubly fed induction machine by position sensorless scheme," *IEEE Transactions on Industry Applications*, vol. 31, pp. 636–642, May 1995.
- [113] M. T. Abolhassani, P. Niazi, H. A. Toliyat, and P. Enjeti, "A sensorless integrated doubly-fed electric alternator/active filter (idea) for variable speed wind energy system," in *38th IAS Annual Meeting on Conference Record of the Industry Applications Conference, 2003.*, vol. 1, pp. 507–514 vol.1, Oct 2003.
- [114] R. Datta and V. T. Ranganathan, "A simple position-sensorless algorithm for rotor-side field-oriented control of wound-rotor induction machine," *IEEE Transactions on Industrial Electronics*, vol. 48, pp. 786–793, Aug 2001.
- [115] K. Huang, G. Chen, S. Huang, and L. Cai, "Experimental evaluation of sensorless control for doubly-fed induction wind power generator," in *2009 International Conference on Electrical Machines and Systems*, pp. 1–6, Nov 2009.
- [116] P. Van Overschee and B. De Moor, "Subspace identification for linear systems: Theory," 05 2019.
- [117] N. Gurung and S. Kamalasan, "Linear-quadratic gaussian based power oscillation damping controller design for doubly fed induction generator," in *2018 IEEE Power Energy Society General Meeting (PESGM)*, pp. 1–5, Aug 2018.

- [118] A. Besançon-Voda, G. Filardi, D. Rey, and A. Franco, "Lqg optimal control strategies for an electro pneumatic actuator," in *2001 European Control Conference (ECC)*, pp. 2670–2675, Sep. 2001.
- [119] A. Niragire, R. Abdulkader, and R. A. McCann, "Linear quadratic gaussian control for resonance damping in microgrids with cascaded converters," in *2017 IEEE Power Energy Society Innovative Smart Grid Technologies Conference (ISGT)*, pp. 1–5, April 2017.
- [120] A. Thakallapelli, S. J. Hossain, and S. Kamalasan, "Coherency based online wide area control of wind integrated power grid," in *2016 IEEE International Conference on Power Electronics, Drives and Energy Systems (PEDES)*, pp. 1–6, Dec 2016.
- [121] J. Sun, "Impedance-based stability criterion for grid-connected inverters," *IEEE Transactions on Power Electronics*, vol. 26, pp. 3075–3078, Nov 2011.
- [122] X. Hou, Y. Sun, H. Han, Z. Liu, W. Yuan, and M. Su, "A fully decentralized control of grid-connected cascaded inverters," *IEEE Transactions on Sustainable Energy*, vol. 10, pp. 315–317, Jan 2019.
- [123] M. C. Chandorkar, D. M. Divan, and R. Adapa, "Control of parallel connected inverters in standalone ac supply systems," *IEEE Transactions on Industry Applications*, vol. 29, pp. 136–143, Jan 1993.
- [124] C. L. DeMarco and C. A. Canizares, "A vector energy function approach for security analysis of ac/dc systems," *IEEE Transactions on Power Systems*, vol. 7, pp. 1001–1011, Aug 1992.
- [125] R. Yousefian, A. Sahami, and S. Kamalasan, "Hybrid transient energy function-based real-time optimal wide-area damping controller," *IEEE Transactions on Industry Applications*, vol. 53, pp. 1506–1516, March 2017.
- [126] E. Sontag, *Mathematical Control Theory: Deterministic Finite-Dimensional Systems*. 01 1998.
- [127] Z. Zhang, F. Liu, J. Deng, Z. Xie, and M. Wang, "An improved lcl filter design method based on stability region and harmonic interaction for grid-connected inverters in weak grid," in *2018 IEEE International Power Electronics and Application Conference and Exposition (PEAC)*, pp. 1–5, 2018.
- [128] M. Liserre, F. Blaabjerg, and S. Hansen, "Design and control of an lcl-filter-based three-phase active rectifier," *IEEE Transactions on Industry Applications*, vol. 41, no. 5, pp. 1281–1291, 2005.
- [129] Q. Liu, L. Peng, Y. Kang, S. Tang, D. Wu, and Y. Qi, "A novel design and optimization method of an lcl filter for a shunt active power filter," *IEEE Transactions on Industrial Electronics*, vol. 61, no. 8, pp. 4000–4010, 2014.
- [130] "Ieee recommended practice and requirements for harmonic control in electric power systems," *IEEE Std 519-2014 (Revision of IEEE Std 519-1992)*, pp. 1–29, 2014.

- [131] R. Pena, J. C. Clare, and G. M. Asher, "Doubly fed induction generator using back-to-back pwm converters and its application to variable-speed wind-energy generation," *IEE Proceedings - Electric Power Applications*, vol. 143, pp. 231–241, May 1996.
- [132] K. Padiyar, *Structure Preserving Energy Functions in Power Systems: Theory and Applications*. 03 2016.
- [133] A. V. Oppenheim, R. W. Schaffer, and J. R. Buck, *Discrete-time signal processing*. Prentice Hall, 2 ed., 1999.
- [134] N. Ahmed, T. Natarajan, and K. R. Rao, "Discrete cosine transform," *IEEE Transactions on Computers*, vol. C-23, no. 1, pp. 90–93, 1974.
- [135] V. Britanak, P. Yip, and K. Rao, *Discrete Cosine and Sine Transforms: General Properties, Fast Algorithms and Integer Approximations*. Elsevier Science, 2010.

APPENDIX A: Machine Parameters

Table A.1: DFIG Parameters

Parameter	Value
Rated Capacity	1.5 MVA
Rated Voltage	575 V L-L
Stator resistance (r_s)	0.0071 p.u.
Stator ref. rotor resistance (r'_r)	0.005 p.u.
Stator leakage inductance (L_{ls})	0.1714 p.u.
Stator ref. rotor leakage inductance (L'_{lr})	0.1563 p.u.
Mutual inductance (L_m)	5.8 p.u.
Number of pole pairs (p)	3
Inertia Constant (H)	0.5 s
Simulation Time Step (T_s)	50 μ s
Identification Time Step (T_i)	5 ms
MVC Time Step (T_c)	2 ms

Table A.2: Synchronous Generator Parameters

Parameter	Value
Rated Voltage	220 V L-L
Rated Current	2.6243kA
Base Angular Frequency	50Hz
Inertial Constant	3.5s
Armature resistance	0.0025 p.u.
Poteir reactance (X_p)	0.182 p.u.
Unsaturated reactance (X_d)	1.84 p.u.
Unsaturated transient reactance (X'_d)	0.27 p.u.
Unsaturated o/c transient time ($T_{d'o'}$)	7.3 s.
Unsaturated subtransient reactance (X''_d)	0.20 p.u.
Unsaturated o/c subtransient time ($T_{d''o''}$)	0.035 s.
Unsaturated reactance (X_q)	1.41 p.u.
Unsaturated transient reactance (X'_q)	0.58 p.u.
Unsaturated o/c transient time ($T_{q'o'}$)	0.91 s.
Unsaturated subtransient reactance (X''_q)	0.20 p.u.
Unsaturated o/c subtransient time ($T_{q''o''}$)	0.06 s.
Airgap factor (p)	1.0

Table A.3: Parameters of WRIM used in HIL

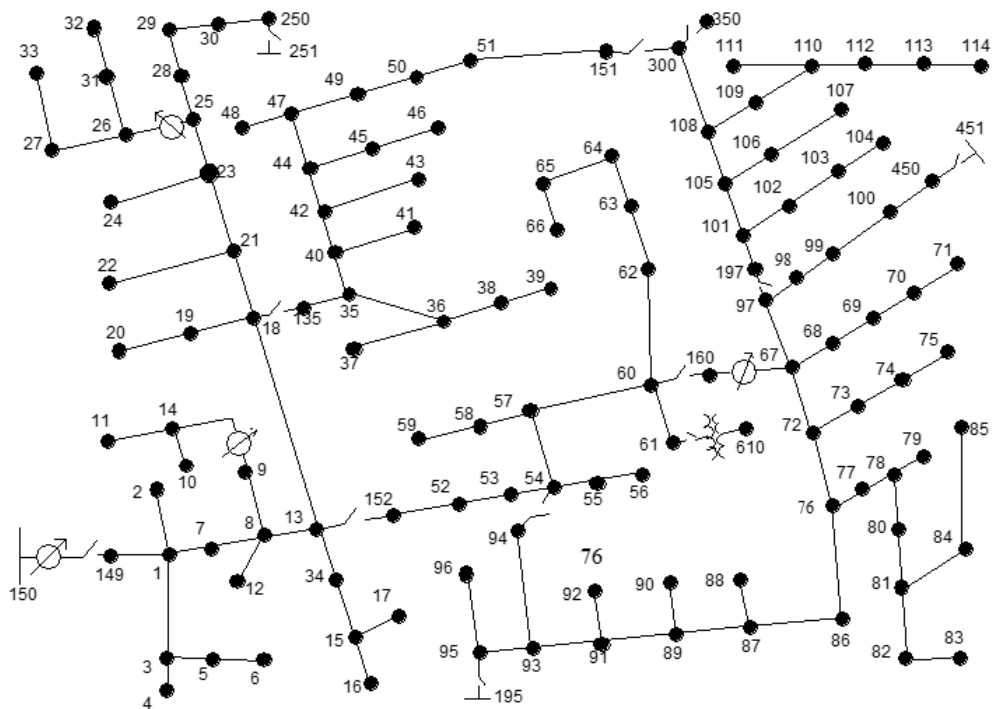
Parameter	Value
Rated Capacity	2 KW
Rated Voltage	120/208 V
Rotor Winding Voltage	624 V L-L
Stator resistance (r_s)	0.6 Ω
Rotor resistance (r_r)	4.3 Ω
Power factor	0.72
Number of pole pairs (p)	2
Simulation Time Step (T_s)	50 μs
Rated frequency	60Hz

Table A.4: Parameters of Synchronous Condenser

Parameter	SC1
Rated Capacity	340MVA
Rated Voltage	13.8KV
Inertial Constant	3.2s
Armature resistance (r_s)	0.0025p.u
Potier reactance (r_r)	0.16 p.u
X_d	1.81p.u
X'_d	0.3 p.u
X''_d	0.217 p.u
X_q	1.76p.u
X'_q	0.61 p.u
X''_q	0.217 p.u
T'_{do}	7.8s
T''_{do}	0.022s
T'_{qo}	0.90s
T''_{qo}	0.074s
Airgap factor	1

APPENDIX B: IEEE Test System

The scalability of most of the works is tested in IEEE 123 bus system to validate their performance in real grid. The one line diagram and details of the test system data is presented in this chapter.

IEEE 123 Node Test Feeder

Line Segment Data

Node A	Node B	Length (ft.)	Config.
1	2	175	10
1	3	250	11
1	7	300	1
3	4	200	11
3	5	325	11
5	6	250	11
7	8	200	1
8	12	225	10
8	9	225	9
8	13	300	1
9	14	425	9
13	34	150	11
13	18	825	2
14	11	250	9
14	10	250	9
15	16	375	11
15	17	350	11
18	19	250	9
18	21	300	2
19	20	325	9
21	22	525	10
21	23	250	2
23	24	550	11
23	25	275	2
25	26	350	7
25	28	200	2
26	27	275	7
26	31	225	11
27	33	500	9
28	29	300	2
29	30	350	2
30	250	200	2
31	32	300	11
34	15	100	11
35	36	650	8
35	40	250	1
36	37	300	9
36	38	250	10
38	39	325	10
40	41	325	11
40	42	250	1
42	43	500	10

42	44	200	1
44	45	200	9
44	47	250	1
45	46	300	9
47	48	150	4
47	49	250	4
49	50	250	4
50	51	250	4
52	53	200	1
53	54	125	1
54	55	275	1
54	57	350	3
55	56	275	1
57	58	250	10
57	60	750	3
58	59	250	10
60	61	550	5
60	62	250	12
62	63	175	12
63	64	350	12
64	65	425	12
65	66	325	12
67	68	200	9
67	72	275	3
67	97	250	3
68	69	275	9
69	70	325	9
70	71	275	9
72	73	275	11
72	76	200	3
73	74	350	11
74	75	400	11
76	77	400	6
76	86	700	3
77	78	100	6
78	79	225	6
78	80	475	6
80	81	475	6
81	82	250	6
81	84	675	11
82	83	250	6
84	85	475	11
86	87	450	6
87	88	175	9
87	89	275	6

Line Segment Data (cont.)

89	90	225	10
89	91	225	6
91	92	300	11
91	93	225	6
93	94	275	9
93	95	300	6
95	96	200	10
97	98	275	3
98	99	550	3
99	100	300	3
100	450	800	3
101	102	225	11
101	105	275	3
102	103	325	11
103	104	700	11
105	106	225	10
105	108	325	3
106	107	575	10
108	109	450	9
108	300	1000	3
109	110	300	9
110	111	575	9
110	112	125	9
112	113	525	9
113	114	325	9
135	35	375	4
149	1	400	1
152	52	400	1
160	67	350	6
197	101	250	3

Three Phase Switches		
Node A	Node B	Normal
13	152	closed
18	135	closed
60	160	closed
61	610	closed
97	197	closed
150	149	closed
250	251	open
450	451	open
54	94	open
151	300	open
300	350	open

Overhead Line Configurations (Config.)

Config.	Phasing	Phase Cond.	Neutral Cond.	Spacing
		ACSR	ACSR	ID
1	A B C N	336,400 26/7	4/0 6/1	500
2	C A B N	336,400 26/7	4/0 6/1	500
3	B C A N	336,400 26/7	4/0 6/1	500
4	C B A N	336,400 26/7	4/0 6/1	500
5	B A C N	336,400 26/7	4/0 6/1	500
6	A C B N	336,400 26/7	4/0 6/1	500
7	A C N	336,400 26/7	4/0 6/1	505
8	A B N	336,400 26/7	4/0 6/1	505
9	A N	1/0	1/0	510
10	B N	1/0	1/0	510
11	C N	1/0	1/0	510

Underground Line Configuration (Config.)

Config.	Phasing	Cable	Spacing ID
12	A B C	1/0 AA, CN	515

Transformer Data					
	kVA	kV-high	kV-low	R - %	X - %
Substation	5,000	115 - D	4.16 Gr-W	1	8
XFM - 1	150	4.16 - D	.480 - D	1.27	2.72

Shunt Capacitors			
Node	Ph-A	Ph-B	Ph-C
	kVAr	kVAr	kVAr
83	200	200	200
88	50		
90		50	
92			50
Total	250	250	250

Spot Loads							
Node	Load	Ph-1	Ph-1	Ph-2	Ph-2	Ph-3	Ph-4
	Model	kW	kVAr	kW	kVAr	kW	kVAr
1	Y-PQ	40	20	0	0	0	0
2	Y-PQ	0	0	20	10	0	0
4	Y-PQ	0	0	0	0	40	20
5	Y-I	0	0	0	0	20	10
6	Y-Z	0	0	0	0	40	20
7	Y-PQ	20	10	0	0	0	0
9	Y-PQ	40	20	0	0	0	0
10	Y-I	20	10	0	0	0	0
11	Y-Z	40	20	0	0	0	0
12	Y-PQ	0	0	20	10	0	0
16	Y-PQ	0	0	0	0	40	20
17	Y-PQ	0	0	0	0	20	10
19	Y-PQ	40	20	0	0	0	0
20	Y-I	40	20	0	0	0	0
22	Y-Z	0	0	40	20	0	0
24	Y-PQ	0	0	0	0	40	20
28	Y-I	40	20	0	0	0	0
29	Y-Z	40	20	0	0	0	0
30	Y-PQ	0	0	0	0	40	20
31	Y-PQ	0	0	0	0	20	10
32	Y-PQ	0	0	0	0	20	10
33	Y-I	40	20	0	0	0	0
34	Y-Z	0	0	0	0	40	20
35	D-PQ	40	20	0	0	0	0
37	Y-Z	40	20	0	0	0	0
38	Y-I	0	0	20	10	0	0
39	Y-PQ	0	0	20	10	0	0
41	Y-PQ	0	0	0	0	20	10
42	Y-PQ	20	10	0	0	0	0
43	Y-Z	0	0	40	20	0	0
45	Y-I	20	10	0	0	0	0
46	Y-PQ	20	10	0	0	0	0
47	Y-I	35	25	35	25	35	25
48	Y-Z	70	50	70	50	70	50
49	Y-PQ	35	25	70	50	35	20
50	Y-PQ	0	0	0	0	40	20
51	Y-PQ	20	10	0	0	0	0
52	Y-PQ	40	20	0	0	0	0
53	Y-PQ	40	20	0	0	0	0
55	Y-Z	20	10	0	0	0	0
56	Y-PQ	0	0	20	10	0	0

58	Y-I	0	0	20	10	0	0
59	Y-PQ	0	0	20	10	0	0
60	Y-PQ	20	10	0	0	0	0
62	Y-Z	0	0	0	0	40	20
63	Y-PQ	40	20	0	0	0	0
64	Y-I	0	0	75	35	0	0
65	D-Z	35	25	35	25	70	50
66	Y-PQ	0	0	0	0	75	35
68	Y-PQ	20	10	0	0	0	0
69	Y-PQ	40	20	0	0	0	0
70	Y-PQ	20	10	0	0	0	0
71	Y-PQ	40	20	0	0	0	0
73	Y-PQ	0	0	0	0	40	20
74	Y-Z	0	0	0	0	40	20
75	Y-PQ	0	0	0	0	40	20
76	D-I	105	80	70	50	70	50
77	Y-PQ	0	0	40	20	0	0
79	Y-Z	40	20	0	0	0	0
80	Y-PQ	0	0	40	20	0	0
82	Y-PQ	40	20	0	0	0	0
83	Y-PQ	0	0	0	0	20	10
84	Y-PQ	0	0	0	0	20	10
85	Y-PQ	0	0	0	0	40	20
86	Y-PQ	0	0	20	10	0	0
87	Y-PQ	0	0	40	20	0	0
88	Y-PQ	40	20	0	0	0	0
90	Y-I	0	0	40	20	0	0
92	Y-PQ	0	0	0	0	40	20
94	Y-PQ	40	20	0	0	0	0
95	Y-PQ	0	0	20	10	0	0
96	Y-PQ	0	0	20	10	0	0
98	Y-PQ	40	20	0	0	0	0
99	Y-PQ	0	0	40	20	0	0
100	Y-Z	0	0	0	0	40	20
102	Y-PQ	0	0	0	0	20	10
103	Y-PQ	0	0	0	0	40	20
104	Y-PQ	0	0	0	0	40	20
106	Y-PQ	0	0	40	20	0	0
107	Y-PQ	0	0	40	20	0	0
109	Y-PQ	40	20	0	0	0	0
111	Y-PQ	20	10	0	0	0	0
112	Y-I	20	10	0	0	0	0
113	Y-Z	40	20	0	0	0	0
114	Y-PQ	20	10	0	0	0	0
Total		1420	775	915	515	1155	635